I.R.Iran

ISSN:2423-5547
e-ISSN:2423-7469

Journal of Renewable Energy and Environment

Volume 9, Number 4, Autumn 2022

Materials and Energy Research Center

Iranian Association of Chemical Engineers

In the Name of God

Journal of Renewable Energy and Environment

DISCLAIMER

Journal of Renewable Energy and Environment: (ISSN: 2423-5547) (e-ISSN: 2423-7469)

Website: www.jree.ir, E-mail: jree@merc.ac.ir

Tel: (+9826)36280040-49 (Ext. 381), Fax: (+9826)36201888

Journal of Renewable Energy and Environment, P. O. Box: 13145-1659, Tehran, Islamic Republic of Iran

Materials and Energy Research Center (MERC); Iranian Association of Chemical Engineers (IAChE)

ISSN: 2423-5547; e-ISSN: 2423-7469

Journal of Renewable Energy and Environment (JREE): Vol. 9, No. 4, (Autumn 2022), 1-121

CONTENTS

AIMS AND SCOPE

Journal of Renewable Energy and Environment (JREE) publishes original papers, review articles, short communications and technical notes in the field of science and technology of renewable energies and environmental-related issues including:

- Generation
- Storage
- Conversion
- Distribution
- Management (economics, policies and planning)
- Environmental Sustainability

INSTRUCTIONS FOR AUTHORS

Submission of manuscript represents that it had neither been published nor submitted for publication elsewhere and is result of research carried out by author(s). Only the extended and upgraded articles presented in a conference and/or appeared in a symposium proceedings could be evaluated for publication.
Authors are required to include a list describing all the symbols and abbreviations in the paper. Use of the international system of measurement units is mandatory.

- On-line submission of manuscripts results in faster publication process and is recommended. Instructions are given in the JREE web sites: www.jree.ir
- References should be numbered in brackets and appear in sequence through the text. List of references should be given at the end of the paper. All journal articles listed in the References section must follow with article doi.
- Figure captions are to be indicated under the illustrations. They should sufficiently explain the figures.
- Illustrations should appear in their appropriate places in the text.
- Tables and diagrams should be submitted in a form suitable for reproduction.
- Photographs should be of high quality saved as jpg files.
- Tables' illustrations, figures and diagrams will be normally printed in single column width (8 cm). Exceptionally large ones may be printed across two columns (17 cm).

Journal of Renewable Energy and Environment

Journal Homepage: www.jree.ir

Materials and Energy Research Center

MERC

Research Article

Development of Rural Tourism in Iran Using PV-Based System: Finding the Best Economic Configuration

Mehdi Jahangiri [a*], Farhad Raeiszadeh [a], Reza Alayi [a,b], Atabak Najafi [c], Ahmad Tahmasebi [d]

[a] *Energy Research Center, Shahrekord Branch, Islamic Azad University, Shahrekord, Iran.*
[b] *Department of Mechanics, Germi Branch, Islamic Azad University, Germi, Iran.*
[c] *Department of Electrical Engineering, Eskisehir Osmangazi University, Eskisehir, Turkey.*
[d] *Department of Research and Development, Pars Regulator Company, Tehran, Iran.*

PAPER INFO

Paper history:
Received: 03 August 2021
Revised in revised form: 09 January 2022
Scientific Accepted: 18 January 2022
Published: 19 July 2022

Keywords:
Rural Tourism,
HOMER Software,
Sustainable Development,
Electricity Cost,
Total NPC

ABSTRACT

Rural tourism is an important factor in achieving economic, social, and cultural development. Given that villages in Iran do not have access to permanent electricity or are associated with high power outages, the provision of sustainable electricity through renewable energy can cause more tourists to choose these villages as their ultimate goal. Therefore, in this paper, for the first time, a hybrid system has been evaluated based on solar energy in 10 tourism target villages in Iran using HOMER software. This study investigated the design of the system with real and up-to-date data on equipment and fossil fuel prices taking into account transportation costs as well as a comprehensive study of energy-economic-environmental with electricity generation approach to the development of rural tourism. The results demonstrated that for the studied stations, the LCOE parameter was in the range of $ 0.615-0.722, the percentage of power supply by solar cells was in the range of 90-99 %, and the prevention of pollutants was 33.9-277 kg/year. According to the results, Meymand village is the most suitable and Mazichal village is the unsuitable station in the field of energy supply required by solar cells. The production pollution in the studied stations is mainly CO_2 and results from the operational phase of the project and its amount is 979.5 kg/year. Given that the rural tourism has grown and become a solution for development, the authors hope that the present work results can be used as a perspective to help energy and rural tourism decision-makers.

https://doi.org/10.30501/jree.2022.298089.1234

1. INTRODUCTION

Concerns about rising global energy demand, greenhouse gas emissions, attention to health, and environmental impacts from the production of non-renewable energy are important reasons that motivate countries to promote renewable energy sources [1-3]. Forecasts show that global demand for primary energy will increase by 37 % until 2040 [4]. One of the solutions for communities is to use renewable energy as a sustainable, free, accessible, and clean source [5-7]. Global statistics show the rapid energy growth in the coming decades and the use of renewable sources should increase in energy production. The renewable energy industry is now expanding more rapidly in developing countries in the face of rapid economic growth and severe energy shortages [8]. Middle Eastern countries, which are the heart of the world's fossil fuel reserves, plan to increase the use of renewable sources by 16 % up to 2035 [9]. The average annual growth of renewable energy sources is estimated at 7.6 % [10]. Among renewable energy sources, wind and solar are estimated to have the greatest potential [11], with photovoltaic and wind energy capacity growth of 28.3 % and 16 % in 2014, respectively [12]. Research shows that using systems that combine these two energies (solar photovoltaic-wind) is also an attractive solution for generating electricity, especially in places with solar and wind energy [13-15].

Nowadays, rural tourism is one of the most important forms of tourism, because it is a valuable source of income and job creation and can be an important tool for the social and economic development of rural communities. In order to protect the environment, which is a necessary condition for tourism, the use of renewable resources helps reduce the level of dependence on imported energy, guarantee energy supply, and increase the potential for regional development [16]. Solar energy provides an opportunity for the tourism industry to continue to expand as its impact on the environment diminishes. In tourism, there are important issues such as accommodation and the comfort of tourists who need a lot of electricity. With proper planning and the use of sustainable energy sources such as solar energy, sustainable development can be achieved.

*Corresponding Author's Email: jahangiri.m@iaushk.ac.ir (M. Jahangiri)
URL: https://www.jree.ir/article_153668.html

Please cite this article as: Jahangiri, M., Raeiszadeh, F., Alayi, R., Najafi, A. and Tahmasebi, A., "Development of rural tourism in Iran using PV-based system: Finding the best economic configuration", ***Journal of Renewable Energy and Environment (JREE)***, Vol. 9, No. 4, (2022), 1-9. (https://doi.org/10.30501/jree.2022.298089.1234).

The following examples illustrate the research conducted in the field of rural tourism and sustainable rural development in recent years.

In 2018, Shams et al. studied the sustainable development of rural tourism with emphasis on the role of valuable tissues using the SWOT model in Hamadan province located in Iran [17]. Based on the results, it was stated that rural revitalization and renewal strengthened the role of rural tourism. Also, if rural tourism is properly planned and managed, it can act as a stimulus in achieving sustainable development in rural areas and the tourism industry.

Rinaldi et al. [18] analyzed the economic feasibility and optimization of hybrid renewable energy systems in Peru. They employed HOMER software and their goal was to supply electricity to a village outside the national grid. Three stations in different weather conditions and seven different configurations were examined. The results showed that the wind turbine-solar cell-diesel generator system was the most economical. The lowest LCOE for these stations was $ 0.478, $ 0.460, and $ 0.504 per kWh. The use of renewable energy for these stations was estimated between 94 and 97 %.

Hoque et al. [19] proposed an energy engineering-based approach for farmers in rural Bangladesh to reduce the impact of COVID-19 on food safety. The system under study included solar cell, battery, and diesel generator and analyses were performed using HOMER software. The results showed that for small, medium, and large farms, the LCOE was $ 0.451, 0.467, and $ 0.508 per kWh, respectively. Also, the solar cell-diesel generator-battery system had a lower total NPC than the solar cell-battery-diesel generator systems and it drastically reduced greenhouse gas emissions.

Anwar et al. [20] evaluated the feasibility and sensitivity of the system including wind, solar, biogas, fuel cell, diesel generator, and battery for a village outside the national grid in India using HOMER software. Seven different scenarios were examined and the results showed that without government support, the minimum LCOE would be $ 0.207 per kWh. With government support and fines set for pollutants, the LCOE was estimated at $ 0.12 per kWh. In addition, the results of sensitivity analysis showed that total NPC was the most sensitive to load changes and the least sensitive to wind speed.

Nebey et al. [21] used Matlab and HOMER software to design a combined power generation system for rural areas in Ethiopia. The optimal system included a solar cell, wind turbine, and hydropower that provided 13, 52, and 35 % of the required electricity, respectively. Then, in MATLAB software, they designed a control system in which the result obtained from combining resources showed that supply and demand were balanced. A fuzzy logic control system was also designed to manage demand and available resources.

Sharma et al. [22] used HOMER software to economically evaluate a renewable energy system in the rural areas of India. They used biomass from agricultural waste and photovoltaics. The purpose was to meet the needs of cooking, water pumping, and street lighting at a rate of 510 kWh per day. The results showed that the optimal system had a total NPC of $ 76837 and the price per kWh of energy produced was $ 0.032. The optimal system had 0.5 kW solar cell, 40 kW diesel generator, and 40 batteries of S460 model and it was a 35-kW electrical converter. Overall, the accuracy of HOMER software is sufficient to show the optimized solution for the changing needs of electricity and to confirm the economic feasibility.

A review of the present article is important from two perspectives:

1. Iran is a country with various potentials and attractions, which can play an effective role as a pole in the development of tourism in the country. Rural areas are also one of the most important tourist destinations in this country, but Iran faces serious challenges in this area, such as management, energy supply, and environmental protection. The pristine, attractive, and clean environment of most tourist villages in Iran is in conflict with fossil fuels. Since the preservation of the environment and responsible circulation in nature is the essence of this type of tourism, the use of clean and renewable energy while having the positive effects of rural tourism also prevents threatening the clean environment of the village.

2. Iran is one of the richest countries in the world in terms of various energy sources and in addition to extensive sources of fossil and non-renewable fuels such as oil and gas, it has a great potential for renewable energy such as wind, solar, biomass, and geothermal. However, Iran is completely dependent on fossil fuels for the industrial, residential, and transportation sectors [23]. Fossil energy carriers provide more than 98 % of energy in Iran. However, according to studies by Aghahseni et al. [24], renewable energy systems are a reliable and low-cost option for Iran in the medium-term future. In this paper, for the first time, 10 special and attractive tourist villages in Iran are selected and the superior features of each are expressed. Then, the possibility of creating an independent solar-diesel generator hybrid system in these villages is investigated using HOMER software. The parameters studied in the present work are the price of kWh for electricity produced, total net present cost, amount of pollutants produced due to the use of diesel generators, determining the percentage of electricity production by solar cells, and investigating the amount of losses in the optimal economic system. The authors of this article hope that the results of the present work are used in the optimal use of rural tourism potentials for the development of rural areas in all economic, socio-cultural, and environmental dimensions.

2. SOLAR ENERGY IN IRAN

Iran is one of the most suitable countries in the world in terms of receiving solar energy and the average annual hours of sunshine are more than 2900 hours [11]. In the central part of Iran, due to its hot and dry climate, it is estimated at 3200 hours per year [25] and this shows that solar energy constitutes a significant part of the country's energy consumption in the future. Iran currently has the world’s 14th largest solar power plant and the total potential of the country to produce solar energy is estimated at 40,000 GWh [11]. Figure 1 shows the average annual radiation in Iran on the horizontal surface [26].

The ten specific villages of Iran, which are shown in Figure 2, are Sar Aqa Seyyed village, Sarakhiyeh village, Makhunik village, Ab Ask village, Abyaneh village, Kandovan village, Meymand village, Hawraman village, Mazichal village, and Nusha village. The locations of the studied villages are shown in Figure 2.

3. HOMER SOFTWARE AND REQUIRED DATA

HOMER Software is one of the best-specialized software for designing microgrid power networks [32, 33], used to model and optimize hybrid renewable energy systems. One of the

most important features of HOMER Software is the possibility of accurate simulation of the examined system over different time periods and the possibility of estimating the final cost and the degree of optimization of the system [34, 35]. The optimization performed by HOMER software is that the various configurations are examined using the available equipment and the configurations with the lowest total NPC value are selected as the optimal systems [36, 37].

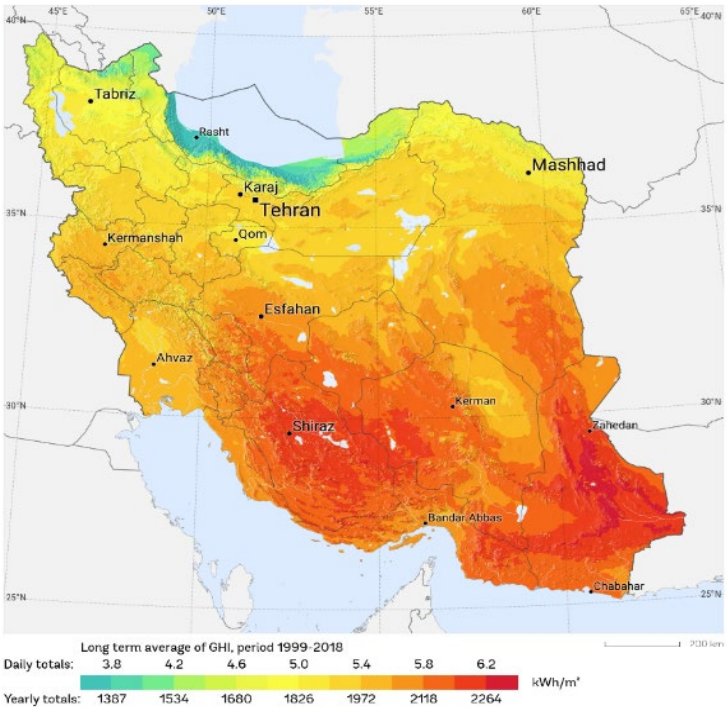

Figure 1. Average annual radiation on the horizontal surface

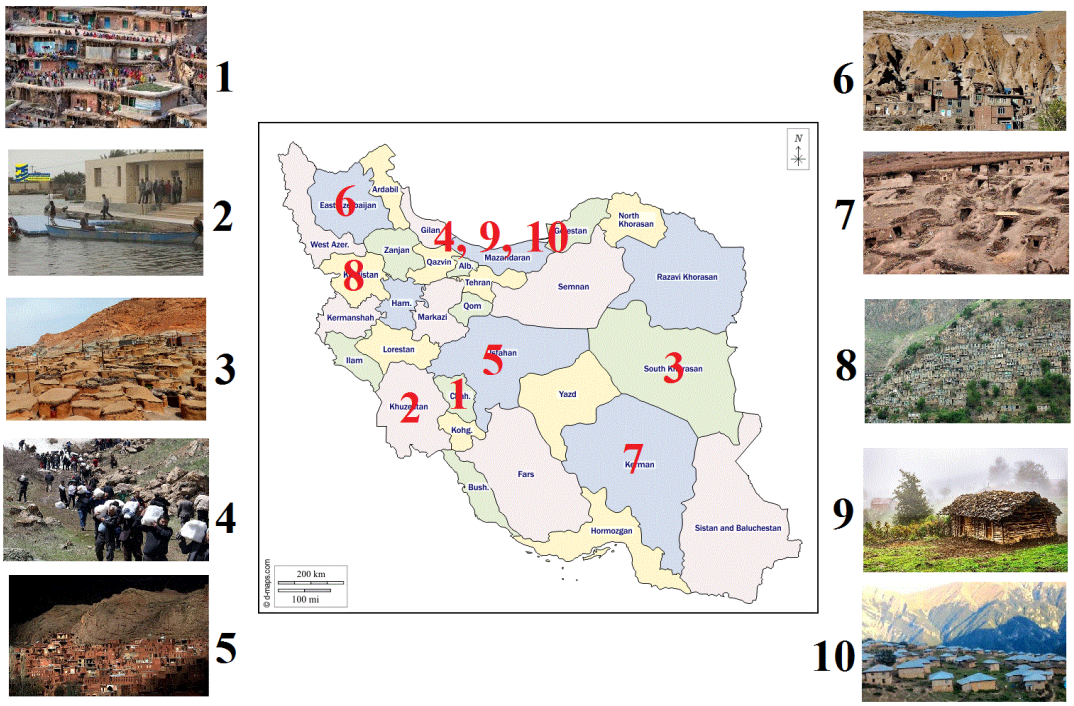

Figure 2. Location of the studied stations

In the present study, the annual interest rate is 10 %, project lifetime is 25 years, pollutants' penalties are zero, fuel prices are $ 0.19214 per liter. In addition, altitude as well as geographical and climatic information are listed in Table 1 and Table 2 and daily electricity consumption is 5.9 kWh with a peak value of 806 W. Considering that both installation and disposal phases affect the total production pollutants, it should be noted that the production pollutants in the present work result from the operational stage and the consumption of diesel fossil fuel by diesel generators.

Schematics of the simulated system and the amount of power required for 24 hours are shown in Figures 3 and 4, respectively. The prices of the equipment used in this project and their other specifications for power supply are given in Table 3 [38-43].

Table 1. Geographical information of the studied stations

Station	Longitude	Latitude	Elevation (m)
Sar Aqa Seyyed	49 52	32 40	2100
Sarakhiyeh	48 32	30 41	3.01
Makhunik	60 24	32 27	1600
Ab Ask	52 8	35 52	1852
Abyaneh	51 35	33 35	2222
Kandovan	46 14	37 47	2232
Meymand	55 22	30 13	2213
Hawraman	46 15	35 15	1417
Mazichal	51 6	36 31	2600
Nusha	50 38	36 36	2006

Table 2. Climatic information of the studied stations

Station	Parameter	Jan.	Feb.	Mar.	Apr.	May	Jun.	Jul.	Aug.	Sep.	Oct.	Nov.	Dec.	Average
Sar Aqa Seyyed	Solar (kWh/m^2-day)	2.970	3.910	4.640	5.550	6.740	7.740	7.310	6.850	5.910	4.450	3.220	2.670	5.169
	Clearness index	0.542	0.578	0.547	0.550	0.607	0.674	0.649	0.657	0.656	0.613	0.560	0.526	0.606
Sarakhiyeh	Solar (kWh/m^2-day)	3.260	4.370	4.830	5.620	6.670	7.590	7.330	6.720	5.770	4.150	3.070	2.830	5.187
	Clearness index	0.562	0.620	0.556	0.552	0.600	0.664	0.652	0.640	0.629	0.552	0.506	0.523	0.597
Makhunik	Solar (kWh/m^2-day)	3.240	4.090	4.900	5.690	6.450	6.970	6.930	6.700	5.790	4.630	3.520	2.960	5.161
	Clearness index	0.588	0.602	0.576	0.563	0.580	0.607	0.615	0.642	0.641	0.636	0.608	0.579	0.604
Ab Ask	Solar (kWh/m^2-day)	2.750	3.580	4.450	5.520	6.390	7.310	6.910	6.370	5.390	3.970	2.890	2.390	4.832
	Clearness index	0.557	0.570	0.548	0.557	0.576	0.633	0.612	0.618	0.619	0.583	0.553	0.528	0.586
Abyaneh	Solar (kWh/m^2-day)	3.090	4.100	4.940	5.830	6.640	7.340	6.960	6.620	5.780	4.430	3.360	2.850	5.166
	Clearness index	0.580	0.619	0.589	0.581	0.598	0.638	0.617	0.636	0.648	0.621	0.600	0.580	0.612
Kandovan	Solar (kWh/m^2-day)	2.550	3.380	4.450	5.320	6.480	7.420	7.210	6.440	5.260	3.770	2.650	2.170	4.765
	Clearness index	0.552	0.565	0.564	0.544	0.586	0.641	0.638	0.630	0.617	0.577	0.539	0.517	0.591
Meymand	Solar (kWh/m^2-day)	3.570	4.550	5.210	5.980	6.920	7.280	7.040	6.750	5.940	4.940	3.890	3.280	5.450
	Clearness index	0.607	0.639	0.596	0.586	0.623	0.637	0.627	0.643	0.645	0.652	0.633	0.598	0.624
Hawraman	Solar (kWh/m^2-day)	2.590	3.370	4.420	5.330	6.810	7.870	7.610	7.030	5.940	4.130	2.940	2.270	5.034
	Clearness index	0.513	0.529	0.540	0.536	0.614	0.682	0.674	0.680	0.677	0.599	0.551	0.490	0.607
Mazichal	Solar (kWh/m^2-day)	1.800	2.410	3.320	4.440	5.600	6.590	6.140	5.620	4.820	3.400	2.270	1.590	4.007
	Clearness index	0.373	0.390	0.413	0.450	0.505	0.570	0.544	0.546	0.557	0.506	0.443	0.360	0.490
Nusha	Solar (kWh/m^2-day)	2.320	3.030	3.910	4.910	5.980	6.750	6.320	5.880	4.970	3.500	2.480	2.000	4.343
	Clearness index	0.482	0.491	0.487	0.498	0.540	0.584	0.560	0.572	0.575	0.522	0.485	0.455	0.531

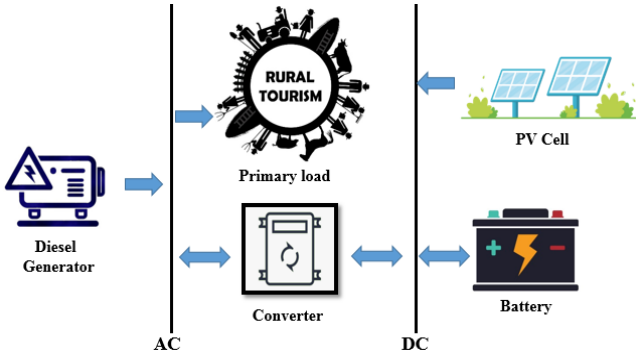

Figure 3. Schematic of the simulated system

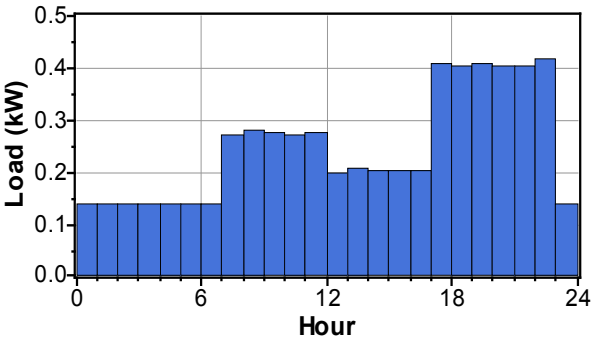

Figure 4. The amount of electricity required within 24 hours

Table 3. Technical and economic information of the equipment used in the solar-diesel system

Equipment	Cost ($)			Size (kW)	Other information
	Capital	Replacement	O & M		
PV [38]	3200	3000	0	0-4	Lifetime: 20 years, Derating factor: 90 %, Ground reflectance: 20 %
Battery T-105 [39]	174	174	5	0-20	Nominal Voltage: 6, Nominal capacity: 225 Ah, Lifetime throughput: 845 kWh
Diesel generator [40, 41]	200	200	0.5	0-2	Lifetime: 15000 hr, Minimum load ratio: 30 %, Max. Efficiency: 31 %
Converter [42, 43]	200	200	10	0-2	Lifetime: 10 years, Efficiency: 90 %

HOMER software uses the following equation to calculate the production capacity of solar cells [44]:

$$P_{pv} = Y_{pv} \times f_{pv} \times \frac{\overline{H}_T}{\overline{H}_{T,STC}} \quad (1)$$

In the above equation, Y_{pv} is the rated capacity of photovoltaic cells in kW, f_{pv} the derating factor, $\overline{H}_T$ the solar radiation hitting the cell surface in operating conditions in terms of kW/m^2, $\overline{H}_{T,STC}$ solar radiation that hits the surface under standard test conditions and is equal to one kW/m^2, and P_{pv} the output power of photovoltaic cells in kW.

The efficiency of the diesel generator is obtained by the following equation [45]:

$$\eta_{gen} = \frac{3.6\ P_{gen}}{\dot{m}_{fuel} \times LHV_{fuel}} \quad (2)$$

In this equation P_{gen} is the electricity produced by diesel generators in kW, $\dot{m}_{fuel}$ is the fuel consumption in liters per hour, and LHV_{fuel} is the low calorific value of fuel in MJ/kg.

Battery performance is calculated as follows [46]:

$$P_{batt.cmax} = \frac{\text{Min}\ (P_{batt.cmax.kbm}, P_{batt.cmax.mcr}, P_{batt.cmax.mcc})}{\eta_{batt.c}} \quad (3)$$

In this equation, $P_{batt,\ cmax}$ maximum is battery charge capacity in kWh, $\eta_{batt,c}$ battery charging efficiency in percentage, $P_{batt,\ cmax,\ kbm}$ maximum battery charging capacity based on kinetic battery model in kWh, $P_{batt,\ cmax,\ mcr}$ maximum battery charge capacity based on maximum charge rate, and $P_{batt,\ cmax,\ mcc}$ the maximum battery charging capacity based on maximum charging current in kWh.

The total net present cost is calculated using the following equation [47]:

$$NPC = \frac{C_{ann,total}}{CRF\ (i, R_{proj})} \quad (4)$$

while $C_{ann,total}$ is the total annual cost, CRF return factor of investment, i real interest rates, and R_{proje} the lifetime of the project. The return factor of investment, which represents the return on investment during N years, is calculated using the following equation [48]:

$$CRF = \frac{i\ (1+i)^N}{(1+i)^N - 1} \quad (5)$$

Also, during the useful lifetime of the project, the cost per kWh of energy is obtained by HOMER software through the following equation [49]:

$$COE = \frac{C_{ann,total}}{E_{Load\ served}} \quad (6)$$

In the above equation, $E_{Load\ Served}$ is the actual electric charge by the hybrid system in kWh/year.

The framework of software performance is shown in Figure 5 [50]. Considering that the penalty for pollutants produced by fossil fuel-based systems in Iran is zero, the optimization of the present work is purely economic and the optimal system is a system that has the lowest total NPC and is not necessarily the system that produces the least pollutants. Another limitation of optimization by HOMER software is that voltage changes and fluctuations cannot be taken into account, power interruptions cannot be simulated, and fluctuations and changes in electrical load in less than an hour cannot be simulated. Also, the limitation in the number of available and accessible equipment is another limitation of optimization by this software.

The limitations of optimization are related to the limitations of software and those of search space to find the optimal configuration. Resizing systems can be about examining different configurations using available equipment and have nothing to do with optimization constraints.

4. RESULTS AND DISCUSSION

The results of the simulations for the studied stations are given in Table 4. The important point that can be seen from the results is that in all the studied villages, the use of solar energy is cost effective. In all villages, according to the electricity required, 2 kW of solar cells, 1 kW of diesel generator, and 1 kW electric converter have been used.

In the economic optimum results for each station, the difference between stations is in the amount of battery usage so that for villages with lower radiation intensity, fewer batteries have been used. The smallest number of batteries (11 batteries) is related to Sarakhiyeh and Meymand villages, while the largest number of batteries (15 batteries) belongs to Mazichal and Nusha villages. The villages of Meymand with $ 12053 and Mazichal with $ 14,166 had the lowest and highest net total costs, respectively, which resulted in a cost of $ 0.615 and $ 0.722 per kWh of generated electricity. Another important point that can be seen from the results of Table 4 is that the generated renewable electricity is cheaper than the generated fossil electricity.

According to the results, the highest and lowest percentages of the usage of renewable energy are 99 % (Makhunik, Abyaneh, and Meymand villages) and 90 % (Mazichal village), respectively. Due to the use of diesel fuel in diesel generators in all villages, annually, maximum of 277 kg of carbon dioxide (Mazichal village) and a minimum of 33.9 kg of carbon dioxide (Meymand village) are produced. According to the results, the highest usage of diesel generators is 341 hours per year which is related to Mazichal village, which leads to 105 liters of diesel consumption per year. The minimum use of diesel generators is 50 hours per year and is related to the villages of Meymand and Makhunik, which leads to the consumption of 13 liters of diesel per year. Based on the results, it can be seen that the Meymand village is most suitable from the economic-environmental point of view for

the use of renewable hybrid systems. Therefore, Table 5 provides more details about the results of the optimal system for Meymand. Based on the results of Table 5, it can be seen that diesel generators are not needed to generate electricity in 9 months of the year and diesel generators are used only in March, April, and August. In total, annually, 3962 kWh of solar electricity is generated which is due to the 4388-hour operation of solar cells and 35 kWh of electricity is generated by diesel generators. During the year, there is about 34 % of surplus electricity (1360 kWh) which would significantly reduce electricity production if sold to the national grid. Regarding the evaluation of hybrid system losses in Meymand village, it should be noted that in batteries, inverters, and rectifiers, there will be 231, 239, and 3 kWh of annual losses, respectively.

Figure 6 shows a comparison of the optimal system (solar cell-diesel generator) with the traditional power generation system (diesel generator only). According to the results, the payback time for an optimal system investment is about 2 years and at the end of the project's useful lifetime (25-year), due to the cheaper solar power, there will be an economic saving of $ 101020.

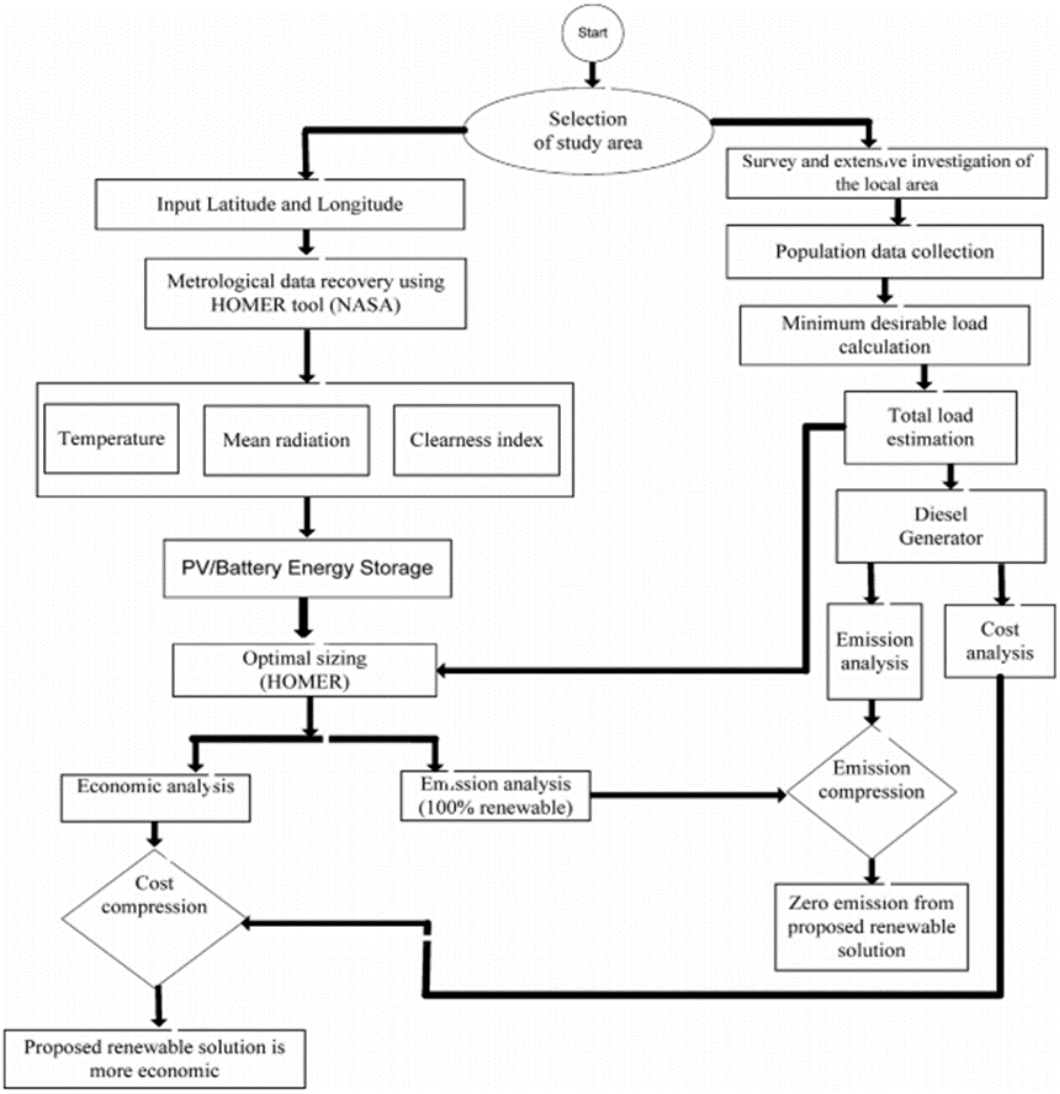

Figure 5. The framework of optimization performed by HOMER software [50]

Table 4. Optimal economic results for each station

Station					Total NPC ($)	COE ($/kWh)	Ren. Frac.	CO_2 (kg/yr)	Diesel (L)	Generator (hrs)
Sar Aqa Seyyed	2	1	12	1	12399	0.632	0.98	74.9	28	92
Sarakhiyeh	2	1	11	1	12529	0.639	0.97	115	44	153
Makhunik	2	1	12	1	12258	0.625	0.99	34.5	13	50
Ab Ask	2	1	13	1	12652	0.645	0.97	80	32	108
Abyaneh	2	1	12	1	12202	0.622	0.99	37.4	14	51
Kandovan	2	1	13	1	12720	0.649	0.97	97.2	37	122
Meymand	2	1	11	1	12053	0.615	0.99	33.9	13	50
Hawraman	2	1	13	1	12584	0.642	0.98	79.6	30	97
Mazichal	2	1	15	1	14166	0.722	0.90	277	105	341
Nusha	2	1	15	1	13392	0.683	0.95	150	57	192

Table 5. Results of the best scenario for Meymand village

Comp.	Jan.	Feb.	Mar.	Apr.	May	Jun.	Jul.	Aug.	Sep.	Oct.	Nov.	Dec.
PV array	0.398	0.455	0.452	0.452	0.473	0.475	0.471	0.487	0.488	0.467	0.425	0.380
Generator	0.000	0.000	0.027	0.010	0.000	0.000	0.000	0.010	0.000	0.000	0.000	0.000

Comp.	Production (kWh/yr)	Excess electricity (kWh/yr)	Hours of operation (hr/yr)	Battery Losses (kWh/yr)	Inverter/Rectifier Losses (kWh/yr)
PV array	3962	1360	4388	231	239/3
Generator	35		50		

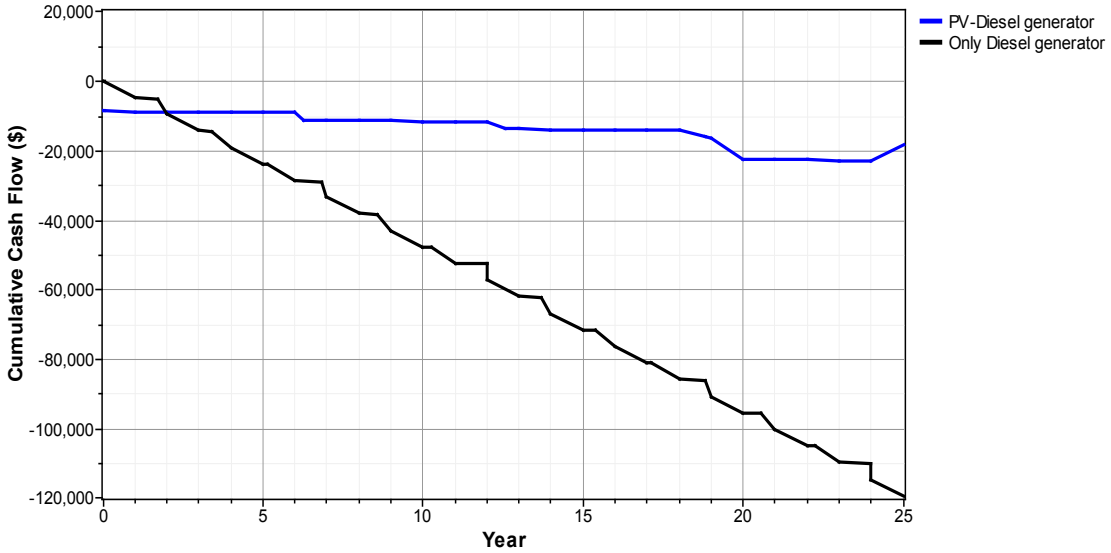

Figure 6. Comparison of the optimal system and the traditional system

5. CONCLUSIONS

Nowadays, rural tourism has become one of the most important economic sectors in many countries of the world and governments have implemented various policies to develop rural tourism on various scales, from local to national level.

Therefore, the purpose of this paper is to evaluate the feasibility of supplying electricity to a rural settlement in ten specific villages of Iran using a solar-diesel generator-battery hybrid system. Using the up-to-date equipment prices and average fuel prices in Iran (including transportation costs), Using 20 years of average solar radiation data, and technical-economic-environmental study of the solar-based hybrid system are other benefits of the present work. The results showed that:

- In all surveyed villages, the use of solar energy was cost effective.

-In the optimal economic results for each station, the difference between the stations was in the amount of battery usage.

- The villages of Meymand with $ 12053 and Mazichal with $ 14,166 had the lowest and highest net total costs, respectively, which yielded costs of $ 0.615 and $ 0.722 per kWh of generated electricity.

- In the studied villages, renewable electricity is cheaper than fossil electricity.

- The highest and lowest percentages of the usage of renewable energy are 99 % (Makhunik, Abyaneh, and Meymand villages) and 90 % (Mazichal village), respectively.

-Due to the use of diesel fuel in diesel generators in all villages, annually, maximum of 277 kg of carbon dioxide (Mazichal village) and a minimum of 33.9 kg of carbon dioxide (Meymand village) are produced.

-Meymand is the most suitable village from the economic point of view for using renewable hybrid systems.

- Only in March, April, and August in the village of Meymand, a diesel generator is needed to generate electricity.

- 3962 kWh of solar electricity and 35 kWh of fossil electricity are produced annually in Meymand village.

- During the year, there is about 34 % of surplus electricity (1360 kWh) in Meymand village.

- In Meymand village and in comparison with the traditional power generation system (diesel generator only), the payback time for an optimal system investment is about 2 years and at the end of the project's useful lifetime (25-year), due to the cheaper solar power, there will be an economic saving of $ 101020.

- Since many villages in Iran are very similar to these villages in terms of natural, cultural, social, and economic characteristics, the results of the present paper can be generalized to other villages.

The authors of this article hope that to create infrastructure services for accommodation facilities in the field of rural tourism, proper planning can improve the economic situation of the studied villages.

6. ACKNOWLEDGEMENT

The authors would like to thank all the organizations that provided data for this work.

REFERENCES

1. Rahman, S., Issa, S., Said, Z., Assad, M.E.H., Zadeh, R. and Barani, Y., "Performance enhancement of a solar powered air conditioning system using passive techniques and SWCNT/R-407c nano refrigerant", ***Case Studies in Thermal Engineering***, Vol. 16, (2019), 100565. (https://doi.org/10.1016/j.csite.2019.100565).
2. Assad, M.E.H., Nazari, M.A. and Rosen, M.A., "Applications of renewable energy sources", Design and performance optimization of renewable energy systems, Academic Press, (2021), 1-15. (https://doi.org/10.1016/B978-0-12-821602-6.00001-8).
3. Prabatha, T., Karunathilake, H., Shotorbani, A.M., Sadiq, R. and Hewage, K., "Community-level decentralized energy system planning under uncertainty: A comparison of mathematical models for strategy development", ***Applied Energy***, Vol. 283, (2021), 116304. (https://doi.org/10.1016/j.apenergy.2020.116304).
4. World Energy Outlook, Executive summary, (2014). (http://www.worldenergyoutlook.org), (Accessed: 10 February 2022).
5. Ahmadi, A., Ehyaei, M.A., Doustgani, A., Assad, M.E.H., Esmaeilion, F., Hmida, A., Jamali, D.H., Kumar, R., Li, Z.X. and Razmjoo, A., "Recent progress in thermal and optical enhancement of low temperature solar collector", ***Energy Systems***, (2021), 1-40. (https://doi.org/10.1007/s12667-021-00473-5).
6. Khosravi, A., Malekan, M. and Assad, M.E.H., "Numerical analysis of magnetic field effects on the heat transfer enhancement in ferrofluids for a parabolic trough solar collector", ***Renewable Energy***, Vol. 134, (2019), 54-63. (https://doi.org/10.1016/j.renene.2018.11.015).
7. Kumar, K.G., Hani, E.H.B., Assad, M.E.H., Rahimi-Gorji, M. and Nadeem, S., "A novel approach for investigation of heat transfer enhancement with ferromagnetic hybrid nanofluid by considering solar radiation", ***Microsystem Technologies***, Vol. 27, No. 1, (2021), 97-104. (https://doi.org/10.1007/s00542-020-04920-8).
8. Ahmadi, A., Ehyaei, M.A., Doustgani, A., Assad, M.E.H., Hmida, A., Jamali, D.H., Kumar, R., Li, Z.X. and Razmjoo, A., "Recent residential applications of low-temperature solar collector", ***Journal of Cleaner Production***, Vol. 279, (2021), 123549. (https://doi.org/10.1016/j.jclepro.2020.123549).
9. Afsharzade, N., Papzan, A., Ashjaee, M., Delangizan, S., Van Passel, S. and Azadi, H., "Renewable energy development in rural areas of Iran", ***Renewable and Sustainable Energy Reviews***, Vol. 65, (2016), 743-755. (https://doi.org/10.1016/j.rser.2016.07.042).
10. Outlook, B.P. Energy outlook 2030, BP Publishers, London, (2012). (https://www.bp.com/content/dam/bp/business-sites/en/global/corporate/pdfs/energy-economics/energy-outlook/bp-energy-outlook-2012.pdf), (Accessed: 10 February 2022).
11. Iran wind map, VORTEX, (2022). (https://www.vortexfdc.com/assets/docs/vortex_3km_iran_wind_map_resource.pdf), (Accessed: 10 February 2022).
12. REN21, Renewables global status report 2015, Technical report, Renewable Energy Policy Network for the 21st century. (https://www.ren21.net/reports/global-status-report), (Accessed: 10 February 2022).
13. Makkiabadi, M., Hoseinzadeh, S., Mohammadi, M., Nowdeh, S.A., Bayati, S., Jafaraghaei, U., Mirkiai, S.M. and Assad, M.E.H., "Energy feasibility of hybrid PV/wind systems with electricity generation assessment under Iran environment", ***Applied Solar Energy***, Vol. 56, No. 6, (2020), 517-525. (https://doi.org/10.3103/S0003701X20060079).
14. Jahangiri, M., Ghaderi, R., Haghani, A. and Nematollahi, O., "Finding the best locations for establishment of solar-wind power stations in Middle-East using GIS: A review", ***Renewable and Sustainable Energy Reviews***, Vol. 66, (2016), 38-52. (https://doi.org/10.1016/j.rser.2016.07.069).
15. Ehyaei, M.A., Ahmadi, A., Assad, M.E.H., Hachicha, A.A. and Said, Z.J.S.E., "Energy, exergy and economic analyses for the selection of working fluid and metal oxide nanofluids in a parabolic trough collector", ***Solar Energy***, Vol. 187, (2019), 175-184. (https://doi.org/10.1016/j.solener.2019.05.046).
16. Zhang, D. and Allagui, A., "Fundamentals and performance of solar photovoltaic systems", In Design and Performance Optimization of Renewable Energy Systems, ***Academic Press***, (2021), 117-129. (https://doi.org/10.1016/B978-0-12-821602-6.00009-2).
17. Rinaldi, F., Moghaddampoor, F., Najafi, B. and Marchesi, R., "Economic feasibility analysis and optimization of hybrid renewable energy systems for rural electrification in Peru", ***Clean Technologies and Environmental Policy***, Vol. 23, No. 3, (2021), 731-748. (https://doi.org/10.1007/s10098-020-01906-y).
18. Hoque, M.N., Ahmed, S.M., Basher, M.K. and Das, N., "Energy engineering approach for rural areas cattle farmers in Bangladesh to reduce COVID-19 impact on food safety", ***Sustainability***, Vol. 12, No. 20, (2020), 8609. (https://doi.org/10.3390/su12208609).
19. Nebey, A.H., "Design of optimal hybrid power system to provide reliable supply to rural areas of Ethiopia using MATLAB and HOMER", ***Renewables: Wind, Water, and Solar***, Vol. 8, No. 1, (2021), 1-7. (https://doi.org/10.1186/s40807-021-00067-w).
20. Anwar, K., Deshmukh, S. and Mustafa Rizvi, S., "Feasibility and sensitivity analysis of a hybrid photovoltaic/wind/biogas/fuel-cell/diesel/battery system for off-grid rural electrification using HOMER", ***Journal of Energy Resources Technology***, Vol. 142, No. 6, (2020), 061307. (https://doi.org/10.1115/1.4045880).
21. Sharma, K.K., Gupta, A., Kumar, R., Chohan, J.S., Sharma, S., Singh, J., Khalilpoor, N., Issakhov, A., Chattopadhyaya, S. and Dwivedi, S.P., "Economic evaluation of a hybrid renewable energy system (HRES) using hybrid optimization model for electric renewable (HOMER) software-a case study of rural India", ***International Journal of Low-Carbon Technologies***, Vol. 16, No. 3, (2021), 814-821. (https://doi.org/10.1093/ijlct/ctab012).
22. Shams, M., Nobakht Nejat, A. and Amiri, M., "Sustainable rural tourism development with emphasis on the role of rural valuable textures using SWOT model (Case study: Simin village of Hamedan)", ***Journal of Tourism Hospitality Research***, Vol. 5, No. 3, (2018), 5-23. (In Farsi). (https://dorl.net/dor/20.1001.1.20089562.2018.5.3.1.7).
23. Mollahosseini, A., Hosseini, S.A., Jabbari, M., Figoli, A. and Rahimpour, A., "Renewable energy management and market in Iran: A holistic review on current state and future demands", ***Renewable and Sustainable Energy Reviews***, Vol. 80, (2017), 774-788. (https://doi.org/10.1016/j.rser.2017.05.236).
24. Aghahosseini, A., Bogdanov, D., Ghorbani, N. and Breyer, C., "Analysis of 100 % renewable energy for Iran in 2030: Integrating solar PV, wind energy and storage", ***International Journal of Environmental Science and Technology***, Vol. 15, No. 1, (2018), 17-36. (https://doi.org/10.1007/s13762-017-1373-4).
25. Edalati, S., Ameri, M., Iranmanesh, M. and Sadeghi, Z., "Solar photovoltaic power plants in five top oil-producing countries in Middle East: A case study in Iran", ***Renewable and Sustainable Energy Reviews***, Vol. 69, (2017), 1271-1280. (https://doi.org/10.1016/j.rser.2016.12.042).
26. Solar resource maps of Iran, SOLRAGIS, Global Horizontal Irradiation, (2021). (https://solargis.com/maps-and-gis-data/download/iran), (Accessed: 31 May 2021).
27. Purohit, I. and Purohit, P., "Wind energy in India: Status and future prospects", ***Journal of Renewable and Sustainable Energy***, Vol. 1, No. 4, (2009), 042701. (https://doi.org/10.1063/1.3156003).
28. Nedaei, M., Assareh, E. and Biglari, M., "An extensive evaluation of wind resource using new methods and strategies for development and utilizing wind power in Mah-shahr station in Iran", ***Energy Conversion and Management***, Vol. 81, (2014), 475-503. (https://doi.org/10.1016/j.enconman.2014.02.025).
29. Mostafaeipour, A., Jadidi, M., Mohammadi, K. and Sedaghat, A., "An analysis of wind energy potential and economic evaluation in Zahedan, Iran", ***Renewable and Sustainable Energy Reviews***, Vol. 30, (2014), 641-650. (https://doi.org/10.1016/j.rser.2013.11.016).
30. Tummala, A., Velamati, R.K., Sinha, D.K., Indraja, V. and Krishna, V.H., "A review on small scale wind turbines", ***Renewable and Sustainable Energy Reviews***, Vol. 56, (2016), 1351-1371. (https://doi.org/10.1016/j.rser.2015.12.027).
31. Jahangiri, M. and Shamsabadi, A.A., "Designing a horizontal-axis wind turbine for South Khorasan province: A case study", ***International Journal of Precision Engineering and Manufacturing***, Vol. 18, No. 10, (2017), 1463-1473. (https://doi.org/10.1007/s12541-017-0174-5).
32. Vahdatpour, S., Behzadfar, S., Siampour, L., Veisi, E. and Jahangiri, M., "Evaluation of off-grid hybrid renewable systems in the four climate regions of Iran", ***Journal of Renewable Energy and Environment (JREE)***, Vol. 4, No. 1, (2017), 61-70. (https://dx.doi.org/10.30501/jree.2017.70107).

33. Jahangiri, M., Khosravi, A., Raiesi, H.A. and Mostafaeipour, A., "Analysis of standalone PV-based hybrid systems for power generation in rural area", ***Proceedings of International Conference on Fundamental Research in Electrical Engineering***, Tehran, Iran, (2017), 1-10. (In Farsi). (https://en.civilica.com/doc/672922).
34. Jahangiri, M., Nematollahi, O., Sedaghat, A. and Saghafian, M., "Techno-economical assessment of renewable energies integrated with fuel cell for off grid electrification: A case study for developing countries", ***Journal of Renewable and Sustainable Energy***, Vol. 7, No. 2, (2015), 023123. (https://doi.org/10.1063/1.4918592).
35. Nematollahi, O., Alamdari, P., Jahangiri, M., Sedaghat, A. and Alemrajabi, A.A., "A techno-economical assessment of solar/wind resources and hydrogen production: A case study with GIS maps", ***Energy***, Vol. 175, (2019), 914-930. (https://doi.org/10.1016/j.energy.2019.03.125).
36. Mostafaeipour, A., Rezaei, M., Jahangiri, M. and Qolipour, M., "Feasibility analysis of a new tree-shaped wind turbine for urban application: A case study", ***Energy & Environment***, Vol. 31, No. 7, (2020), 1230-1256. (https://doi.org/10.1177%2F0958305X19888878).
37. Rezaei, M., Khalilpour, K.R. and Jahangiri, M., "Multi-criteria location identification for wind/solar based hydrogen generation: The case of capital cities of a developing country", ***International Journal of Hydrogen Energy***, Vol. 45, No. 58, (2020), 33151-33168. (https://doi.org/10.1016/j.ijhydene.2020.09.138).
38. Ariae, A.R., Jahangiri, M., Fakhr, M.H. and Shamsabadi, A.A., "Simulation of biogas utilization effect on the economic efficiency and greenhouse gas emission: A case study in Isfahan, Iran", ***International Journal of Renewable Energy Development***, Vol. 8, No. 2, (2019), 149-160. (https://doi.org/10.14710/ijred.8.2.149-160).
39. Jahangiri, M., Haghani, A., Heidarian, S., Mostafaeipour, A., Raiesi, H.A. and Shamsabadi, A.A., "Sensitivity analysis of using solar cells in regional electricity power supply of off-grid power systems in Iran", ***Journal of Engineering, Design and Technology***, Vol. 18, No. 6, (2020), 1849-1866. (https://doi.org/10.1108/JEDT-10-2019-0268).
40. Shamsabadi, A.A., Jahangiri, M., Bardei, F.K. and Raeisi, H.A., "Investigation of sensitivity analysis in the generation of renewable electricity for a hybrid system in Iran", ***Proceedings of The 12th International Energy Conference (IEC 2018)***, Tehran, Iran, (2018), 1-14. (In Farsi). (https://en.civilica.com/doc/848589).
41. Jahangiri, M., Haghani, A., Mostafaeipour, A., Khosravi, A. and Raeisi, H.A., "Assessment of solar-wind power plants in Afghanistan: A review". ***Renewable and Sustainable Energy Reviews***, Vol. 99, (2019), 169-190. (https://doi.org/10.1016/j.rser.2018.10.003).
42. Ghaderian, A., Jahangiri, M. and Saghaei, H., "Emergency power supply for NICU of a hospital by solar-wind-based system, a step towards sustainable development", ***Journal of Solar Energy Research***, Vol. 5, No. 3, (2020), 506-515. (https://dx.doi.org/10.22059/jser.2020.306423.1166).
43. Moein, M., Pahlavan, S., Jahangiri, M. and Alidadi Shamsabadi, A., "Finding the minimum distance from the national electricity grid for the cost-effective use of diesel generator-based hybrid renewable systems in Iran", ***Journal of Renewable Energy and Environment (JREE)***, Vol. 5, No. 1, (2018), 8-22. (https://dx.doi.org/10.30501/jree.2018.88377).
44. Jahangiri, M., Soulouknga, M.H., Bardei, F.K., Shamsabadi, A.A., Akinlabi, E.T., Sichilalu, S.M. and Mostafaeipour, A., "Techno-econo-environmental optimal operation of grid-wind-solar electricity generation with hydrogen storage system for domestic scale, case study in Chad", ***International Journal of Hydrogen Energy***, Vol. 44, No. 54, (2019), 28613-28628. (https://doi.org/10.1016/j.ijhydene.2019.09.130).
45. Jahangiri, M., Haghani, A., Heidarian, S., Alidadi Shamsabadi, A. and Pomares, L.M., "Electrification of a tourist village using hybrid renewable energy systems, Sarakhiyeh in Iran", ***Journal of Solar Energy Research***, Vol. 3, No. 3, (2018), 201-211. (https://jser.ut.ac.ir/article_68643.html).
46. Pahlavan, S., Jahangiri, M., Alidadi Shamsabadi, A. and Rahimi Ariae, A., "Assessment of PV-based CHP system: The effect of heat recovery factor and fuel type", ***Journal of Energy Management and Technology***, Vol. 3, No. 1, (2019), 40-47. (https://dx.doi.org/10.22109/jemt.2018.137207.1106).
47. Mostafaeipour, A., Jahangiri, M., Haghani, A., Dehshiri, S.J.H., Dehshiri, S.S.H., Sedaghat, A., Saghaei, H., Akinlabi, E.T., Sichilalu, S.M., Chowdhury, M.S. and Techato, K., "Statistical evaluation of using the new generation of wind turbines in South Africa", ***Energy Reports***, Vol. 6, (2020), 2816-2827. (https://doi.org/10.1016/j.egyr.2020.09.035).
48. Jahangiri, M., Shamsabadi, A.A., Riahi, R., Raeiszadeh, F. and Dehkordi, P.F., "Levelized cost of electricity for wind-solar power systems in Japan, A review", ***Journal of Power Technologies***, Vol. 100, No. 3, (2020), 188-210. (https://papers.itc.pw.edu.pl/index.php/JPT/article/view/1359).
49. Jahangiri, M., Nematollahi, O., Haghani, A., Raiesi, H.A. and Alidadi Shamsabadi, A., "An optimization of energy cost of clean hybrid solar-wind power plants in Iran", ***International Journal of Green Energy***, Vol. 16, No. 15, (2019), 1422-1435. (https://doi.org/10.1080/15435075.2019.1671415).
50. Chaurasia, R., Gairola, S. and Pal, Y., "Technical, economic feasibility and sensitivity analysis of solar photovoltaic/battery energy storage off-grid integrated renewable energy system", ***Energy Storage***, (2021), e 283. (https://doi.org/10.1002/est2.283).

Journal of Renewable Energy and Environment

Journal Homepage: www.jree.ir

Materials and Energy Research Center

MERC

Technical Note

Development of a Solar Energy Operated Weeder for Wetland Paddy Crop

Gunasagar Sahu, Hifjur Raheman*

Department of Agricultural and Food Engineering, Indian Institute of Technology Kharagpur, Kharagpur, West Bengal, P. O. Box: 721302, India.

PAPER INFO

Paper history:
Received: 10 September 2021
Revised in revised form: 25 January 2022
Scientific Accepted: 23 November 2021
Published: 25 July 2022

Keywords:
Solar Photovoltaic,
Weeding Wheel,
Weeding Efficiency,
Cost of Weeding,
Brake-Even Point

ABSTRACT

A solar energy operated two-row weeder was developed for weeding in wetland paddy crop. Its major components are power source, power transmission system, weeding wheels, and a float. The power source comprised a DC motor, solar panel, and power storage unit with maximum power point tracker and motor controller. Solar panel/power storage unit through a motor controller supplied power to the DC motor and it was transmitted to the shaft of the weeding wheel through a dog clutch. A pair of wheels attached with jaw tooth and plane blades at wheel circumference was used for carrying out weeding and movement of the weeder in the field. A float was used to prevent sinkage of the weeder in soft soil which, in turn, ensured stability during operation. The developed weeder could do weeding at a rate of 0.06 ha per hour with field efficiency, weeding efficiency, and plant damage of 83.3 %, 83 % and 2-3 %, respectively. As compared to cono-weeder, the cost of weeding was 41.2 % lower due to higher field capacity and fewer labor requirements. Annual use less than 4.13 ha for the developed weeder was found uneconomical for carrying out weeding. The developed powering system comprising solar photovoltaic panels could supply power to do weeding continuously for 2 hours with a maximum discharge of 20 % from the battery.

https://doi.org/10.30501/jree.2022.304080.1255

1. INTRODUCTION

India has been cultivating rice on about 438 lakh ha agricultural land that produces about 113 million tonnes each year [1]. The rice cultivating farmers face losses in the production due to various reasons, among which weeds are the major one which compete with the main crop for nutrients, sunlight, spaces, water, etc. and the main crop gets weakened leading to lower grain productivity. De Dutta [2] reported a reduction in yield of rice in unweeded plots due to weed growth as much as 34 %, 45 %, and 67 % in transplanted rice, direct-seeded rainfed lowland rice, and upland rice, respectively. Gunasena and Arceo [3] reported that rice was very sensitive to weed competition in the first three weeks after seeding and failure to control weeds in this period could reduce the yield by 50 %. It was also reported that weed competition period up to 45 days after sowing (DAS) significantly affected the yield of wetland paddy [4].

Most of the traditional Indian farmers follow different methods of weeding such as manual hand weeding, weeding with some tools, weeding with push-pull weeders, and power weeders. Parthasarathi and Negi [5] reported that under lowland conditions in India, the labor requirement for hand weeding was 200-250 h/ha, whereas in row seeded or transplanted rice, it took about 50-60 h/ha using manually operated mechanical weeders depending upon weed infestation and soil conditions. Khan and Diesto [6] designed a push type cono-weeder for paddy crop which uprooted and buried the weeds in one pass without making back-forth movement. They reported that the machine required labor about 120 man-h/ha saving half the time of operation compared to that of manual weeding. Remesan et al. [7] evaluated performance of a rotary weeder and a cono-weeder in wetland paddy conditions and compared the same with hand weeding. It was reported that the time required for hand weeding per hectare with male and female operators was 333.3 h and 399.8 h on average, respectively. The average time required by male labor to carry out weeding per hectare with rotary and cono-weeder was 47.7 h and 41.0 h, respectively, on average as compared to 80.7 and 76.3 h with female labor. Hossen et al. [8] designed and developed a weeder to carry out weeding in lowland as well as upland conditions, which used hoe as the weeding tool with an overall width of 120 mm. The average effective field capacity and degree of weeding were reported as 0.034 ha/h and 90 % in the lowland and 0.027 ha/h and 83 % in upland conditions, respectively.

Ambujam [9] developed a rotary paddy weeder powered by a 1 kW engine. This weeder operated at a depth of 70 mm and weeding efficiency, actual field capacity, and performance index were reported as 80 %, 0.022 ha/h, and 587, respectively, with an average fuel consumption of 0.86 l/h. The cost of weeding with this power weeder was Rs.503/ha as compared to Rs.438/ha with hand weeding.

*Corresponding Author's Email: hifjur@agfe.iitkgp.ac.in (H. Raheman)
URL: https://www.jree.ir/article_154022.html

Please cite this article as: Sahu, G. and Raheman, H., "Development of a solar energy operated weeder for wetland paddy crop", ***Journal of Renewable Energy and Environment (JREE)***, Vol. 9, No. 4, (2022), 10-20. (https://doi.org/10.30501/jree.2022.304080.1255).

Victor and Verma [10] developed 0.373 kW petrol engine powered wet-land paddy weeder, which consisted of prime mover, belt and pulley transmission system, 4 L-shaped weeding blades, two traction wheels, and a gauge wheel. With 200 mm width of weeder when operated in paddy field with standing water of 50-70 mm, the field capacity was found to be between 0.04 to 0.06 ha/h with the weeding efficiency of 90.5 % and field efficiency of 71 %. The cost of the weeding was reported as Rs. 882/ha. Alizadeh [11] evaluated the performance of four types of mechanical weeders in paddy crop: single-row conical weeder (W1), two- row conical weeder (W2), rotary weeder (W3), and power weeder (W4) and compared their performances with hand weeding (W5). Among the mechanical weeders, the highest (84.33 %) and lowest (72.80 %) weeding efficiency rates were obtained with power weeder and rotary weeder, respectively. The damaged plants were observed to be 3.83 % with mechanical weeders as compared to 0.13 % with hand weeding. The cost of weeding with W1, W2, W3, and W4 as compared to W5 was reduced by 15.70, 38.51, 22.32, and 48.70 %, respectively.

Deshmukh and Tiwari [12] conducted a study on the impact of different types of weeders in System of Rice Intensification (SRI) where plant-to-plant and row-to-row spacings were maintained at 250 mm. They reported that cono-weeder and rotary weeder were suitable for weeding in wetland conditions and twin wheel hoe in dry-land condition adopting SRI methods. In SRI, the rotary weeder was found to be the best weeder with a field capacity of 0.18 per ha/day/labour and cost of weeding of Rs. 500/ha with 50 % saving in time.

Ojomo et al. [13] studied the performance of a 1.5 kW petrol engine powered weeding machine with three types of cutting blades (flat, spike tooth and curved blades). At 16 % soil moisture content, the highest average weeding efficiency of 76.62 % was obtained with the spike tooth blade followed by 71.84 % with the curved blade and 68.56 % with the flat blade. Olaoye et al. [14] developed a 3.73 kW petrol engine operated rotary power weeder. It consisted of a frame, rotary hoe (disc), tines, power unit, and transmission unit. The field capacity of the rotary power weeder was reported to be 0.071 ha/h with a weeding efficiency rate of 73 %. The cost of weeding with this machine was Rs. 12,600 per year against Rs. 56,000 per year when weeding manually.

Said et al. [15] evaluated the performance of a power operated single row paddy weeder and compared it with manual weeders such as cono-weeder and Ambika paddy weeder. The weeding efficiency and percent tiller damaged for power operated single-row paddy weeder, cono-weeder, and Ambika paddy weeder were reported as 74.50 %, 72.45 %, 83.87 % and 1.15 %, 0.52 %, 0.75 %, respectively. The average time required for weeding one hectare of the field was 12.82 h, 62.50 h, and 47.62 h for power operated weeder, cono-weeder, and Ambika paddy weeder, respectively. They suggested the application of power operated paddy weeder for carrying out weeding in paddy field from 15 days after transplanting up to 45 days with an interval of 10 days.

Shakya et al. [16] developed a cono-weeder that consisted of two conical rotors of 100 mm diameter with serrated bladed weeding unit at 30° blade angle and compared its performance with the TNAU (Tamil Nadu Agricultural University) cono-weeder comprising two conical drums with alternative smooth and serrated blades on it. The weeding efficiency, plant damage, and soil handled with the developed cono-weeder were reported as 87.77 %, 4.58 %, 6.5 m^3/h, respectively, as compared to 77.41 %, 9.17 %, 4.54 m^3/h, with TNAU cono-weeder. The average value of performance indices for the developed cono-weeder and TNAU cono-weeder obtained was 2300 and 1153.60, respectively.

Kunnathadi et al. [17] developed a self-propelled cono-weeder powered by a 0.9 kW engine with specific fuel consumption of 650 g/kWh. The average field capacity of this weeder when operated at a speed of 2.0-3.0 km/h was reported as 0.1 ha/h. with a weeding efficiency at par with that of the manual cono-weeder operating twice in 15 and 30 days after transplanting.

Seerangurayar et al. [18] evaluated performance of one 3-row and two 2-row commercially available power weeders powered by 1.5 kW, 1.3 kW, and 1.3 kW petrol engines, respectively, for carrying out weeding in paddy crop in south India and compared it with the manual weeding. Out of these two 2-row weeders, one (1.3 kW engine) was fitted with wheels and the other had 'L'-type blade as weeding element. The weeding efficiency, plant damage, field capacity, and field efficiency for these weeders were found to be in the range of 60.8-64 %, 1.2-2.7 %, 0.074-0.131 ha/h, and 76-78 %, respectively. The highest field efficiency, weeding efficiency, and plant damage among the 2-row weeders were found for weeder fitted with 'L'-type blades. The field capacity observed with 3-row power weeder was highest (0.131 ha/h) followed by 2-row 'L'-type blades weeder (0.091ha/h) and 2-row wheel type weeder (0.074 ha/h). The cost of weeding with power weeders as compared to manual weeding was reduced by 56 to 64 % with a saving of time up to 95 to 97 %.

Sirmour and Verma [19] developed and evaluated a single-row 1.49 kW petrol engine powered weeder for paddy crop. 'L' type weeding blades were arranged in a rotating disc for weeding and the working width of this weeder was made adjustable between 140 mm and 250 mm. The performance of weeder was studied in the field using three sets of blade (i.e., 4, 6, and 8 numbers) at a depth 30 to 80 mm and at a rotor speed of 176 rpm. It was reported that power requirement for weeding after 15 days of sowing was maximum with 8 blades, i.e., 380 W, followed by 313 W with 6 blades and, then, 290 W with 4 blades. The average fuel consumption of power weeder was reported as 0.55 l/h with a maximum field capacity of 0.054 ha/h and weeding efficiency of 88.62 %. Use of these weeders could save 60 % cost of weeding and 65 % time required for carrying out weeding as compared to manual weeding.

The push-pull weeders and cono-weeders are mostly used by the marginal and small farmers, which are efficient in removing weeds, but with low field capacity and high drudgery to the operators. These manual weeders require longer time as well as much labor for carrying out weeding in paddy crop as frequent machine cleaning and rest for the operator are required during weeding. The power (engine operated) weeders produce much vibration, create noise pollution, and also cause environmental pollution due to burning of fossil fuel. The working elements used in the power weeders were mostly 'L'-type blades, which were good in uprooting weeds in the wet-land condition, but poor in burying weed in the soil. Hence, the addition of weeds to the soil to enhance its organic manure is not possible and there is a possibility for the regrowth of the weeds from the weed residue left. The existing weeding blades are also prone to frequent clogging with weeds, which create problem in smooth operation and consume unnecessary energy in cleaning the clogged working elements. To overcome these

difficulties, a suitable weeder powered by solar energy is very much required. Though a few solar energy operated tillers and weeders were developed [20-22] for tilling in dryland for carrying out weeding operation in maize and ground nut crops, their applicability to wetland where the soil is soft and standing water is available is not known. Hence, an attempt was made to develop an effective and non-polluting weeder for carrying out weeding in the wetland paddy field.

2. EXPERIMENTAL

2.1. Development of power weeder

A two-row wetland paddy weeder, as shown in Figure 1(a), was developed. It comprised the main frame with a wooden box, a prime mover, transmission system, two weeding wheels, and a float. A DC motor of 450 W and 480 rpm with controller was used to supply power to the weeding wheels using a chain and sprocket transmission system. This DC motor was fixed on the main frame, and was used as the prime mover for carrying out weeding operation. Chain-sprocket transmission was used to transmit power from the motor to a clutch shaft and, subsequently, from the clutch shaft to shaft fitted with weeding wheels at both of the ends at 1:3 and 1:1 reduction ratios, respectively. A dog clutch arrangement was provided to disconnect the power flow from motor to the rotating wheel while taking a turn from one row to the adjacent row during field operation. The developed paddy weeder was fitted with cage wheel type weeding wheels of 250 mm diameter and 125 mm width so that both forward movement and weeding operation could be done simultaneously. On the periphery of each of the wheels, three jaw tooth and three plane blades were arranged alternatively at equal spacing (Figure 1 (b)). The jaw-toothed blades were used to uproot the weeds and the plain blades helped to cut and bury the weeds in the soil. The blade angle of the weeding elements was kept at 30° for effective weeding operation. A float was attached to the bottom of the weeder to support its weight and stabilize it during operation in the wet and muddy soil conditions. It also prevented the weeder from sinking into the muddy soil during operation. During operation, the float was sliding on the middle row with rotating weeding wheel on either side. The weeding elements provided on the wheel could cut and bury the weeds into the soil up to a maximum depth of 70 mm. The weeder had a provision to operate the machine at three different depths such as 30 mm, 50 mm, and 70 mm by adjusting the gap between float and axle of the weeding wheel. This weeder can operate in different row-to-row spacing conditions for paddy crop such as 200 mm, 250 mm, and 300 mm. Power requirement for carrying out weeding operation with this type weeder in actual wetland field condition was studied and, then, a suitable powering system comprising Solar Photo-Voltaic (SPV) panels was designed and developed to operate the weeder.

2.2. Power requirement of the weeder for carrying out weeding

A 100 Nm torque transducer (Datum make) was attached to the main shaft for power transmission, as shown in Figure 1(a). After measuring the torque required with this transducer and speed of the weeding wheel during weeding operation, the power requirement of the weeder was computed, i.e., product of torque and angular speed. A photograph of the developed weeder during field operation for measurement of torque and speed is shown in Figure 2. The DC motor used as the power source to operate the weeder was receiving power from batteries (inside the wooden box, Figure 2). A data displaying and storing device called Datum Universal Interface (DUI) was employed to acquire speed and torque data from the transducer during operation of the weeder. The operator used the handle for guiding the implement during operation in between the rows.

Clutch actuating lever was provided with the handle so that the operator could easily disconnect power supply to the weeding wheels for taking a turn from one row to the adjacent row. The torque transducer measured the torque and speed requirement during weeding operation and transmitted that to DUI for storing data using a simple pen drive for future usage.

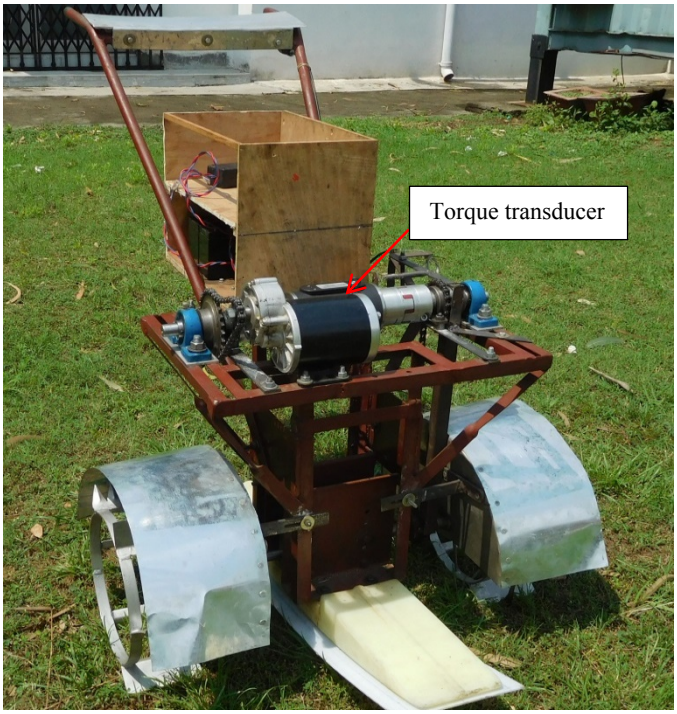

(a) The developed weeder

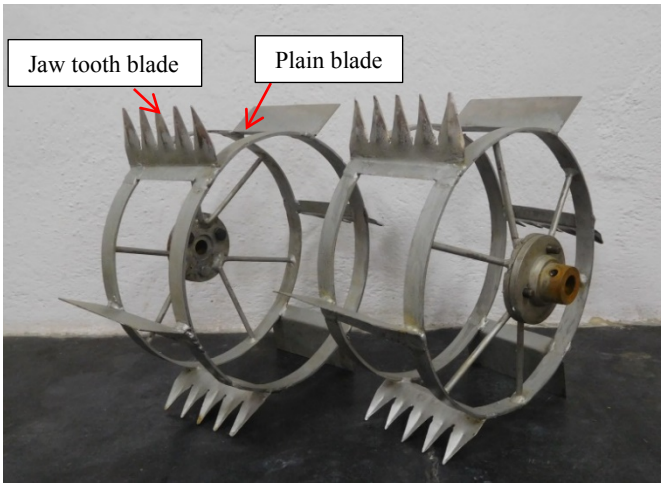

(b) Cage wheel with weeding elements

Figure 1. The developed wetland paddy weeder

2.3. Development of solar energy operated wetland paddy weeder

The solar energy operated wetland paddy weeder comprised a stand-alone solar photo voltaic (SPV) system that supplied power to the two weeding wheels for weeding operation. The

power flow in the stand-alone SPV system used in the developed weeder is shown in Figure 3.

Figure 2. The developed wetland paddy weeder

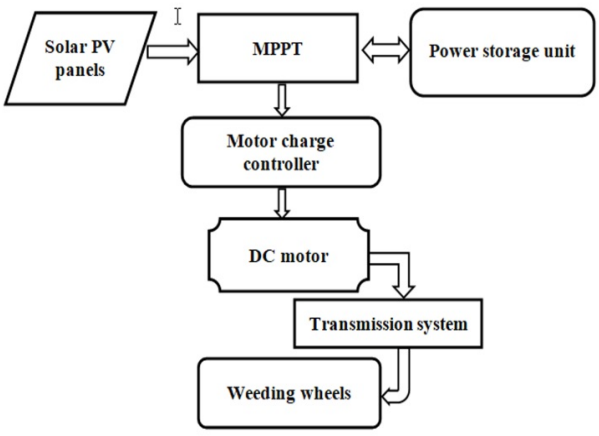

Figure 3. Flow chart for power flow in the stand-alone SPV system

2.3.1. Development of the SPV powering system for the weeder

The powering system for the developed weeder comprised four components, namely DC motor, power storage (battery), power source (solar PV panels), and controllers.

2.3.1.1. Selection of DC motor

In this SPV powering system, the DC motor has a major role as the prime mover for the paddy weeder. Considering the maximum torque and speed requirement to carry out weeding operation as obtained in the field (30 N.m and 350 W, respectively, considering 20 % reserve), a DC motor of 450 W was selected and its specifications are summarized in Table 1. As the speed required for carrying out weeding operation was 150 rpm but the rated speed for DC motor was 480 rpm, a chain-sprocket transmission with a speed reduction of 3:1 was used. The fabricated model with the DC motor was applied in the wetland field condition using batteries and the current and voltage required for this operation were measured. Based on these requirements, battery size was decided.

Table 1. Specifications of DC motor for weeder

Sl. No.	Parameters	Values
1.	Rated power, W	450
2.	Rated voltage, V	24
3.	Actual speed, rpm	480
4.	No load current, A	2.5
5.	Full load current, A	24
6.	Rated torque, kg.cm	90
7.	Motor weight, kg	5.6

2.3.1.2. Selection of battery

During the field operation of the weeder, the voltage and current required for carrying out weeding were measured to be 24 V DC and 10 to 13 A, respectively. Taking an operating time of 6 hours per day with 3 hours autonomy and a battery discharge rate of 0.6, the battery capacity was determined using Eq. 1.

$$\text{Size of battery (A-h)} = \frac{\text{Total Watthours required per day} \times \text{Days of autonomy}}{\text{Discharge rate of battery} \times \text{nominal battery voltage}(V)} \quad (1)$$

$$\text{Battery capacity (A-h)} = \frac{(24 \times 13 \times 6) \times 3}{24 \times 0.6 \times 24} = 16.25 \text{ A-h}$$

As 24 VDC and 20 A-h Lithium-ion battery was available in the market, which is light in weight and easy to use. Hence, this was selected for this purpose and its specifications are given in Table 2.

Table 2. Specifications of the battery (Lithium-ion battery)

Sl. No.	Parameters	Values
1.	Nominal voltage, V	24
2.	Capacity, Ah	20
3.	Depth of discharge, %	50
4.	No. of batteries	1
5.	Efficiency, %	90

2.3.1.3. Selection of solar PV panel

The size of solar PV panel is basically decided considering two factors: daily solar radiations available during the operation period (solar peak hour) and the energy required to carry out weeding. Weeding operation is generally carried out during March to April and September to October for paddy crops in Rabi and Kharif seasons, respectively. Solar radiation available at Kharagpur (22.35° N, 87.23° E) for Rabi and Kharif seasons during these periods is about 5.5 to 6 kWh/m^2/day. Hence, the peak solar hour for this location is 5.5 to 6 h/day (@1000 W/m^2). The average power required for carrying out weeding operation was in the range of 300 W in the wetland paddy field condition. The size of solar panel was decided using Eq. 2.

$$\text{Solar panel size} = \frac{\text{Energy consumption per day } (\frac{\text{Wh}}{\text{day}})}{\text{Peak sun hour } (\frac{\text{h}}{\text{day}})} = \frac{300 \times 6}{5.75} = 313.04 \text{ W}_\text{p} \quad (2)$$

Hence, two flexible solar PV panels, each with 160 Wp, were selected for this powering system and the panels were connected in series to give the desired output. The specifications of these panels are summarized in Table 3.

Table 3. Specifications of flexible solar panel selected

Sl. No.	Parameters	Values
1.	Nominal max. power (P_{max}), W	160
2.	Optimum operating voltage (V_{mp}), V	19.60
3.	Optimum operating current (I_{mp}), A	8.20
4.	Open circuit voltage (V_{oc}), V	21.60
5.	Short circuit current (I_{sc}), A	9.80
6.	Conversion efficiency, %	19.0

2.3.1.4. Selection of controllers

Solar charge controller and DC motor controller were included in this developed powering system.

Solar charge controller

The output of the solar panel was about 39.20 V DC and 8.20 A, which did not match with the load requirement; hence, to address the problem, a device called solar charge controller was used. Because of higher efficiency of Maximum Power Point Tracker (MPPT) charge controller over the Pulse Width Modulation (PWM) type charge controller [23], it was selected to be coupled with the solar panels for getting maximum current and voltage output. The specifications of the MPPT selected for use are given in Table 4. The controller not only maximized the power from the panel to match with the load operating point but also prevented the power over flow to the DC motor, which might damage it. The advance controller MPPT had also a provision to display and store the power, voltage and current data of the solar panel, battery, and load through solar monitor software using a personal computer.

Table 4. Specifications of solar MPPT charge controller

Sl. No.	Parameters	Values
1.	Model	TRIRON3210N
2.	System voltage, VDC	12/24
3.	Maximum PV open circuit voltage, V	100
4.	Rated charge/discharge current, A	30
5.	Maximum rated charge power, W	390W (12V), 780W (24V)
6.	Battery voltage range, V	Aug-32
7.	Efficiency, %	99.5

DC motor controller

A DC motor charge controller was selected based on the maximum current requirement during weeding operation and by controlling its power input from the SPV powering system, the speed of the DC motor was regulated during weeding operation. The specifications of the selected DC motor controller are summarized in Table 5.

Table 5. Specifications of DC motor controller

Sl. No.	Parameters	Values
1.	Output power for 24 V(max.), W	960
2.	Range of operating voltage, V	10-50
3.	Peak current, A	40
4.	Adjustable speed range, %	5-100
5.	Operating temperature, ºC	-20 to 40

2.4. Performance evaluation of the Solar Energy Operated Weeder (SEOPW)

Performance of the developed two-row SEOPW was evaluated in wetland paddy fields with 20-30 mm standing water, available in the Research Farm of Indian Institute of Technology Kharagpur, India. It comprised two major parts:

• Performance of the paddy weeder in the field

• Performance of the SPV powering system developed for the SEOPW

2.4.1. Field performance of the paddy weeder

Field performance of the developed paddy weeder was evaluated following the procedure outlined in Indian standard for testing manual weeders [24] and it was compared with that of a manual push-pull type cono-weeder. The following parameters were measured:

Effective field capacity was computed by measuring the total time required to carry out weeding in plots of size 15×10 m. It included time loss during turning. Theoretical field capacity was calculated by multiplying the width of weeding by the forward speed of the weeder during operation.

Field efficiency of the weeder was computed using Eq. 3:

$$\text{Field efficiency} = \frac{\text{Actual field capacity}}{\text{Theoretical field capacity}} \times 100 \quad (3)$$

Plant damage percentage was computed using Eq. 4.:

$$\text{Plant damage (\%)} = \frac{\text{Number of plants damaged in a plot}}{\text{Total number of plants in the plot}} \times 100 \quad (4)$$

Weeding efficiency was computed using Eq. 5:

$$\text{Weeding efficiency} = \frac{\text{Total no. of weeds present before weeding} - \text{Total no.no.of weeds present fter weedingg}}{\text{Total no. of weeds present before weeding}} \times 100 \quad (5)$$

2.5. Economic analysis of weeding with SEOPW

The initial costs of SEOPW and conventional cono-weeder are Rs. 60,000 and Rs. 2,000, respectively. Cost of weeding in paddy crop with conventional cono-weeder and SEOPW was computed following the Indian Standard IS-9164 [25]. The useful life of the SEOPW as well as cono-weeder was considered as 8 years with an annual use and 250 h. Fixed costs of the weeders were computed considering the salvage value of SEOPW and cono-weeder as Rs. 3000 and Rs. 100, respectively (following a straight method), interest (7 % per annum), insurance, taxes (2 % of average purchase price of weeders), and housing cost (1.5 % average price of weeders). The operating cost of SEOPW included the cost of batteries, the cost of electricity for recharging the batteries, lubricant

cost, operator's wages, and repair and maintenance charges. The labor cost for carrying out weeding was computed using a daily wage of unskilled labor as Rs. 350. Labor required for weeding in paddy crop using SEOPW and cono-weeder was recorded. The cost of weeding in paddy crop with SEOPW and cono-weeder was compared. Break Even Analysis of SEOPW was computed and it is defined as the minimum area required to be weeded using the SEOPW per year to have economic advantage over weeding with conventional cono-weeder. The break-even point for the SEOPW was estimated using Eq. 6.

Break even point (ha/year) =

$$\frac{\text{Annual fixed cost of weeding with SEOPW } \left(\frac{\text{Rs}}{\text{year}}\right)}{\text{Cost of weeding with conoweeder } \left(\frac{\text{Rs}}{\text{ha}}\right) - \text{Cost of weeding with SEOPW} \left(\frac{\text{Rs}}{\text{ha}}\right)} \quad (6)$$

3. RESULTS AND DISCUSSION

3.1. Determination of torque and power requirement of the weeder

Experiments were carried out in the wetland paddy field using a pair of weeding wheels with alternative three jaw toothed and plain blades on its periphery at a speed of 150 rpm. Both torque and power requirement while carrying out weeding operation were recorded with the help of torque transducer and DUI. A sample plot of these parameters with time is shown in Figure 4 (a and b). From these figures, maximum torque and power required to carry out weeding operation in the wetland condition were found to be 30 N.m and 350 W, respectively. The average torque and power requirement of the weeder to carry out weeding were found to be 25 N.m and 300 W, respectively. Based on these experimental results, a solar PV powering system was designed and developed.

3.2. Developed solar energy operated paddy weeder

The developed Solar Energy Operated two-row Paddy Weeder (SEOPW) is shown in Figure 5 and its detail specifications are given in Table 6.

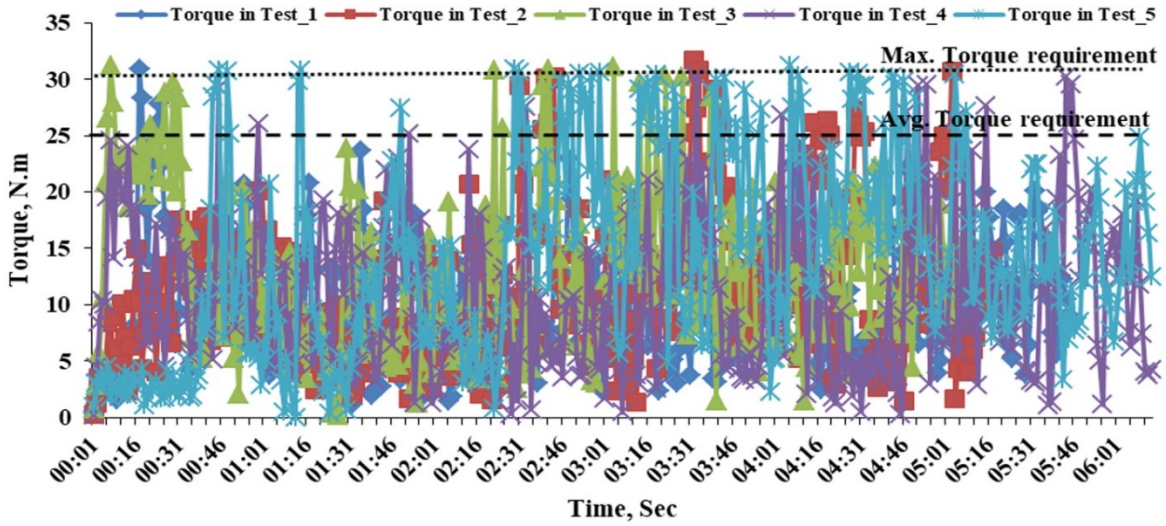

(a) Torque requirement for carrying out weeding

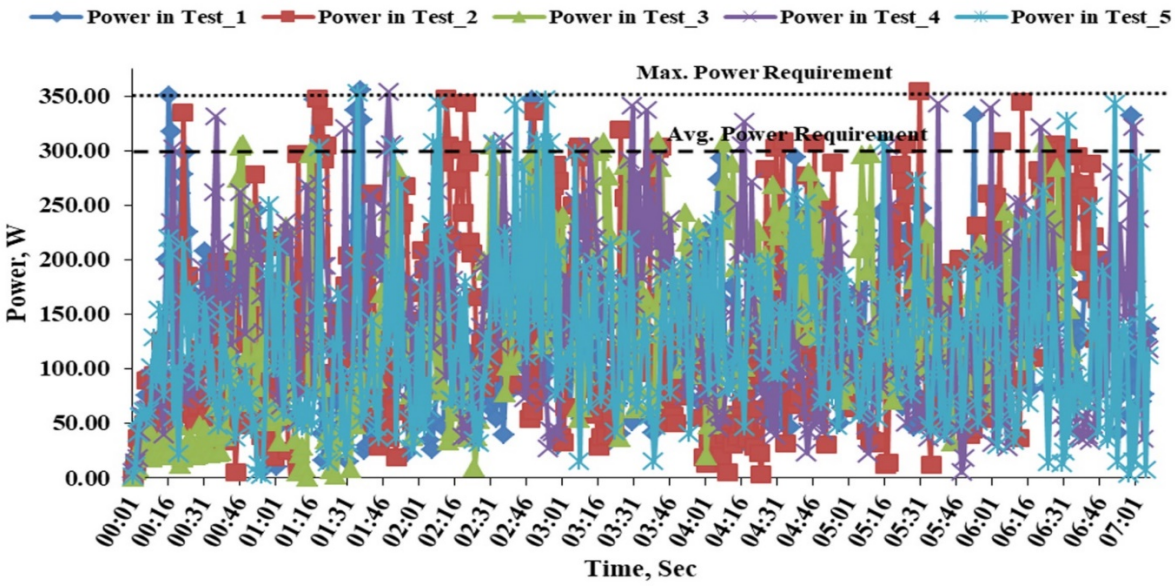

(b) Power requirement for carrying out weeding

Figure 4. Torque and power requirement for carrying out weeding operation in the wetland paddy field

1. Solar panels; 2. Panel holding frame; 3. Stand for frame; 4. DC motor; 5. Transparent protection; 6. Main frame; 7. Float; 8. Mud guard; 9. Weeding wheel; 10. Weeding elements; 11. Rotating shaft; 12. ON/OFF switch; 13. Speed regulator; 14. Clutch lever; 15. Handle; 16. MPPT; 17. Battery

Figure 5. The developed solar energy operated paddy weeder (SEOPW)

Table 6. Specifications of the developed two-row SEOPW

Sl. No.	Particulars	Details
1.	Overall dimension (l×w×h), mm	1450×950×700
2.	Capacity of DC motor, W	450
3.	Rated speed of motor, rpm	480
4.	Rated torque of motor, N.m	8.95
5.	Speed of weeding wheel, rpm (m/s)	125 (1.64), 150 (1.96), 175 (2.30)
6.	Depth of operation, mm	30 - 70
7.	Suitable for row space, mm	200, 250, 300 (Adjustable)
8.	Dimension of float (l×w×h), mm	1000×200×55
Details of weeding mechanism		
9.	Type	Cage wheel type
10.	Width of the weeding wheel, mm	125
11.	Diameter of the weeding wheel, mm	250
12.	Weeding element	Plain and jaw toothed blade
13.	Total no. of plain and jaw-toothed blades	6 (3 each type)
14.	No. of jaws per blade (jaw-toothed blade)	5
15.	Dimension of blades (w×h×t), mm	125×50×2
16.	Lug angle of blades, degree	30

3.3. Performance of the developed SEOPW

A photograph of the developed weeder during operation in the field is shown in Figure 6. In the paddy field, indigenous local weeds and aquatic weeds mainly were found, as shown in Figure 7(a). In Figure 7(b), it can be clearly seen that the developed SEOPW not only uprooted the weeds in between the rows but also buried the uprooted weeds in muddy soil with its weeding elements. Some paddy plants were partly damaged while carrying out weeding as well as taking turn at the headland, which could be avoided with a skilled operator. All the performance parameters measured are summarized in Table 7 and are compared with those obtained with a manually operated cono-weeder.

Figure 6. Field testing of the developed SEOPW

(a) Before weeding

(b) After weeding

Figure 7. Field condition before and after the weeding operation with the developed SEOPW

Table 7. Performance of the developed weeder and cono-weeder

Sl. No.	Variables	SEOPW	Manual cono-weeder
1.	Actual field capacity, ha/h	0.06	0.034
2.	Field efficiency, %	83.3	60.2
3.	Labour requirement, man-h/ha	17-19	29-30
4.	Plant damage, %	2-3	4-5
5.	Weeding efficiency, %	83-85	75-77

In Table 7, it can be seen that the actual field capacity of the developed SEOPW was 0.06 ha/h and it was 1.78 times higher than that of the manually operated cono-weeder due to higher width of coverage. The SEOPW could perform weeding with higher field capacity (76.47 %), weeding efficiency (10.4 %), and field efficiency (38.37 %) with lower plant damage (45 %).

There was a saving of 12 man-h labor requirement per hectare as compared to manually operated cono-weeder. This was due to higher cutting width and powered weeding wheels for which the operator had to take less rest during weeding operation unlike the cono-weeder.

3.4. Performance of the developed SPV powering system

Performance of the developed SPV powering system was evaluated during weeding operation for a period of two hours (from 10 AM to 12 PM). Different parameters such as power consumption by the weeder, battery power (recharge/ discharge), solar panel output power, and the corresponding solar intensity during the operation period were recorded with the help of the MPPT and Personal Computer (PC) with solar energy data monitoring software. The solar radiation data were measured with the help of an automatic electronic Pyranometer. All the recorded data stored in the PC are plotted in Figure 8. In this Figure, it can be seen that power required for carrying out weeding operation (shown as vertical bars) is varying from 195 W to 300 W. This much power was required to be provided by the SPV powering system. During this weeding period, the solar intensity was varying in the range of 700 to 825 W/m^2 and power supplied by the solar panels for carrying out weeding operation was about 195 W to 225 W. Thus, there was mismatch between the power required for carrying out weeding and the power available from the SPV powering system. Hence, this mismatch was overcome by drawing power from the battery. The battery power available during this period, shown in Figure 8, was characterized as negative as the power of battery was discharged during the weeding operation. However, the discharge amount from the battery was not a high amount for the selected battery capacity. The charge of battery was 100 % before the operation and after two hours of operation, about 20 % got discharged from the battery. During weeding operation, when the power requirement for weeding was reduced due to resting or turning of the weeder, the power output from the panel was used to charge the battery.

3.5. Cost of weeding in wetland

The cost analysis of the developed weeder vis-a-vis cono-weeder was carried out and the details are given in Table 8.

The costs of weeding and labor requirement to carry out weeding with SEOPW and conventional cono-weeder were computed to be Rs. 3607 per ha and 17 man-h per ha, respectively, as compared to Rs. 6133 per ha and 29 man-h per ha with conventional cono-weeder. Although the initial cost of the developed weeder was higher than the manual cono-weeder, the operational cost for the developed weeder per hectare was about 41.2 % lower than that of the manual push-pull type cono-weeder. This was due to higher field capacity and fewer labor requirements with the developed SEOPW. Thus, weeding with SEOPW would save money, time, and energy of farmers and increase the productivity. Break-even point for the SEOPW was computed as 4.13 ha/year and annual use below this area was found uneconomical for weeding with SEOPW.

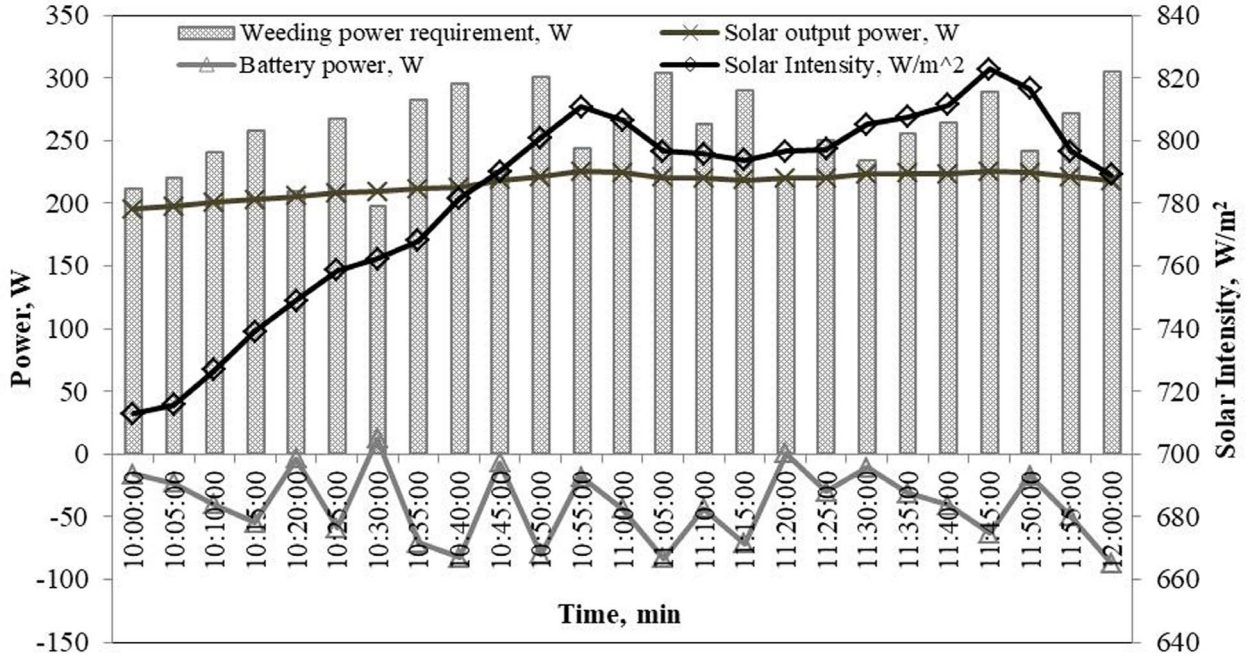

Figure 8. Performance of the developed SPV powering system during weeding operation on 10th March 2020 in the Research Farm of IIT Kharagpur

Table 8. Details of cost analysis of SEOPW and Cono-weeder and their comparison

Sl. No.		Parameters	SEOPW	Cono-weeder
1.		**Fixed cost**		
	i.	Initial cost, Rs.	60000	2000
	ii.	Useful life, years	8	8
	iii.	Annual use, hour	250	250
	iv.	Salvage value, Rs.	3000	100
	v.	Depreciation cost per hour, Rs./h	28.5	0.95
	vi.	Interest on capital (@ 7 % per annum) per hour, Rs./h	8.82	0.29
	vii.	Average purchase price of machine, Rs.	31500	1050
	viii.	Insurance and taxes per hour (@ 2 %), Rs./h	2.52	0.08
	ix.	Housing per hour (@ 1.5 %), Rs./h	1.89	0.06
2.		**Total Fixed cost, Rs./h (USD/h)**	**41.73 (0.572)**	**1.39 (0.019)**
3.		**Variable cost**		
	i.	Field capacity, ha/h	0.06	0.034
	ii.	Daily hours of operation, h	6	7
	iii.	Repair and maintenance cost per hour, Rs/h	24	0.8
	iv.	Man-hour required per ha	17	29
	v.	Cost of battery per hour (Replacement of battery in every 3 years), Rs/h	9	-
	vi.	Cost of labor per hour, Rs/h	141.67	207.14
	vii.	Total cost of weeding per hour, Rs	216	209
4.		**Cost of weeding operation, Rs/ha (USD/ha)**	**3607 (49.47)**	**6133 (84.11)**

4. CONCLUSIONS

Application of solar energy in carrying out weeding in paddy crop is an excellent attempt to mechanize paddy cultivation where access to continuous supply of electricity and availability of conventional fossil fuel are remote. The following specific conclusions are drawn from the study conducted:

• The developed two-row SEOPW had a field capacity 1.78 times that of a manual drawn cono-weeder with 41 % fewer labor requirements, 10.5 % higher field efficiency, and 45 % lower plant damage.

• The developed powering system for operating the weeder using solar photovoltaic could charge the battery in less than 2 hours when the solar intensity available was above 450 W/m^2. The weeder with a fully charged battery was continuously operating for a maximum period of 2 hours without recharging.

• The operating cost of the developed SEOPW was Rs 3607 (49.47USD) per ha as compared to Rs 6133 (84.11 USD) with cono-weeder. This was due to its higher field capacity and fewer labor requirements. In order to make the weeding operation with SEOPW economical as compared to cono-weeder, the minimum area required for weeding is 4.13 ha/year.

From the experiments conducted, it was finally concluded that the developed weeder was successful in carrying out weeding in the paddy crop using solar energy with higher field capacity and field efficiency and also with fewer manpower requirements than the commonly used manual drawn cono-weeder.

5. ACKNOWLEDGEMENT

Financial assistance provided by the Department of Science & Technology, Govt. of India, New Delhi to carry out this study is sincerely acknowledged.

REFERENCES

1. Annual report, Department of Agriculture, Cooperation and Farmers Welfare, Ministry of Agriculture and Farmers Welfare, New Delhi, India, (2018), 4. (https://agricoop.nic.in/sites/default/files/AR_2018-19_Final_for_Print.pdf).
2. De Dutta, S.K., Principles and practices of rice production, John Wiley and Sons, USA, (1981), 469-472. (https://books.google.co.in/books?hl=en&lr=&id=Yxa5Sz_Puv4C&oi=fnd&pg=PR1&ots=pVZjBecXID&sig=XzxhlyopXDW7ux6VWtgLRM9rIu0&redir_esc=y#v=onepage&q&f=false).
3. Gunasena, H.P. and Arceo, L.M., "Weed control studies with butachlor in direct seeded rice in Shri Lawlea", ***Proceedings of 8th Asian Pacific Weed Science Society Conference***, Bangalore, India, (1981), 27-29. (https://www.isws.org.in/Documents/Proceedings_of_conference/1981_8th_Asian-Pacific_Weed_Science_Society_Conference_Proceedings_(Volume2).pdf).
4. Sathyamoorthy, K. and Kandasamy, O.S., "Critical period of crop weed competition in different rice culture (lowland transplanted and wet seeded rice)", Summary and Research Achievements, AICRPWC (ICAR), Coimbatore Centre, Tamil Nadu Agricultural University, Coimbatore, India, (1998). (https://www.academia.edu).
5. Parthasarathi, M.N., "Control of rice weed with butachlor", ***Proceedings of Weed Science Conference, Indian Society of Weed Science***, Andhra Pradesh Agricultural University, Rajendranagar, India, (1977), 179-180. (https://www.isws.org.in).
6. Khan, A.V. and Diesto, M., "Push type cono weeder for small rice farms", ***Investigation Intelligence***, Vol. 23, (1987), 236-237. (http://ijaast.com/publications/vol6issue12/V6I1201).
7. Remesan, R., Roopesh, M.S., Remya, N. and Preman P.S., "Wet land paddy weeding-A comprehensive comparative study from south India", ***Agricultural Engineering International: The CIGR E-Journal***, Vol. 9, (2007), 1-21. (https://hdl.handle.net/1813/10717).
8. Hossen, M.A., Islam, M.S., Huda, M.D., Zami, M.A., Bhuyan, M.G.K. and Nath, B.C., "Design and development of a weeder for both lowland and upland conditions", ***AMA-Agricultural Mechanization in Asia Africa and Latin America,*** Vol. 42, No. 2, (2011), 56. (http://www.shin-norin.co.jp/english/pdf/VOL_42_NO2_SPRING_2011.pdf#page=56).
9. Ambujam, N.K., "Performance evaluation of power weeder", ***Agricultural Mechanization in Asia, Africa & Latin America***, Vol. 24, (1993), 16-18. (https://www.cabdirect.org), (Accessed: 12 June 2016).
10. Victor, V.M. and Verma, A., "Design and development of power-operated rotary weeder for wetland paddy", ***Agricultural Mechanization in Asia Africa and Latin America***, Vol. 4, (2003), 27-29. (https://www.researchgate.net/publication/285531721_Design_and_Development_of_Power-operated_Rotary_Weeder_for_Wetland_Paddy), (Acessed: 10 May 2016).
11. Alizadeh M.R., "Field performance evaluation of mechanical weeders in the paddy field", ***Scientific Research and Essays***, Vol. 6, (2011), 5427-5434. (https://academicjournals.org/article/article1380826459_Alizadeh.pdf).
12. Deshmukh, G. and Tiwari R.K., "Impact of weeders for weed management in system of rice intensification (SRI)", ***Indian Journal of Weed Science***, Vol. 43- No. 3-4, (2011), 243-244. (https://www.indianjournals.com/ijor.aspx?target=ijor:ijws&volume=43&issue=3and4&article=029).
13. Ojomo, A.O., Ale, M.O. and Ogundele, J.O., "Effect of moisture content on the performance of a motorized weeding machine", ***IOSR Journal of Engineering (IOSRJEN)***, Vol. 2, No. 8, (2012), 49. (http://iosrjen.org/Papers/vol2_issue8%20(part-1)/G0284953.pdf), (Acessed: 12 May 2016).
14. Olaoye, J.O., Samuel O.D. and Adekanye, T.A., "Performance evaluation of an indigenous rotary power weeder", ***Energy and Environmental Engineering Journal***, Vol. 1, No. 1, (2012), 94-97. (https://eprints.lmu.edu.ng/123/1/2012.Performance%20Evaluation%20of%20an%20Indigenous%20Rotary%20Power%20Weeder.pdf), (Accessed: 10 June 2017).
15. Said P.P, Shukla A. and Sahu K.R., "Field performance of power operated paddy weeder in comparison with manual weeders", ***Advancements in Life Sciences***, Vol. 5, (2016), 2200-2203. (http://www.als-journal.com/archive/).
16. Shakya, H.B., Parmar, M.R., Kumpavat, M.T. and Swarnkar, R., "Development and performance evaluation of manually operated cono-weeder for paddy crop", ***International Refereed Journal of Engineering and Science***, Vol. 5, No. 7, (2016), 6-17. (http://www.irjes.com/Papers/vol5-issue7/B570617.pdf).
17. Kunnathadi, M., Jayan, P.R. and Abraham. C.T., "Development and testing of self-propelled cono-weeder for mechanized rice cultivation", ***Indian Journal of Weed Science***, (2016), 25-28. (https://www.indianjournals.com/ijor.aspx?target=ijor:ijws&volume=48&issue=1&article=005).
18. Seerangurayar, T., Shridar, B., Kavitha, R. and Manickavasagan A., "Performance evaluation of power weeders for paddy cultivation in south India", ***AMA, Agricultural Mechanization in Asia, Africa and Latin America***, Vol. 48, No. 4, (2017), 76-81. (https://www.shin-norinco.com), (Accessed: 18 July 2018).
19. Sirmour, A., and Verma, A., "Design and development of single row power weeder for rice", ***Journal of Crop and Weed***, Vol. 14, No. 1, (2018), 163-169. (https://www.cropandweed.com/archives/2018/vol14issue1/14.1.30.pdf) .
20. Waghmode, R.S., Shinde, S.R., Dixit, A.K., Chanchure, A.A., Jadhav, K.H. and Gudur, S.E., "Solar power tiller", ***International Journal of Engineering Science & Advanced Technology***, Vol 5, No. 3, (2015), 149-156. (https://www.ijesat.org/Volumes/2015_Vol_05_Iss_03/IJESAT_2015_05_03_01.pdf).
21. Kumari S., Mehta, A.K. and Meena, S.S., "Development and performance evaluation of solar operated power weeder", ***International Research Journal of Engineering and Technology (IRJET)***, Vol. 06, No. 7, (2019), 1340-1342. (https://www.irjet.net/archives/V6/i7/IRJET-V6I7479.pdf).

22. Kachhot, A.R., Dulawat, M.S. and Vadher, A.L., "Development of solar operated walking type power weeder", ***Agricultural Science and Green Energy***, Vol. 2, No. 2, (2021), 30-41. (https://agrilscience.com/wp-content/uploads/2021/02/2-2-5.pdf).

23. Laguado–Serrano, M. A., Luna Paipa, E.A., Bustos–Márquez, L.F. and Sepulveda–Mora, S.B., "Performance comparison between PWM and MPPT charge controllers", ***Scientia et Technica***, Vol. 24, No. 1, (2019), 6-11. (https://www.redalyc.org/journal/849/84959429001/84959429001.pdf).

24. Anonymous, Indian Test Code, IS: 7927, "Method of field testing for manually operated paddy weeder", Bureau of Indian Standard (Indian Standard Institution), New Delhi, India, (1975). (https://archive.org/details/gov.in.is.7927.1975), (Acessed: 10 July 2016).

25. Fagiolari, L. and Bella, F., "Carbon-based materials for stable, cheaper and large-scale processable perovskite solar cells", ***Energy & Environmental Science***, Vol. 12, No. 12, (2019), 3437-3472. (https://doi.org/10.1039/C9EE02115A).

JREE: Vol. 9, No. 4, (Autumn 2022) 21-33

Journal of Renewable Energy and Environment

Journal Homepage: www.jree.ir

Materials and Energy Research Center

MERC

Research Article

Energy Demand of Supplementary Lighting in Agricultural Greenhouses: Solar Energy Utilization

Iman Ayoobi, Ramin Roshandel *

Department of Energy Engineering, Sharif University of Technology, P. O. Box: 11365-9567, Tehran, Tehran, Iran.

PAPER INFO

Paper history:
Received: 17 September 2021
Revised in revised form: 05 February 2022
Scientific Accepted: 10 February 2022
Published: 25 July 2022

Keywords:
Greenhouse,
Natural Light,
Artificial Light,
Greenhouse Locations,
Greenhouse Shapes,
Photovoltaic Panel

ABSTRACT

Light is a critical parameter for plant growth such that providing enough light for the plant can ensure better quality and higher yield in greenhouses. In many areas, in the cold seasons of the year, not enough natural light reaches the plant. Thus, to compensate for the natural light deficit, artificial light is used. Since the use of artificial light leads to energy consumption, effective parameters in the energy consumption of the lighting system such as available natural light, greenhouse shape, and the on-off plan of the lighting system should be considered. In this paper, available natural light is estimated based on greenhouse structure in five cities of Iran. Then, the natural light deficit was investigated. Finally, to achieve clean cultivation, the utilization of photovoltaic panels is investigated to compensate for the electrical energy needed for supplementary lighting. The results show that although Iran is recognized as a region with high solar energy potential, natural light is not enough for optimum tomato lighting demand. Using supplementary lighting in greenhouses could compensate for the lack of natural light in proportion to the capacity of the lighting system. In 73.22 % to 91.32 % of days in the period of September to April, the natural light is not sufficient for optimum lighting. Therefore, 98 (kWh m^{-2} y^{-1}) to 377 (kWh m^{-2} y^{-1}) electricity is needed to supply power for supplementary lighting system. Accordingly, the photovoltaic area and its associated with costs to compensate electrical energy consumption for the supplementary lighting is estimated to be 0.47 m^2_{PV} to 2.58 m^2_{PV} per m^2 of greenhouse area, which is equal to $ 171.08 to $ 939.12 per m^2 of greenhouse area, respectively.

https://doi.org/10.30501/jree.2022.305230.1258

1. INTRODUCTION

Plants need light for photosynthetic operations to provide the energy needed for their activity by converting light energy into chemical energy [1]. Photosynthesis is only caused by the wavelength including Photosynthetic Active Radiation (PAR), which is generally considered be ranging from 400 nm to 700 nm [2]. Insufficient PAR light leads to impaired delivery of sufficient energy to the plant and ultimately lack of optimal growth and poor-quality yields. For tomatoes, it is generally estimated that every 1 % reduction in light leads to a 0.7-1 % reduction in tomato yield [3]. In many areas, due to the high day length and higher altitude of the sun in the summer, sufficient light is provided by the sun. However, in cold seasons when the altitude is lower and the day length is short, it can lead to insufficient light reaching the plant [4]. Since greenhouses involve out-of-season cultivation, lack of natural light generally occurs in greenhouses [5]. Therefore, using an artificial light system to compensate for the lack of natural light seems necessary. The most crucial challenge of using a lighting system is its electrical energy consumption [4, 6] which can significantly raise the operation cost of growing plants. Therefore, it is necessary to study the plant's needs and requirement for light and control how much the lighting system is on.

Greenhouse shapes affect incoming solar radiation. In general, greenhouses can be categorized into two types: single-span and multi-span greenhouse [7]. Each type of greenhouse includes different shapes. Even-span, uneven-span, vinery, modified-arch, and quonset types are the most commonly used single-span shapes of greenhouses [8]. In addition, Venlo, modified arch (arch-shaped roof), and tunnel greenhouses are the most commonly used multi-span shapes for greenhouses [9]. To analyze the energy demand of supplementary lighting, it is important to study the effect of greenhouse shapes on available natural light. Gupta and Chandra [10] studied three types of greenhouse shapes in northern India. Their result indicates that the Gothic arch greenhouse is more energy-efficient than the gable roof and Quonset shape. Sethi [8] studied available solar radiation in five different greenhouse shapes and found that uneven-span greenhouse received highest solar radiation, while Quonset-shaped greenhouse received the lowest solar radiation. Ghasemi et al. [11] investigated six different greenhouse shapes in Tabriz, Iran. Their results showed that the single-span greenhouse received the highest solar radiation, while vinery greenhouse received the lowest. All the above-

*Corresponding Author's Email: roshandel@sharif.edu (R. Roshandel)
URL: https://www.jree.ir/article_154023.html

Please cite this article as: Ayoobi, I. and Roshandel, R., "Energy demand of supplementary lighting in agricultural greenhouses: Solar energy utilization", ***Journal of Renewable Energy and Environment (JREE)***, Vol. 9, No. 4, (2022), 21-33. (https://doi.org/10.30501/jree.2022.305230.1258).

mentioned researchers studied the effect of greenhouse shapes to find the most energy-efficient greenhouse shapes, while in this study, two types of multi-span greenhouse were studied to explore the effect of greenhouse shapes on available natural light.

After evaluating the available natural light according to the structure and location of the greenhouse, the effect of artificial light will be investigated. According to Dorais [12], the quantity and quality of light affect plant growth. The quantity of light is indicated by daily light integral (DLI), the intensity of the light, and the photoperiod. The quality of light means the spectral distribution of the available light. While examining each of the parameters related to the quantity and quality of light, Dorais states the desired amount of these parameters and the results of not achieving the desired amount for tomatoes, cucumbers, and sweet peppers. When natural light is not enough in the cold seasons of the year, artificial lighting is used to ensure the quantity and quality of light suitable for the plants. In the past, High-Pressure Sodium (HPS) lamps were the most popular technology used in greenhouses to meet the need for plant light [13]. Nowadays, due to longer life, less power consumption, less heat loss, and achieve wavelength specificity, Light Emitting Diode (LED) technology has been noticed [14]. Several researchers around the world studied the effect of artificial lighting system on the plant. Paucek et al. [15] conducted a study on the effect of supplementary LED lamps in the Mediterranean greenhouse. Their results showed that a capacity of 170 $\mu mol\ m^{-2}\ s^{-1}$ for 16 hours had a positive effect on the tomato plant, which led to an increase in fruit size. Gomez and Mitchell [16] investigated the effect of artificial lighting systems on tomatoes in two scenarios, 1) with intracanopy LED Towers and 2) with overhead HPS Lamps. Their results showed that in West Lafayette, USA, the presence of artificial light compared to its absence increases fruit number and yields. They also showed that the LED system could save up to 75 % energy.

As mentioned before, while supplementary lighting has a favorable effect on plant growth and yields, the noticeable cost of the lighting system is a major concern for growers. For this reason, it is essential to schedule the on-off program for the lighting system to minimize cost while maintaining the level of light required by plants. Growers usually follow a fixed scheme to control the lighting system; whenever the sunlight is less than a certain amount, the lighting system turns on [17]. A dynamic lighting plan proposed by Heuvelink and Challa [18], in this lighting plan, suitable on-off scheme for lighting system resulted of economic optimization. Niu et al. [19] used another approach based on the Daily Light Integral (DLI); the lighting system switches off when the DLI threshold is met.

In this paper, first, based on the most prevailing climates type, five different cities of Iran were selected, then the natural light available in these cities was estimated. For this purpose, the effect of Venlo and modified arc greenhouse structure on solar transmission coefficient was investigated. After that, by introducing two indicators, an attempt was made to assess the natural light available relative to the light required by tomatoes. In section 2.3, to investigate the effect of the lighting system, the on-off program was proposed, which determines the lighting system program both by considering the available solar radiation at each hour and the DLI. In the following, according to the proposed program, the effect of two capacities of the lighting system (100 and 200 $\mu mol\ m^{-2}\ s^{-1}$) on the available DLI is investigated. Finally, in section 2.4 the area of the photovoltaic (PV) panel required to meet the electrical energy requirements of the lighting system is calculated. The main novelties of this work is (1) to study the effect of greenhouse structure and climate condition on available natural light and (2) presenting a new lighting plan for a lighting system based on DLI requirements and available solar radiation for HPS and LED lamps in greenhouses.

The main contribution of this paper can be presented as follows:

1- the amount of available natural light for two different greenhouse designs in Iran is determined.
2- the algorithm for estimation of supplementary lighting to compensate light deficit is presented.
3- the minimum capacity for a photovoltaic system is determined to supply the electricity demand for supplementary lighting.
4- The presented algorithm is applied to five cities in Iran with different climates as the case studies.

2. METHOD

2.1. Case study

In this article, five cities were selected to estimate the demand for artificial light and its energy requirements. Criteria for selecting different cities to achieve this goal are the climate and population concentration of the studied areas. To classify the climate of Iran, the Köppen–Geiger climate classification was used. According to Kottek et al. [20] and Rahimi et al. [21], different regions of Iran can be divided into nine different climates. In this paper, five different climates have been selected that cover more than 87 % of the area of Iran. These climates are BWh, BWk, BSk, BSh, and Csa. The first letter means the main climate (B: arid and C: warm temperate), the second letter means precipitation (S: steppe, W: desert, and s: summer dry), and the last letter means temperature (h: hot arid, k: cold arid, and a: hot summer) [20]. After nominating several cities in each climate, the study area was selected based on other criteria (population concentration and distribution of major greenhouse cultivation areas). Selected cities and their location are seen in Table 1 and Figure 1.

2.2. Incoming solar radiation

The intensity of solar radiation varies according to the location, season, day, time of day, and cloud cover of the studied area. In addition, in greenhouses, the covering material of greenhouse structure also affects the radiation reaching the plants. These two affect the solar radiation passing through the greenhouse cover and thus, reaching the plant. In this paper, only radiation reaching the horizontal surface of the greenhouse is considered because this part that reaches the plant leads to meeting the plant's light needs. Solar radiation reaching the greenhouse ground consists of two parts of direct and diffuse radiation extracted from the www.renewables.ninja with the help of latitude and longitude presented in Table 1. The method used in this web site is based on Pfenninger et al. [22] and Staffell et al. [23]. The cultivation period in this paper is considered from September 24, 2018 (day 1) to April 20 (day 210), 2019. Two common types of greenhouse structures are shown in Figure 2. In

commercial greenhouses, a significant part of the sunlight enters from the roof of the greenhouse; thus, to investigate the effect of the structure on the radiation entering the greenhouse, only its roof is considered.

Table 1. Geographical and meteorological information of the selected cities

City	Lat. (°N)	Long. (°E)	Climate type*
South of Tehran-Varamin	35.35	51.65	BSh
Ahvaz	31.32	48.67	BWh
Mashhad	36.26	59.62	BSk
Isfahan	32.65	51.66	BWk
Rasht	37.27	49.58	Csa
* Base on Köppen climate classification			

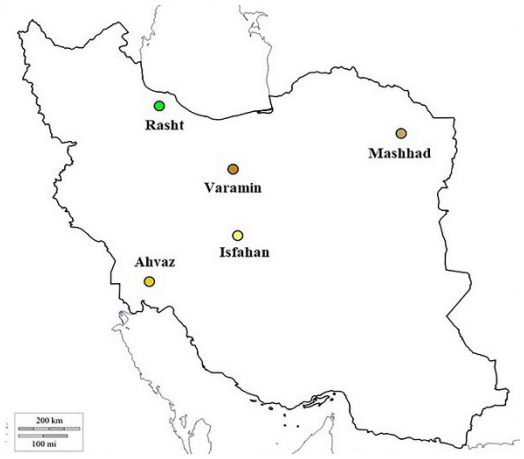

Figure 1. Geographical location of the studied cities

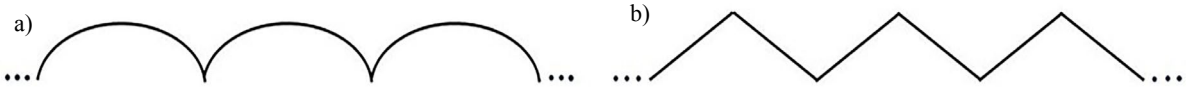

Figure 2. Greenhouse structures: a) modified arc and b) Venlo

Assuming that the incident angle of solar radiation on the greenhouse roof is known, the light transmission coefficient can be calculated with the help of the Fresnel equation. Based on Kalogirou [24], the angle of refraction (θ_2) is first calculated using Eq. (1), where n is the refraction index and for glass, it is equal to 1.526 [24]. Based on Eq. (1), the transmittance of solar radiation is equal to the product of (τ_r) and (τ_a), where subscripts r and a indicate that only reflection losses and absorption losses are considered, respectively. (τ_r) can be calculated from the average transmittance of the two components ($r_{||}$ and $r_{\perp}$) considering Eq. (2) and (τ_a) is calculated based on Eq. (3), where K is the extinction coefficient, which is assumed to be equal to 30 m^{-1} for glass and L is the thickness of the glass cover that is assumed to be 4 mm [24]. Equations (1) to (6) are shown in Table 2.

Table 2. The equations for calculation of transmittance of solar radiation

Transmittance of solar radiation calculation	Equations No.	Reference
$n = \frac{\sin(\theta_1)}{\sin(\theta_2)}$	(4)	[24]
$\tau \cong \tau_a \tau_r$	(5)	
$\tau_r = \frac{1}{2}\left(\frac{1-r_{\parallel}}{1+r_{\parallel}} + \frac{1-r_{\perp}}{1+r_{\perp}}\right)$	(6)	
$r_{\parallel} = \frac{\tan^2(\theta_2-\theta_1)}{\tan^2(\theta_2+\theta_1)}$	(7)	
$r_{\perp} = \frac{\sin^2(\theta_2-\theta_1)}{\sin^2(\theta_2+\theta_1)}$	(8)	
$\tau_a = \exp\left(-\frac{KL}{\cos(\theta_2)}\right)$	(9)	

Factors affecting the incident angle of solar radiation can be generally divided into two categories, the first one related to the position of the sun and the second part related to the structural characteristics of the greenhouse. The width, eaves, and ridge height of each span in the two studied structures are the same and assumed to be 5, 3, and 4 m, respectively. The main difference between these two structures is the tilted angle of the roof.

In Venlo structure, the roof slope angle is always constant; however, in the modified arc structure, the roof slope angle is changed based on the position x from the origin (Figure 3-a). The equation of the modified arc greenhouse roof is shown in Eq. (7). Then, through the derivation, the slope angle of the roof (β) is calculated in terms of x, as shown in Eq. (8). In order to calculate the slope angle using the coordinates of that point, the point of incidence of the sun's rays must be determined. For this purpose, first, with the help of Eq. (9), Eq. (8) is expressed in polar coordinates. (α) is the height of the sun because it is assumed that the point O is located exactly at the center of the span (Figure 3). (r) is also calculated based on Eq. (10) and through the use of the angle of the height of the sun (α), the width of the span (2a), and the height of the roof (b).

Table 3. The equations for estimating titled angle in the modified arc structure

Tilted angle calculation in the modified arc structure	Equations No.
$\frac{x^2}{a^2} + \frac{y^2}{b^2} = 1$	(10)
$\tan(\beta) = \frac{dy}{dx} = \frac{b}{a^2}\frac{x}{\sqrt{1-\frac{x^2}{a^2}}}$	(11)
$x = r\cos(\alpha)$	(12)
$r = \frac{ab}{\sqrt{b^2\cos^2(\alpha) + a^2\sin^2(\alpha)}}$	(13)

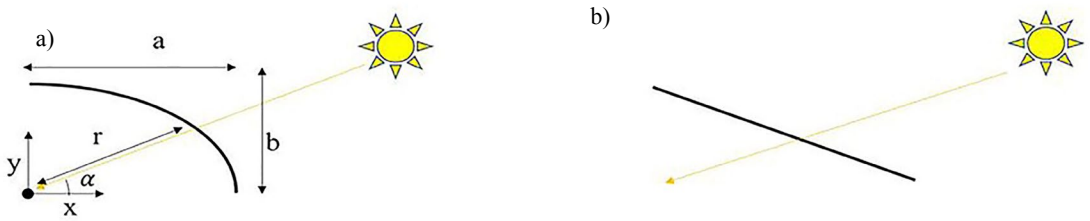

Figure 3. The effect of solar radiation on two structures: a) modified arc and b) Venlo

2.3. Available natural light and supplementary lighting demand

According to the radiation reaching the greenhouse floor, the natural light reaching the plant can be calculated. The portion of the light spectrum utilized for photosynthesis is in the range of 400-700 nm, called Photosynthetically Active Radiation (PAR) [25]. The ratio of PAR to solar radiation has been reported in previous studies. Tsubo and Walker [26] reported this ratio in the range of 0.45 to 0.5. Rao [27] estimated this ratio in the range of 0.44 to 0.46. Udo [28] also reported this ratio in the range of 0.42 to 0.47. Therefore, according to the reported ranges, the constant ratio of 0.45 was used to approximate PAR to solar radiation.

In the present paper, two indicators are considered to examine the available natural light. The first indicator based on the Eq. (11) indicates the Percentage of Days with a Natural Light Deficit (PDNLD) or, in other words, the percentage of days when the amount of natural light is less than the ideal amount required for tomatoes (30 $\text{mol m}^{-2}\ \text{day}^{-1}$) in the whole cultivation period (210 day in our case study). Also, the second indicator that is presented in Eq. (12) indicates the Amount of Light Deficit (ALD) which must be provided to achieve ideal conditions.

The demand for artificial light can be estimated based on the natural light received by the plant and Daily Light Integral (DLI) required for the plant. First, it is necessary to determine the photoperiod according to the plant type, which is Tomato in our research. Dorais and Gosselin [29] reported that tomato plants needed at least 6 hours of dark period. Dorais [12] also reported that in several cases, leaf chlorosis was observed for tomato plants in photoperiod more than 17 hours. In this paper, progressive photoperiod was used so that the photoperiod was determined based on the natural light available during the day. In this work, the photoperiod can be increased up to 16 hours.

It is assumed that supplementary lighting starts at 4 am and continues until 7 pm at maximum. At each hour, if solar radiation is less than a certain amount (300 W m^{-2}) and the daily light integral is less than what the plants need (30 mol m^{-2}), the supplementary lighting system will turn on. This process continues until the required DLI or maximum photoperiod interval is met. Then, according to the capacity of artificial light, the amount of moles of light reaching the plant can be calculated, and knowing the efficacy of lighting system, the electrical energy related to the lighting system can be estimated. In this paper, two types of lighting system technology including Light Emitting Diode (LED) and High-Pressure Sodium (HPS) have been used. Their efficacy is the average of the values reported by Runkle [30], which are equal to 4.8 mol kWh^{-1} and 7.2 mol kWh^{-1} for LED and HPS lamps, respectively. Figure 4 show the supplementary lighting plan to calculate the energy consumption of supplementary lighting system.

Table 4. Indicators related to the evaluation of natural light in the studied cities

Two indexes for examine the available natural light	Equations No.
$\text{PDNLD} = \dfrac{\text{The number of days that is less than the required amount of light}}{\text{Total days in caltivation period}}$	(14)
$\text{ALD} = \sum_{i} \text{Light deficit on the ith day}$	(15)

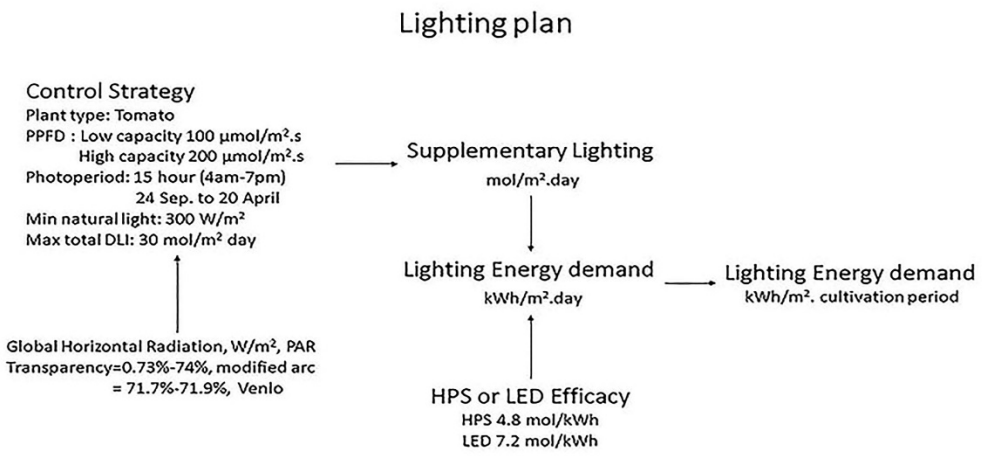

Figure 4. Lighting plan algorithm for supplementary lighting energy consumption [12, 31]

2.4. Meeting supplementary lighting energy demand by photovoltaic panel

After determining the lighting plan with the help of lamp efficacy, electricity demand can be calculated. In order to find the required panel area to meet the electricity demand of the lighting system, the peak-hour approach was used based on Masters [32]. In this approach, since 1-sun is defined as 1 kW m^{-2}, the daily insolation in that area can be defined based on the available hours of 1-sun. Average daily insolation in selected cities on the optimal tilted angle of the panel is shown in Table 5. According to Jacobson et al. [33], the optimal tilted angle can be calculated by latitude of location. Jacobson et al. first estimated the optimal tilt angle derived from the National Renewable Energy Laboratory's PVWatts program at 1-4 sites in a number of countries worldwide. The optimal tilt angle at each site was determined by a tilted angle obtained from maximum panel output. Then, the 3rd-order polynomial fits of optimal tilted angel versus latitude were derived. The resulting function is shown in Eq. (13). In this paper, by knowing the latitude of each location, the optimal tilt angle can be calculated.

According to the electricity demand, the number of peak hours, and the number of days, the required ac power can be estimated based on Eq. (14). For converting ac into dc power under Standard Test Condition (STC), it is necessary to estimate the impacts of temperature, inverter efficiency, module mismatch, and dirt, all of which are considered as conversion efficiency. Upon determining the conversion efficiency, the dc power is calculated according to Eq. (15). Then, the collector area can be estimated with dc power and collector efficiency based on Eq. (16).

Table 5. Average daily solar insolation and daily maximum temperature in the cultivation period

Region	Optimal tilted angle (°)	Insolation (kWh m^{-2} day^{-1})	Average daily maximum temperature (°C)
Varamin	29.40	5.44	23.87
Ahvaz	27.34	5.18	34.94
Mashhad	29.83	5.49	19.48
Isfahan	28.04	6.07	22.86
Rasht	30.30	4.32	23.84

Table 6. The equations for calculation of required area of the solar panel

Required area of the solar panel calculation	Equations No.
$\beta_{PV.opt} = 1.3793 + Lat(1.2011 + Lat(-0.014404 + Lat \times 0.000080509)$	(16)
$P_{ac} = \frac{ALED}{(h/day) \times NOD}$	(17)
$P_{dc,STC} = \frac{P_{ac}}{Conversion\ efficiency}$	(18)
$A_{PV} = \frac{P_{dc,STC}}{1\ sun\ of\ insolation \times \eta_{PV}}$	(19)
$T_{cell} = T_{amb} + (\frac{NOCT - 20^{\circ}}{0.8}) \times I$	(20)
$TIE = 1 - PR \times (T_{cell} - 25)$	(21)

The panel's efficiency is estimated according to the average efficiency of ten best-selling panels of 2021, reported by www.cleanenergyreviews.info and shown in Table 7. This value is equal to 21.18 %. Based on Masters [32], inverter, module mismatch, and dirt efficiency are assumed to be 90 %, 97 %, and 96 %, respectively, and the effect of temperature on panel performance is calculated using Eq. (17) and Eq. (18). For this purpose, the LG-Neon R panel is first selected from Table 7 and then, the temperature effect is calculated using the parameters reported in the panel characteristics [34]. These parameters include Nominal Operating Cell Temperature (NOCT) and power reduction due to the temperature difference (PR), reported as 44 °C and 0.3 % $°C^{-1}$, respectively.

Table 7. Top 10 solar panels 2021 [35]

Manufacture	Model	Cell type	Max efficiency
LG Energy	Neon R	N-type IBC	22.00 %
Sunpower	Maxeon 3	N-type IBC	22.60 %
REC	Alpha	N-type HJT MBB	21.70 %
Panasonic	EverVolt	N-type HJT MBB	21.20 %
Solaria	Power XT	P-type Half-cut MBB	20.50 %

Qcells	QPeak DUO G9	P-type Half-cut MBB	20.60 %
Trina Solar	Vertex S	P-type Half-cut MBB	21.10 %
Winaico	WST-375MG	P-type Half-cut MBB	20.60 %
JinkoSolar	Tiger Pro N-type	N-type Half-cut MBB	20.70 %
Canadian Solar	HiKu6	N-type Half-cut MBB	20.80 %

3. RESULTS AND DISCUSSION

3.1. Effect of greenhouse structure on incoming solar radiation into the greenhouse

In order to investigate the effect of Venlo and modified arc structures in commercial greenhouses, Section 2.2 was followed and the results are shown in Figure 5 for two specific days, September 24 and January 1. The first point that can be seen from Figure 5 is that the effect of the greenhouse structure on solar transmittance is visible more at sunrise and sunset and is almost constant in the middle of the day. The main reason for this difference at sunrise and sunset is the solar incident angle. According to Equation (2), the solar transmittance is approximately equal to the product of τ_r and τ_a. τ_a depends on the material and thickness of the greenhouse cover and the angle of refraction. Assuming the refraction index equal to 1.526, the refraction angle varies from zero to about 41 degrees for the incident angle of zero to 90 degrees. Since other factors affecting the τ_a are constant, it changes from 0.88 to 0.85, which changes by only about 3.4 percent, while during the regular day, the incident angle does not have such wide changes. Therefore, τ_a does not have a significant effect on justifying changes in the solar transmittance. On the other hand, based on Equation (3), τ_r depends on solar incident angle and angle of refraction. τ_r changes are exponential. Thus, if the incident angle changes from 30 to 50 degrees, the τ_r decreases by only 0.51 percent; however, this change becomes more severe at high angles so that by increasing the incident angle from 80 to 85 degrees, τ_r decreases by almost 7 percent. This leads to the fact that at sunrise and sunset, when the incident angle is high (more than 75 degrees), τ_r has a noticeable effect on the solar transmittance. However, in the middle of the day, when the incident angle is much lower, it has no noticeable effect.

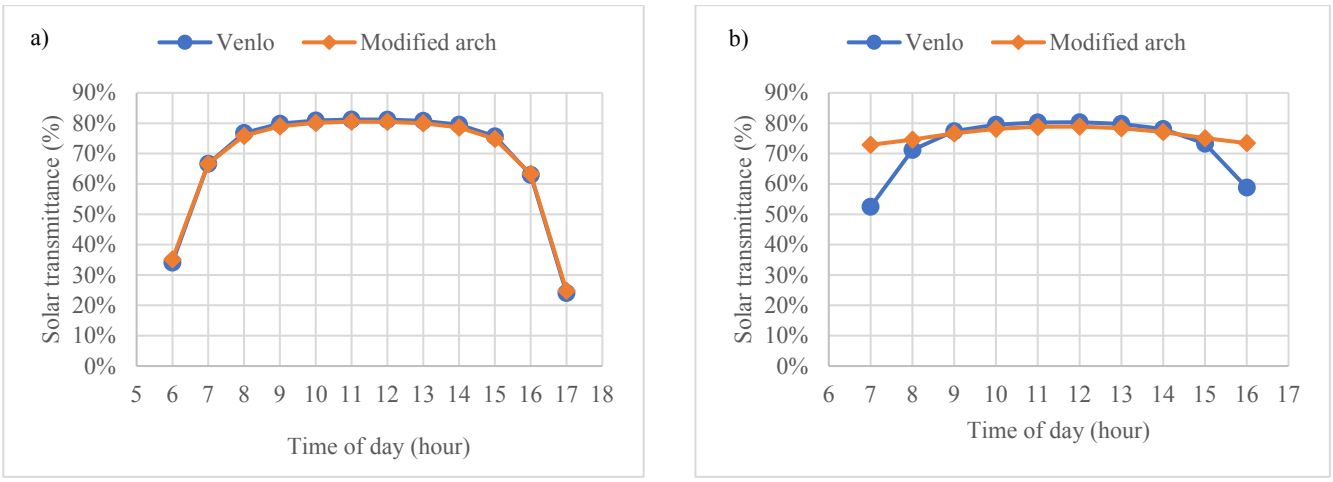

Figure 5. The effect of greenhouse structure on solar transmittance on a) September 24 and b) January 1

Another point that can be deduced from Figure 5 for January 1 and September 24 is that on January 1, especially at sunrise and sunset, there is a difference in the light transmittance of the two structures Venlo and modified arc, while there is no difference at sunrise and sunset on September 24. The reason for this difference is in the roof's shape of modified arc structure. As mentioned earlier, τ_r has an exponential behavior in proportion to changes at the incident angle. On January 1, the incident angle at sunrise is 80.5 degrees for the modified arc structure and 88.4 degrees for the Venlo structure. This fact means that at sunrise and sunset on January 1, the solar transmittance in the Venlo structure is less than that in the modified arc structure. There is no such difference in the incident angle on September 24.

Sunrise light is essential to the initiation of photosynthesis, but it is responsible for only a small part of total incoming light into the greenhouse. Thus, in this paper, the average solar transmittance throughout the cultivation period for two different structures is used, as indicated in Table 8.

Table 8. Average solar transmittance throughout the cultivation period for Venlo and modified arc structures

	Average solar transmittance, Venlo (%)	**Average solar transmittance, Modified arc (%)**
Varamin	71.64	73.08
Ahvaz	71.98	73.33
Mashhad	71.71	74.04
Isfahan	71.93	73.06
Rasht	71.61	73.14

3.2. Evaluation of available natural light

According to Section 2.3, the natural light available in the five selected regions during the cultivation period is shown in Figure 6 to Figure 10. According to Dorais [12], the optimum PAR Light (DLI) for Tomato is 30 mol m^{-2} day^{-1}. As shown in Figures 6 to 10, during the cultivation period, which starts on September 24 (Day 1) and lasts until April 20 (Day 210), there are many days in all the studied cities where the available natural DLI is less than the desired amount. It can also be seen that there is no significant difference between Venlo and modified arc structures in terms of natural DLI deficit.

As shown in Figure 6 to 10, in all regions, the general trend of available natural DLI is reduced to a minimum between days 80 and 110, equivalent to late December and early January, and then the available natural DLI has increased again. Rasht has been experiencing a natural DLI deficit since the first days of the cultivation period, while in other cities, there is a natural DLI deficit from about the 10th day.

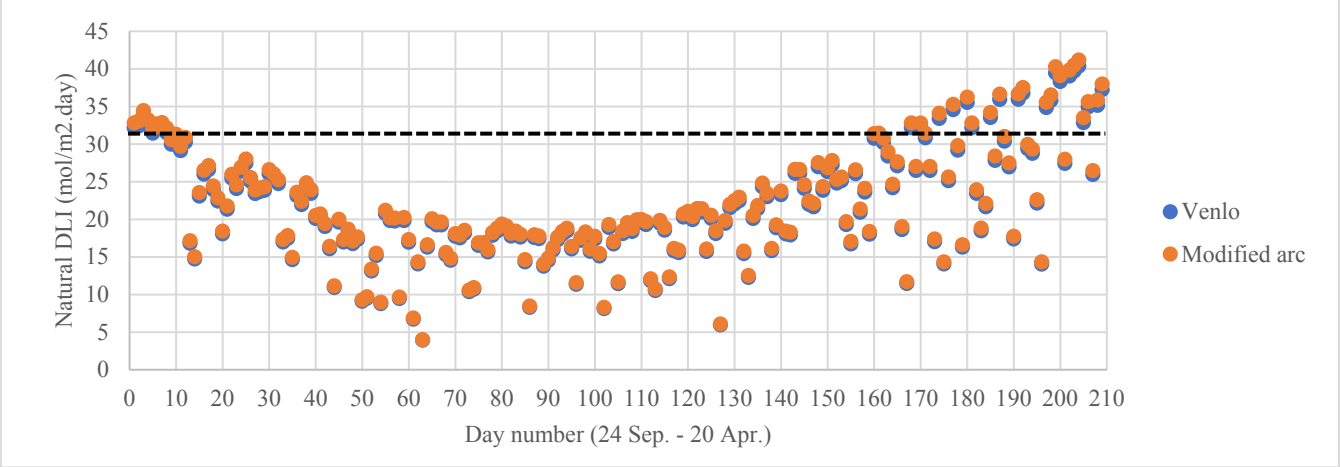

Figure 6. Available daily light integral during the cultivation period in Varamin

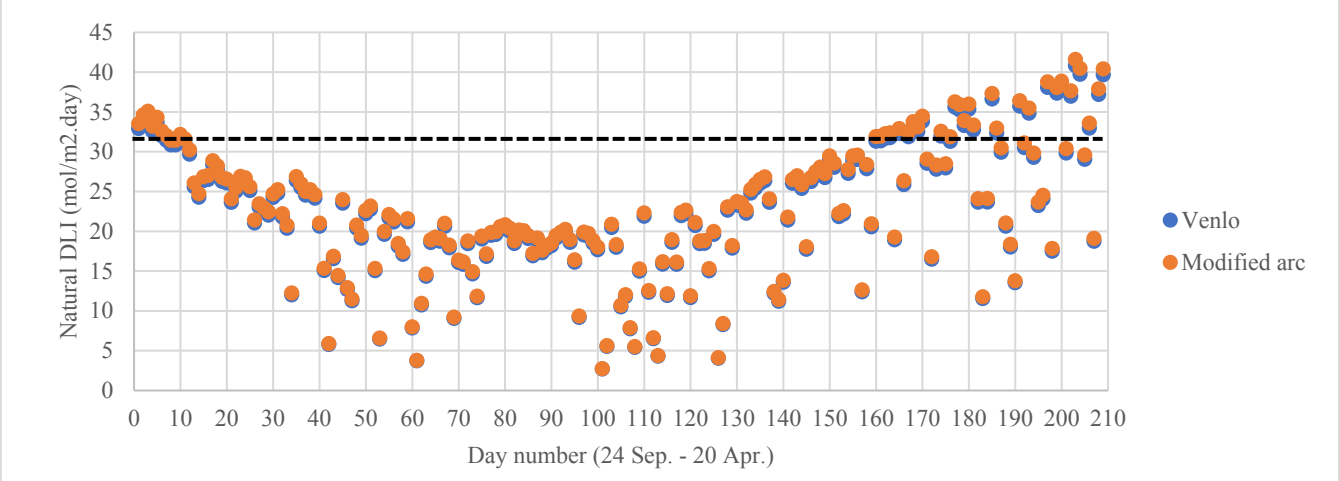

Figure 7. Available daily light integral during the cultivation period in Ahvaz

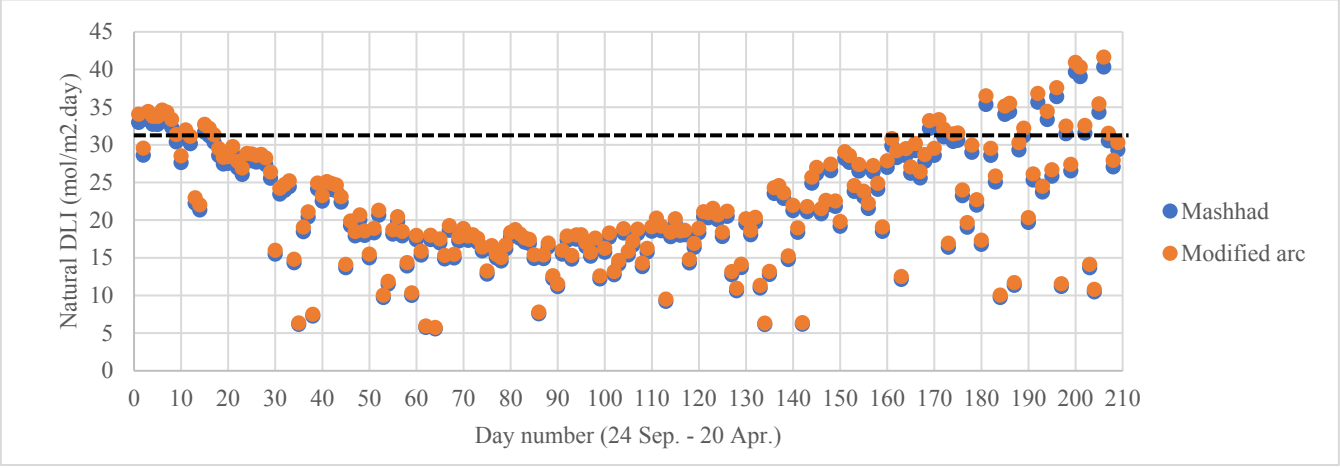

Figure 8. Available daily light integral during the cultivation period in Mashhad

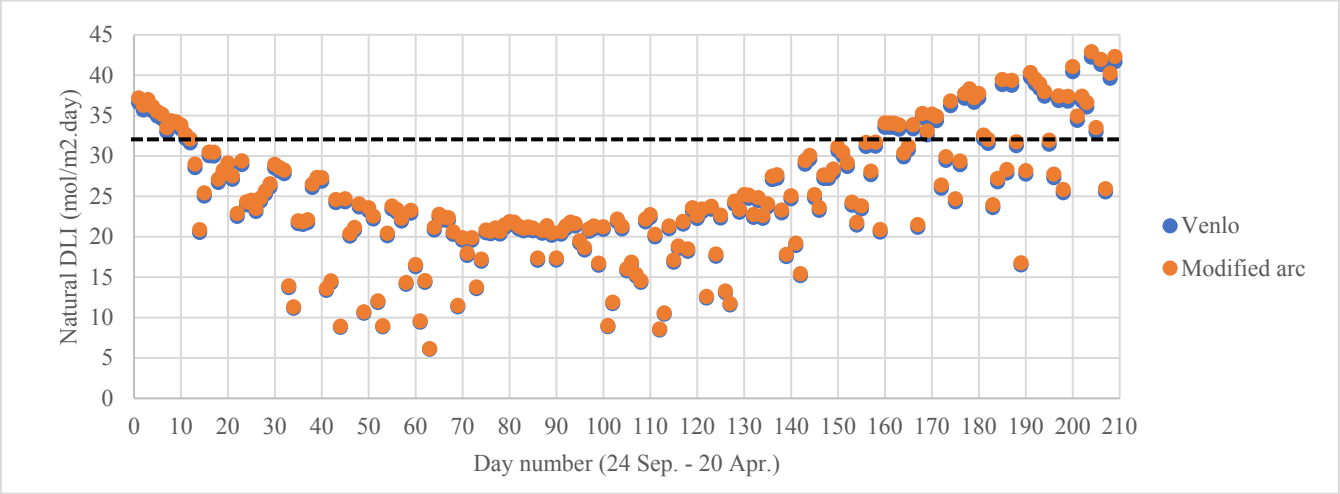

Figure 9. Available daily light integral during the cultivation period in Isfahan

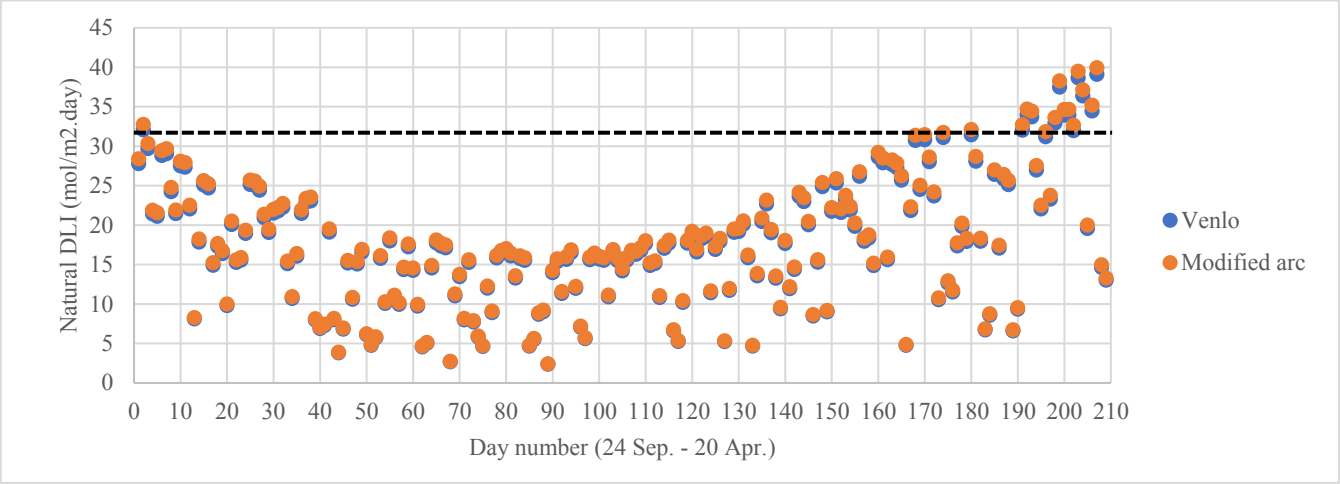

Figure 10. Available daily light integral during the cultivation period in Rasht

In order to evaluate the natural DLI deficit, the indicators introduced in Table 4 have been used. The first indicator is the PDNLD which is shown in Table 9. The percentage of days with a natural light deficit in the best case is equal to 75 % that belongs to Isfahan, and the worst one with 91 % belongs to Rasht. This fact indicates that even the best case faces light deficit in a high percentage of days during the cultivation period. Between Venlo and modified arc structures, the percentage of days when the insufficient light reaches the plant is slightly lower in the modified arc structures.

The second indicator, shown in Table 9, is the amount of light deficit (ALD). Modified arc structure in Isfahan with 1321.9 mol m^{-2} has the least amount of light deficiency, while Venlo structure in Rasht with 2653.5 mol m^{-2} has the highest amount of light deficiency. While the difference in the percentage of days with light deficiency between Isfahan and Rasht is 16.27 %, the amount of light deficiency in Rasht is 93 % more than Isfahan. This fact shows that although the number of days with light deficiency for Isfahan is high, the amount of light deficiency is much less than that in other cities. Among other cities, Varamin and Mashhad are close to each other in terms of light deficit. There is only a difference of 3 mol m^{-2} between the two cities in the modified arc structure regarding the light deficit; in the Venlo structure, this difference increases to 40 mol m^{-2}.

Table 9. The percentage of day with a natural light deficit and the amount of light deficit for 5 different regions and two greenhouse structures from Sep. 24 to April 20

	Venlo		Modified arc	
	PDNLD (%)	**ALD (mol m^{-2})**	**PDNLD (%)**	**ALD (mol m^{-2})**
Varamin	82.7	1859.7	81.9	1793.4
Ahvaz	80.3	1749.6	78.9	1688.9
Mashhad	84.6	1899.6	82.7	1790.3
Isfahan	75.1	1373.0	73.2	1321.9
Rasht	91.3	2653.5	90.9	2588.1

3.3. Evaluation of the artificial light impact

In this section, the effect of adding a supplementary lighting system on the greenhouse lighting indicators is investigated. The lighting plan strategy is developed according to supplementary lighting algorithm, which was previously illustrated in the methodology section. Figures 11 to 15 show the effect of the lighting system for Venlo structure for two different light capacities: (1) high lighting capacity at Photosynthesis Photon Flux Density (PPFD) of 200 $\mu mol\ m^{-2}\ s^{-1}$ and (2) low lighting capacity at PPFD of 100 $\mu mol\ m^{-2}\ s^{-1}$. These figures show the Natural Daily Light Integral (NDLI) and the Total Daily Light Integral (TDLI). TDLI is the sum of NDLI and Artificial Daily Light Integral (ADLI).

As shown in Figure 11 to Figure 15, artificial light has improved the daily light integral in the greenhouse, but even PPFD 200 $\mu mol\ m^{-2}\ s^{-1}$ has not completely met the needs of the tomato plant. Detailed information available in Figure 11 to Figure 15 as well as in Table 10 is provided by two indicators, PDNLD and ALD. Comparison between Table 9 and Table 10 shows the effect of adding artificial light. As can be seen, for PDNLD, the low light capacity leads to 6.2 % and 13.88 % decrease rates in Varamin and Mashhad, respectively. Also, it leads to a decrease of 17.7 % in Rasht to 32 % in Isfahan in high capacity. The ALD index shows that although the number of days with light deficiency has been reduced to 30 % in the best case, the amount of light deficiency has changed significantly due to the lighting system so that in the case of high light capacity, the amount of light deficiency in Isfahan for Venlo structure with 1373.07 mol m^{-2} (Table 9) has decreased to 288 mol m^{-2} (Table 10) or, in other words, 78 %. As shown in Table 10, the amount of light deficiency has also decreased significantly in other cities.

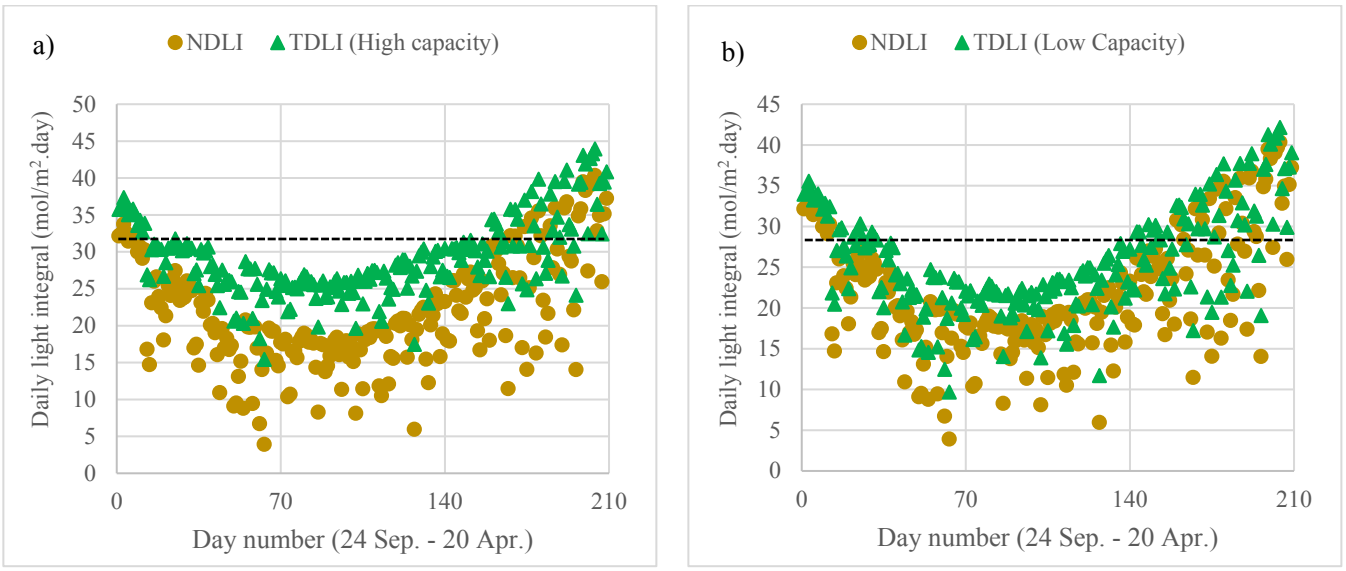

Figure 11. Natural daily light integral and Total Daily Light Integral (TDLI) for Venlo structure in two different artificial light capacities of a) 200 $\mu mol\ m^{-2}\ s^{-1}$ and b) 100 $\mu mol\ m^{-2}\ s^{-1}$ in Varamin

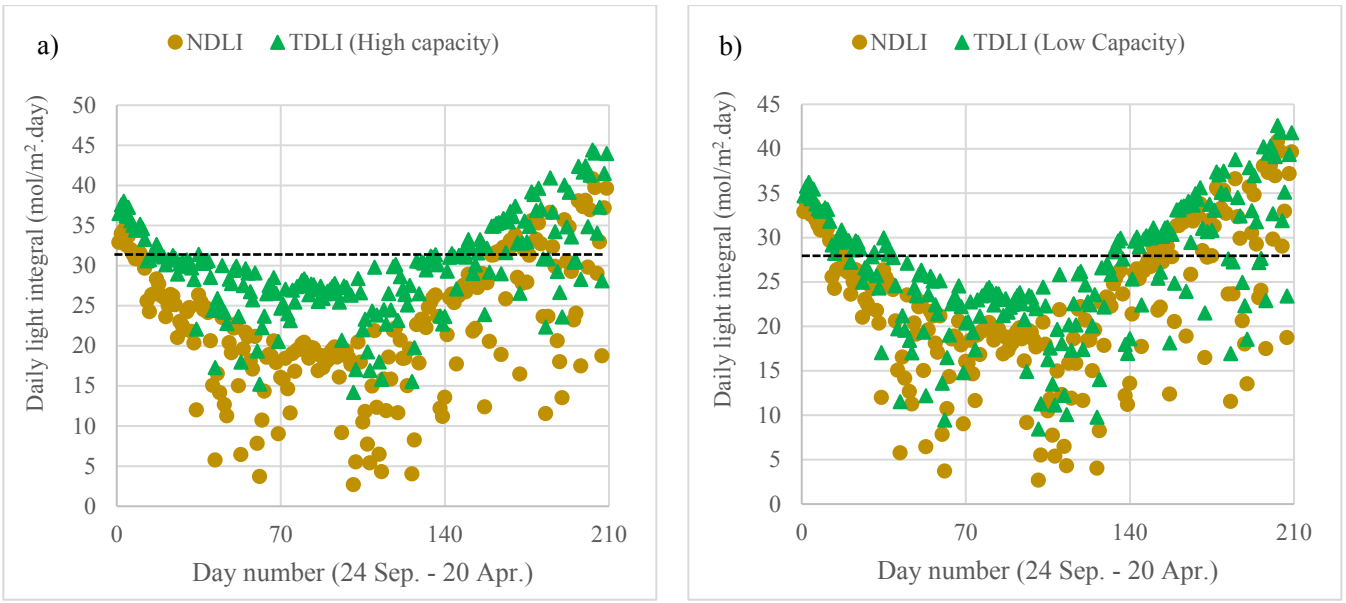

Figure 12. Natural daily light integral and Total Daily Light Integral (TDLI) for Venlo structure in two different artificial light capacities of a) 200 $\mu mol\ m^{-2}\ s^{-1}$ and b) 100 $\mu mol\ m^{-2}\ s^{-1}$ in Ahvaz

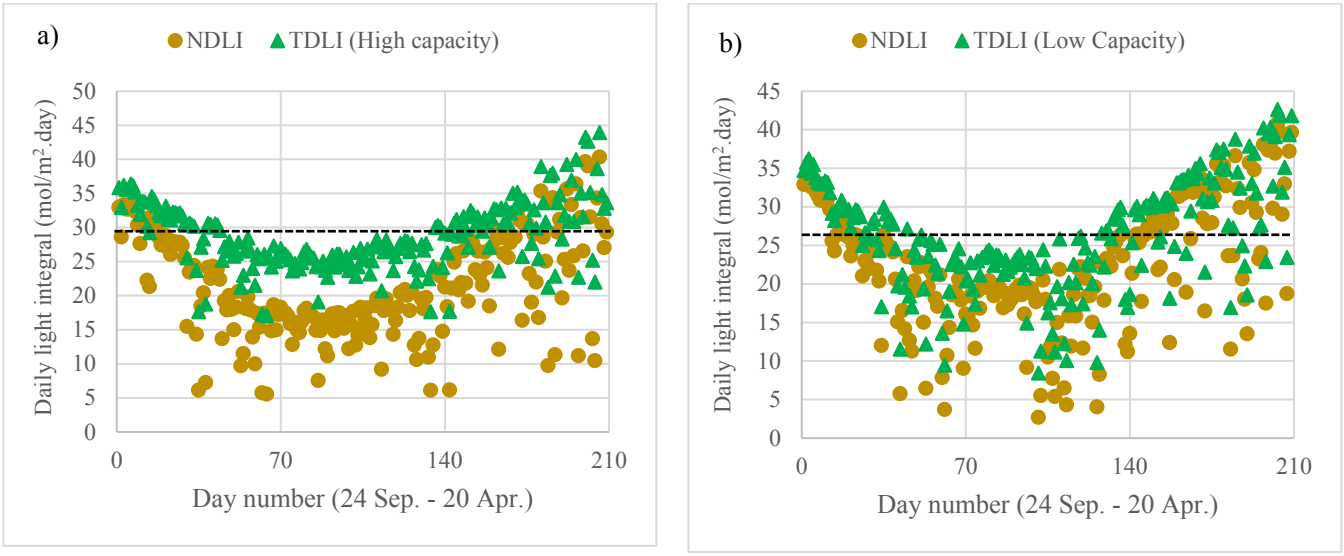

Figure 13. Natural daily light integral and Total Daily Light Integral (TDLI) for Venlo structure in two different artificial light capacities of a) 200 µmol m^{-2} s^{-1} and b) 100 µmol m^{-2} s^{-1} in Mashhad

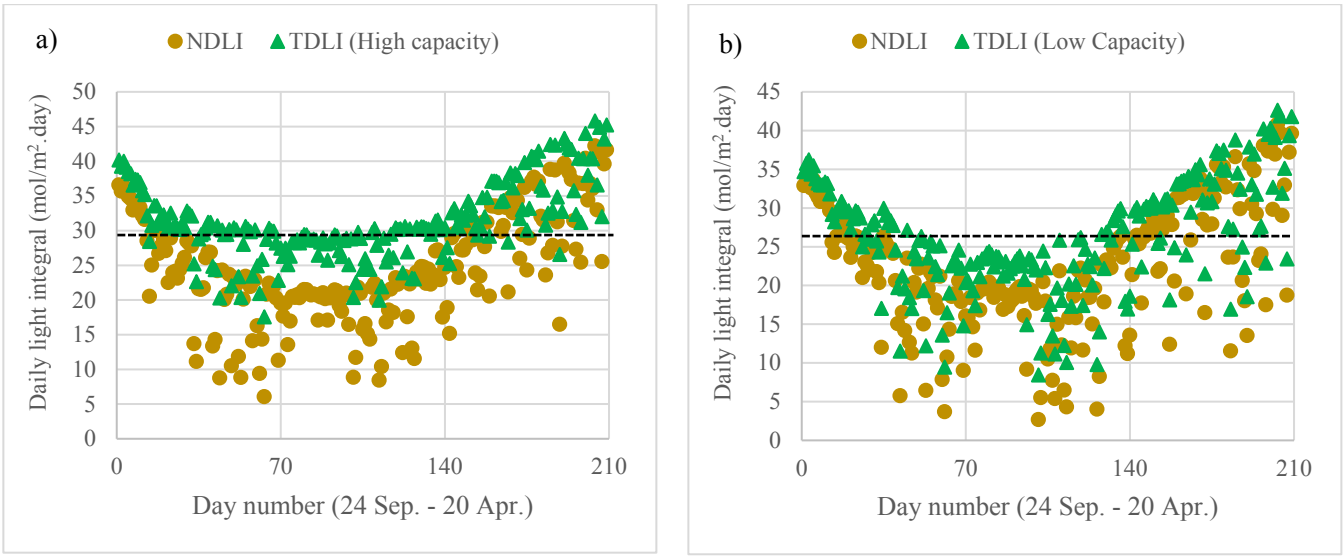

Figure 14. Natural daily light integral and Total Daily Light Integral (TDLI) for Venlo structure in two different artificial light capacities of a) 200 µmol m^{-2} s^{-1} and b) 100 µmol m^{-2} s^{-1} in Isfahan

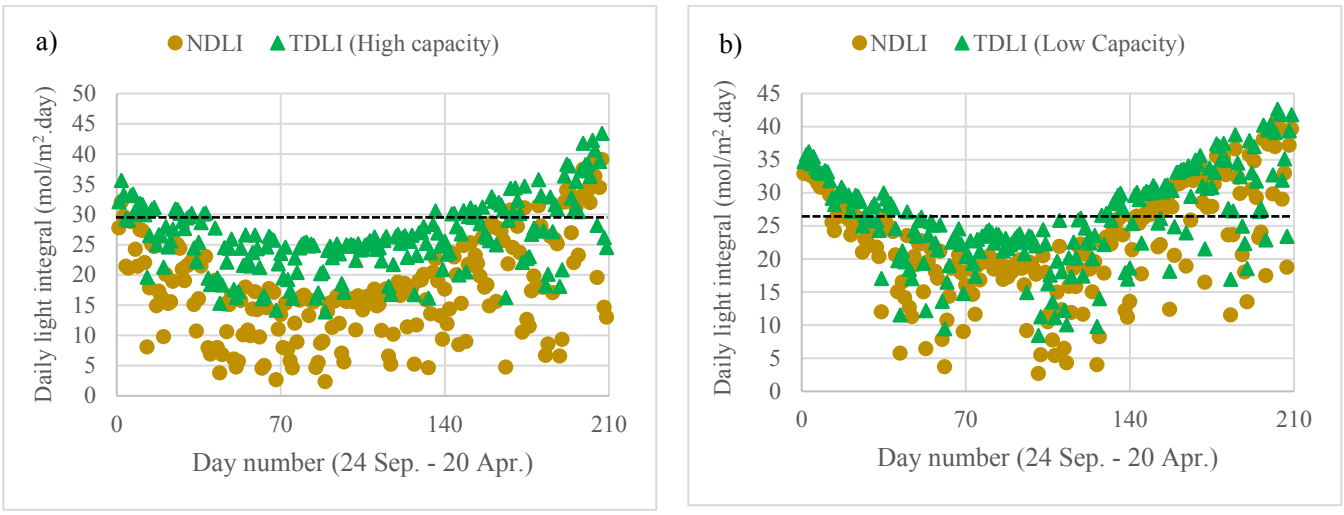

Figure 15. Natural daily light integral and Total Daily Light Integral (TDLI) for Venlo structure in two different artificial light capacities of a) 200 µmol m^{-2} s^{-1} and b) 100 µmol m^{-2} s^{-1} in Rasht

Table 10. The percent of day with a natural light deficit and the amount of light deficit for 5 regions and Venlo structure, from September 24 to April 20

	High capacity		Low capacity	
	PDNLD (%)	ALD (mol m^{-2})	PDNLD (%)	ALD (mol m^{-2})
Varamin	76.5%	1148.5	58.3%	529.8
Ahvaz	70.8%	1070.9	52.1%	502.4
Mashhad	70.8%	1181.8	57.8%	566.4
Isfahan	61.7%	774.7	41.1%	288.5
Rasht	84.6%	1777.4	73.2%	966.8

3.4. The required area of the photovoltaic panel to meet the energy demand of the lighting system

Based on the methodology presented in Section 2.4, the first step is to calculate the energy demand during the year, as shown in Table 11. After calculating ac and dc power, the required area of the panel for a square meter of greenhouse can be estimated with the help of conversion efficiency and panel efficiency, as shown in Table 12. The conversion efficiency rates for Varamin, Ahvaz, Mashhad, Isfahan, and Rasht are calculated to be 0.77, 0.74, 0.78, 0.77, and 0.77, respectively.

Table 12 shows the ratio of the photovoltaic panel area to the greenhouse area. The color green, which indicates low values of this ratio, is mainly in the low-capacity LED section. Venlo greenhouse in Rasht with a high capacity of HPS lamp is the largest, and the modified arc greenhouse in Isfahan with low capacity of LED lamp has the lowest ratio. Isfahan has the lowest ratio of PV area to greenhouse area, followed by Mashhad, Varamin, Ahvaz, and Rasht, respectively. In all cities, the performance of the modified arc structure is slightly better than that of the Venlo structure.

Another point of view shown in Table 12 is the impact of LED technology on reducing the PV area required to meet the energy demand of the lighting system. The impact of LED and HPS technologies is particularly effective in regions with high lighting demand similar to the situation with a high capacity in Rasht. The difference between the two technologies is close to 0.8 $m^2_{PV}\ m^{-2}_{greenhouse}$. It is implied that 50 % energy saving could be achieved when LED lamps are used; this result is in the range reported in Martineau et al. [36], illustrating that energy savings by LED lamps could be between 33.8 % to 77.8 % in comparison to HPS lamps.

The LG Neon model panel cost is about $ 364 per square meter [37] due to its advanced technology and high efficiency. Therefore, the cost of photovoltaic panels to compensate for the energy consumption of supplementary lighting ranges from $ 171 per greenhouse area in Isfahan (modified arc with LED technology) to $ 939 per greenhouse area in Rasht (Venlo with HPS technology). Also, it can be seen that up to $ 291 per greenhouse area can be saved using LED technology instead of HPS in Rasht with the high-capacity lighting system. However, the cost of photovoltaic panels is decreasing which can improve the economic aspect of supplementary lighting in the future. Of note, the application of the semi-transparent photovoltaic technology could also diminish the land use for photovoltaic system, which is to be the subject of our future study.

Table 9. Annual Energy Demand of the lighting system in greenhouses for two different lighting technologies, LED and HPS

City	LED (kWh m^{-2} y^{-1})				HPS (kWh m^{-2} y^{-1})			
	Low capacity		High capacity		Low capacity		High capacity	
	Venlo	Modified arc	Venlo	Modified arc	Venlo	Modified arc	Venlo	Modified arc
Varamin	109.90	108.65	211.10	207.90	164.85	162.98	316.65	311.85
Ahvaz	108.10	106.15	206.80	203.00	162.15	159.23	310.20	304.50
Mashhad	110.05	107.10	211.40	205.90	165.08	160.65	317.10	308.85
Isfahan	99.45	97.90	189.40	186.10	149.18	146.85	284.10	279.15
Rasht	128.20	126.05	251.40	246.90	192.30	189.08	377.10	370.35

Table 10. Panel area required for each square meter of the greenhouse to supply energy consumption of the lighting system for two different lighting technologies, LED and HPS, from Sep. 24 to April 20

City	LED ($m^2_{PV}\ m^{-2}_{greenhouse}$)				HPS ($m^2_{PV}\ m^{-2}_{greenhouse}$)			
	Low capacity		High capacity		Low capacity		High capacity	
	Venlo	Modified arc	Venlo	Modified arc	Venlo	Modified arc	Venlo	Modified arc
Varamin	0.60	0.59	1.14	1.13	0.89	0.88	1.72	1.69
Ahvaz	0.64	0.63	1.22	1.20	0.96	0.94	1.83	1.80
Mashhad	0.58	0.57	1.12	1.09	0.87	0.85	1.68	1.64
Isfahan	0.48	0.47	0.92	0.90	0.72	0.71	1.38	1.35
Rasht	0.88	0.86	1.72	1.69	1.31	1.29	2.58	2.53

4. CONCLUSIONS

Due to the natural light deficiency for optimal plant growth, there is a tremendous interest to investigate the effect of adding a supplementary lighting system in conventional greenhouses systems. For this purpose, first, the available natural light considering greenhouse structures (Venlo or modified arc) in the five regions of Iran including Varamin, Ahvaz, Mashhad, Isfahan, and Rasht were estimated. After determining the amount of natural light deficiency, the effects of adding two artificial light system with capacities of 100 and 200 $\mu mol\, m^{-2}\, s^{-1}$ were investigated. Finally, the electrical energy consumption of the lighting system was calculated considering the efficacies of two lamp technologies (LED and HPS), and the area of the photovoltaic panel required to supply this energy was calculated. The most important results of this study are as follows:

- The effect of greenhouse structure on solar radiation transmission coefficient was greater at sunrise and sunset, but was almost the same during the day.
- In winter, when the solar altitude angle was low, the modified arc greenhouse had a higher light transmission coefficient due to its roof structure and solar incidence angle.
- In general, the Venlo and modified arc structures of the greenhouse did not have much effect on the total light integral during the year.
- The natural light deficiency in the studied regions was significant, e.g., Isfahan with the most natural light available in about 75 % of the cultivation days (24 Sep.-20 Apr.) suffers from insufficient light considering optimum light, which is reported for tomato by 1373.07 mol m^{-2}.
- Among the case study regions, the lowest available natural light belonged to the city of Rasht such that in more than 91 % of the cultivation days, the optimum DLI (30 mol/m^2.day) is not achieved during considered cultivation period (24 Sep.-20 Apr.).
- The low and high capacities of artificial lighting system can effectively compensate for the natural light deficiency. The low capacity of artificial light on average leads to nearly a 10 % reduction in the number of days with the light deficit and 38.3 % in the total amount of light deficiency. The high capacity on average leads to a 25 % reduction in the number of days with light deficiency and 70 % in the amount of light deficiency.
- LED technology can save energy from 48.95 kWh per square meter in Isfahan to 123.45 kWh per square meter in Rasht during the cultivation period in comparison with HPS technology.
- Due to the greater availability of natural light, the electricity demand for lighting system in the modified structure was less than that for the Venlo structure.
- The area of photovoltaic panels to compensate the energy consumption of supplementary lighting ranged from 0.47 m^2 per greenhouse area in Isfahan (modified arc with LED technology) to 2.58 m^2 per greenhouse area in Rasht (Venlo with HPS technology).
- Among the studied regions, Isfahan has the lowest PV area to meet energy demand, orderly followed by Mashhad, Varamin, Ahvaz, and Rasht.
- The prospects of current research are (1) studying other common shapes or innovative new structures of greenhouses (e.g., advances solar greenhouses); (2) improving the on-off scheme of the lighting system by predicting natural light availability through previous horizon methodologies; (3) using semi-transparent Photovoltaic technology to diminish the land use for photovoltaic system; and (4) investigating the environmental impact of the greenhouse lighting system, e.g., life cycle analysis of supplementary lighting system.

5. ACKNOWLEDGEMENT

The authors would like to thank the Department of Energy Engineering of Sharif University of Technology.

NOMENCLATURE

A	Area (m^2)
ALED	Artificial light energy demand (kWh m^{-2})
h	Hour
I	Solar radiation (W m^{-2})
K	Extinction coefficient (m^{-1})
L	Thickness of the glass cover (mm)
Lat	Latitude (°)
Lon	Longitude (°)
n	Refraction index
NOCT	Nominal operating cell temperature (°C)
NOD	Number of days
P	Power (kW)
PR	Power reduction due to the temperature difference (% $°C^{-1}$)
PPFD	Photosynthetic photon flux density
PV	Photovoltaics
$r_{\parallel}$	Parallel component of unpolarized radiation
$r_{\perp}$	Perpendicular component of unpolarized radiation
T	Temperature (°C)
TIE	Temperature impact efficiency
Greek letters	
α	Solar altitude angle (°)
B	Tilted angle (°)
η	Efficiency
θ_1	Incident angle (°)
θ_2	Angle of refraction (°)
τ	Transmissivity
Subscripts	
a	Absorption
ac	Alternating current
amb	Ambient
dc	Direct current
opt	Optimum
r	Reflection
STC	Standard test conditions

REFERENCES

1. Agrios, G.N., "Chapter three-Effects of pathogens on plant physiological functions", Plant pathology, Fifth Edition, Agrios, G.N. Ed., Academic Press, San Diego, (2005), 105-123 (https://doi.org/10.1016/B978-0-08-047378-9.50009-9).
2. Serale, G., Gnoli, L., Giraudo, E. and Fabrizio, E., "A supervisory control strategy for improving energy efficiency of artificial lighting systems in greenhouses", ***Energies***, Vol. 14, No. 1, (2021), 202. (https://doi.org/10.3390/en14010202).
3. Wien, H.C. and Stützel, H., "Chapter seven, Tomato", The physiology of vegetable crops, CABI, (2020), 163-164. (https://www.cabi.org/bookshop/book/9781786393777/).
4. Tewolde, F.T., Lu, N., Shiina, K., Maruo, T., Takagaki, M., Kozai, T. and Yamori, W., "Nighttime supplemental LED inter-lighting improves growth and yield of single-truss tomatoes by enhancing photosynthesis

in both winter and summer", ***Frontiers in Plant Science***, Vol. 7, (2016), 448. (https://doi.org/10.3389/fpls.2016.00448).

5. De Pascale, S., Maggio, A., Orsini, F., Stanghellini, C. and Heuvelink, E., "Growth response and radiation use efficiency in tomato exposed to short-term and long-term salinized soils", ***Scientia Horticulturae***, Vol. 189, (2015), 139-149. (https://doi.org/10.1016/j.scienta.2015.03.042).
6. Xu, D., Du, S. and van Willigenburg, G., "Double closed-loop optimal control of greenhouse cultivation", ***Control Engineering Practice***, Vol. 85, (2019), 90-99. (https://doi.org/10.1016/j.conengprac.2019.01.010).
7. Ahamed, M.S., Guo, H. and Tanino, K., "Energy saving techniques for reducing the heating cost of conventional greenhouses", ***Biosystems Engineering***, Vol. 178, (2019), 9-33. (https://doi.org/10.1016/j.biosystemseng.2018.10.017).
8. Sethi, V.P., "On the selection of shape and orientation of a greenhouse: Thermal modeling and experimental validation", ***Solar Energy***, Vol. 83, No. 1, (2009), 21-38. (https://doi.org/10.1016/j.solener.2008.05.018).
9. Von Elsner, B., Briassoulis, D., Waaijenberg, D., Mistriotis, A., Von Zabeltitz, C., Gratraud, J., Russo, G. and Suay-Cortes, R., "Review of structural and functional characteristics of greenhouses in European Union countries, Part II: Typical designs", ***Journal of Agricultural Engineering Research***, Vol. 75, No. 2, (2000), 111-126. (https://doi.org/10.1006/jaer.1999.0512).
10. Gupta, M.J. and Chandra, P., "Effect of greenhouse design parameters on conservation of energy for greenhouse environmental control", ***Energy***, Vol. 27, No. 8, (2002), 777-794. (https://doi.org/10.1016/S0360-5442(02)00030-0).
11. Mobtaker, H.G., Ajabshirchi, Y., Ranjbar, S.F. and Matloobi, M., "Solar energy conservation in greenhouse: Thermal analysis and experimental validation", ***Renewable Energy***, Vol. 96, (2016), 509-519. (https://doi.org/10.1016/j.renene.2016.04.079).
12. Dorais, M., "The use of supplemental lighting for vegetable crop production: Light intensity, crop response, nutrition, crop management, cultural practices", ***Proceedings of Canadian Greenhouse Conference***, Vol. 9, (2003). (https://www.agrireseau.net/legumesdeserre/documents/cgc-dorais2003fin2.pdf).
13. Garcia-Caparros, P., Chica, R.M., Almansa, E.M., Rull, A., Rivas, L.A., García-Buendía, A., Barbero, F.J. and Lao, M.T., "Comparisons of different lighting systems for horticultural seedling production aimed at energy saving", ***Sustainability***, Vol. 10, No. 9, (2018), 3351. (https://doi.org/10.3390/su10093351).
14. Lu, N., Maruo, T., Johkan, M., Hohjo, M., Tsukagoshi, S., Ito, Y., Ichimura, T. and Shinohara, Y., "Effects of supplemental lighting with light-emitting diodes (LEDs) on tomato yield and quality of single-truss tomato plants grown at high planting density", ***Environmental Control in Biology***, Vol. 50, No. 1, (2012), 63-74. (https://doi.org/10.2525/ecb.50.63).
15. Paucek, I., Pennisi, G., Pistillo, A., Appolloni, E., Crepaldi, A., Calegari, B., Spinelli, F., Cellini, A., Gabarrell, X. and Orsini, F., "Supplementary LED interlighting improves yield and precocity of greenhouse tomatoes in the Mediterranean", ***Agronomy***, Vol. 10, No. 7, (2020), 1002. (https://doi.org/10.3390/agronomy10071002).
16. Gómez, C. and Mitchell, C., "Supplemental lighting for greenhouse-grown tomatoes: Intracanopy LED towers vs. overhead HPS lamps", ***Proceedings of ISHS Acta Horticulturae 1037: International Symposium on New Technologies for Environment Control, Energy-Saving and Crop Production in Greenhouse and Plant Factory-Greensys 2013***, (2013), 855-862. (https://doi.org/10.17660/ActaHortic.2014.1037.114).
17. Körner, O., Andreassen, A.U. and Aaslyng, J.M., "Simulating dynamic control of supplementary lighting", ***Proceedings of ISHS Acta Horticulturae 711: V International Symposium on Artificial Lighting in Horticulture***, (2005), 151-156. (https://doi.org/10.17660/ActaHortic.2006.711.17).
18. Heuvelink, E. and Challa, H., "Dynamic optimization of artificial lighting in greenhouses", ***Proceedings of ISHS Acta Horticulturae 260: International Symposium on Growth and Yield Control in Vegetable Production***, (1989), 401-412. (https://doi.org/10.17660/ActaHortic.1989.260.26).
19. Niu, G., Heins, R.D., Cameron, A.C. and Carlson, W.H., "Day and night temperatures, daily light integral, and CO_2 enrichment affect growth and flower development of *Campanula carpatica* 'Blue Clips'", ***Scientia Horticulturae***, Vol. 87, No. 1-2, (2001), 93-105. (https://doi.org/10.1016/S0304-4238(00)00164-3).
20. Kottek, M., Grieser, J., Beck, C., Rudolf, B. and Rubel, F., "World map of the Köppen-Geiger climate classification updated", ***Meteorologische Zeitschrift***, (2006). (https://doi.org/10.1127/0941-2948/2006/0130).
21. Rahimi, J., Laux, P. and Khalili, A., "Assessment of climate change over Iran: CMIP5 results and their presentation in terms of Köppen–Geiger climate zones", ***Theoretical and Applied Climatology***, Vol. 141, No. 1, (2020), 183-199. (https://doi.org/10.1007/s00704-020-03190-8).
22. Pfenninger, S. and Staffell, I., "Long-term patterns of European PV output using 30 years of validated hourly reanalysis and satellite data", ***Energy***, Vol. 114, (2016), 1251-1265. (https://doi.org/10.1016/j.energy.2016.08.060).
23. Staffell, I. and Pfenninger, S., "Using bias-corrected reanalysis to simulate current and future wind power output", ***Energy***, Vol. 114, (2016), 1224-1239. (https://doi.org/10.1016/j.energy.2016.08.068).
24. Kalogirou, S.A., "Chapter two, Environmental characteristics", Solar energy engineering: processes and systems, Academic Press, (2013), 80-82. (https://doi.org/10.1016/B978-0-12-397270-5.00002-9).
25. Carruthers, T.J., Longstaff, B.J., Dennison, W.C., Abal, E.G. and Aioi, K., "Measurement of light penetration in relation to seagrass", ***Global Seagrass Research Methods***, (2001), 370-392. (https://doi.org/10.1016/B978-044450891-1/50020-7).
26. Tsubo, M. and Walker, S., "Relationships between photosynthetically active radiation and clearness index at Bloemfontein, South Africa", ***Theoretical and Applied Climatology***, Vol. 80, No. 1, (2005), 17-25. (https://doi.org/10.1007/s00704-004-0080-5).
27. Rao, C.N., "Photosynthetically active components of global solar radiation: Measurements and model computations", ***Archives for Meteorology, Geophysics, and Bioclimatology, Series B***, Vol. 34, No. 4, (1984), 353-364. (https://doi.org/10.1007/BF02269448).
28. Udo, S. and Aro, T., "Global PAR related to global solar radiation for central Nigeria", ***Agricultural and Forest Meteorology***, Vol. 97, No. 1, (1999), 21-31. (https://doi.org/10.1016/S0168-1923(99)00055-6).
29. Dorais, M. and Gosselin, A., "Physiological response of greenhouse vegetable crops to supplemental lighting", ***Proceedings of* ISHS Acta Horticulturae 580: *IV International ISHS Symposium on Artificial Lighting***, (2000), 59-67. (https://doi.org/10.17660/ActaHortic.2002.580.6).
30. Runkle, E., "An update on LED lighting efficacy", Department of Horticulture, Michigan State University, (2018). (https://www.canr.msu.edu/floriculture/uploads/files/updateefficacy.pdf).
31. Heuvelink, E., Bakker, M., Hogendonk, L., Janse, J., Kaarsemaker, R. and Maaswinkel, R., "Horticultural lighting in the Netherlands: New developments", ***Proceedings of* ISHS Acta Horticulturae 711: *V International Symposium on Artificial Lighting in Horticulture***, (2005), 25-34. (https://doi.org/10.17660/ActaHortic.2006.711.1).
32. Masters, G.M., "Chapter nine, Photovoltaic systems", Renewable and efficient electric power systems, John Wiley & Sons, (2013), 528-533. (https://doi.org/10.1002/0471668826).
33. Jacobson, M.Z. and Jadhav, V., "World estimates of PV optimal tilt angles and ratios of sunlight incident upon tilted and tracked PV panels relative to horizontal panels", ***Solar Energy***, Vol. 169, (2018), 55-66. (https://doi.org/10.1016/j.solener.2018.04.030).
34. LG NeON® R 380 W. (https://www.lgenergy.com.au/uploads/download_files/739b577232b1635cf7a223264706e8d9fa58ccf5.pdf).
35. "Top 10 solar panels-Latest solar panel and PV cell technology," (2021). (https://www.cleanenergyreviews.info/blog/2017/9/11/best-solar-panels-top-modules-review), (Accessed: May 2, 2021).
36. Martineau, V., Lefsrud, M., Naznin, M.T. and Kopsell, D.A., "Comparison of light-emitting diode and high-pressure sodium light treatments for hydroponics growth of Boston lettuce", ***HortScience***, Vol. 47, No. 4, (2012), 477-482. (https://doi.org/10.21273/HORTSCI.47.4.477).
37. "LG NeON® R price". (https://www.solaris-shop.com/lg-neon-r-lg380q1c-v5-380w-mono-solar-panel/).

JREE: Vol. 9, No. 4, (Autumn 2022) 34-47

Journal of Renewable Energy and Environment

Journal Homepage: www.jree.ir

Materials and Energy Research Center

MERC

Research Article

The Problem of Resilient Stochastic Unit Commitment with Consideration of Existing Uncertainties Using the Rate of Change of Frequency

Moslem Geravandi, Hassan Moradi CheshmehBeigi *

Department of Electrical Engineering, Faculty of Engineering, Razi University, P. O. Box: 67144-14971, Kermanshah, Iran.

PAPER INFO

Paper history:
Received: 24 September 2021
Revised in revised form: 09 December 2021
Scientific Accepted: 08 January 2022
Published: 16 August 2022

Keywords:
Resilience,
Unit Commitment,
Uncertainty,
Wind and Solar Power Plants,
Load Interruption Contracts,
Adaptive Frequency Load Shedding

ABSTRACT

The ability of power systems against severe events shows their increased resilience, which in turn reduces the operation costs and recovery time of the system. This study presents a new resilient stochastic unit commitment model using the frequency change rate as a new index of system resilience. Furthermore, uncertainties of wind and solar power plants and demanded load are considered simultaneously. In the proposed method that considers the occurrence of a destructive incident in important production units in the worst-case scenarios and by using the generation capacity, adaptive frequency load shedding, and interrupting contracts, an effective strategy was provided to solve the unit commitment problem of thermal units to prevent instability in system frequency and to minimize unwanted load shedding. The proposed model was tested and evaluated on the IEEE 39-bus system with a wind power plant and a solar power plant. Moreover, the results obtained from simulation were reported. The effectiveness of this innovative approach in increasing the resilience of the power system against different degrees of uncertainty was confirmed based on the results.

https://doi.org/10.30501/jree.2022.306473.1262

1. INTRODUCTION

Nowadays, due to the depletion of conventional energy sources and emission of greenhouse gases, the use of wind and solar resources has increased significantly. Despite the many advantages of Wind and Solar Power Plants (WSPP), the output power of these sources is variable and cannot be predicted accurately. This issue has significant impact on the performance of power systems [1-3]. Unit Commitment Problem (UCP) is a complex multi-objective optimization problem employed to schedule the generation of the power system in the day-ahead given net load predictions and various operational constraints upon maintaining system security at a minimal cost [4, 5]. To meet this goal, the amount of load demand and WSPP must be predicted with maximum accuracy. The existence of many WSPPs in the power system causes high uncertainty in production scheduling [6]. Robust optimization and stochastic programming are two common frameworks for resolving uncertainties in the UCP. In the analysis of models using stochastic programming, uncertainty is shown through probability distribution [7, 8].

Severe events and destructive blackouts, in addition to the imposition of heavy damages, deprive many subscribers of access to electricity. In the past few years, a new concept called resilience in the electricity industry was considered by researchers, which is the boundary between system robustness and system reliability [9]. Resilience represents a set of capacities and capabilities that help the power system to operate with minimal damage and blackout in the event of a severe incident [10, 11]. Thus, despite the very low probability of such events due to the high costs imposed, extensive studies on the resilience of power systems independent of reliability studies are ongoing [12]. One of the new methods for evaluating the resilience of the power system in various studies is the use of graph theory. One advantage of this method is that the power system components can be represented as a graph and the system resilience is evaluated by studying the topological properties of the graph [13, 14]. In [15], a two-stage comparative robust formulation for microgrid disturbance scheduling was proposed considering various uncertainties using the column-constraint generation algorithm to minimize the destructive consequences of the islanding state. In [16], the fuzzy logic was employed to formulate a model in order to accurately predict the possible outage of equipment during severe incidents. In [17], a resilience-constrained day-ahead unit commitment model was presented using a decomposition algorithm based on the row-column production as a two-stage robust optimization problem to increase the system's resilience against extreme events.

In UCP, consumption-side management programs are of particular importance by setting up appropriate load-response

*Corresponding Author's Email: ha.moradi@razi.ac.ir (H. Moradi CheshmehBeigi)
URL: https://www.jree.ir/article_154881.html

Please cite this article as: Geravandi, M. and Moradi CheshmehBeigi, H., "The problem of resilient stochastic unit commitment with consideration of existing uncertainties using the rate of change of frequency", ***Journal of Renewable Energy and Environment (JREE)***, Vol. 9, No. 4, (2022), 34-47. (https://doi.org/10.30501/jree.2022.306473.1262).

contracts that aim to resolve problems such as balancing power and maintaining system frequency [18, 19]. In [20], the applications and types of microgrids were reviewed and the following economic studies and control of microgrids were explained. In [21], the imbalance between production and demand was studied using adaptive load shedding in the microgrids isolated from the grid considering uncertainties. This study respectively measured and evaluated the appropriate amount and location of load shedding without measuring the effect of load interruption contracts to maintain the system frequency in an acceptable range. In [22], the effect of the coordination between pumped storage and wind power plants considering the energy and reserve market on the normal and emergency performance (resilience) of the power system was investigated using integer linear combinational programming. In [23], a risk-constrained stochastic framework was employed to maximize the expected profit of a microgrid operator along with the uncertainties of renewable resources and demand. In this model, the balance between maximizing the operator's expected profit and the risk of receiving low profit in adverse scenarios was modeled using the conditional value at risk index and the impact of consumer participation in demand response programs.

In [24, 25], a method that considered the history of destructive hurricanes in the region and their path in the system for occurrence prediction was proposed in order to determine the units with outage risk. In [26], to reduce the effects of events on transmission lines in terms of time and place in the day-ahead market from a probabilistic perspective, the resilient UCP (R-UCP) was formulated as a distributionally robust optimization problem. One of the objectives of system automation is to use switching, which prevents the occurrence of events by taking necessary corrective actions [27]. Switching of transmission lines in UCP due to stress, physical tensions, and stability considerations within a limited time interval and in emergency such as a severe event that leads to line outage or congestion in other lines was investigated and evaluated [28]. In [29], to reduce the computational burden and solution time in UCP with several predicted line outages, the machine learning model was employed to determine the unnecessary constraints.

Given the above, most studies have not thoroughly studied the R-UCP because they failed to simultaneously consider uncertainties of WSPP and load demand, load interruption contracts, and adaptive frequency load shedding. As a result of previous research in this paper, WSPP is modeled as negative loads to ensure consistency with the basic concept of UCP, which is at the transmission voltage level. Also, due to the effects of WSPP on the power system, following the occurrence of an incident, improper WSPP conditions sometimes lead to the worsening of the system condition. Hence, the uncertainties of WSPP and load demand are considered to make more realistic decisions. Moreover, the effects of load interruption contracts and adaptive frequency load shedding on the system are evaluated. Then, by introducing an index for resilience, a resilient model is presented for the UCP. Finally, to demonstrate the effectiveness of the proposed R-UCP model, the proposed R-UCP is compared with the Traditional Two-Stage Stochastic Unit Commitment (TTSSUC) method combined with the load interruption contracts and adaptive frequency load shedding. Given the above, the innovations of this study are summarized as follows:

- Presentation of a new R-UCP model so that the working point of the system will change only in the event of a severe incident.
- Introduction of a new index to measure system resilience.
- Considering the effects of existing uncertainties on system resilience to make system operator decisions more realistic.
- Use of load management programs (adaptive frequency load shedding and load interruption contracts) and application of the production capacity to prevent instability in the system frequency and minimize the amount of unwanted load shedding.

The organization of this paper is as follows. In Section 2, the problem formulation is expressed. Section 3 describes the R-UCP solution method. Section 4 describes the result of numerical studies. Section 5 concludes the paper.

2. PROBLEM FORMULATION

2.1. Modeling the uncertainties of WSPP and load demand

As mentioned earlier, power generation using a power system with WSPP is subject to uncertainty. A well-known method for modeling uncertainty is the use of normal probability distribution functions [30]. In this research, by considering different forecasts for the WSPP power and load demand and using the prediction error probability distribution function with zero mean and different standard deviations, the value of uncertainties of WSPP power and load demand is obtained. According to the above, for the WSPP power or load demand, probable distributions with different standard deviations are considered. Each probable distribution is then divided into seventeen equal parts. In the following, seventeen error values are calculated relative to the mean value, with a specific probability for each error and standard deviation [31]. Therefore, seventeen prediction error modes are obtained with a specified probability for each mode of WSPP power or load demand. To combine different states of uncertainties of WSPP power and load demand and obtain the probability of each scenario, the scenario tree method is used in the proposed model. For each standard deviation and each WSPP power forecast error, there are seventeen load demand forecast errors. Therefore, 289 scenarios are developed for each standard deviation, taking into account all WSPP power prediction error modes. Based on the explanations given, there are a total of 4624 scenarios for all standard deviations. To ensure the robustness of the proposed model against changes in different input data, the average absolute error of the predicted data is considered to be ± 20 %.

2.2. Objective function

The objective function of resilient UCP, the value of which must be minimized, is represented by (1):

$$\min\{C^{UC} + C^{L.cut} + C^{L.sh}\} \quad (1)$$

where C^{UC} is the operation cost of the thermal units, which is defined in (2) considering the uncertainties, obtained using the two-stage stochastic programming method.

In the two-stage stochastic UCP, the on/off status decisions are fixed at the beginning of the day and production decisions are adapted to existing uncertainties [32-35].

$$C^{UC} = \sum_{t=1}^{T}\sum_{g=1}^{G}[(\sum_{\varphi=1}^{\phi} P_{\varphi}.(FC_{g,t,\varphi} + (e.E_{g,t,\varphi}))) + (SC_{g,t}.U_{g,t}.(1-U_{g,t-1})) + (DC_{g,t}.U_{g,t-1}.(1-U_{g,t}))] \quad (2)$$

where $FC_{g,t}$ is the fuel cost function of unit g at hour t and $E_{g,t}$ is the emission function of unit g at hour t, as expressed in (3) and (4).

$$FC_{g,t,\varphi} = U_{g,t}.(a_g + b_g P_{g,t,\varphi} + c_g P_{g,t,\varphi}^2) \quad \forall g \in G, t \in T, \forall \varphi \in \phi \quad (3)$$

$$E_{g,t,\varphi} = U_{g,t}.(\alpha_g + \beta_g P_{g,t,\varphi} + \gamma_g P_{g,t,\varphi}^2) \quad \forall g \in G, t \in T, \forall \varphi \in \phi \quad (4)$$

The startup cost SCg, depending on the hours when the unit g is off, is equal to one of the hot or cold startup costs as expressed in (5).

$$SC_g = \begin{cases} HSC_g & \text{if } DT_g \le CSH_g \\ CSC_g & \text{if } DT_g \succ CSH_g \end{cases} \quad (5)$$

The load costs consist of two parts: load interruption cost expressed in (6) and the cost resulting from adaptive frequency load shedding expressed in (7).

$$C^{L.cut} = \sum_{t=1}^{T}\sum_{\varphi=1}^{\phi} e_{L.cut}.P_{\varphi}.P_{t,\varphi}^{L.cut} \quad (6)$$

$$C^{L.sh} = \sum_{t=1}^{T}\sum_{\varphi=1}^{\phi} e_{L.sh}.P_{\varphi}.P_{t,\varphi}^{L.sh} \quad (7)$$

where $C^{L.cut}$ denotes the load interruption contracts cost in which $e_{L.cut}$ is the cost coefficient of load interruption according to the contract concluded with the participants in these programs. This cost coefficient during low load hours has its minimum value, while it has its maximum value during critical and peak hours. In addition, $C^{L.sh}$ shows the cost of adaptive frequency load shedding in which $e_{L.sh}$ is the cost coefficient of load shedding. This cost coefficient during low load hours has its minimum value and has its maximum value during critical and peak hours.

ΔP^H is a negative value that indicates the lack of active power for each scenario at each hour after the incident and can be calculated according to (8) [18, 36]:

$$\Delta P^H = (\sum_{g=1}^{G} P_{g,t,\varphi}) - P_{t,\varphi}^D + P_{w,t,\varphi} + P_{s,t,\varphi} \quad (8)$$

Equation (9) shows the load interruption value of the existing demand for each scenario per hour in the load interruption contracts to adjust the system frequency.

$$\Delta P_{L.cut}^H = -\Delta P^H \quad (9)$$

Equation (10) shows the unwanted load shedding value of the existing demand for each scenario per hour in the adaptive frequency load shedding to adjust the system frequency.

$$\Delta P_{L.sh}^H = -\Delta P^H - \Delta P_{L.cut}^H \quad (10)$$

In this paper, the rate of frequency change is introduced as a new index for measuring the resilience of the system [18, 36]. Equation (11) shows how to calculate the value of system frequency variations.

$$\frac{d\varpi_{el}}{dt} = \frac{\Delta P^H}{2H_{sys}} \times \varpi_{el} \quad (11)$$

2.3. Problem constraints

The main constraints of the UCP can be generally divided into two categories of equal and unequal constraints, which are expressed in (12) to (19) [32-35].

Power balance and spinning reserve constraints:

$$\sum_{g=1}^{G} P_{g,t,\varphi}.U_{g,t} = P_{t,\varphi}^D - P_{w,t,\varphi} - P_{s,t,\varphi} - P_{t,\varphi}^{L.cut} - P_{t,\varphi}^{L.sh} \quad \forall g \in G, \forall t \in T, \forall \varphi \in \phi \quad (12)$$

$$\sum_{g=1}^{G} P_g^{max}.U_{g,t} \ge P_{t,\varphi}^D - P_{w,t,\varphi} - P_{s,t,\varphi} - P_{t,\varphi}^{L.cut} - P_{t,\varphi}^{L.sh} + SR_{t,\varphi} \quad \forall g \in G, \forall t \in T, \forall \varphi \in \phi \quad (13)$$

$$SR_{t,\varphi} = 0.05P_{t,\varphi}^D \quad \forall t \in T, \forall \varphi \in \phi \quad (14)$$

Output power constraint of unit g at time t and scenario φ:

$$P_g^{min} \le P_{g,t,\varphi} \le P_g^{max} \quad \forall g \in G, \forall t \in T, \forall \varphi \in \phi \quad (15)$$

Constraints related to ramp-up/ramp-down and startup/shutdown limitation of unit g:

$$P_{g,t,\varphi} - P_{g,t-1,\varphi} \le SU_g(U_{g,t} - U_{g,t-1}) + RU_g.U_{g,t-1} \quad \forall g \in G, \forall t \in T, \forall \varphi \in \phi \quad (16)$$

$$P_{g,t-1,\varphi} - P_{g,t,\varphi} \le SD_g(U_{g,t-1} - U_{g,t}) + RD_g.U_{g,t} \quad \forall g \in G, \forall t \in T, \forall \varphi \in \phi \quad (17)$$

Constraints related to a minimum on/off time of unit g:

$$U_{g,t} - U_{g,t-1} \le U_{g,\tau} \quad \forall g \in G, \forall t \in T, \forall \tau \in \{t+1, ..., \min\{t, UT_g, T\}\} \quad (18)$$

$$U_{g,t-1} - U_{g,t} \le 1 - U_{g,\tau} \quad \forall g \in G, \forall t \in T, \forall \tau \in \{t+1, ..., \min\{t, DT_g, T\}\} \quad (19)$$

3. THE UCP SOLUTION METHOD

The proposed R-UCP model for scheduling thermal units is a hybrid model that has been proposed to increase the system resilience and minimize unwanted load shedding during a severe incident.

3.1. Proposed model algorithm

Figure 1 shows the flowchart of the R-UCP algorithm. Initially, by solving the UCP for system operation in the normal mode for all scenarios, considering all the constraints and uncertainties using two-stage stochastic programming, production information and scheduling of units are obtained. Then, the information of the studied scenarios, including the time of occurrence of incidents and the number of units that have been outages due to the incidents, is received as input.

After the incident, to use the production capacity by modifying the scheduling table of the thermal units in each hour after the incident with emphasis on all the constraints, the units that are online and produce power with a fraction of the nominal capacity, their capacity is increased up to the allowable limit. If the lack of production capacity is not

resolved, the thermal units that are off every hour after the incident and are allowed to operate will be turned on to overcome the system inertia and reduce production capacity. If the production capacity cannot overcome the lost capacity, load interruption programs, which consist of load interruption contracts, are implemented. If the dimensions of the incident are wider and the production capacity and load interruption programs cannot overcome the reduction in production capacity, adaptive frequency load shedding is used to balance the power in the system. If the system frequency does not reach its allowable range, it is not logical to maintain the system in its integrated form and the operator must command to prevent further failure in the islanding state.

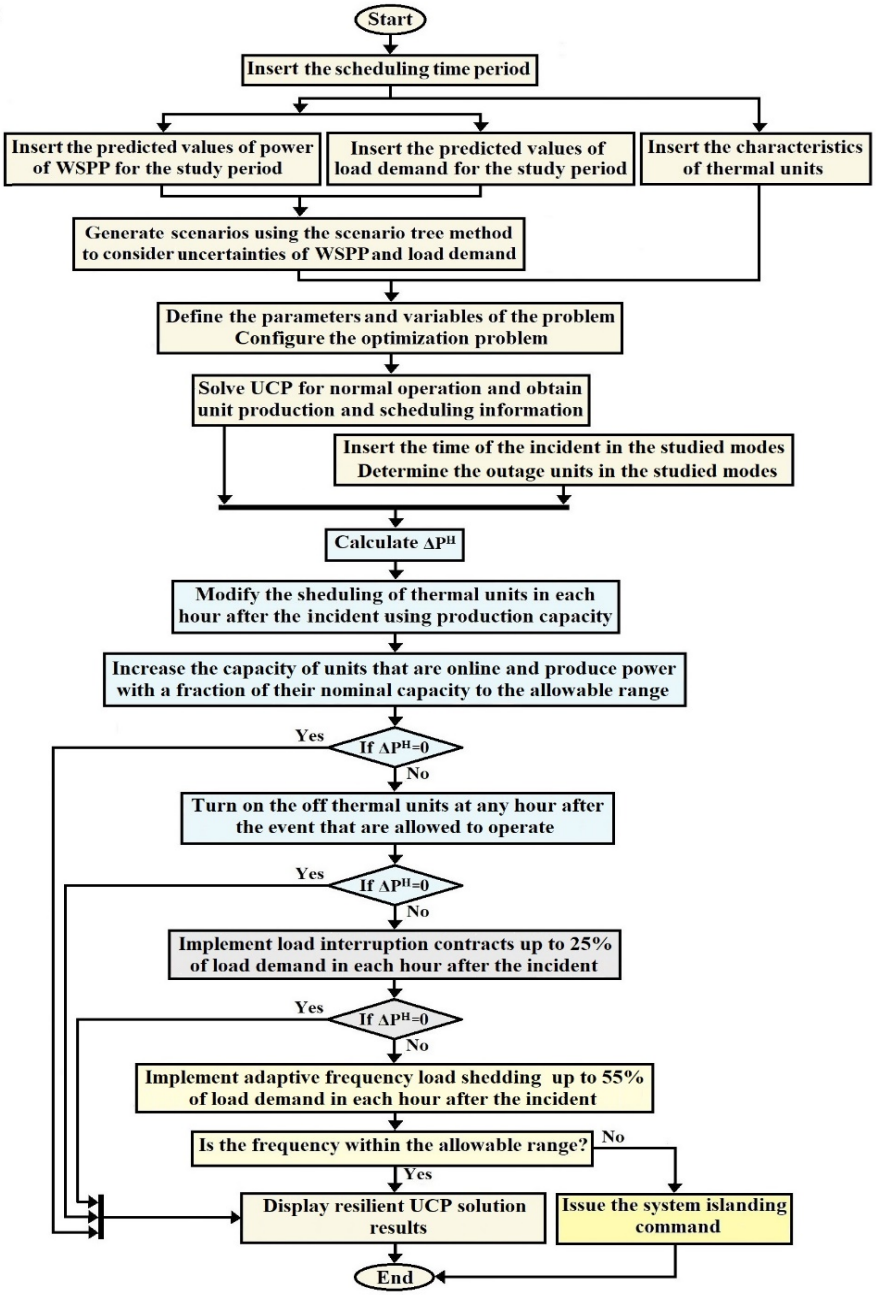

Figure 1. Algorithm of the proposed R-UCP model

3.2. Load interruption contracts and adaptive frequency load shedding

In this paper, to increase system resilience, load interruption contracts are considered as flexible resources. Load interruption contracts are concluded before the occurrence of events between the volunteer loads and the system operator. These loads are prioritized for cut-off by receiving rewards from the system operator. These concessions are modeled in the form of fees paid to subscribers participating in load interruption programs. If the thermal units (production capacity) cannot overcome the lost capacity, load interruption contracts are implemented. The number of load interruption contracts at each hour is assumed to be up to 25 % of the total demand at that hour. The cost of payment for the participating loads is calculated using (6). Finally, adaptive frequency load shedding has been considered the last approach to dealing with frequency decline.

According to (11), the frequency change rate is directly related to the reduction of active power in the system. Therefore, to maintain the system frequency, the value of active power reduction (ΔP^H) must be zero. At this stage,

assuming that all production capacity and load interruption sources are used, the required amount of frequency load shedding is performed to stabilize the frequency. The cost of blackout damage due to adaptive frequency load shedding is calculated using (7). The value of frequency load shedding to adjust the system frequency can be calculated using (10). The value of load shedding in adaptive frequency load shedding at each hour is assumed to be up to 55 % of the total demand at that hour. In case of the inability of this solution to stabilize the system frequency and force the operator to eliminate more than 80 % of the system demand, islanding will be a higher priority.

4. NUMERICAL STUDIES

The R-UCP model was evaluated on the 39-bus IEEE test system with the WSPP. This system has ten thermal units. Specifications of thermal units and the amount of load demand are presented in Table 1 and Figure 2 [37, 38]. The mean predicted output power of WSPP connected to the system at each hour is presented in Figure 2 [39-41]. The cost of producing each ton of emission by thermal units is assumed to be 0.05 $, and the amount of spinning reserve at each hour is assumed to be 0.05 times the load demand at that hour. The cost coefficient of load interruption contracts for different hours is presented in Table 2. The cost coefficient of adaptive frequency load shedding is assumed to be 130 % of the cost coefficient of load interruption contracts for different hours [42].

The probability of each prediction error of WSPP power or load demand for different standard deviations is shown in Table 3. Each time interval is considered equal to one hour, and the total scheduling time is one day. For a comprehensive review of the proposed model, the peak load demand time is selected as the worst time of the incident and case studies are reviewed and evaluated at this time. The case studies here are categorized in Table 4. For each case study, in the case of every standard deviation of the prediction error of WSPP and load according to the scenario tree method, 289 scenarios are defined. Therefore, for all prediction errors and standard deviations, a total of 4624 scenarios are obtained. To guarantee the robustness of the simulation results, the average absolute error of the predicted data is considered to be 20 %. All calculations are performed in a MATLAB environment with a machine running at Intel(R) Core (TM) i5-8250u 1.6 GHz CPU and 8GB RAM.

Table 1. Specifications of thermal units [37, 38]

	Unit 1	Unit 2	Unit 3	Unit 4	Unit 5	Unit 6	Unit 7	Unit 8	Unit 9	Unit 10
P_{max} (MW)	455	455	130	130	160	80	85	55	55	55
P_{min} (MW)	150	150	20	20	25	20	25	10	10	10
UT (h)	8	8	5	5	6	3	3	1	1	1
DT (h)	8	8	5	5	6	3	3	1	1	1
Initial state (h)	+8	+8	-5	-5	-6	-3	-3	-1	-1	-1
a ($/h)	1000	970	700	680	450	370	480	660	665	670
b ($/MWh)	16	17	16	16	19	22	27	25	27	27
c ($/MW^{2}h)	0.00048	0.00031	0.0020	0.0021	0.00398	0.00712	0.00079	0.00413	0.0022	0.00173
HSC ($/h)	4500	5000	550	560	900	170	260	30	30	30
CSC ($/h)	9000	10000	1100	1120	1800	340	520	60	60	60
CSH (h)	5	5	4	4	4	2	2	0	0	0
DC ($/h)	4500	5000	550	560	900	170	260	30	30	30
RU	225	225	50	50	60	60	60	135	135	135
RD	455	455	130	130	160	80	85	55	55	55
SU	150	150	20	20	25	20	25	10	10	10
SD	150	150	20	20	25	20	25	10	10	10
α (ton/h)	10.33908	10.33908	30.0391	30.0391	32.00006	32.00006	33.00056	33.00056	35.00056	36.00012
β (ton/MWh)	-0.24444	-0.24444	-0.40695	-0.40695	-0.38132	-0.38132	-0.39023	-0.39023	-0.39524	-0.39864
γ (ton/ MW^{2}h)	0.00312	0.00312	0.00509	0.00509	0.00344	0.00344	0.00465	0.00465	0.00465	0.00470

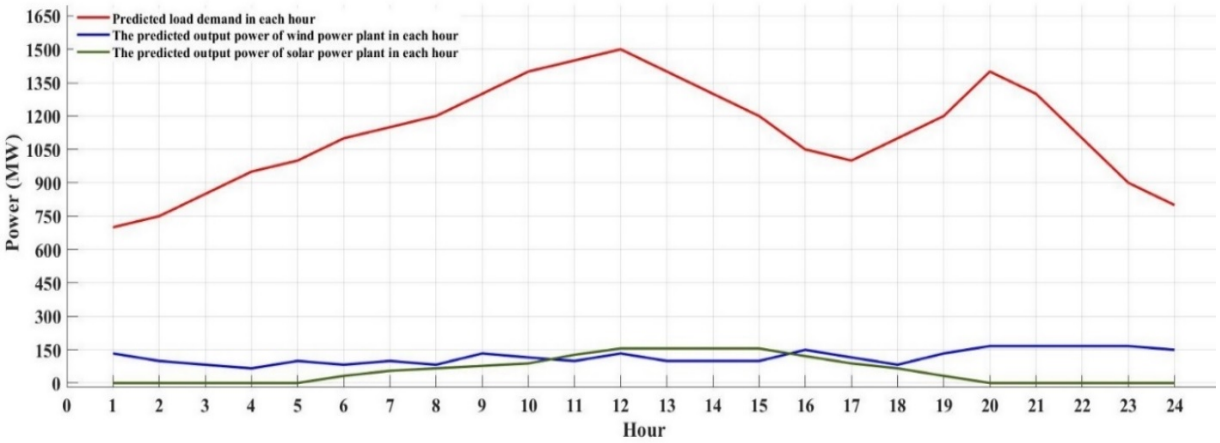

Figure 2. Predicted values of load demand and output power of wind and solar power plants per hour [37, 39-41]

Table 2. The cost coefficient of load interruption contracts [42]

Hour	1	2	3	4	5	6	7	8	9	10	11	12	13	14	15	16	17	18	19	20	21	22	23	24
Cost ($)	14	14	14	14	14	14	14	17	17	17	17	27	27	27	27	17	17	17	27	27	27	27	14	14

Table 3. The probability of each prediction error of WSPP power or load demand for different standard deviations

		Probability of prediction error for standard deviation= 0.025	Probability of prediction error for standard deviation= 0.050	Probability of prediction error for standard deviation= 0.075	Probability of prediction error for standard deviation= 0.100
Percentage prediction error	20.0 %	0	0.0001	0.0024	0.0076
	17.5 %	0	0.0005	0.0089	0.0217
	15.0 %	0	0.0024	0.0182	0.0325
	12.5 %	0	0.0092	0.0334	0.0457
	10.0 %	0.0002	0.0278	0.0549	0.0605
	7.5 %	0.006	0.0656	0.0807	0.0752
	5.0 %	0.0606	0.1210	0.1062	0.0878
	2.5 %	0.2417	0.1747	0.1253	0.0964
	0.0 %	0.383	0.1974	0.14	0.1452
	-2.5 %	0.2417	0.1747	0.1253	0.0964
	-5.0 %	0.0606	0.1210	0.1062	0.0878
	-7.5 %	0.006	0.0656	0.0807	0.0752
	-10.0 %	0.0002	0.0278	0.0549	0.0605
	-12.5 %	0	0.0092	0.0334	0.0457
	-15.0%	0	0.0024	0.0182	0.0325
	-17.5 %	0	0.0005	0.0089	0.0217
	-20.0 %	0	0.0001	0.0024	0.0076

Table 4. Case studies

		Disconnected WPSS and thermal units
Case	1	Simultaneous outage of G1, WSPP
	2	Simultaneous outage of G1, G2
	3	Simultaneous outage of G1, G2, G5, Solar power plant

Initially, the UCP is solved through two-stage stochastic programming and based on all operational constraints and uncertainties for the normal operation mode during the operation period. Table 5 shows the scheduling table of the thermal units for a sample scenario in the entire operation period for both R-UCP and TTSSUC methods. It should be noted that both R-UCP and TTSSUC methods are quite similar for the normal operation mode and in the hours before the incident.

Table 5. Scheduling table of thermal units for a sample scenario in the whole operation period for the normal operation mode

		Production power of thermal units (MW)									
		G1	G2	G3	G4	G5	G6	G7	G8	G9	G10
Hour	1	455	278.6	0	0	0	0	0	0	0	0
	2	455	345.8	20	0	0	0	0	0	0	0
	3	455	434.4	20	20	25	0	0	0	0	0
	4	455	455	70	70	37.2	0	0	0	0	0
	5	455	455	120	45.8	25	20	0	0	0	0
	6	455	455	130	95.8	73	20	0	0	0	0
	7	455	455	130	130	66.8	20	0	0	0	0
	8	455	455	130	130	121.6	20	0	10	0	0
	9	455	455	130	130	157	20	25	10	10	0
	10	455	455	130	130	160	80	32.6	55	10	10
	11	455	455	130	130	160	80	74.2	55	10	10
	12	455	455	130	130	160	80	84.6	55	10	10
	13	455	455	130	130	160	80	25	21.8	10	10
	14	455	455	130	130	131.8	20	25	10	0	0
	15	455	455	130	130	46.8	20	0	0	0	0
	16	455	455	69	20	25	20	0	0	0	0
	17	455	455	62.6	20	25	20	0	0	0	0
	18	455	455	112.6	70	85	24	0	0	0	0
	19	455	455	130	120	73	20	25	10	10	10
	20	455	455	130	130	133	80	85	55	14.2	10
	21	455	455	130	130	160	42.2	25	10	10	10
	22	455	455	130	92.2	25	20	0	10	0	0
	23	455	427.2	20	20	25	0	0	0	0	0
	24	455	365.8	20	0	0	0	0	0	0	0

According to Table 5, two important thermal units with high production capacity (G1, G2) are on due to the low cost of production during the whole operation period. Also, at hours 10 to 13 and 19 to 21, which is the peak of load demand, it is observed that all thermal units are online to meet the load demand and spinning reserve. On the other hand, the total operation cost of the system, taking into account not only all constraints during 24 hours but also uncertainties, is 513042 $ and without considering uncertainties is 512923 $. As stated earlier, the total operation cost of the system in the mode with uncertainty is 0.023 % higher than that in the mode without uncertainty, which can be concluded that in calculating the total operation cost of the system, uncertainties have minor impact. According to the load demand, the system has the highest load demand at 12 o'clock. Therefore, to evaluate the performance of the proposed R-UCP, peak demand time is selected as the worst time occurrence of the incident and case studies are evaluated at this time.

4.1. Case study 1

In Case Study 1, with the simultaneous outage of thermal unit G1 and WSPP at 12 o'clock, 27.4 % of the production capacity of thermal units and total WSPP production capacity are lost. In this case, the proposed R-UCP model is solved to prevent system frequency instability and minimize unwanted load shedding. Table 6 shows the modified scheduling table of the thermal units of the system, taking into account all the constraints and existing uncertainties for a sample scenario at each hour during the operation period using the R-UCP method. According to Table 6, it can be seen that after the occurrence of the incident at the peak load time, to use the production capacity to compensate for the lost capacity, the scheduling of the thermal units was modified every hour after the incident. In the hours after the incident, the units that are on and produce power with a fraction of their nominal capacity, according to all the constraints, their capacity will increase to the allowable range. If the lack of production capacity is not compensated, the thermal units that are off and allowed to operate are turned on and committed.

As can be seen in Table 6, blue houses in the schedule table are thermal units that are on in the hours after the incident and their production capacity has increased compared to the normal state in order to overcome the lost capacity. In addition, the red houses in the scheduling table are off thermal units that allowed to turn on in the hours after the incident. These units are turned on and committed in the hours after the incident to resolve the issue of the lost capacity.

Table 7 shows the values of load interruption in load interruption contracts as well as load shedding in adaptive frequency load shedding for each hour after the incident in the case of the proposed R-UCP and TTSSUC methods. According to Table 7, it is observed that in the proposed R-UCP method in modes with and without uncertainty, the value of load interruption in most hours after the incident is much lower than the TTSSUC method. Also, in the proposed R-UCP method in modes with and without uncertainty, the value of unwanted load shedding in most hours after the incident is equal to zero or a small value. However, in the TTSSUC method, in modes with and without uncertainty, the value of unwanted load shedding at hours 23 and 24 is large. Therefore, in Case Study 1, the proposed R-UCP model, unlike the TTSSUC, has successfully prevented unwanted load shedding in all hours after the incident by using production capacity and load side management programs.

Table 6. Modified scheduling table of thermal units for a sample scenario in the case of the proposed R-UCP method in the whole operation period for Case Study 1

		Production power of thermal units (MW)									
		G1	G2	G3	G4	G5	G6	G7	G8	G9	G10
Hour	1	455	278.6	0	0	0	0	0	0	0	0
	2	455	345.8	20	0	0	0	0	0	0	0
	3	455	434.4	20	20	25	0	0	0	0	0
	4	455	455	70	70	37.2	0	0	0	0	0
	5	455	455	120	45.8	25	20	0	0	0	0
	6	455	455	130	95.8	73	20	0	0	0	0
	7	455	455	130	130	66.8	20	0	0	0	0
	8	455	455	130	130	121.6	20	0	10	0	0
	9	455	455	130	130	157	20	25	10	10	0
	10	455	455	130	130	160	80	32.6	55	10	10
	11	455	455	130	130	160	80	74.2	55	10	10
	12	outage	455	130	130	160	80	85	55	55	10
	13	outage	455	130	130	160	80	85	55	55	10
	14	outage	455	130	130	160	80	85	55	55	55
	15	outage	455	130	130	160	80	85	55	55	55
	16	outage	455	130	130	160	80	85	55	55	55
	17	outage	455	130	130	160	80	85	55	55	55
	18	outage	455	130	130	160	80	85	55	55	55
	19	outage	455	130	130	160	80	85	55	55	55
	20	outage	455	130	130	160	80	85	55	55	55
	21	outage	455	130	130	160	80	85	55	55	55
	22	outage	455	130	130	160	80	85	55	55	55
	23	outage	455	130	130	160	80	50	55	10	10
	24	outage	455	130	130	160	50	25	10	0	0

Table 7. The value of load interruption in load interruption contracts and that of load shedding in adaptive frequency load shedding for each hour after the incident in Case Study 1 for TTSSUC and proposed R-UCP methods

		Hour												
		12	13	14	15	16	17	18	19	20	21	22	23	24
The value of load interruption in load interruption contracts at each hour after the incident (MW)	R-UCP method with uncertainty	289.8	195.4	100.7	25.82	0.39	0	2.71	25.82	195.4	100.7	2.66	0	0
	TTSSUC method with uncertainty	289.8	278.8	293.3	239.6	97.97	53.71	145.6	189.3	195.4	241.6	193.1	221.4	192
	R-UCP method without uncertainty	295	195	95	0	0	0	0	0	195	95	0	0	0
	TTSSUC method without uncertainty	295	285	310	245	95	45	145	190	195	245	195	225	200
The value of unwanted load shedding in adaptive frequency load shedding at each hour after the incident (MW)	R-UCP method with uncertainty	5.2	0.39	0	0	0	0	0	0	0.39	0	0	0	0
	TTSSUC method with uncertainty	5.2	6.2	16.69	5.4	0	0	0.2	0.93	0.39	3.43	1.9	48.53	23.01
	R-UCP method without uncertainty	0	0	0	0	0	0	0	0	0	0	0	0	0
	TTSSUC method without uncertainty	0	0	0	0	0	0	0	0	0	0	0	45	15

Table 8 shows the operation cost of the system and the operation cost of the thermal units in the entire period of operation as well as the costs of load interruption contracts and adaptive frequency load shedding for hours after the incident for both TTSSUC and proposed R-UCP methods. The value of the operation cost of the system, taking into account all the constraints during 24 hours, is equal to the sum of the operation cost of the thermal units, costs of load interruption contracts, and costs from adaptive frequency load shedding. In the proposed R-UCP method, the value of the operation cost of the system during 24 hours is 599754 $ for the mode with uncertainty and 599392 $ for the mode without uncertainty, which is 16.9 % higher than the normal operation mode. In the TTSSUC method, the value of the operation cost of the system during 24 hours is 579565$ for the mode with uncertainty and 579216$ for the mode without uncertainty, which is 12.9 % higher than the normal operation mode. Considering that 27.4 % of the production capacity of thermal units and total WSPP production capacity has been lost following the occurrence of an incident during peak hour, the proposed R-UCP model with only a 16.9 % increase in the operation cost of the system compared to normal operation has effectively prevented the frequency instability and unwanted load shedding in the system, which is quite satisfactory. Although the operation cost of the system in the TTSSUC method is about 20,000$ less than that in the proposed R-UCP method, it should be noted that in the event of an incident, the main objective is to reduce unwanted load shedding rather than the operation cost of the system.

Table 8. The operation cost of the system and that of the thermal units in the entire period of operation as well as the costs of load interruption contracts and adaptive frequency load shedding in the hours after the accident in Case Study 1 for both TTSSUC and proposed R-UCP methods

		R-UCP method				TTSSUC method			
		The operation cost of the system	The operation cost of the thermal units	The costs of load interruption contracts	The costs due to adaptive frequency load shedding	The operation cost of the system	The operation cost of the thermal units	The costs of load interruption contracts	The costs due to adaptive frequency load shedding
cost ($)	With uncertainty	599754	574213	25331	210	579565	514138	62711	2716
	Without uncertainty	599392	575767	23625	0	579216	514409	63715	1092

According to the results obtained from Case Study 1, in the case of the proposed R-UCP method, unlike the TTSSUC method in the hours after the incident, all the allowable capacity of the turned-on units is utilized. In addition, in the proposed R-UCP method, in the hours after the incident, the off thermal units that are allowed to be operated are terned on and committed. Unlike the TTSSUC method, given that much of the lost capacity is compensated by the thermal units in the proposed R-UCP method, the unwanted load shedding is lower than that in the TTSSUC method. The reason for increasing the operating cost of the system in the R-UCP method compared to the TTSSUC method is the use of more thermal units and costs resulting from emission.

4.2. Case study 2

In Case Study 2, with the simultaneous outage of thermal units G1, G2 at 12 o'clock, 54.82 % of the production capacity of thermal units is lost. Table 9 shows the modified scheduling table of the thermal units of the system, considering all the constraints and existing uncertainties for a sample scenario for each hour during the operation period using the R-UCP method. According to Table 9, similar to Case Study 1, it is observed that after the occurrence of an incident at peak hour, to use the production capacity to overcome the lost capacity, scheduling the thermal units at each hour after the incident was modified. In this case,

compared to the normal mode, blue houses in the scheduling table were the units that were on in the hours after the incident and their production capacity increased, while red houses in the scheduling table were off units which were allowed to go on in the hours after the incident and were turned on and committed after the incident.

Table 9. Modified scheduling table of thermal units for a sample scenario for the proposed R-UCP method in the whole operation period for Case Study 2

		Production power of thermal units (MW)									
		G1	G2	G3	G4	G5	G6	G7	G8	G9	G10
Hour	1	455	278.6	0	0	0	0	0	0	0	0
	2	455	345.8	20	0	0	0	0	0	0	0
	3	455	434.4	20	20	25	0	0	0	0	0
	4	455	455	70	70	37.2	0	0	0	0	0
	5	455	455	120	45.8	25	20	0	0	0	0
	6	455	455	130	95.8	73	20	0	0	0	0
	7	455	455	130	130	66.8	20	0	0	0	0
	8	455	455	130	130	121.6	20	0	10	0	0
	9	455	455	130	130	157	20	25	10	10	0
	10	455	455	130	130	160	80	32.6	55	10	10
	11	455	455	130	130	160	80	74.2	55	10	10
	12	outage	outage	130	130	160	80	85	55	55	10
	13	outage	outage	130	130	160	80	85	55	55	10
	14	outage	outage	130	130	160	80	85	55	55	55
	15	outage	outage	130	130	160	80	85	55	55	55
	16	outage	outage	130	130	160	80	85	55	55	55
	17	outage	outage	130	130	160	80	85	55	55	55
	18	outage	outage	130	130	160	80	85	55	55	55
	19	outage	outage	130	130	160	80	85	55	55	55
	20	outage	outage	130	130	160	80	85	55	55	55
	21	outage	outage	130	130	160	80	85	55	55	55
	22	outage	outage	130	130	160	80	85	55	55	55
	23	outage	outage	130	130	160	80	85	55	55	55
	24	outage	outage	130	130	160	50	85	55	55	55

Table 10 shows the values of load interruption in load interruption contracts and load shedding in adaptive frequency load shedding for each hour after the incident in the case of the proposed R-UCP and TTSSUC methods. According to Table 10, it is observed that in the proposed R-UCP method in modes with and without uncertainty, the values of load interruption and load shedding in most hours after the incident are much less than those in the TTSSUC method. According to Table 10, for the TTSSUC method, in modes with and without uncertainty, the entire capacity of load interruption contracts is utilized in all hours after the incident. However, in the proposed R-UCP method, the entire capacity of load interruption contracts is used at some hours. Therefore, due to the high volume of production capacity lost for modes with and without uncertainty, the proposed R-UCP method, unlike the TTSSUC method, successfully prevents large unwanted load shedding in the hours after the incident.

Table 10. The value of load interruption in load interruption contracts and the value of load shedding in adaptive frequency load shedding for each hour after the incident in Case Study 2 for TTSSUC and proposed R-UCP methods

		Hour												
		12	13	14	15	16	17	18	19	20	21	22	23	24
The value of load interruption in load interruption contracts in each hour after the incident (MW)	R-UCP method with uncertainty	370.2	340.1	283.2	194.9	44.09	55.67	199.5	269.7	349	318.9	182.8	14.92	0.85
	TTSSUC method with uncertainty	370.2	349	325	299.8	249.8	245.4	275	300	349	325	275	225	200
	R-UCP method without uncertainty	375	350	296	196	30	47	202	285	350	325	184	0	0
	TTSSUC method without uncertainty	375	350	325	300	262.5	250	275	300	350	325	275	225	200
The value of unwanted load shedding in adaptive frequency load shedding in each hour after the incident (MW)	R-UCP method with uncertainty	91.78	55.92	12.76	1.34	0	0	2.53	15.28	134.9	65.06	1.36	0	0
	TTSSUC method with uncertainty	91.78	136.9	186	146.2	30.18	51.62	177	180	134.9	209	209	334	321
	R-UCP method without uncertainty	87	46	0	0	0	0	0	0	134	59	0	0	0
	TTSSUC method without uncertainty	87	136	186	146	17.5	47	177	180	134	209	209	334	321

Table 11 shows the operation cost of the system and the operation cost of the thermal units in the entire period of operation, and the costs of load interruption contracts and adaptive frequency load shedding for hours after the incident for both TTSSUC and proposed R-UCP methods. In the proposed R-UCP method, the value of the operation cost of the system during 24 hours is 572430 $ for the mode with uncertainty and 572348 $ for the mode without uncertainty, which is 11.56 % higher than the normal operation mode. In the TTSSUC method, the value of the operation cost of the system during 24 hours is 552239 $ for the mode with uncertainty and 552025 $ for the mode without uncertainty, which is 7.64 % higher than the normal operation mode. Similar to Case Study 1, the reason for the increased operating cost of the system in the proposed R-UCP method compared to the TTSSUC method is the emission-related costs. The reason for the lower operating cost of the system in Case Study 2 compared to Case Study 1 is the existence of WSPP and the supply of a part of the demand by it.

Table 11. The operation cost of the system and the operation cost of the thermal units in the entire period of operation and the costs of load interruption contracts and adaptive frequency load shedding in the hours after the accident in Case Study 2 for both TTSSUC and proposed R-UCP methods

		R-UCP method				TTSSUC method			
		The operation cost of the system	The operation cost of the thermal units	The costs of load interruption contracts	The costs due to adaptive frequency load shedding	The operation cost of the system	The operation cost of the thermal units	The costs of load interruption contracts	The costs due to adaptive frequency load shedding
cost ($)	With uncertainty	572430	491440	67649	13341	552239	400125	89055	63059
	Without uncertainty	572348	492415	68490	11443	552025	400056	89537	62432

4.3. Case study 3

In Case Study 3, with the simultaneous outage of thermal units G1, G2, G5 and solar power plant at 12 o'clock, 64.45 % of the production capacity of thermal units and total solar power plant production capacity are lost. Table 12 shows the modified scheduling table of the thermal units of the system, considering all the constraints and existing uncertainties for a sample scenario for each hour during the operation period using the R-UCP method. In the case of Study 3, as in Case Studies 1 and 2, it is observed that after the occurrence of an incident at peak hour, to use the production capacity to compensate for the lost capacity, scheduling the thermal units at each hour after the incident has been modified.

Table 12. Modified scheduling table of thermal units for a sample scenario for the proposed R-UCP method in the whole operation period for Case Study 3.

		Production power of thermal units (MW)									
		G1	G2	G3	G4	G5	G6	G7	G8	G9	G10
Hour	1	455	278.6	0	0	0	0	0	0	0	0
	2	455	345.8	20	0	0	0	0	0	0	0
	3	455	434.4	20	20	25	0	0	0	0	0
	4	455	455	70	70	37.2	0	0	0	0	0
	5	455	455	120	45.8	25	20	0	0	0	0
	6	455	455	130	95.8	73	20	0	0	0	0
	7	455	455	130	130	66.8	20	0	0	0	0
	8	455	455	130	130	121.6	20	0	10	0	0
	9	455	455	130	130	157	20	25	10	10	0
	10	455	455	130	130	160	80	32.6	55	10	10
	11	455	455	130	130	160	80	74.2	55	10	10
	12	outage	outage	130	130	outage	80	85	55	55	10
	13	outage	outage	130	130	outage	80	85	55	55	10
	14	outage	outage	130	130	outage	80	85	55	55	55
	15	outage	outage	130	130	outage	80	85	55	55	55
	16	outage	outage	130	130	outage	80	85	55	55	55
	17	outage	outage	130	130	outage	80	85	55	55	55
	18	outage	outage	130	130	outage	80	85	55	55	55
	19	outage	outage	130	130	outage	80	85	55	55	55
	20	outage	outage	130	130	outage	80	85	55	55	55
	21	outage	outage	130	130	outage	80	85	55	55	55
	22	outage	outage	130	130	outage	80	85	55	55	55
	23	outage	outage	130	130	outage	80	85	55	55	55
	24	outage	outage	130	130	outage	50	85	55	55	55

Table 13 shows the values of load interruption in load interruption contracts and load shedding in adaptive frequency load shedding for each hour after the incident for the proposed R-UCP and TTSSUC methods. According to Table 13, it is observed that in the TTSSUC and proposed R-UCP methods in modes with and without uncertainty, the value of load interruption is equal in most hours after the incident. The proposed R-UCP method uses the full capacity of the load

interruption contracts except at hours 23 and 24, while the TTSSUC method uses the full capacity of the load interruption contracts in all hours after the incident. Also, it is observed that in the proposed R-UCP method in modes with and without uncertainty, the value of load shedding in most hours after the incident is much less than that in the case of the TTSSUC method. Therefore, similar to the previous case studies, due to the high volume of production capacity lost for modes with and without uncertainty, the proposed R-UCP method, unlike the TTSSUC method, successfully prevents large unwanted load shedding in the hours after the incident.

Table 13. The value of load interruption in load interruption contracts and the value of load shedding in adaptive frequency load shedding for each hour after the incident in Case Study 3 for TTSSUC and proposed R-UCP methods

		Hour												
		12	13	14	15	16	17	18	19	20	21	22	23	24
The value of load interruption in load interruption contracts in each hour after the incident (MW)	R-UCP method with uncertainty	375	350	325	300	257.7	245.3	275	300	350	325	272.1	143.3	64.37
	TTSSUC method with uncertainty	375	350	325	300	262.5	250	275	300	350	325	275	225	200
	R-UCP method without uncertainty	375	350	325	300	262.5	250	275	300	350	325	275	144	61
	TTSSUC method without uncertainty	375	350	325	300	262.5	250	275	300	350	325	275	225	200
The value of unwanted load shedding in adaptive frequency load shedding in each hour after the incident (MW)	R-UCP method with uncertainty	402	361	286	211	53.3	49.7	153	177	294	219	71.9	0.85	0
	TTSSUC method with uncertainty	402	401	501	461	298.5	295	403	372	294	369	369	359	321
	R-UCP method without uncertainty	402	361	286	211	48.5	45	153	177	294	219	69	0	0
	TTSSUC method without uncertainty	402	401	501	461	298.5	295	403	372	294	369	369	359	321

Table 14 shows the operation cost of the system and the operation cost of the thermal units in the entire period of operation as well as the costs of load interruption contracts and adaptive frequency load shedding for hours after the incident for both TTSSUC and proposed R-UCP methods. In the proposed R-UCP method, the value of the operation cost of the system during 24 hours is 612371 $ for the mode with uncertainty and 612037 $ for the mode without uncertainty, which is 19.36 % higher than the normal operation mode. In the TTSSUC method, the value of the operation cost of the system during 24 hours is 596375 $ for the mode with uncertainty and 596070 $ for the mode without uncertainty, which is 16.24 % higher than the normal operation mode.

Table 14. The operation cost of the system and the operation cost of the thermal units in the entire period of operation as well as the costs of load interruption contracts and adaptive frequency load shedding in the hours after the accident in Case Study 3 for both TTSSUC and proposed R-UCP methods

		R-UCP method				TTSSUC method			
		The operation cost of the system	The operation cost of the thermal units	The costs of load interruption contracts	The costs due to adaptive frequency load shedding	The operation cost of the system	The operation cost of the thermal units	The costs of load interruption contracts	The costs due to adaptive frequency load shedding
cost ($)	With uncertainty	612371	449473	86255	76643	596375	359452	89537	147386
	Without uncertainty	612037	449265	86457	76315	596070	359147	89537	147386

It should be noted that the operation cost of the system in the proposed R-UCP method for the scheduling the thermal units depends on the number and production capacity of the lost units and differs from the operation cost of the system in the normal mode. In normal operation, the purpose of the system operator is to respond 100 % to all consumers with the minimum operating cost. However, in the proposed R-UCP method, the aim is to increase resilience in the event of an incident, to reduce the consequences of sudden outage of production units, and prevent system frequency instability along with the maximum possible response to demand. According to the results of all the three case studies, it is observed that the proposed R-UCP method has a much better performance than the TTSSUC method.

4.4. Comparison of the results of methods in modes with uncertainty and without uncertainty for all case studies

Figure 3 shows the operation cost of the system and the operation cost of the thermal units for both methods, considering all the constraints during 24 hours for all case studies in both modes, with uncertainty and without uncertainty. Figure 4 shows the value of load interruption in

the load interruption contracts at each hour after the incident for all case studies for both TTSSUC and proposed R-UCP methods. Figure 5 shows the value of load shedding in the adaptive frequency load shedding at each hour after the incident for all case studies for both TTSSUC and proposed R-UCP methods. According to Figure 3, it is clear that the operation cost of the system and the operation cost of the thermal units in both methods are almost the same for all case studies in both modes with and without uncertainty. On the other hand, according to Figures 4 and 5, it can be seen that the value of load interruption in load interruption contracts and the value of load shedding in the adaptive frequency load shedding in each hour after the incident for all case studies in mode with uncertainty are different from the mode without uncertainty.

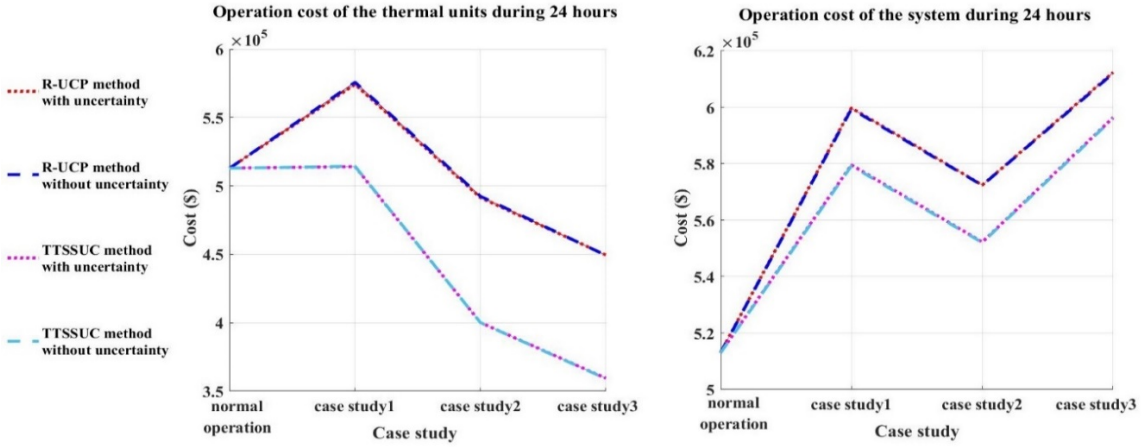

Figure 3. The operation costs of the system and the thermal units during 24 hours for both of the two methods

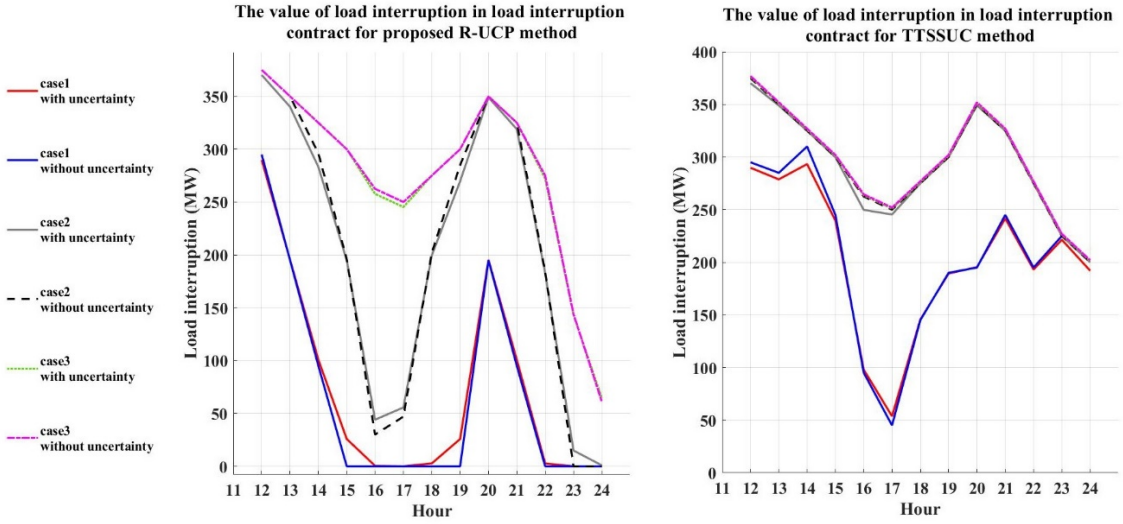

Figure 4. The value of load interruption in the load interruption contracts in each hour after the incident

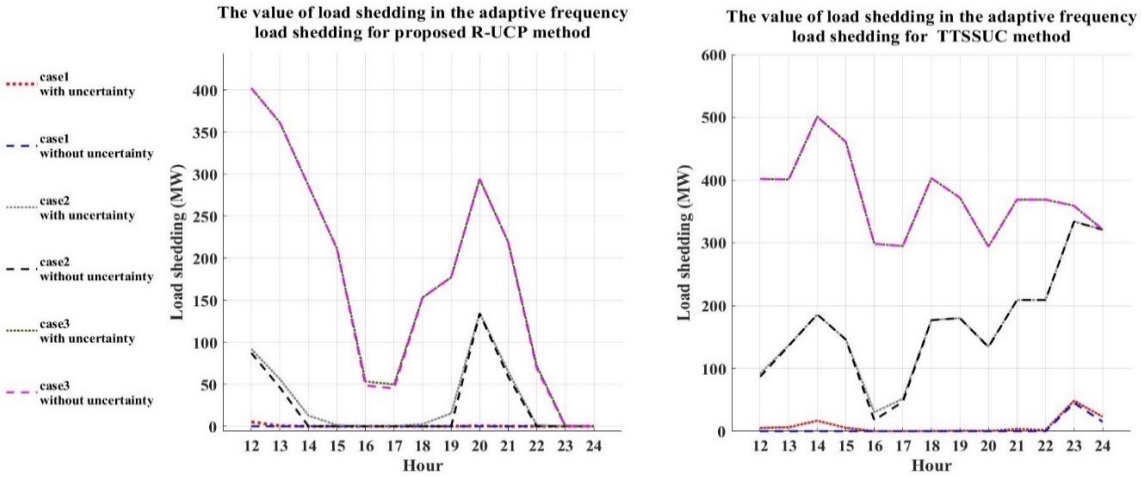

Figure 5. The value of load shedding in the adaptive frequency load shedding in each hour after the incident

Therefore, in both methods, if the objective is only to determine the operation costs of the system and thermal units, the existing uncertainties can be ignored for simplicity of calculations. However, in addition to calculating the operation cost of the system, it is necessary to accurately calculate and determine the value of load interruption in load interruption contracts and load shedding in adaptive frequency load shedding. Therefore, according to the given explanations, in the proposed R-UCP method employed for accurate scheduling of the system in the hours after the accident, the existing uncertainties must be carefully considered.

5. CONCLUSIONS

In this study, an R-UCP model was introduced along with the existing uncertainties. In this model, in the event of an accident using the production capacity, load interruption contracts, and adaptive frequency load shedding, system frequency instability and widespread unwanted load shedding in the system were prevented. In this model, the frequency change rate was introduced as a new resilience index. According to the results of case studies, in the proposed RUCP method, the value of unwanted load shedding in each hour after the incident in all case studies was much less than that in the case of the TTSSUC method. Therefore, the proposed R-UCP method was much more powerful for system scheduling in the hours after an incident than the widely used TTSSUC method.

According to the obtained results in Case Study 3, with the occurrence of the most destructive incident at peak load time, the proposed R-UCP method in the hours after the incident used the entire production capacity, the maximum value of load interruption contracts, and adaptive frequency load shedding. In this case study, the R-UCP method at the peak load time with only 19.36 % increase in the operation cost of the system compared to the normal operation mode and with a maximum value of unwanted load shedding equal to 26.8 % of the system load at peak hours managed to well prevent widespread unwanted load shedding and system frequency instability. However, in this case study, the minimum value of unwanted load shedding in the TTSSUC method was equal to the maximum value of unwanted load shedding in the proposed method. Also, the results of Case Studies 1 and 2 show that the presence of WSPP had a significant impact on reducing the operation cost of the system.

According to the results obtained by the R-UCP method, the system operator must carefully consider the existing uncertainties to accurately schedule the system in the hours after the incident. Upon comparing R-UCP with TTSSUC, it can be concluded that the proposed RUCP method is very powerful as a temporary scheme to maintain system frequency and reduce unwanted load shedding until the lost units are ready to be used again.

6. ACKNOWLEDGEMENT

The authors wish to thank the support of Razi University.

NOMENCLATURE

a_g	Constant coefficient of the quadratic production cost function of unit g ($/h)
b_g	First-order coefficient of the quadratic production cost function of the unit g ($/MWh)
c_g	Second-order coefficient of the quadratic production cost function of the unit g ($/MW^{2}h)
CSH_g	The maximum permissible time that the unit g has been offline to become hot (h)
DTi_g	The number of hours that the unit g has been shut down before the startup (h)
SU_g/SD_g	Startup/Shutdown ramp limit of unit g
RU_g	Ramp-up limit of unit g
UT_g	Minimum up-time of unit g (h)
DT_g	Minimum down-time of unit g (h)
Pw,t,φ	The mean predicted output power of wind power plant connected to the system at time t and in scenario φ (MW)
Ps,t,φ	The mean predicted output power of solar power plant connected to the system at time t and in scenario φ (MW)
Ug,t	State of unit g at hour t
P_t^D	Forecasted load demand at hour t (MW)
SR_t	Spinning reserve requirement at period t (MW)

Greek letters

α_g	Constant coefficient of the emission production function of unit g (ton/h)
β_g	First-order coefficient of the emission production function of unit g (ton/MWh)
γ_g	Second-order coefficient of the emission production function of unit g (ton/ MW^{2}h)
$P\varphi$	Probability of occurrence of scenario φ

REFERENCES

1. Khani, K., Shahgholian, Gh., Fani, B., Moazzami, M., Mahdavian, M. and Janghorbani, M., "A comparsion of different structures in wind energy conversion systems", ***Proceedings of 14th International Conference on Electrical Engineering/Electronics, Computer, Telecommunications and Information Technology (ECTI-CON)***, Phuket, Thailand, (2017), 58-61. (https://doi.org/10.1109/ECTICon.2017.8096172).
2. Wang, J., Zobaa, A.F., Huang, C. and Chen, C., "Day-ahead allocation of operation reserve in composite power systems with large-scale centralized wind farms", ***Journal of Modern Power Systems and Clean Energy***, Vol. 4, No. 2, (2016), 238-247. (https://doi.org/10.1007/s40565-015-0149-4).
3. Hosseini, E., Shahgholian, Gh., Mahdavi-Nasab, H. and Mesrinejad, F., "Variable speed wind turbine pitch angle control using three-term fuzzy controller", ***International Journal of Smart Electrical Engineering***, Vol. 11, No. 2, (2022), 63-70. (http://ijsee.iauctb.ac.ir/article_686590.html).
4. Huang, Y., Pardalos, P.M. and Zheng, Q.P., Electrical power unit commitment: Deterministic and two-stage stochastic programming models and algorithms, Springer, (2017), 50-80. (https://doi.org/10.1007/978-1-4939-6768-1).
5. Scuzziato, M.R., Finardi, E.C. and Frangioni, A., "Solving stochastic hydrothermal unit commitment with a new primal recovery technique based on Lagrangian solutions", ***International Journal of Electrical Power & Energy Systems***, Vol. 127, (2021), 1-11. (https://doi.org/10.1016/j.ijepes.2020.106661).
6. Li, G., Li, G. and Zhou, M., "Model and application of renewable energy accommodation capacity calculation considering utilization level of inter-provincial tie-line", ***Protection and Control of Modern Power Systems***, Vol. 4, No. 1, (2019), 1-12. (https://doi.org/10.1186/s41601-019-0115-7).
7. Håberg, M., "Fundamentals and recent developments in stochastic unit commitment", ***International Journal of Electrical Power & Energy Systems***, Vol. 109, (2019), 38-48. (https://doi.org/10.1016/j.ijepes.2019.01.037).
8. Mohammadi, F. and Ardakani, M.S., "Tractable stochastic unit commitment for large systems during predictable hazards", ***IEEE Access***, Vol. 8, (2020), 115078-115088. (https://doi.org/10.1109/ACCESS.2020.3004391).
9. Gholami, A., Shekari, T., Aminifar, F. and Shahidehpour, M., "Microgrid scheduling with uncertainty: The quest for resilience", ***IEEE Transactions on Smart Grid***, Vol. 7, No. 6, (2016), 2849-2858. (https://doi.org/10.1109/TSG.2016.2598802).
10. Gholami, A., Aminifar, F. and Shahidehpour, M., "Front lines against the darkness: Enhancing the resilience of the electricity grid through microgrid facilities", ***IEEE Electrification Magazine***, Vol. 4, No. 1, (2016), 18-24. (https://doi.org/10.1109/MELE.2015.2509879).
11. Fesagandis, H.S., Jalali, M., Zare, K., Abapour, M. and Karimipour, H., "Resilient scheduling of networked microgrids against real-time

failures", ***IEEE Access,*** Vol. 9, (2021), 21443-21456. (https://doi.org/10.1109/ACCESS.2021.3052653).

12. Mishra, D.K., Ghadi, M.J., Azizivahed, A., Li, L. and Zhang, J., "A review on resilience studies in active distribution systems", ***Renewable and Sustainable Energy Reviews***, Vol. 135, (2021), 1-20. (https://doi.org/10.1016/j.rser.2020.110201).
13. Ezzeldin, M. and El-dakhakhni, W.E., "Robustness of Ontario power network under systemic risks", ***Sustainable and Resilient Infrastructure***, Vol. 6, No. 3-4, (2019), 252-271. (https://doi.org/10.1080/23789689.2019.1666340).
14. Li, B., Boateng, D.O., Gel, Y.R. and Zhang, J., "A hybrid approach for transmission grid resilience assessment using reliability metrics and power system local network topology", ***Sustainable and Resilient Infrastructure***, Vol. 6, No. 1-2, (2021), 26-41. (https://doi.org/10.1080/23789689.2019.1708182).
15. Gholami, A., Shekari, T. and Grijalva, S., "Proactive management of microgrids for resiliency enhancement an adaptive robust approach", ***IEEE Transactions on Sustainable Energy***, Vol. 10, No. 1, (2019), 470-480. (https://doi.org/10.1109/TSTE.2017.2740433).
16. Chen, P.C. and Kezunovic, M., "Fuzzy logic approach to predictive risk analysis in distribution outage management", ***IEEE Transactions on Smart Grid***, Vol. 7, No. 6, (2016), 2827–2836. (https://doi.org/10.1109/TSG.2016.2576282).
17. Trakas, D.N. and Hatziargyriou, N.D., "Resilience constrained day-ahead unit commitment under extreme weather events", ***IEEE Transactions on Power Systems***, Vol. 35, No. 2, (2019), 1242-1253. (https://doi.org/10.1109/TPWRS.2019.2945107).
18. Zheng, Q.P., Wang, J. and Liu, A.L., "Stochastic optimization for unit commitment—A review", ***IEEE Transactions on Power Systems***, Vol. 30, No. 4, (2015), 1913-1924. (https://doi.org/10.1109/TPWRS.2014.2355204).
19. Cao, Y., Huang, L., Li, Y., Jermsittiparsert, K., Nezamabad, H.A. and Nojavan, S., "Optimal scheduling of electric vehicles aggregator under market price uncertainty using robust optimization technique", ***International Journal of Electrical Power & Energy Systems***, Vol. 117, (2020), 1-7. (https://doi.org/10.1016/j.ijepes.2019.105628).
20. Shahgholian, Gh., "A brief review on microgrids: Operation, applications, modeling, and control", ***Electrical Energy Systems***, Vol. 31, No. 6, (2021), 1-28. (https://doi.org/10.1002/2050-7038.12885).
21. Marzband, M., Moghaddam, M.M., Akorede, M.F. and Khomeyrani, G., "Adaptive load shedding scheme for frequency stability enhancement in microgrids", ***Electric Power Systems Research***, Vol. 140, (2016), 78-86. (https://doi.org/10.1016/j.epsr.2016.06.037).
22. Choopani, K., Effatnejad, R. and Hedayati, M., "Coordination of energy storage and wind power plant considering energy and reserve market for a resilience smart grid", ***Journal of Energy Storage***, Vol. 30, (2020), 1-8. (https://doi.org/10.1016/j.est.2020.101542).
23. Vahedipour, M., Moghaddam, A.A. and Guerrero, J.M., "Evaluation of reliability in risk-constrained scheduling of autonomous microgrids with demand response and renewable resources", ***IET Renewable Power Generation***, Vol. 12, No. 6, (2018), 657-667. (https://doi.org/10.1049/iet-rpg.2017.0720).
24. Wang, Y., Huang, L., Shahidehpour, M., Lai, L.L. and Zhou, Y., "Impact of cascading and common-cause outages on resilience-constrained optimal economic operation of power systems", ***IEEE Transactions on Smart Grid***, Vol. 11, No. 1, (2020), 590-601. (https://doi.org/10.1109/TSG.2019.2926241).
25. Eskandarpour, R., Khodaei, A. and Lin, J., "Event-driven security constrained unit commitment with component outage estimation based on machine learning method", ***Proceedings of the North American Power Symposium (NAPS)***, Denver, CO, USA, (2016), 1-6. (https://doi.org/10.1109/NAPS.2016.7747873).
26. hao, T., Zhang, H., Liu, X., Yao, S. and Wang, P., "Resilient unit commitment for day-ahead market considering probabilistic impacts of hurricanes", ***IEEE Transactions on Power Systems***, Vol. 36, No. 2, (2021), 1082-1094. (https://doi.org/10.1109/TPWRS.2020.3025185).
27. Wang, Y., Li, Z., Shahidehpour, M., Wu, L., Guo, C.X. and Zhu, B., "Stochastic co-optimization of midterm and short-term maintenance outage scheduling considering covariates in power systems", ***IEEE Transactions on Power Systems***, Vol. 31, No. 6, (2016), 4795-4805. (https://doi.org/10.1109/TPWRS.2016.2521720).
28. Sayyed-Mahdavi, S. and Javidi, M.H., "VPP decision making in power markets using benders decomposition", ***International Transactions on Electrical Energy Systems***, Vol. 24, No. 7, (2014), 960-975. (https://doi.org/10.1002/etep.1748).
29. Mohammadi, F., Sahraei-Ardakani, S., Trakas, D. and Hatziargyriou, N.D., "Machine learning assisted stochastic unit commitment during hurricanes with predictable line outages", ***IEEE Transactions on Power Systems***, Vol. 36, No. 6, (2021), 5131-5142. (https://doi.org/10.1109/TPWRS.2021.3069443).
30. Zakariazadeh, A., Jadid, S. and Siano, P., "Economic-environmental energy and reserve scheduling of smart distribution systems: A multi objective mathematical programming approach", ***Energy Conversion and Management***, Vol. 78, (2014), 151-164. (https://doi.org/10.1016/j.enconman.2013.10.051).
31. Reddy, S.S., Bijwe, P.R. and Abhyankar, A.R., "Joint energy and spinning reserve market clearing incorporating wind power and load forecast uncertainties", ***IEEE Systems Journals***, Vol. 9, No. 1, (2015), 152-164. (https://doi.org/10.1109/JSYST.2013.2272236).
32. Arab, A., Khodaei, A., Khator, S.K. and Han, Z., "Electric power grid restoration considering disaster economics", ***IEEE Access***, Vol. 4, (2016), 639-649. (https://doi.org/10.1109/ACCESS.206.2523545).
33. Roy, P.K., "Solution of unit commitment problem using gravitational search algorithm", ***International Journal of Electrical Power & Energy Systems***, Vol. 53, (2013), 85-94. (https://doi.org/10.1016/j.ijepes.2013.04.001).
34. Govardhan, M. and Roy, R., "Economic analysis of unit commitment with distributed energy resources", ***International Journal of Electrical Power & Energy Systems***, Vol. 71, (2015), 1-14. (https://doi.org/10.1016/j.ijepes.2015.01.028).
35. Mahmutoğulları, A.I., Ahmed, S., Çavuş, Ö. and Aktürk, M.S., "The value of multi-stage stochastic programming in risk-averse unit commitment under uncertainty", ***IEEE Transactions on Power Systems***, Vol. 4, No. 5, (2019), 3667-3676. (https://doi.org/10.1109/TPWRS.2019.2902511).
36. Tielens, P. and Hertem, D., "Grid inertia and frequency control in power systems with high penetration of renewables", ***Proceedings of the Young Researchers Symposium in Electrical Power Engineering***, Delft, Netherlands, (2012), 1-6. (https://lirias.kuleuven.be/1731030?limo=0).
37. Carrión, M. and Arroyo, J.M., "A computationally efficient mixed-integer linear formulation for the thermal unit commitment problem", ***IEEE Transactions on Power Systems***, Vol. 21, No. 3, (2006), 1371-1378. (https://doi.org/10.1109/TPWRS.2006.876672).
38. Venkatesan, T. and Sanavullah, M.Y., "SFLA approach to solve PBUC problem with emission limitation ", ***International Journal of Electrical Power & Energy Systems,*** Vol. 46, (2013), 1-9. (https://doi.org/10.1016/j.ijepes.2012.09.006).
39. Elia Power System, (2021). (http://www.elia.be/en/grid-data/powergeneration), (Accessed: 11 November 2021).
40. Wan, Y.H., "Wind power plant behaviors: Analyses of long-term wind power data", National Renewable Energy Laboratory (NREL) Report, Golden, CO, USA, (2004). (https://www.osti.gov/biblio/15009608), (Accessed: 1 September 2004).
41. Hummon, M., Cochran, J., Weekley, A., Lopez, A., Zhang, J. and Stoltenberg, B., "Variability of photovoltaic power in the state of gujarat using high resolution solar data", National Renewable Energy Laboratory (NREL) Report, Golden, CO, USA, (2014). (https://www.osti.gov/biblio/1126817), (Accessed: 1 March 2014).
42. Wood, A.J., Wollenberg, B.F. and Sheblé, G.B., Power generation, operation, and control, John Wiley & Sons, (2013), 147-167. (https://www.amazon.com/Power-Generation-Operation-Control-Allen/dp/0471790559).

Journal of Renewable Energy and Environment

Journal Homepage: www.jree.ir

Materials and Energy Research Center

MERC

Research Article

Sustainable Backup Power Supply of a Hospital by Designing a Hybrid Renewable Energy System

Setare Peirow, Fateme Razi Astaraei *, Amir Ali Saifoddin Asl, Hossein Yousefi

Department of Renewable Energies and Environment, Faculty of New Sciences and Technologies, University of Tehran, P. O. Box: 14399-56191, Tehran, Tehran, Iran.

PAPER INFO

Paper history:
Received: 13 September 2021
Revised in revised form: 18 June 2022
Scientific Accepted: 20 May 2022
Published: 22 August 2022

Keywords:
Hospital's Energy System,
Design-Builder Software,
Photovoltaic Panel,
PVsyst Software,
Economic and Environmental Assessment,
HOMER Pro Software

ABSTRACT

The issue of power supply in hospitals is of special importance because of its direct effect on people's health conditions and vital treatment and care measures. Hospitals are among buildings with high energy consumption. The possibility of using renewable sources in their energy supply is one of the issues and challenges that specialists encounter. This paper discusses the possibility of installing a small solar power generation unit on a hospital rooftop to improve the quality of power supply systems. The case study is a hospital located in Tehran, Iran. For this purpose, the hospital energy system was modeled with the Design-Builder software. The obtained results were validated based on the actual consumption of the model specified in the hospital energy bills. According to the modeling step results, the annual consumption of the current energy system was 3.08 GWh of electricity and 4.23 GWh of gas. In the second step, a renewable power generation unit consisting of photovoltaic panels and battery was designed for the hospital's roof using PVsyst software. The designed power generation unit could produce 132 MWh of solar energy per year, of which 85 MWh may be sold to the main grid. The techno-economic and environmental feasibility study for the proposed system was performed using HOMER Pro software. The evaluation results revealed that considering the 20-year lifetime of the project, the proposed system achieved a lower energy cost and lower net present cost than the current system. Environmental assessment of the model by considering emission penalty indicated that the proposed system emitted fewer pollutant gases into the environment than the current system. Sensitivity analysis was also applied to investigate the effect of discounting and diesel fuel price variation on the system's energy cost. According to the results, a 4 % increase in the discount rate leads to a 14 % growth in the cost of energy for the project. Also, there was a direct relation between enhancement of the expected inflation rate and raising the net present cost of the project.

https://doi.org/10.30501/jree.2022.304704.1257

1. INTRODUCTION

Hospitals are considered one of the main energy consumers in building sectors. Since hospitals and health centers constitute an energy-intensive group of buildings that must operate 24 h and 365 days a year, uninterrupted energy access is crucial for them [1, 2].

The issue of energy supply in hospitals is of special importance because of its direct effect on people's health conditions and vital treatment and care measures [3]. The energy-related issues have not received enough attention in constructing most of the existing hospitals [4]. Over the past few decades, hospitals have been designed and constructed only to meet required health standards, neglecting the environmental effect of energy systems due to the low cost of energy and disregarding the economic and environmental sustainability of human activities [5].

Since electricity consumption is higher in hospitals than in other buildings, renewable resources are a suitable option to employ to meet their electricity requirements [6]. On the other hand, including these resources in the energy basket of the healthcare sector facilitates sustainable energy development [7].

Considering the potential of solar energy in most parts of Iran and the incentives offered by the energy ministry to produce solar power for hospitals, a solar power generation unit is a suitable option to improve the power system. Also, generated solar power may be sold to the main network. Accurate sizing and quality equipment selection according to the climatic region are essential in order to reduce the probability of system failure [8].

2. EXPERIMENTAL

Different studies have been published with different viewpoints on the case of power supply in hospitals. Isa et al. (2016) evaluated the possibility of developing a combined

*Corresponding Author's Email: razias_m@ut.ac.ir (F. Razi Astaraei)
URL: https://www.jree.ir/article_155087.html

Please cite this article as: Peirow, S., Razi Astaraei, F., Saifoddin Asl, A.A. and Yousefi, H., "Sustainable backup power supply of a hospital by designing a hybrid renewable energy system", ***Journal of Renewable Energy and Environment (JREE)***, Vol. 9, No. 4, (2022), 48-63. (https://doi.org/10.30501/jree.2022.304704.1257).

heat and power generation system for a Malaysian hospital [9]. The proposed cogeneration system included grid-connected photovoltaic, fuel cell, and battery. The simulation result indicated that the proposed cogeneration system had the lowest total net present cost, levelized cost of energy, and operating cost. Biglia et al. (2017) also performed a techno-economic feasibility analysis of CHP[1] systems in large hospitals through the Energy Hub method. Integration of a CHP system (internal combustion engine) into a multi-purpose energy system of the hospital has been studied since cogeneration is recognized as one of the most effective ways to convert energy. The proposed model is a valuable tool for examining potential energy and economic savings and for designing and optimizing every kind of multi-energy system of generic buildings, including hospitals [10].

Lagrange et al. (2020) studied different cases that required the use of renewable energies besides diesel generators and energy storage systems to increase the resilience of a microgrid so as to feed critical facilities of a hospital. The work aimed to quantify the benefits provided by an improvement of the energy resilience that could be achieved by installing a microgrid at a hospital fed by renewable energy sources [11]. Jahangir et al. and Dursan et al. (2021) also discussed the possibility of implementing hybrid renewable energy systems to supply the power demand for a hospital by making a comparison between techno-economic-environmental parameters [1, 12].

Shabnam Vaziri and Babak Rezaee et al. [13] tasted the PV[2]/WT[3]/Grid model for a hospital in Iran. According to the results, hospital costs were reduced by 2.7 %, while hospital loads decreased during peak hours. Their model discovered a tradeoff between costs and satisfaction of patients and medical practitioners. Another study by Andrea Franco and Marjan Shaker et al. [14] in Switzerland reported that a hybrid configuration consisting of renewable energy resources, a battery, and a diesel generator was the best option for medium-to-large healthcare facilities, especially for those in off-grid settings. Table 1 tabulates a list of the mentioned articles with the key subject and final result. The main difference between recent articles and current study is also addressed in the Table 1.

The main challenge of recent studies has been complete and accurate modeling of the hospital energy system as a large-scale and complex structure, which need all of the building plans, section usage, and details of its energy system. So far, few studies have been conducted on simulating the energy system of a complicated hospital. Furthermore, identification of the environmental benefits of integrating the energy system of hospitals as a complex structure with renewable energies was not considered in recent studies.

Iran is a vast country with many hospitals, health centers, and medical buildings. Most of the energy needs of these areas are met by fossil fuels which impose environmental impacts on the country. The grid is typically used to meet the load demand of hospitals, and diesel generator is often implemented as backup for power supply. Using renewable energies in the power supply system is an appropriate choice that may help improve the quality of the power supply system and have an influential role in reducing pollution in medical buildings.

[1] Combined Heat and Power

[2] Photovoltaic

[3] Wind Turbine

This paper proposed photovoltaic modules with batteries to integrate with the power supply system. The hybridization with the solar system and battery enhances the energy security in the model. To this end, using the solar power plant with a weak network support strategy was proposed. First, the hospital's energy system was modeled using Design-Builder Software (version 6.1.0.006). The software was applied to model the building from different aspects, namely building physics (construction materials), building architecture, cooling and heating systems, and lighting systems [18]. Second, a hybrid energy system consisting of photovoltaic modules and batteries was modeled with PVsyst software (version 6.8.1) to add to the previous backup power supply consisting of only a diesel generator. Finally, a techno-economic and environmental evaluation of the proposed system was performed to justify the project's feasibility. HOMER Pro software was used for this section and sensitivity analysis was applied to indicate the effect of financial factors on the system's cost variation.

3. METHOD

3.1. Methodology

In this research, the hospital energy system was modeled using Design-Builder software (version 6.1.0.006), which is convenient for modeling different aspects of the building. The software can utilize the climate data files of different cities to calculate the energy input, consumption, and losses for the region the building is located in. The modeling engine in the software is EnergyPlus developed by American Energy Department and is considered a highly accurate and capable software product. System modeling in EnergyPlus is performed based on the following computational relationships.

3.2. Basis for the zone and air system integration

The basis for the zone and air system integration is to formulate energy and moisture balances for the zone air and solve the resulting ordinary differential equations using a predictor-corrector approach. The formulation of the solution scheme starts with a heat balance on the zone air tabulated in Table 2.

Air systems provide hot or cold air to the zones to meet heating or cooling loads. The system energy provided to the zone, $\dot{Q}_{sys}$, can thus be formulated from the difference between the supply air enthalpy and the enthalpy of the air leaving the zone as in Equation (2). This equation assumes that the zone supply air mass flow rate is equal to the sum of the air flow rates leaving the zone through the system return air plenum and being exhausted directly from the zone. Both air streams exit the zone at the zone mean air temperature.

The sum of zone loads and air system output now equals the change in energy stored in the zone. Typically, the capacitance Cz would be that of the zone air only. However, thermal masses assumed to be in equilibrium with the zone air could be included in this term. EnergyPlus provides three different solution algorithms to solve the zone air energy and moisture balance equations.

3.3. Conduction transfer function module

The most basic time series solution is the response factor equation that relates the flux on one surface of an element to

an infinite series of temperature histories on both sides, as shown by Equation (3) in Table 3.

Table 1. Summary of literature review

Reference	Subject	Result	Difference with present study
[9]	Possibility of developing a combined heat and power generation system for a Malaysian hospital.	The proposed cogeneration system has the lowest total net present cost, levelized cost of energy, and operating cost.	Type of hybrid system proposed for the hospital differs from the one in the current study.
[10]	Techno-economic feasibility analysis of CHP systems in large hospitals.	The proposed model was a useful tool to examine potential energy and economic savings and design and to optimize every multi-energy system.	Renewable energies for the hospital power supply were not addressed in this study.
[11]	Use of renewable energies in addition to diesel generators and energy storage systems with the aim of increasing the resilience of a micro grid feeding critical facilities of a hospital.	With high solar resources and for the electricity tariff studied, the addition of solar PV makes it possible to increase the resilience of a microgrid in the event of power outages.	This study focused on the resiliency of microgrids, while the current article deals with the techno-economic and environmental assessment of the hybrid system.
[12-15]	The possibility of implementing hybrid renewable energy systems to supply the power demand for a hospital.	The proposed hybrid system has the lowest total net present cost, levelized cost of energy, and operating cost.	Environmental evaluation and sensitivity analysis were not addressed in these studies.

Table 2. Heat balance in the zone air equation [16]

Zone air heat balance relations	Equations No.
$C_z \frac{dT_z}{dT} = \sum_{i=1}^{Ns1} \dot{Q}_i + \sum_{i=1}^{N_{surface}} h_i A_i (T_{si} - T_z) + \sum_{i=1}^{N_{zone}} \dot{m} C_p (T_{zi} - T_z) + \dot{m}_{inf} C_p (T_\infty - T_z) + \dot{Q}_{sys}$	(1)
$\dot{Q}_{sys} = \dot{m}_{sys} C_p (T_{sup} - T_z)$	(2)
$C_z \frac{dT_z}{dT}$ = energy stored in zone air ($Cz = \rho_{air} CpCT$; ρ_{air} = zone air density; Cp = zone air specific heat; CT = sensible heat capacity multiplier)	
$\sum_{i=1}^{Ns1} \dot{Q}_i$= sum of the internal convective loads $\sum_{i=1}^{N_{surface}} h_i A_i (T_{si} - T_z)$ = convective heat transfer from the zone surfaces $\sum_{i=1}^{N_{zone}} \dot{m} C_p (T_{zi} - T_z)$= heat transfer due to interzone air mixing $\dot{m}_{inf} C_p (T_\infty - T_z)$ = heat transfer due to infiltration of outside air $\dot{Q}_{sys}$ = air systems output T_{sup}= supply air temperature	

Table 3. The equations of change and rates for anode and cathode [16]

Conduction transfer relations	Equations No.
$q''_{ko}(t) = \sum_{j=0}^{\infty} X_j T_{o,t-j\delta} - \sum_{j=0}^{\infty} Y_j T_{o,t-j\delta}$	(3)
$q''_{ki}(t) = -Z_0 T_{i,t} - \sum_{j=1}^{nz} Z_j T_{i,t-j\delta} + Y_0 T_{0,t} + \sum_{j=1}^{nz} Y_j T_{o,t-j\delta} + \sum_{j=1}^{nq} \Phi_j q''_{ki,t-j\delta}$	(4)
$q''_{ko}(t) = -Y_0 T_{i,t} - \sum_{j=1}^{nz} YT_{i,t-j\delta} + X_o T_{o,t} + \sum_{j=1}^{nz} X_j T_{o,t-j\delta} + \sum_{j=1}^{nq} \Phi_j q''_{ko,t-j\delta}$	(5)
In Eq. 3, "q" is heat flux, T temperature, i the inside of the building element, o the outside of the building element, t the current time step, and X and Y the response factors.	
In Eqs 4 and 5, the outside heat flux is: q"=q/A Xj = Outside CTF coefficient, j= 0, 1, nz. Yj = Cross CTF coefficient, j= 0, 1, nz. Zj = Inside CTF coefficient, j= 0, 1, nz. Φ_j = Flux CTF coefficient, j = 0, 1, nz. Ti = Inside face temperature To = Outside face temperature q''_{ko}= Conduction heat flux on the outside face q''_{ki}= Conduction heat flux on the inside face	

While the terms in the series decay fairly rapidly in most cases, the infinite number of terms needed for an exact response factor solution makes it less than desirable. Fortunately, the similarity of higher-order terms can be used to replace them with flux history terms. The new solution contains elements that are called Conduction Transfer Functions (CTFs). The basic form of a conduction transfer function solution is shown by Equations 4 and 5 in Table 3.

The subscript following the comma indicates the period for the quantity in terms of the time step δ. Note that the first terms in the series (those with subscript 0) have been separated from the rest in order to facilitate the resolution at the current temperature in the solution scheme. These equations state that the heat flux at either face of the surface of any generic building element is linearly related to the current and some of the previous temperatures on both the interior and exterior surfaces, as well as some of the previous flux values on the interior surface.

The final CTF solution form reveals why it is so elegant and powerful. The conduction heat transfer through an element can be calculated with a single, relatively simple, linear equation with constant coefficients. The coefficients (CTFs) in the equation are constants that only need to be determined once for each construction type. The only data required for storage include the CTF and a limited number of temperature and flux terms. The formulation is valid for any surface type and does not require the calculation or storage of element interior temperatures.

Additional information on modeling details of different parts of the system and the formulation used is given in the reference [16].

3.4. Simulation in Design-Builder

In order to start modeling, first, the Three-Dimansional (3D) model of the building was drawn in the Design-Builder software. The 3D plan models were generated using the model files, which are in the format of AutoCAD plans. The plan includes the building, its orientation, how doors and windows are built-in, and also the different zones on the floors. Figure 1 shows a view of the building floors and plans in Design-Builder.

Ghiasi specialized hospital in the south-western part of Tehran was selected for this study. This hospital has a total area of 17300 square meters and 16000 meters of space on all the floors. Different diagnostic and therapeutic departments such as laboratories, Computed Tomography (CT) scans, ophthalmology, emergency unit, pharmacy, etc. are located on the ground floor. In contrast, hospital wards, operation rooms, Coronary Care Unit (CCU) and Intensive Care Unit (ICU) departments are located on the higher floors.

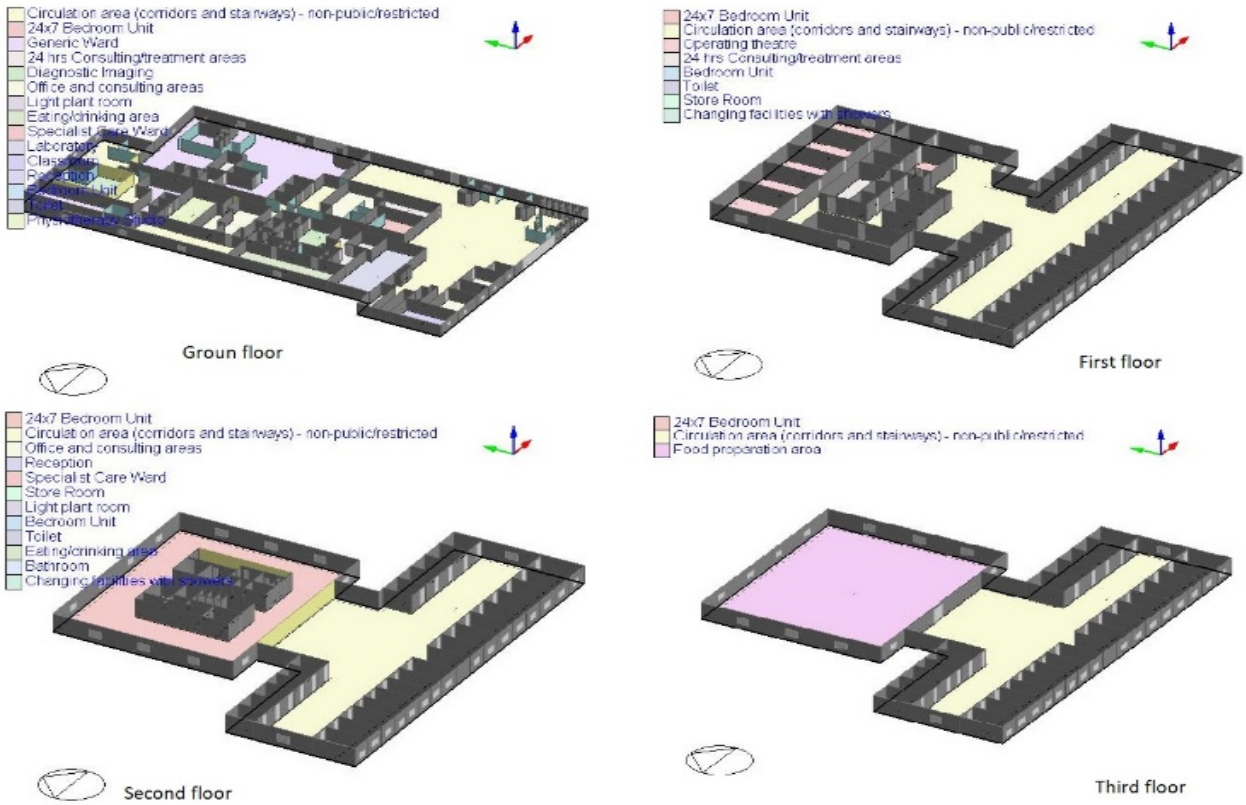

Figure 1. Plan of Hospital floors

Figure 2 shows an aerial photograph of the hospital. Considering the solar energy potential in Tehran, the hospital's roof, which has an area of about 900 square meters, is a suitable place to install solar panels.

After designing the building plan, the energy system's data and installation information were entered into the software. Some of these data are listed in Table 4.

3.5. Design of a small solar power generation unit on the roof of the hospital

The current energy system of the hospital operates using fossil resources. The power demand is supported by the main grid and diesel generators are installed as the backup system. Due to the great potential of solar power generation in Tehran [17], the hospital's energy system is recommended to combine with

the solar energy system. Iran is located between 25° and 40° north latitudes in one of the earth's regions with suitable sun radiation. The solar average radiation intensity in Iran is higher than the global average, and more than 280 sunny days have been recorded in more than 90 % of Iranian lands [18]. Figure 3 shows the average monthly radiation in Tehran.

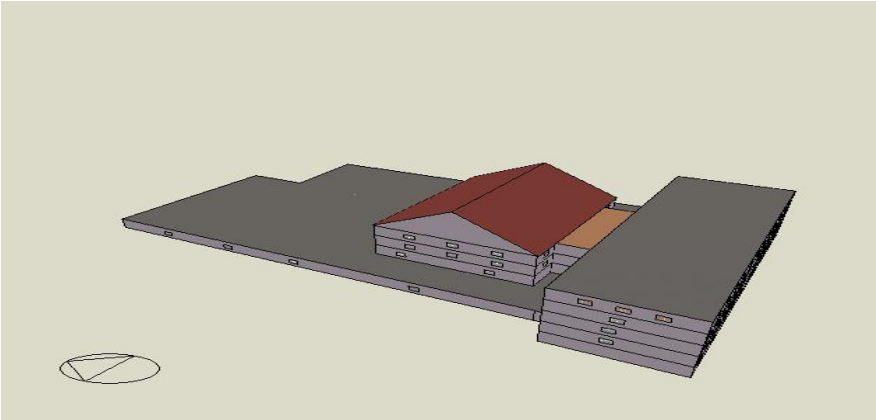

Figure 2. Aerial photograph of the hospital (Map designed in Design-Builder)

Table 4. Input data in Design-Builder

Input data	Value entered in Design-Builder
Geographical location of hospital	Tehran-Mehrabad
Latitude and longitude	35.69° N, 51.31° E
Building plan	3D design is produced by calling the DXF file
Location of doors, windows, and building spaces	Based on the building plans
Building use	The use of each space is entered (e.g., laboratory, ward, clinic, etc.)
Frequency of occupants' presence in each space	It is determined according to the use of each space
Comfort temperature in winter	22-25 °C
Comfort temperature in summer	25-28 °C
Hot water consumption	It is determined according to the use of each space
Energy consumption for computers, office supplies, etc.	It is determined according to the use of each space and the time schedule
Energy required for cooking	The required energy and its source are determined for the food-cooking space (200 W/m^2)
Building wall materials and their thickness	Brick walls of the thickness of 40 cm (based on the intended building features)
Building façade	Cement façade of thickness 5 cm
Quality of sealing	Medium
Type of window	Transparent and double-glazed
Type of lamps	Low standard (15 W/m^2)
Type of air-conditioning system	Fan coil unit (4 pipes), Air-cooled chiller
COP of cooling system	2
COP of heating system	0.85
Hot water supply system	Boiler with 85 % efficiency
Energy source of cooling system	Electricity
Energy source of heating system	Natural gas
Energy source of hot water supply	Natural gas
Energy source for cooking	Natural gas

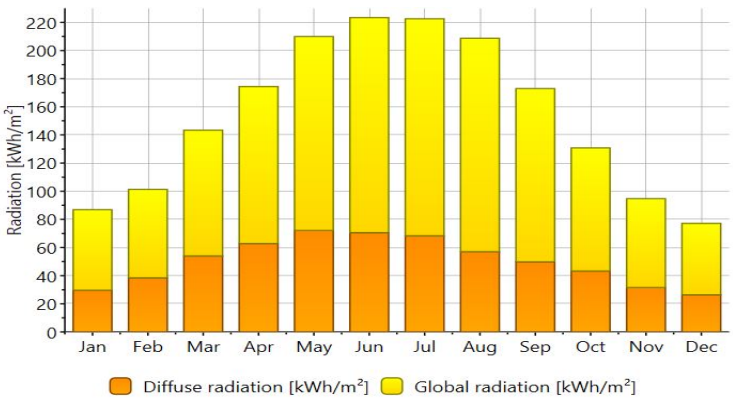

Figure 3. Monthly diffuse and global radiation in Tehran (Meteonorm output)

The windows, building facades, and roof can be employed for solar power generation in the model. To generate power from solar energy, the type of glasses and materials used in the façade must be replaced, which is a costly and unavailable option. The easiest way to produce solar power is to install photovoltaic panels on the roof of the hospital.

The Photovoltaic (PV) panels and the installation process on the rooftop were modeled using the PVsyst software (version 6.8.1). Design parameters such as module orientation, near shading, and inter-row spacing were evaluated.

PVsyst is a versatile software product for designing solar photovoltaic panels that can help the operator accurately design and simulate a power plant by utilizing a package of built-in libraries and the desired brands in any configuration. It also enables the user to add new equipment to the software environment, manipulate the system to extract the highest efficiency from the solar power plant, and select the best configuration by calculating the effect of different parameters on the solar power plant.

Shadow analysis is one of the essential steps in the phase of solar energy system design or analysis. In solar cells, it is important to analyze shading caused by surrounding objects and/or vegetation [19]. The shaded solar cell acts as a power load instead of a power producer. The reverse voltage exceeds the breakdown voltage that leads to hotspot formation. In this study, shading analysis is done in the PVsyst workspace and the final design consists of a possible minimum shadow effect.

In this case, considering the total available space area for use as 900 m^2, 80 kilowatts of solar panel capacity has been selected to be installed on the rooftop. The type of selected panels is 250 W from the Sharp brand. To size a solar PV array, cells are assembled in the form of a series-parallel configuration for requisite energy.

To compensate for emergencies and electricity deficiency from the grid, the Weak Grid and Islanding mode strategies in PVsyst were suggested for the installation of PV panels on the rooftop.

The national electricity grid meets most of the hospital's electricity demand. However, due to the unavailability of the grid during network disruption, other electricity resources are needed to support the system.

Grid reliability is defined in the model by three parameters. These items are mean outage frequency, mean repair time, and repair time variability, which are quantified in Table 5. These items are considered based on the reliability of the electricity supplier network in the study. The electricity cut-off profile of the hospital is illustrated based on the field research by visiting the considered hospital and technical assistants' reported statistics about the number of annual electricity cutoffs. The times of these cut-offs and repairing networks are determined according to obtained statistics from the hospital in one year. By specifying these items, a random chart of grid outages through the year is generated by the software (Figure 4). Most of these outages occur during the day because of the pick power demand and more loads are imposed on the network during the day.

Table 5. Grid reliability parameters

Parameter	Unit	Value
Mean outage frequency	1/year	60
Mean repair time	h	0.5
Repair time variability	%	30

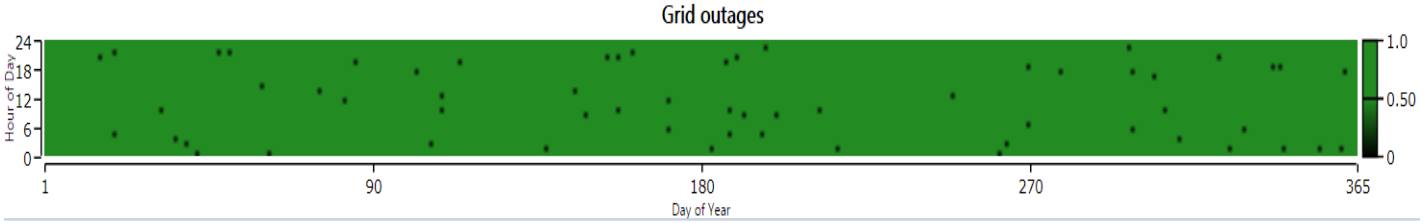

Figure 4. Random graph of grid outages through the year

The Weak Grid strategy uses batteries resource to prevent electricity deficiency. In this scenario, batteries will be used to cover a self-consumption load profile. However, the battery source depletion will be limited to a certain threshold, which allows the load profile to stay in the safe region in case of possible interruptions. When there is an interruption, the energy saved in the battery system is allowed to exceed the limits and reach depletion.

To reach this goal, the selected battery for this project, which is from the Tesla brand, has a nominal capacity of 268 Ah. Self-consumption load profile was considered to be 10 kW. This load is enough to cover the power demand of hospital emergency corridors. Therefore, a reliable electricity supplier was defined for emergency corridors to promote hospital security in case of unexpected events.

When there is a network failure, there should be a mechanical switch for the physical disruption of the network from the connected mode. In this condition, the system will operate in islanding mode and the battery inverter supplies all the energy required by the consumer. In the connected mode, the user AC[1] circuit is directly connected to the grid; this gives the network the possibility of injecting additional solar energy, even though this is not always allowed by the network administrator. Figure 5 shows a schematic of the proposed network.

[1] Alternating Current

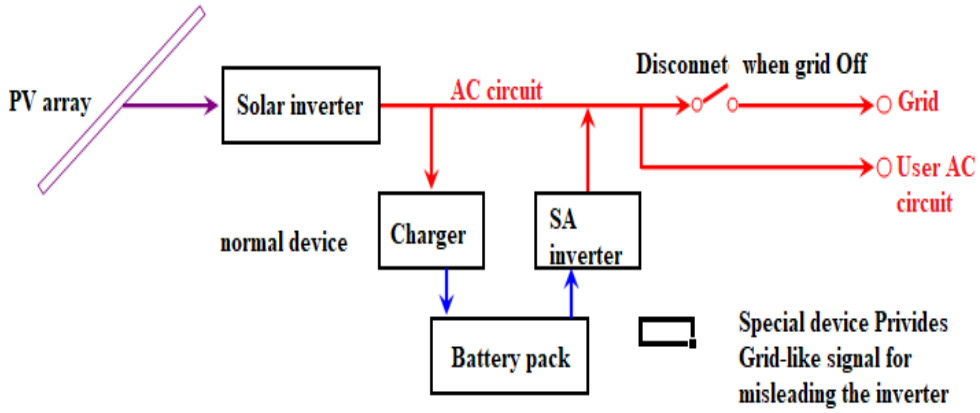

Figure 5. Proposed configuration for supporting the weak network and islanding mode

3.6. Designed model in PVsyst

The system comprises 324 panels with a total area of 532 m^2. In the designed model in PVsyst, there are 12 cells connected in series and 27 modules connected in parallel. The panels were installed in a fixed position and at an angle of 33° relative to the horizon. The total number of 9 unit inverters from the SMA brand were installed to convert solar power. Table 6 presents additional information about the plant.

Table 6. Input data in PVsyst

System type	Sheds on ground
Tilt 33°	Azimuth 0°
Number of sheds: 27	Sheds spacing: 6.7 m
Collector width: 3.36 m	Ground cover ratio (GCR): 50.1%
Charging strategy	When excess solar power is available
Discharging strategy	As soon as power is needed

Table 7 represents the specifications of the solar panel and the inverters, while Table 8 shows the properties of the batteries. Table 9 shows the details of the place where the power plant will be constructed. Figure 6 shows the configuration of installed panels on the hospital rooftop.

A suitable controller is responsible for managing the energy flux all the time. There are multiple scenarios in this case. If the solar energy is sufficient for the user, the excess energy would be used to charge the batteries. In the case of fully charged batteries, the rest of the energy will be injected into the grid. In case of insufficient sun energy or during the nights, the energy demand will be supplied by the batteries.

The current backup system of the model comprises a diesel generator with a capacity of 1000 kW.

Table 7. Specifications of panel and inverter installed at the power plant

Specification	Inverter	Panel
Brand	SMA	Sharp
Capacity	7.7 kW	250 Wp
Voltage	300-480 V	26 V
Manufacturing technology	LF-TR	Si-Poly
Model	Sunny boy 8000 U-240	ND-RC250
Year manufacture	2010	2016

Table 8. Battery specifications

Type	Lithium-Ion
Brand	Tesla
Model	Powerwall 2
Voltage	50.4 V
Nominal capacity	268 Ah
Stored energy (DOD 80 %)	10.8 kWh
Weight	125 Kg
Total stored energy during battery life	10186 MWh
Global capacity	804 Ah

Table 9. Geographical location

Country	Iran
Geographical site	Shahrak-e Farhangian
Latitude	35.70° N
Longitude	51.28° E
Altitude	1230 m
Albedo	0.2

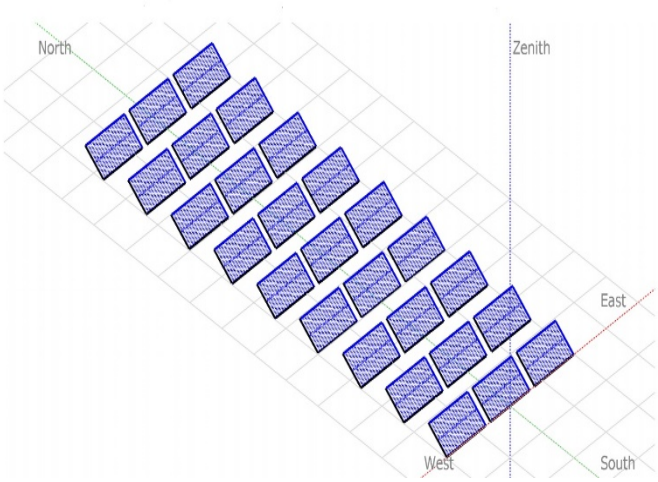

Figure 6. Arrangement of the panels installed on the hospital ceiling

3.7. Economic and environmental analysis

The economic and environmental analysis of the suggested system was performed using HOMER Pro software. HOMER is known as wide-ranging software for the investigation and development of hybrid sources. This software is made and developed by US National Renewable Energy Laboratory

(NREL). Its name stands for Hybrid Optimization Model for Electrical Renewable. This software (version 3.14.2) is ready to detect the most cost-effective system for a given load by considering incident solar radiation, electrical demand profile, and equipment properties.

The energy load demand of the hospital is obtained from the Design-Builder output. Thus, the monthly and daily electrical output of the Design-Builder is used as the input data for HOMER pro software. Figure 7 shows the average monthly load of the hospital.

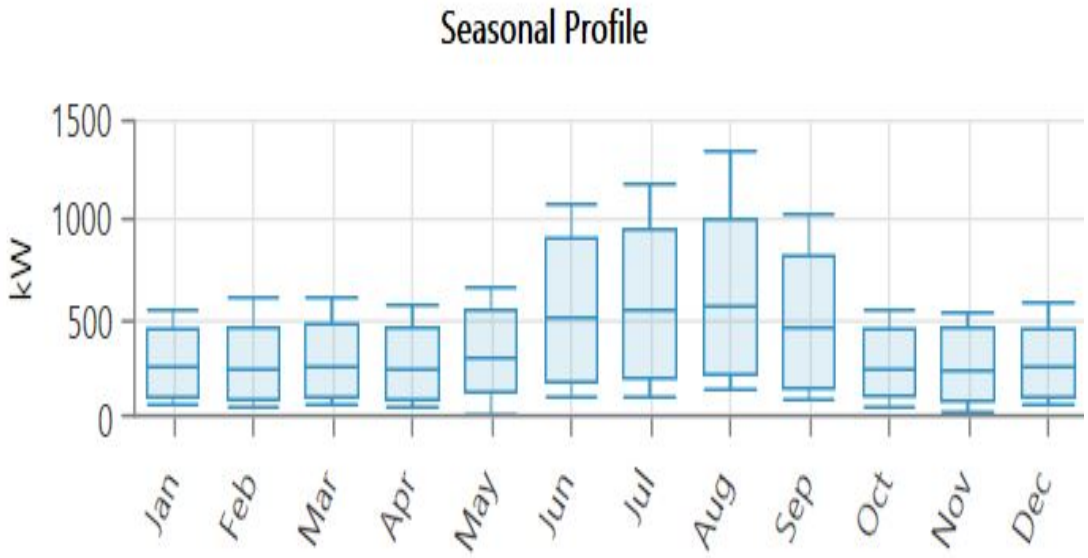

Figure 7. Monthly average load profile for the hospital

3.7.1. Calculating the cost of the system

The system designed in the PVsyst includes photovoltaic panels and a battery in the grid-connected mode. A 700 kW diesel generator is also connected to the power supply system to support the power supply in case of an emergency. Thus, the system consists of photovoltaic panels (sharp ND-250QCS), an inverter, a battery (Tesla Powerball 2), and a diesel generator (Generic Medium Genset). In order to calculate the total cost of the system, techno-economic specifications of components should be entered into HOMER software. Tables 10-13 show technical factors and cost assumptions of the system's components.

Table 10. Technical parameters of solar PV array and cost assumptions

Parameter	Unit	Value
Nominal max. power	W	5000
Capital cost	$/kW	1000
Replacement cost	$/kW	1000
Operation and maintenance cost	$/kW/yr	10
Lifetime	Years	20
Efficiency	%	15.3

Table 11. Technical parameters and cost assumptions for the battery

Parameter	Unit	Value
Nominal voltage	volt	220
nominal capacity	Ah	60
maximum charge current	A	31.8
round-trip efficiency	%	90
capital cost	$	65000
replacement cost	$	65000
operation and maintenance cost	$/year	600
life time throughput	kWh	67500
life time	years	10

Table 12. Techno-economic parameters of the converter

Parameter	Unit	Value
Capital cost	$/kW	500
Replacement cost	$/kW	500
Operation and maintenance cost	$/kW/yr	10
lifetime	Years	20
Inverter efficiency	%	95
Rectifier efficiency	%	85

Table 13. Technical parameters and cost assumptions for diesel generator

Parameter	Unit	Value
Capital cost	$/kW	900
Replacement cost	$/kW	700
Operation and maintenance cost	$/kW/yr	0.02
lifetime	Hours	15000
Rated capacity	kW	1000

The economic factors consisting of the inflation rate, the discount rate, the project's life time, and diesel fuel price are the essential software entries for the economic optimization. These factors are tabulated in Table 14.

Table 14. Financial input factors for simulation of hybrid energy systems

Input factor	Value	Ref
Inflation rate (%)	15	[20]
Discount rate (%)	18	[20]
Life time of the project (years)	20	
Diesel fuel price ($/L)	0.1	[15]

Figure 8 specifies the yearly electricity prices and network power purchase rate in Iran, specified by the government. Based on the mentioned rates, energy prices differ in cold and

hot months. On the other hand, while the demand rate is high, the electricity price is twice the low demand rate [21].

Rate	Period	Price ($/kWh)	Color
1	Low electricity consumption hours in cold months	0.05	
2	Medium electricity consumption hours in cold months	0.07	
3	High electricity consumption hours in cold months	0.1	
4	Low electricity consumption hours in hot months	0.06	
5	Medium electricity consumption hours in hot months	0.08	
6	High electricity consumption hours in hot months	0.12	

Figure 8. Grid annual electricity tariffs in Iran [21]

Annual system total cost is dependent on two fundamental economic factors: NPC and COE. NPC defines the net present cost of the system, while COE describes the cost of energy of the model. NPC comprises the annual cost of components consisting of capital cost, operation and maintenance (O&M) cost, and replacement cost, excluding any miscellaneous expenses such as CO_2 emissions [22, 23]. COE is the cost of enegy of the system which means the amount of cost imposed on the system to produce each kilowatt of energy. In fact, NPC has a mathematical concept, while COE is kind of arbitrary [23]. Hence, NPC is more dependable as an economic parameter and is calculated using the following equation in Table 15.

Table 15. Economic parameters and related equations [23]

Cost relations	Equations No.
$NPC=\frac{C_T}{CRF\ (i,n)}$	(6)
$C_T = C_{acap} + \sum_{j=1}^{m} C_{OM,j} + C_f + \sum_{j=1}^{m} C_{R,j}$	(7)
$C_{acap} = C_{cap} \times CRF$	(8)
$CRF(i,n)=\frac{i(1+i)^n}{(1+i)^n-1}$	(9)
In Eq. 6, C_T is the total annualized cost ($/year), i the annual real interest rate (%), n the project's lifetime, and CRF the capital recovery factor.	
In Eq. 7, C_{acap} is the annualized capital cost of each component and C_{cap} is the initial capital cost of a component defined as the total installed cost of that component at the beginning of the project. m=The number of all devices in the system. $C_{OM,j}$= The annual operation and maintenance (O&M) cost for the j^{th} component of the system. C_f =The total annual fuel cost. $C_{R,j}$ = The annualized replacement cost for the j^{th} component of the system.	

3.7.2. Evaluating environmental impacts

For the sake of environmental impact analysis of the proposed system, the amounts of emitted greenhouse gases should be detected. Considering emission penalties for various industries is a common policy that helps reduce and control harmful emissions. Therefore, for each ton of emissions, the penalty must be paid to the government by factory owners. The amounts of considerable emissions for Iran's power plants are shown in Table 16. CO_2 with an emission content of 660.65 g/kWh has the maximum contribution. Therefore, the higher values of penalty are related to more harmful emissions, which lead to more dangerous circumstances for the environment and human health. Since Particulate Matter (PM) has the most severe impact on the whole environment, it owes the most considerable value of penalty (1228.60 $/ton) [20].

Table 16. The emission content of Iran's power plants [20]

Kind of emission	Value (g/kWh)	Penalty of emission ($/ton)
Carbon Dioxide (CO_2)	660.65	2.86
Carbon Monoxide (CO)	0.62	54
Unburned Hydrocarbons (UHC)	180.18	60
Nitrogen Oxides (NO_X)	2.38	171.5
Sulfur Dioxide (SO_2)	1.66	521.5
Particulate Matter (PM)	0.12	1228.6

HOMER software estimates the release rate of each configuration. Therefore, the environmental state of the proposed model can be evaluated by calculating its pollution level and compared with the current model.

4. RESULTS AND DISCUSSION

4.1. Basic Model

The energy system modeling outputs for Ghiasi hospital during a one-year[1] simulation in Design-Builder are as follows. The annual electricity consumption is 3.08 GWh and the annual gas consumption is 4.23 GWh. Natural gas and electrical energy account for 58 % and 42 % of the annual consumption basket, respectively (Figure 9). Figure 10 shows the yearly power required for cooling and heating systems, hot water production, lighting, electrical equipment and devices, and cooking. The building heating system and electrical equipment, with 1.91 GWh and 0.86 GWh energy usage, have the highest and lowest contribution, respectively. Figure 11 illustrates the contribution of each different consumer to the annual energy consumption of the hospital. The yearly heating by 26 % of the energy required is the highest annual consumption.

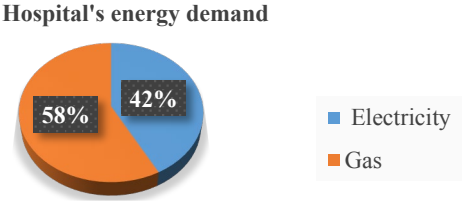

Figure 9. Circular diagram of gas and electricity contribution to annual energy consumption (obtained by Design-Builder)

[1] The year of running simulation was 2020.

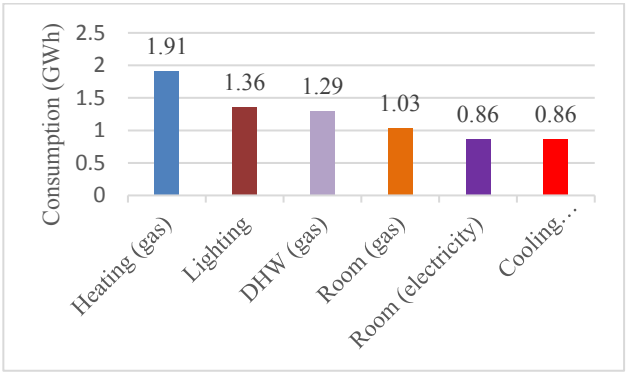

Figure 10. Energy consumption in the hospital (obtained by Design-Builder)

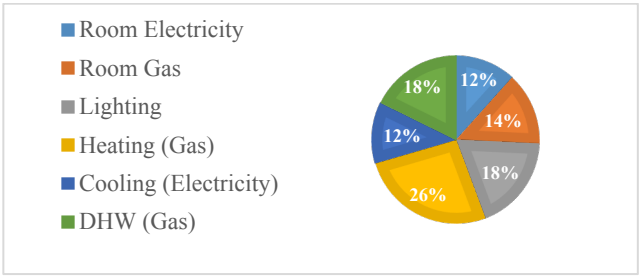

Figure 11. Contribution of different consumers to the annual energy consumption (DHW stands for district hot water)

4.2. Validation of the model

In order to validate the obtained results and compare them with the energy system performance in the hospital, the outputs are represented in a monthly manner according to the date of the hospital's utility bills, making it easy to compare the amount of gas and electricity consumption of the model with the existing system. Therefore, the electricity consumption intensity of the model has little difference from the hospital's electricity bill, and the modeling error is less than 10 %, which proves the accuracy of the modeling process.

Electricity consumption

Table 17 demonstrates data on the hospital's electricity bill (2020) and the model's power consumption amount. According to this table, the electricity consumption of specified periods based on model output slightly differs from energy bills (Figure 12). The model error is recorded at each measuring interval. According to this table, the model's power consumption is 3.045 GWh during the simulation period, while the actual consumption based on the electricity bill is about 3.012 GWh. Therefore, the modeling error is 1 %, which is an acceptable value and represents the accuracy of the modeling process.

Table 17. Electricity bills data and comparison with model outputs

Period number	length of the billing cycle (date)	Duration	Actual consumption (MWh)	Model consumption (MWh)	Relative error (%)
1	13 Feb.-9 Apr.	55	379.2	344	**9**
2	9 Apr.-8 May	29	192	181	**5**
3	8 May-9 Jun.	32	352	376	**6**
4	9 Jun.-12 Jul.	33	448	455	**1**
5	12 Jul.-6 Aug.	25	374.4	386	**3**
6	6 Aug.-6 Sep.	31	427.2	450	**5**
7	6 Sep.-4 Oct.	28	353	380	**7**
8	4 Oct.-3 Nov.	30	245.4	263	**3**
9	3 Nov.-7 Dec.	34	233.6	210	**9**
Total		297	3012.8	3054	**1**

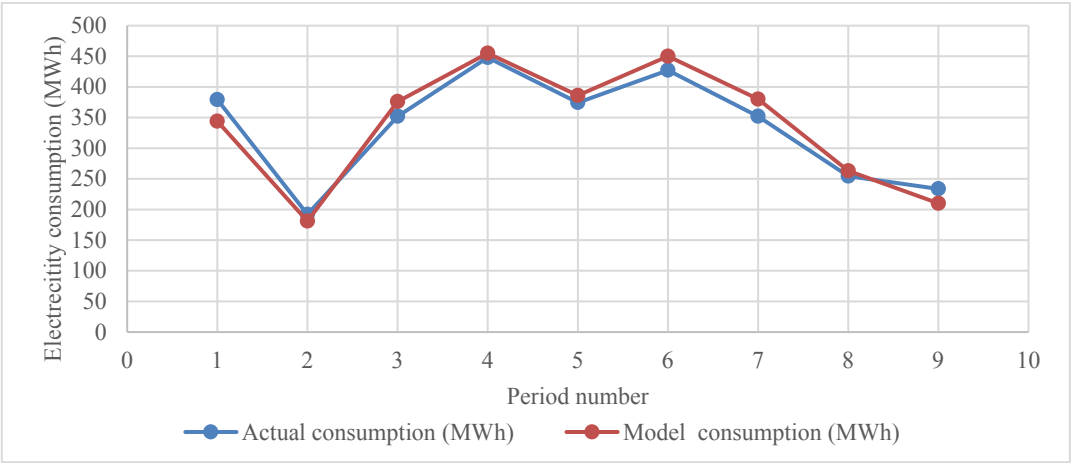

Figure 12. Electricity consumption of the specified periods based on model output and energy bill

4.3. Solar power unit

After entering the data required in PVsyst and running the simulation, the following results are obtained. Table 18 shows the monthly and annual power generated by panels. According to Table 7, 137.7 MWh can be generated by panels annually, and 87.6 MWh can be consumed to provide the self-consumed constant-profile electricity defined in the program (part of the lighting in the hospital corridors). The rest is either stored in a battery or sold to the network. According to the table, 85.56 of solar electricity is sold to the grid annually. Figure 13 displays monthly solar power production versus power injected into the grid. The difference between these two diagrams shows the amount of solar power consumed in the system. As shown in the figure, in summer, the power production reaches its maximum due to the greater intensity of sunlight in these months.

The output currents of the generated power on the panel surface are plotted in the Sanki diagram (Figure 13). Figure 14 also displays the monthly solar power production versus the power injected to grid. The difference between these two diagrams shows the amount of solar power consumed in the system. As shown in the figure, the amount of the power production in summer reaches its maximum, which is due to the greater intensity of sunlight in these months.

Figure 15 displays the performance ratio of the solar power plant in different months of the year. The performance ratio of the power plant is defined as the ratio of the modules' actual power on the panel surface to their rated capacity. The performance ratio is an index of the photovoltaic power plant quality; therefore, it is often described as a quality factor. The PR is expressed as a percentage and describes the relationship between the actual and theoretical energy output of the PV power plant. Figure 15 indicates that the power plant's the impact of increased temperature on the panel surface. The annual average of PR is 0.766.

Table 18. Monthly information on solar radiation and production (balances and results from PVsyst)

	GlobHor (kWh/m^2)	DiffHor (kWh/m^2)	T_Amb (°C)	GlobInc (kWh/m^2)	GlobEff (kWh/m^2)	EArray (MWh)	E_user (MWh)	E_Grid (MWh)	EFrGrid (MWh)	E_Miss (MWh)
January	85.8	24.76	4.30	142.5	135.0	8.82	7.44	6.805	4.804	0.10
February	99.1	37.37	7.33	138.3	131.8	9.79	6.720	6.745	4.100	0.08
March	140.8	49.27	12.99	172.0	163.9	11.81	7.44	7.995	4.282	0.00
April	171.4	73.08	17.67	180.9	170.4	12.14	7.20	8.280	3.753	0.14
May	207.1	68.06	23.31	196.8	185.5	12.77	7.44	8.633	3.759	0.13
June	221.7	69.55	28.38	201.2	189.6	12.70	7.20	8.639	3.611	0.03
July	220.2	75.92	31.32	205.0	193.0	12.75	7.44	8.188	3.729	0.02
August	206.3	68.04	30.82	211.1	199.7	13.19	4.44	9.118	3.862	0.02
September	170.8	52.81	26.08	199.4	189.8	12.76	7.20	8.649	3.846	0.11
October	125.7	40.58	20.45	171.3	163.7	11.31	7.44	7.44	4.404	0.08
November	93.9	30.69	11.73	148.7	141.0	10.11	7.20	6.795	4.426	0.09
December	76.1	25.56	6.05	128.4	121.0	8.43	7.44	5.558	5.021	0.06
Year	1820.9	615.69	18.43	2095.5	1984.5	137.57	87.600	92.849	49.598	0.860

GlobHor	Horizontal global irradiation	EArray	Effective energy at the output of the array
DiffHor	Horizontal diffuse irradiation	E_User	Energy supplied to the user
T_amb	Ambient temperature	E_Grid	Energy injected into the grid
GlobInc	Global incident in coll. Plane	EFrGrid	Energy from the grid
GlobEff	Effective Global, corr. for IAM and shading	E_Miss	Missing energy

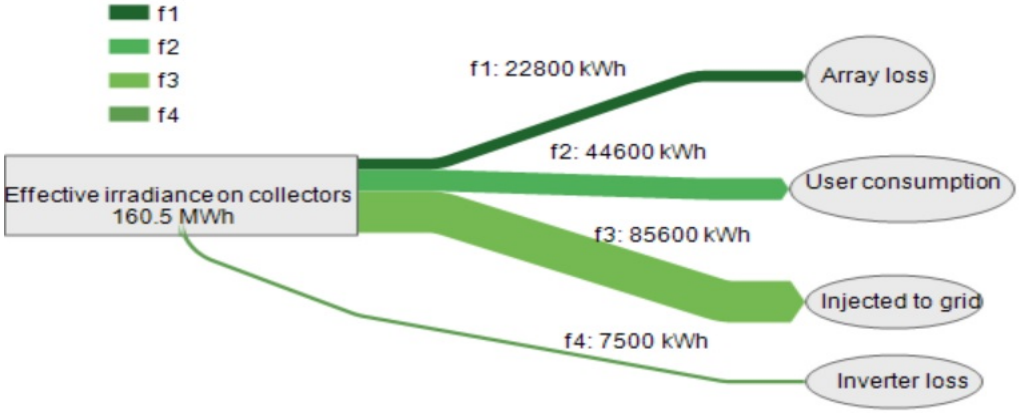

Figure 13. Sankey diagram of the electric current generated by collectors

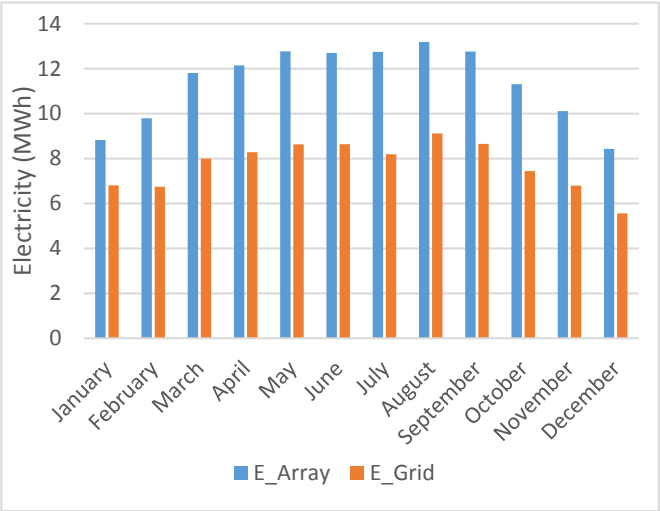

Figure 14. Monthly solar power production (E_Array) versus power injected into the grid (E_Grid)

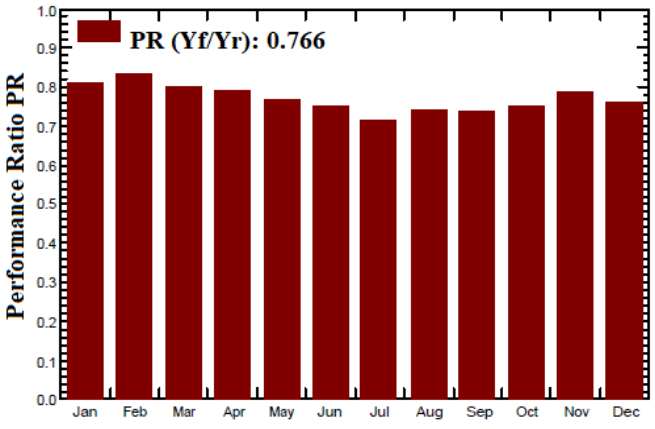

Figure 15. Performance ratio of the solar power plant in different months

Figure 16 shows the arrow loss diagram of the solar plant. As can be seen, from 1958 kWh of solar radiation energy that is incident on a square meter unit of panels with 15.9 % efficiency (in Standard Test Conditions (STC)), only 160.5 MWh can be produced in the rated condition (STC) on the array surface. 38 % of the energy generated is wasted by the loss of radiation associated with the irradiance level. These losses arise from the intrinsic behavior of the PV module since a certain amount of solar radiation is not absorbed in the morning and evening by the cells due to the insufficient space between two consecutive rows of solar cells, resulting in radiation losses. The second factor of energy loss is temperature. The cell efficiency decreases by increasing its temperature, which causes the loss of 10 % of the energy generated in the module. Other energy loss factors have a lower contribution, as shown in the figure. Finally, after deducting all the losses available, 137.7 MWh is generated at the panel level, of which 3.91 % is wasted by passing from the inverter, and 132.3 MWh can be achieved at the inverter outlet. This energy is used for recharging the battery, self-consumption constant profiles and injection into the main grid. When the battery is charging, 0.67 % of the generated energy is dissipated, while it is 0.96 % when the battery is filled as unused energy. Finally, 44.6 MWh is used to supply a constant electricity profile and 85.6 MWh is sold to the grid.

Figure 17 shows the Meteonorm horizon for the the power plant site. Blue lines indicate the tangential limits of the plane (i.e., when the sun rays are parallel to the plane). The solar radiation and PV output will change if local hills or mountains block the sunlight during some periods of the day; thus, the horizon profile helps achieve accurate output data. The horizon profile may be defined manually by a set of (Azimuth/Height) points in degrees. These may be from on-site measurements (using land-surveyors instruments like compass and clinometer). They can also be imported from several sources. In this project, the Meteonorm software produces horizon profiles imported in PVsyst.

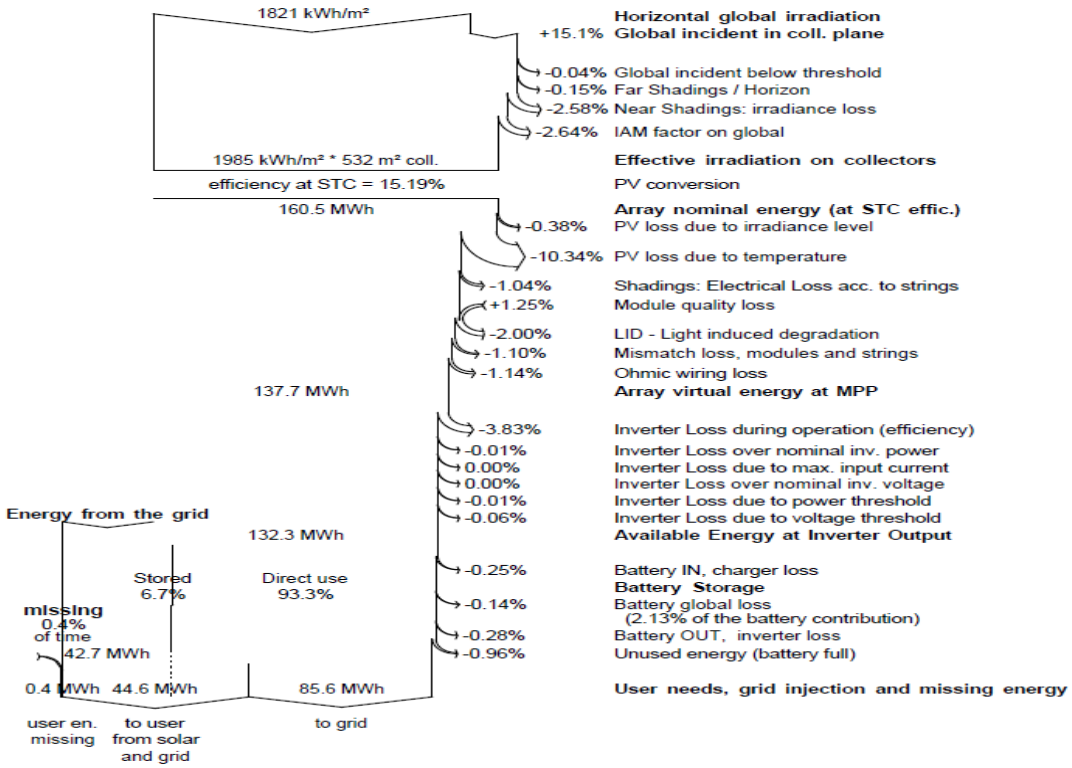

Figure 16. Arrow loss diagram (PVsyst output)

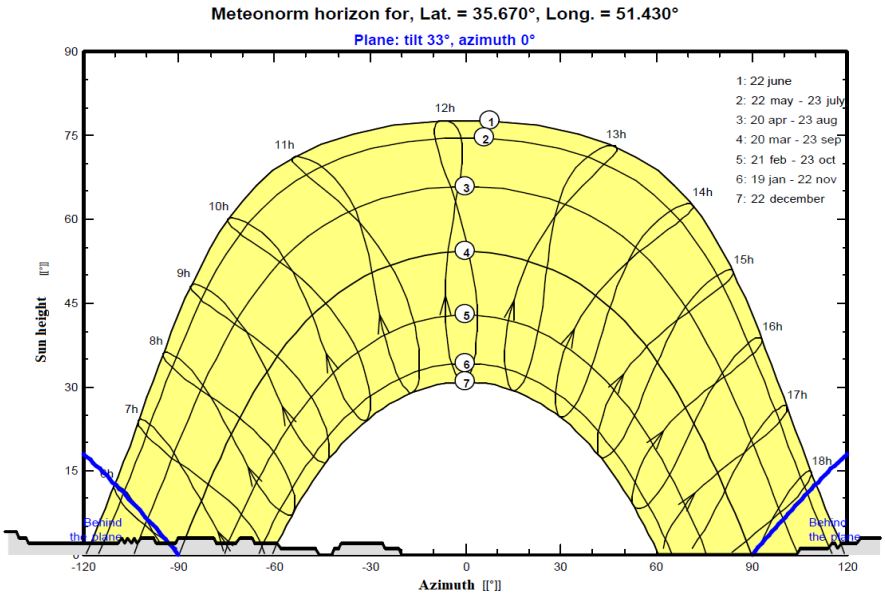

Figure 17. Meteonorm horizon diagram for the power plant site

4.4. Economic evaluation

By considering the 20-year lifespan for the project and entering the cost specifications of the used components as well as the discount rate and annual inflation rate, Homer software can be used to calculate the model's net present cost and energy cost. Table 19 shows the results of running economic optimization in HOMER Pro software. Technical and economic data of the current system (DG (1000 kW)) versus the proposed configuration (DG (1000 kW)/PV (80 kW)/Battery) in the grid-connected mode are shown in this table.

Table 19. The technical and economic data of the current configurations

Scenario	COE[1] ($/kWh)	NPC[2] (M$)	Operating cost ($)	Grid purchased (kWh/yr)
Basic model	0.0241	3.22	150,063	248,023
Proposed system	0.0235	3.17	139,825	202,773

The information obtained in the economic evaluation of the project shows that the net present cost and cost of energy of the proposed system are lower than those of the current system. Thus, the implementation of this project is economically justified. On the other hand, operating cost and payment costs for grid electricity in the proposed configuration are 7 and 18 percent lower than those for the current system, respectively.

4.5. Environmental assessment

A summary of the emissions produced by the present system in addition to the proposed configuration is presented in Table 20. Using this configuration, carbon dioxide, carbon monoxide, Unburned Hydro Carbon (UHC), PM, and sulfur dioxide emissions decreased compared with the current system. Meanwhile, the reduction of unburned hydrocarbons (UHC) is significant, exhibiting a reduction of 17 % compared to the base model. Information in the table proves that the deployment of the proposed model is also environmentally explainable.

Table 20. Current energy systems emission versus hybrid configuration emission

Quantity (kg/y)	Basic model	Proposed configuration
CO_2	6,348,930	6,336,802
CO	42,406	42,148
UHC	46,388	38,246
PM	198	194
SO_2	15,567	15,539
NO_x	3,950	3,865

4.6. Sensitivity analysis

Based on economic theories, there is a positive relationship between interest rate and inflation rate in many countries, and the interest rate's value reflects the inflation trend. The positive relationship between interest rate and expected inflation is a classical theory introduced by Irving Fisher and known as the Fisher effect in economic literature (Anari & Kolari, 2016).

On the other hand, the fuel price in Iran is lower than world prices due to Iran's geopolitics conditions; this leads to fuel contraband abroad and overuse of the fuel. Hence, increasing fuel prices in line with world prices is one of the government's purposes (Mukhtarov et al., 2022). On the other hand, enhancing the energy carriers' prices increases the inflation rate significantly. Consequently, enhancing fuels price (as one of the general policies of Iran) is considered along with inflation rate enhancement.

According to the above contents, a sensitivity analysis is applied to the proposed system to investigate the effect of variation in the inflation rate, discount rate, and diesel fuel price on NPC and COE.

The effects of changing the discount rate, inflation rate, and fuel price on the COE and NPC of the system are shown in Figure 18. The cost of diesel fuel is considered to vary between 0.1 $/L and 0.4 $/L, while the discount rate varies between 16 % and 20 %, and the inflation rate fluctuates between 13 and 17 percent. According to the results, by

[1] Cost of Energy
[2] Net Present Cost

growing the discount rate and fuel cost, the COE of the system increases. The minimum value of COE (0.0240 $/kWh) occurs when the cost of diesel is 0.1 $/L, the discount rate is 16 %, and the inflation rate is 13 %. On the other hand, the highest value of COE (0.102 $/kWh) is related to the 0.4 $/L diesel price, 20 % discount rate, and 17 % inflation rate.

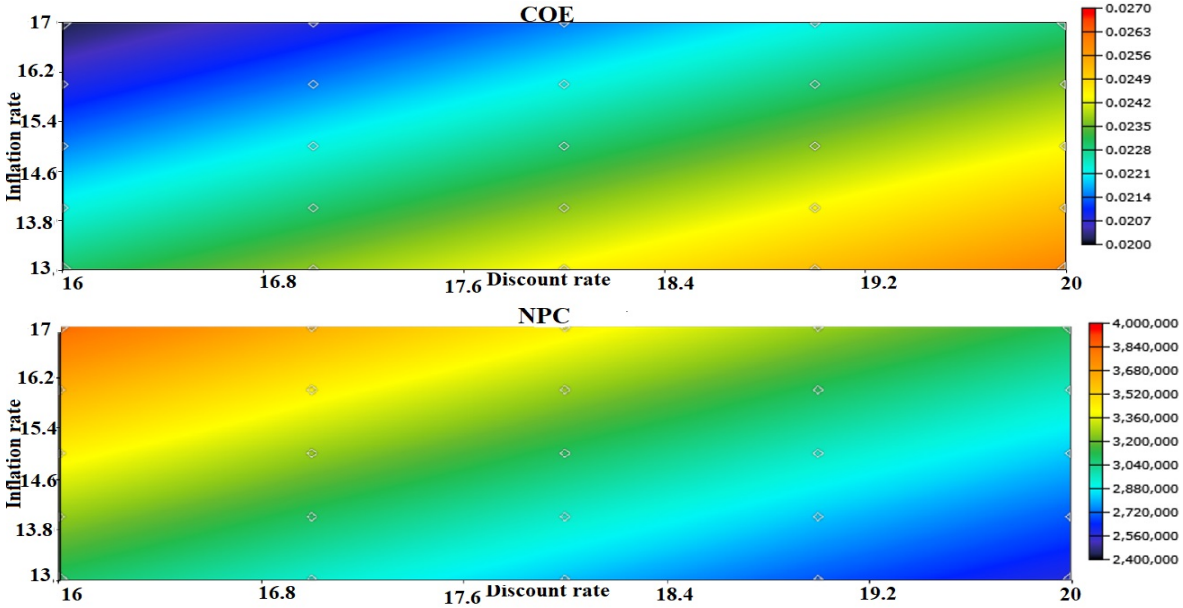

Figure 18. Effect of nominal discount and inflation rate on NPC and COE of the system

The current cost of diesel in Iran is stated as 0.1 $/L. Therefore, by considering this cost as constant, the discount rate is raised by 4 % the COE growth is 14 % (Figure 19-Plot A). On the other hand, increasing the diesel price leads to the reduction of CO_2 emission and increase of renewable fraction because the higher price of diesel fuel causes less usage of diesel generator and switching to renewable resources. Figure 19-Plot B indicates a direct relationsheep between increasing the expected inflation rate and NPC growth. As seen in Figure 19-Plot C, the COE of the system is increased by growing the diesel fuel price from 0.1 $/L to 0.2 $/L, but an increase to more than this value has minor effect on the system because photovoltaic power compensates for less diesel generator production.

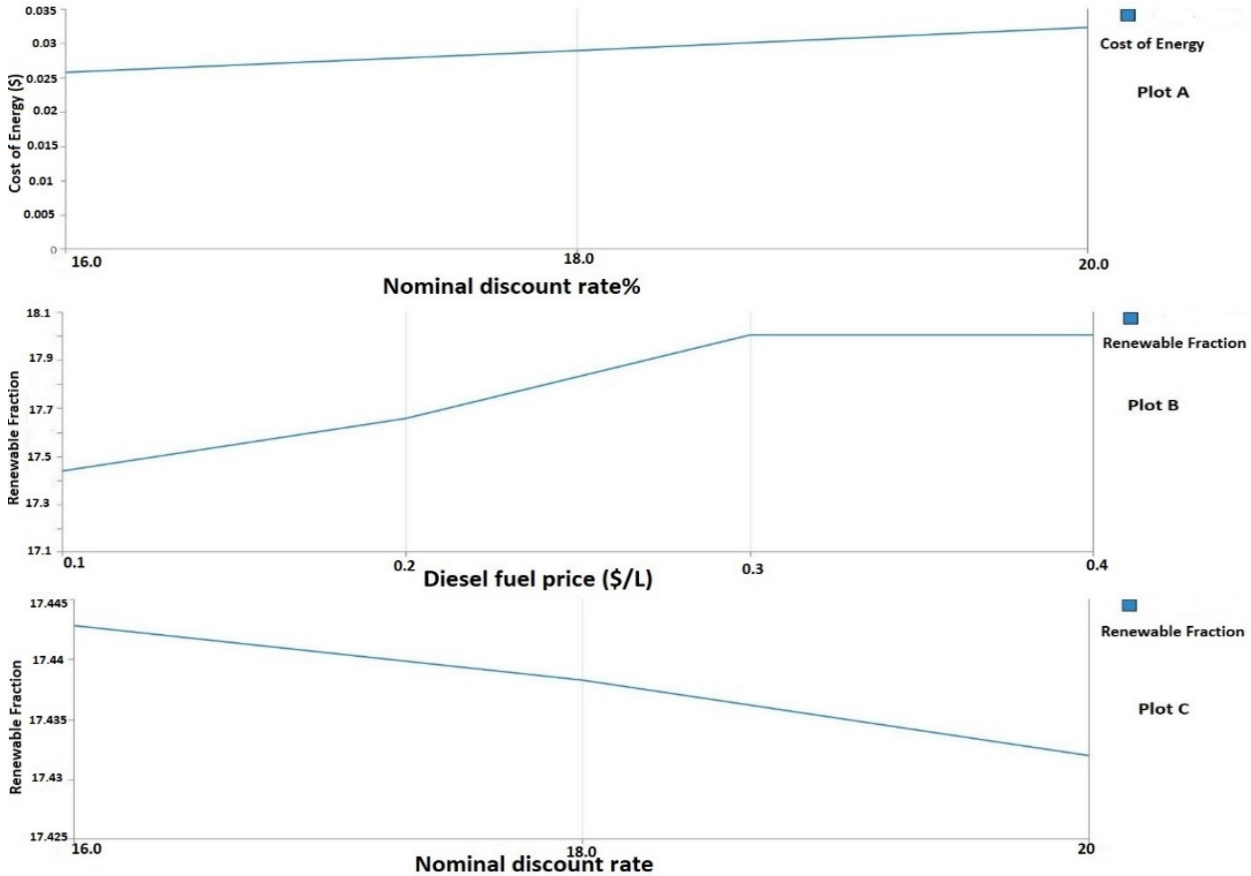

Figure 19. Linear diagram of a variation of A) COE by growing nominal discount rate; B) NPC by increasing expected inflation rate; C) COE by raising diesel fuel price

5. CONCLUSIONS

The hospital energy system was modeled with detailed information as a large-scale and complex structure in this investigation. The case study was a large hospital located in the southwest of Tehran, and the energy system of this hospital was modeled with Design-Builder software. Then, the obtained results were validated with accurate information on the hospital's energy consumption based on energy bills. In the next step, a small solar power generation unit was designed on the hospital's rooftop with the possibility of selling surplus power to the grid using PVsyst software. Design parameters such as module orientation, near shading, and inter-row spacing were evaluated. Then, the economic feasibility study of the proposed system was done using HOMER Pro software. Environmental evaluation and sensitivity analysis were also applied to the hybrid model. Finally, the project's feasibility was technically, economically, and environmentally proven. This study's most important results are summarized as follows:

- The annual electricity demand of the hospital is 3.08 GWh.
- The power plant can generate 132 MWh of solar electricity annually.
- This system can inject 85.6 MWh of its annual power into the grid.
- The net present cost of the proposed model was calculated to be 3.17 million dollars, while the cost of energy of the system was 0.0235 $/kWh.
- Growing the discount rate and fuel cost led to an increase in the COE of the system (the discount rate is raised by 4 % and the COE growth is 14 %).

The study revealed that a hybrid renewable energy system was an appropriate choice for hospitals and health centers. It is concluded from the results that renewable energies represent a valuable tool for improving the quality of power supply in hospitals. The attained results of this study can be simplified to other health centers and hospitals worldwide with each climate and weather. Applying renewable energy systems to welfare areas such as hospitals can incentivize the community to use new renewable technologies instead of traditional ones. From this research, it can be determined that hybrid renewable energy systems can compensate for the weakness of diesel generators as backup power supply and improve the total reliability of the power system, in addition to its role in reducing total emissions.

6. ACKNOWLEDGEMENT

The authors would like to acknowledge the Iran International Science Foundation (INFS, Project number: 98003237) for the financial support of this work.

NOMENCLATURE

Cp	Zone air specific heat (kJ/kg.K)
CT	Sensible heat capacity multiplier
h	Convective heat transfer coefficient (kW/m^2.K)
A	Surface (m^2)
T	Temperature (K)
Q	Internal load (kW)
m	Mass rate (kg/s)
q	Conduction heat flow (kW)
q"	q/A: conduction heat flux (kW/m^2)
CTF	Conduction Transfer Function
nz	Number of zones
Xj	Outside CTF coefficient, j= 0, 1, nz
Yj	Cross CTF coefficient, j= 0, 1, nz
Zj	Inside CTF coefficient, j= 0, 1, nz
NPC	Net Present Cost ($)
COE	Cost of Energy ($/kWh)
CT	Total annualized cost ($/year)
i	Interest rate (%)
CRF	Capital Recovery Factor
Cap	The initial capital cost of a component ($)
Cacao	The annualized capital cost of each component ($)
n	Lifetime of the project (year)
m	Number of all devices in the system
COM,	Annual operation and maintenance (O&M) cost ($/year)
Cf	Total annual fuel cost ($/year)
CR	Annualized replacement cost ($/year)
CO_2	Carbon Dioxide
CO	Carbon Monoxide
UHC	Unburned Hydrocarbons
NO_X	Nitrogen Oxides
SO_2	Sulfur Dioxide
PM	Particulate Matter
PR	Performance ratio
Greek letters	
ρ	Density (kg/m^3)
δ	Time step
Φ_j	Flux CTF coefficient, j = 0, 1, nz
Subscript	
j	Number of system's components

REFERENCES

1. Jahangir, M.H., Eslamnezhad, S., Mousavi, S.A. and Askari, M., "Multi-year sensitivity evaluation to supply prime and deferrable loads for hospital application using hybrid renewable energy systems", ***Journal of Building Engineering***, Vol. 40, No. April, (2021), 102733. (https://doi.org/10.1016/j.jobe.2021.102733).
2. Morgenstern, P., Li, M., Raslan, R., Ruyssevelt, P. and Wright, A., "Benchmarking acute hospitals: Composite electricity targets based on departmental consumption intensities?", ***Energy and Buildings***, Vol. 118, (2016), 277-290. (https://doi.org/10.1016/j.enbuild.2016.02.052).
3. Wang, T., Li, X., Liao, P.-C. and Fang, D., "Building energy efficiency for public hospitals and healthcare facilities in China: Barriers and drivers", ***Energy***, Vol. 103, (2016), 588-597. (https://doi.org/10.1016/j.energy.2016.03.039).
4. García-Sanz-Calcedo, J., "Analysis on energy efficiency in healthcare buildings", ***Journal of Healthcare Engineering***, Vol. 5, No. 3, (2014), 361-374. (https://doi.org/10.1260/2040-2295.5.3.361).
5. Ascione, F., Bianco, N., De Stasio, C., Mauro, G. and Vanoli, G., "Multi-stage and multi-objective optimization for energy retrofitting a developed hospital reference building: A new approach to assess cost-optimality", ***Applied Energy***, Vol. 174, (2016), 37-68. (https://doi.org/10.1016/j.apenergy.2016.04.078).
6. Paksoy, H., Andersson, O., Abaci, S., Evliya, H. and Turgut, B., "Heating and cooling of a hospital using solar energy coupled with seasonal thermal energy storage in an aquifer", ***Renewable Energy***, Vol. 19, No. 1-2, (2000), 117-122. (https://doi.org/10.1016/S0960-1481(99)00060-9).
7. Santika, W.G,. Urmee, T., Simsek, Y., Bahri, P.A. and Anisuzzaman, M., "An assessment of energy policy impacts on achieving Sustainable Development Goal 7 in Indonesia", ***Energy for Sustainable Development***, Vol. 59. (2020), 33-48. (https://doi.org/10.1016/j.esd.2020.08.011).
8. Tamir, K., Urmee, T. and Pryor, T., "Issues of small scale renewable energy systems installed in rural Soum centers in Mongolia", ***Energy for Sustainable Development***, Vol. 27. (2015), 1-9. (https://doi.org/10.1016/j.esd.2015.04.002).
9. Isa, N.M., Das, H.S., Tan, C.W., Yatim, A.H.M. and Lau, K.M., "A techno-economic assessment of a combined heat and power photovoltaic/fuel cell/battery energy system in Malaysia hospital", ***Energy***, Vol. 112, (2016). (https://doi.org/10.1016/j.energy.2016.06.056).
10. Biglia, A., Caredda, F.V., Fabrizio, E., Filippi, M. and Mandas, N., "Technical-economic feasibility of CHP systems in large hospitals

through the Energy Hub method: The case of Cagliari AOB", ***Energy Building***, Vol. 147, (2017), 101-112. (https://doi.org/10.1016/j.enbuild.2017.04.047).

11. Lagrange, A., de Simón-Martín, M., González-Martínez, A., Bracco, S. and Rosales-Asensio, E., "Sustainable microgrids with energy storage as a means to increase power resilience in critical facilities: An application to a hospital", ***International Journal of Electrical Power and Energy Systems***, Vol. 119, No. August (2019), (2020), 105865. (https://doi.org/10.1016/j.ijepes.2020.105865).
12. Dursun, S., Aykut, E. and Dursun, B., "Assessment of optimum renewable energy system for the Somalia–Turkish training and research hospital in Mogadishu", ***Journal or Renewable Energy and Environment (JREE)***, Vol. 8, No. 3, (2021), 54-67. (https://doi.org/10.30501/jree.2021.245232.1140).
13. Vaziri, S.M., Rezaee, B. and Monirian, M.A., "Utilizing renewable energy sources efficiently in hospitals using demand dispatch", ***Renewable Energy***, Vol. 151, (2020), 551-562. (https://doi.org/10.1016/j.renene.2019.11.053).
14. Franco, A, Shaker, M., Kalubi, D. and Hostettler, S., "A review of sustainable energy access and technologies for healthcare facilities in the Global South", ***Sustainable Energy Technologies and Assessments***, Vol. 22, (2017). (https://doi.org/10.1016/j.seta.2017.02.022).
15. Jahangir, M.H., Mousavi, S.A. and Vaziri Rad, M.A., "A techno-economic comparison of a photovoltaic/thermal organic Rankine cycle with several renewable hybrid systems for a residential area in Rayen, Iran", ***Energy Conversation and Management***, Vol. 195, (2019), 244-261. (https://doi.org/10.1016/j.enconman.2019.05.010).
16. EnergyPlus, "The board of US Department of Energy (DOE), October 1, (2013)", ***EnergyPlus Eng. Ref.***, (2016).
17. Rezaei, M., Boushehri, A. and Bagheri Moghaddam, N., "Factors affecting photovoltaic technology application in decentralized electricity", ***Journal or Renewable Energy and Environment (JREE)***, Vol. 5, No. 3, (2018), 27-41. (https://doi.org/10.30501/jree.2018.93451).
18. Firouzjah, K.G., "Assessment of small-scale solar PV systems in Iran: Regions priority, potentials, and financial feasibility", ***Renewable and Sustainable Energy Reviews***, Vol. 94. (2018), 267-274. (https://doi.org/10.1016/j.rser.2018.06.002).
19. "Shading Analysis", (2022). (https://www.pvresources.com/en/siteanalysis/shadinganalysis).
20. Kasaeian, A., Rahdan, P., Vaziri Rad, M.A. and Yan, W.M., "Optimal design and technical analysis of a grid-connected hybrid photovoltaic/diesel/biogas under different economic conditions: A case study", ***Energy Conversion and Management***, Vol. 198, (2019), 111810. (https://doi.org/10.1016/j.enconman.2019.111810).
21. Mousavi, S.A., Zarchi, R.A., Astaraei, F.R., Ghasempour, R. and Khaninezhad, F.M., "Decision-making between renewable energy configurations and grid extension to simultaneously supply electrical power and fresh water in remote villages for five different climate zones", ***Journal of Cleaner Production***, Vol. 279, (2021), 12361. (https://doi.org/10.1016/j.jclepro.2020.123617).
22. Hafez, O. and Bhattacharya, K.,"Optimal planning and design of a renewable energy-based supply system for microgrids", ***Renewable Energy***, Vol. 45, (2012), 7-15. (https://doi.org/10.1016/j.renene.2012.01.087).
23. Haghighat Mamaghani, A., Avella Escandon, S.A., Najafi, B., Shirazi, A. and Rinaldi, F., "Techno-economic feasibility of photovoltaic, wind, diesel and hybrid electrification systems for off-grid rural electrification in Colombia", ***Renewable Energy***, Vol. 97, (2016), 293-305. (https://doi.org/10.1016/j.renene.2016.05.086).

JREE: Vol. 9, No. 4, (Autumn 2022) 64-75

Journal of Renewable Energy and Environment

Journal Homepage: www.jree.ir

Materials and Energy Research Center

MERC

Research Article

Numerical Modeling and Evaluation of a Downwind Pre-Aligned Wind Turbine with an Innovative Blade Geometry Concept

Amir Hossein Zare [a,b], Esmail Mahmoodi [c*], Mohsen Boojari [a], Ali Sarreshtehdari [a]

[a] Department of Mechanical Engineering, Shahrood University of Technology, P. O. Box: 3619995161-316, Shahrood, Semnan, Iran.
[b] Fars Power Generation Management Company, Shiraz, Fars, Iran.
[c] Department of Mechanical Engineering of Biosystem, Shahrood University of Technology, P. O. Box: 3619995161-316, Shahrood, Semnan, Iran.

PAPER INFO

Paper history:
Received: 03 October 2021
Revised in revised form: 27 January 2022
Scientific Accepted: 27 February 2022
Published: 04 September 2022

Keywords:
Extreme-Scale Wind Turbines,
Pre-Aligned Rotor,
CFD Simulation,
Wake Simulation

ABSTRACT

Significant growth of the wind power market has led to a dramatic increase in the scale and capacity of wind turbines over the past decades. As these extreme-scale structures are expected to pose a wide range of challenges, an innovative concept which both lightens blade's mass and improves their aerodynamic performance, is vital for the future of rotor's design. In the present study, modeling and evaluating of an innovative pre-aligned rotor design based on SANDIA SNL100-00 wind turbine blade were accomplished. To evaluate the aerodynamic performance of the proposed rotor, CFD simulation was used as a well-developed technique in fluid mechanic. In the new rotor design, the swept area was increased using an equal blade length and the blade sections were more appropriately aligned with the wind flow compared to the reference model. This enhancement attained due to transferring the bending position from the root to a certain point alongside the length of blade. According to simulation assessments, this modification led to the overall improvement of main performance parameters in terms of the mean power and the applied torque on the blades. The simulation revealed that the novel concept is capable of increasing the mean power coefficient by 13.21 % compared to the conventional rotor designs. Analysis of the axial induction in front of the rotor plane displayed a greater drop in the flow velocity streaming up to the rotor, which could lead to have a more efficient configuration for harnessing the upcoming wind's power.

https://doi.org/10.30501/jree.2022.306692.1264

1. INTRODUCTION

Renewable energy systems have witnessed an increase in power generation capacity over the last years. Given that this growth is envisioned to continue, it is expected of future systems to have rated power in the range of 10-20 megawatt and a rotor diameter of 170 to 240 meters in order to decrease the Levelized Cost of Energy (LCOE) [1]. This means that modern wind turbines designed for offshore application would become the most gigantic rotary system on earth, with the length of one blade at least equal to the entire wing of a Boeing 747 [2]. To achieve these dimensions, several design factors in different fields including aerodynamics, structures, and active or passive control systems need to be simultaneously considered in the design process of large-scale turbines [3].

Various scientific research works including Fischer [4] have focused on this research area and explored different airfoil designs to reduce the overall loads on the blade. Studies by Sartori [5] and Griffith [6] have shown promising results through optimizing blades to provide a good starting point to design wind turbine blades. Deshmukh et al. [7] introduced an integrated approach to optimizing the wind turbine design by applying a co-design method; a design procedure that accounts directly for the synergistic coupling between physical and control system design. It was shown that employing a multidisciplinary strategy would result in the performance improvement of up to 8 % compared to conventional sequential design methods.

Wind turbines harness wind energy with the purpose of power generation which is scaled with V_{wind}^3 However, the fabrication, transportation, and assembly processes of extreme-scale turbines face wide-ranging obstacles. In particular, the most critical issue for conventional rotor configurations on large scales is the blade's mass. It is worth mentioning that the blade mass increases cubically or sub-cubically with its length [8]. For example, it is estimated that the mass per blade could exceed 75,000 kg for a 20 megawatt three-bladed turbine [9]. Hence, blade mass saving is essential to the designing and manufacturing of these wind turbines.

Various approaches have been applied with the aim of blade lightening. These methods could be classified into two groups.

*Corresponding Author's Email: esmail.mahmoodi@gmail.com (E. Mahmoodi)
URL: https://www.jree.ir/article_156017.html

Please cite this article as: Zare, A.H., Mahmoodi, E., Boojari, M. and Sarreshtehdari, A., "Numerical modeling and evaluation of a downwind pre-aligned wind turbine with an innovative blade geometry concept", ***Journal of Renewable Energy and Environment (JREE)***, Vol. 9, No. 4, (2022), 64-75. (https://doi.org/10.30501/jree.2022.306692.1264).

The first type of solution involves using advanced material and structure design. Carbon fiber material is utilized to replace a portion of the glass fiber-reinforced plastics due to the carbon fiber's high strength and low density [10, 11]. Nonetheless, the expensive cost of stronger materials has curbed their applicability.

The other practical methods are those that reduce the material demands by alleviating the aerodynamic loads exerted on turbine blades. This set of methods involves optimization of the blade plies, location, and thickness [12, 13], flexible pre-aligned rotor [14, 15], adaptable blade geometry [9, 16], and the morphing blade with the flap or smart structure [17-22].

In this regard, two novel concepts have been developed based on load-alignment for extreme-scale systems namely Segmented Ultralight Morphing Rotors (SUMR) [23] and Segmented Ultralight Pre-aligned Rotors (SUPAR) [24]. Both models introduce a load alignment strategy that orients the loads along the blade span-wise direction to significantly reduce the bending moments at the root. Upon taking full advantage of the load reduction in the SUMR concept, a number of challenges in developing extreme-scale wind turbines can potentially be addressed [25]. There are prominent research works that have been dedicated to investigating conceptual design, aerodynamics, and control system design of the SUMR wind turbines [26-28].

As an example, Noyes et al. [29] proposed a two-bladed downwind morphing rotor that was compared with a three-bladed conventional upwind rotor. The simulation results indicated that their SUMR rotor could bring about 27 % material saving and 8.56 % reduction in the blade lifetime damage in return for a 0.5 % decrease in the average generated power. Similarly, Ichter et al. [30] introduced a Morphing Downwind-Aligned Rotor (MDAR) in which the rotor had stiff elements in blades. Besides, to provide moment-free alignment in downwind conditions, they considered hub-joints in the rotor configuration. They observed that the morphing idea would increase the energy capture in low-speed conditions even though coning and reduction of blade number result in the reduction of rated power. Additionally, it was reported that the alignment of the centrifugal, gravitational, and thrust forces with the direction of the blade's path would reduce the cantilever loads.

In addition to the above research works, a deeper insight is provided herein by reviewing several studies to investigate the idea of load-alignment for rotors on extreme scales.

Loth et al. [9, 24] proposed a downwind rotor design with regard to the load-alignment concept. In their plan, since blades generally tolerate the exerted tensional force, they experience fewer bending moments than conventional types. Moreover, application of load-alignment to downwind turbines with larger tower clearance removed the rotor-tower clearance constraint, which allowed more flexible and lighter blades to be manufactured. Employing this concept for a two-bladed rotor resulted in a mass reduction of about 27 % based on a 13.2 MW reference rotor [26, 31]. Qin et al. [32] upscaled the load-aligned design from 13.2 MW to 25 MW with a downwind two-bladed configuration. Additionally, they employed a fully redesigned 25 MW model to demonstrate the capability of integrating morphing to harness even more wind energy while limiting the applied loads. In parallel, segmented blades and outboard pitching ideas were examined as a promising solution to overcome the increased edge-wise loads of load-alignment. Similarly, Yao et al. [33] attempted performing an aero-structural design study to achieve a 50 MW two-bladed wind turbine with a rotor diameter exceeding than 500 m. Their research involved initial study and investigations of structural design and performance of a baseline 250 m blade, along with implementing an optimization strategy to satisfy the need for a mass/cost-reduced rotor design. The optimization process, accomplished by investigating different airfoil thickness designs and chord designs, resulted in more than a 25 % mass reduction and saved over 30 % in overall cost.

Bortolotti et al. [34] compared 10 MW upwind and downwind three-bladed rotors, with and without active cone control. It was reported that although downwind rotors benefited from reduced cantilever loadings, no evident advantages were seen compared to upwind designs. To sum up, discussion of the downwind and load-alignment concepts continues and the switch to downwind designs demands further research.

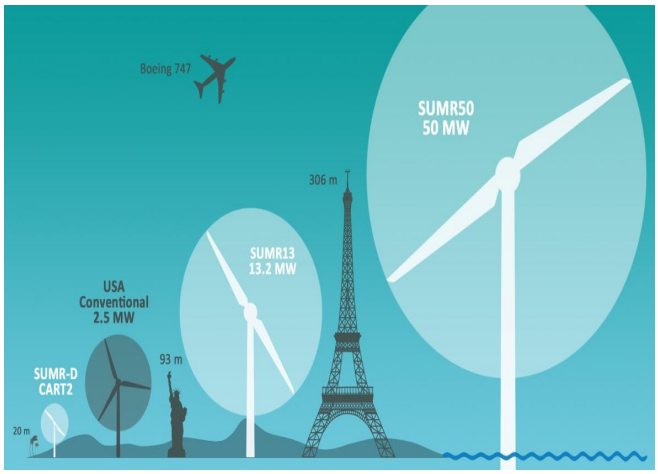

Figure 1. Schematic view of a 50 MW wind turbine and comparison of its size with a 13.2 MW two-bladed downwind turbine and conventional 2.5 MW three-bladed upwind turbine [33]

Taking advantage of previous studies concerning new concepts for large-scale rotors, a new downwind, pre-aligned rotor with a novel blade configuration referred to as "bent blade" has been proposed in this paper. Unlike prior pre-aligned rotor concepts, the proposed blades are not deformed or bent from a particular point in the span-wise direction; instead, they are slightly angled from the root toward the hub by inserting a special joint at the hub. The novelty of the current study lies in determining the location of the blade's bending point. In this research, the blade's bending point is designated somewhere between the cylindrical section and the very first airfoil profile. Moreover, a series of parameters in terms of power coefficient, thrust force, and applied torque on the blades are calculated and compared to conventional blade design in an attempt to evaluate the aerodynamic performance of the proposed concept.

The topics addressed in this paper include definition of load-alignment concepts in extreme-scale wind turbines in Section 2, highlighting the importance of this issue in the design process. Section 3 presents the simulation methodology that describes the fundamental equations, turbulence modeling, CAD design procedure, meshing strategy, and boundary conditions. Section 4 provides the corresponding CFD (computational fluid dynamics) results for the proposed rotor concept in terms of aerodynamic performance parameters. Section 5 presents the results and discussion.

2. LOAD ALIGNMENT AND FORCE DISTRIBUTION

The load alignment concept is inspired by nature, especially the flow adaptability of certain trees. For instance, the natural aero-elastic design of palm trees reduces aerodynamic loads while maintaining structural mass at its minimum. Under moderate wind conditions, the flexible configuration can bend downstream and alleviate destructive cantilever aerodynamic loads [35]. Similarly, since cantilever loads are extremely significant for large-scale wind turbines, the alignment allows a greater reduction of moments experienced by rotor blades.

There are two main methods to apply the load alignment concept: (a) to set a constant pre-cone angle to obtain load alignment in one specific condition (pre-aligned) and partial alignment in other conditions using aeroelastic deflection; (b) to make use of a hinge configuration that provides active full-load alignment by changing the coning angle as a function of wind speed. Since the pre-aligned technique reduces the need for an additional actuator, hinge, and controller, it is more straightforward for implementation. On the other hand, the active coning method can moderate the flap-wise bending moment for a wider range of wind speeds.

As mentioned before, this concept is capable of reducing rotor mass through disregard for the conventional stiffness constraint and alternatively, adjusting a downwind geometry to ensure alignment with the load path [9], as shown in Figure 2. Here, it is seen that the conventional blade loading leads to cantilever forces in the downstream direction. In contrast, the aligned concept employs a geometry that orients the loads in the span-wise direction so that the structural loads can be mainly exerted in the tension mode. The resulting load-path angles (β) slightly vary as a function of radius and azimuthal angle. By converting loads to tensile, this concept effectively reduces mass by minimizing cantilever-based shear loads [9].

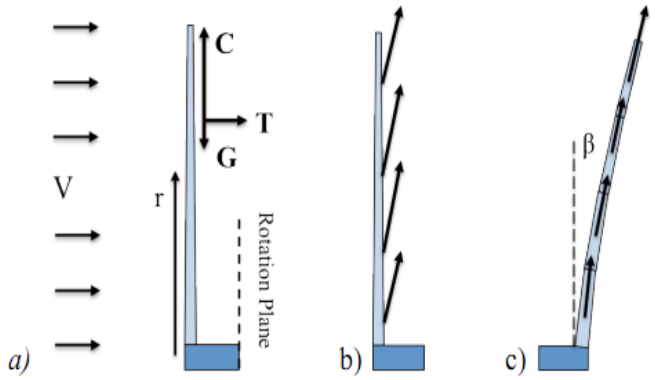

Figure 2. a) The non-torque forces on the blade of a wind turbine; b) net-force distribution in a conventional upwind blade; c) force distribution of a SUMR blade [32]

The spanwise load-path angle (β) can be quantified as a function of blade azimuthal angle (φ) using Equation (1) [1]:

$$\beta = \tan^{-1}\left(\frac{T}{C - G\cos\varphi}\right) \quad (1)$$

where T is the downstream aerodynamic thrust force, C the centrifugal force, and G the gravity force. The blade azimuthal angle (φ) is defined as 0 for a blade that is pointed vertically upwards and π for a blade that is pointed downwards. Of note, the load-path angles (β) for extreme-scale turbines are large, e.g., can be more than 20° for a 20 MW system [1]. As a system approaches extreme scales, not only downwind cantilever stresses but also gravity stresses get larger and more challenging for the conventional rotor design. However, both of these problems can be mitigated with the downstream curvature aligned with these forces, as shown in Figure 2(c).

In terms of aerodynamic force, the load alignment concept involves finding a balance between the downwind thrust force and the radial centrifugal force in an attempt to align the longitudinal axis with the net resultant force [36, 37]. The decomposition of forces acting on a turbine blade along with its resultant force for a downwind Coned rotor is shown in Figure 3. These forces include the gravity force (FG), the centrifugal force (FC), the downstream aerodynamic thrust force (FT), where all summed into resultant force (FR), and the in-plane aerodynamic torque-wise force (FQ). Note that the latter two forces result from the lift force (L) if drag (D) is neglected.

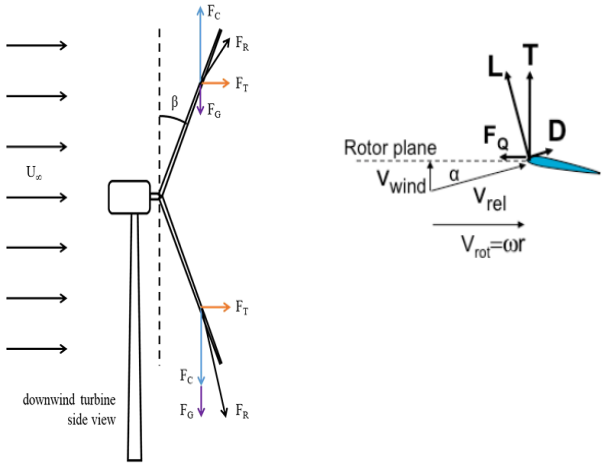

Figure 3. Forces and velocities for a horizontal wind turbine blade from a) side-view [29], b) chord-wise

The integrated transverse force, which is a function of coning angle, leads to root flap-wise bending moments. Load alignment decreases the flap-wise bending moments by setting the coning angle such that the contributions from the centrifugal and thrust loads are roughly eliminated. This can merely be achieved when coning is in the direction of the wind as in the case of a downwind rotor so that the centrifugal component is upwind and opposite to the downwind thrust component. While load alignment does not directly lower the lead-lag bending moments, the rotor mass reduction may cause lower gravity load and accordingly, lower lead-lag bending load [29].

3. SIMULATION METHODOLOGY

3.1. Governing equations

3.1.1. Incompressible Navier-Stokes equations

In the last decade, Wind Turbine Computational Fluid Dynamics (WTCFD) are substantially concentrated on solving Navier-Stokes equations in incompressible conditions. The freestream velocity passing wind turbines varies between 5 and 25 m/s, which is categorized as incompressible. Traces of compressibility could be seen at the blades' tips due to high-speed rotations. Mach number at the tip is lower than 0.25, which explains the possibility of neglecting compressibility.

Therefore, Navier-Stokes equations in incompressible conditions, as in Equations (2) and (3), are suitable for wind turbine modeling [38].

$$\nabla . u = 0 \tag{2}$$

$$\frac{\partial u}{\partial t} + (u.\nabla)u = -\frac{1}{\rho}\nabla p + \nu\nabla^2 u \tag{3}$$

where u is the velocity, ρ the density, p the pressure, t the time, and ν the kinematic viscosity.

3.1.2. Aerodynamic performance of wind turbines

3.1.2.1. Thrust coefficient

Thrust is the axial force that is applied by the wind to a rotor disk. While the power output of a wind turbine describes only the amount of power transferred into the electrical system, the thrust is related to all the losses of the kinetic energy of the flow, including the energy transformed into turbulent kinetic energy [39]. It must be considered that a lower thrust is beneficial, since less construction material would be needed to strengthen the supporting tower. Coefficient of thrust (C_T) is a non-dimensionalized parameter that represents the force on an actuator disc (turbine's rotor) caused by the pressure drop and it can be expressed using Equation (4) [40]:

$$C_T = \frac{T}{\frac{1}{2}\rho U_\infty^2 A_d} \tag{4}$$

where ρ is the air density, A_d the rotor cross-sectional area, and U_∞ the far upstream flow velocity.

3.1.2.2. Generated torque

Torque is a crucial parameter that affects different aspects of the performance of a wind turbine including the ability to overcome the resistive torque induced by friction [41]. According to Burton et al. [39], the total driving torque (Q) which a wind turbine rotor is capable of developing can be defined through Equation (5):

$$Q = \frac{1}{2}\rho U_\infty^2 \pi R^3 \lambda \left[\int_0^R \mu^2 \left[8á(1-a)\acute{\mu} - \frac{W}{U_\infty}\frac{B\frac{c}{R}}{\pi} C_d(1+á)\right] d_\mu\right] \tag{5}$$

Herein, λ represents tip speed ratio, a and á are axial and tangential flow induction factors, respectively, W relative wind velocity, B the number of blades, c the chord length, C_d the drag coefficient, and the parameter $\mu = {}^{r}/_{R}$.

3.1.2.3. Turbine power

The available power of the wind with speed U_∞ through a cross-sectional area A is defined as follows:

$$P = \frac{1}{2}\rho U_\infty^3 A \tag{6}$$

The shaft extracted power of a wind turbine can be represented by the following equation:

$$P = \frac{1}{2} C_p \rho U_\infty^3 A \tag{7}$$

where C_p is a dimensionless variable called power coefficient, which is calculated to deduce the aerodynamic efficiency of a wind turbine. According to Betz theory [42], the maximum theoretical value of C_p is 0.593, which is called Betz limit. Power coefficient depends on several parameters including the free stream velocity, the electrical and mechanical efficiencies of the generator, the drag force magnitude, and the viscosity on the blade's surface. In this study, the overall electrical and mechanical efficiencies of the generator and shaft are assumed to be 0.9, as stated by Loth et al. [9]. Considering the above equations, the coefficient of power can fairly be defined as [39]:

$$C_p = \frac{\text{Power Extracted}}{\text{Power Available}} = \frac{Q\Omega}{\frac{1}{2}\rho U_\infty^3 \pi R^2} \tag{8}$$

where Q denotes total driving torque on the rotor shaft, Ω rotational speed of rotor, and R blade radius.

3.1.3. Turbulence modeling

Over the years, various two-equation turbulence models have been introduced to study the flow field around wind turbines. In the present work, Menter's k-ω Shear-Stress Transport (SST) model [43] is employed. This turbulence model uses k-ω model [44] in the inner region of the boundary layer and switches to k-ε model [45] in the free shear flow to enhance the prediction of adverse pressure gradients. The change is smoothly controlled by the weight function of the coefficients on both models. The primary equations are written as follows [42]:

$$\frac{D\rho k}{Dt} = \tau_{ij}\frac{\partial u_i}{\partial x_j} - \beta^*\rho\omega k + \frac{\partial}{\partial x_j}\left[(\mu + \sigma_k\mu_t)\frac{\partial k}{\partial x_j}\right] \tag{9}$$

$$\frac{D\rho\omega}{Dt} = \frac{\gamma}{\nu_t}\tau_{ij}\frac{\partial u_i}{\partial x_j} - \dot{\beta}\rho\omega^2 + \frac{\partial}{\partial x_j}\left[(\mu + \sigma_\omega\mu_t)\frac{\partial \omega}{\partial x_j}\right] + 2\rho(1 - F_1)\sigma_{\omega 2}\frac{1}{\omega}\frac{\partial k}{\partial x_j}\frac{\partial \omega}{\partial x_j} \tag{10}$$

where k is turbulence kinetic energy, ω turbulent frequency, τ_{ij} turbulent Reynolds stress tensor, μ_t eddy viscosity, ν_t kinematic eddy viscosity, (γ, σ, β^*, $\dot{\beta}$) represent turbulence modeling constants, and F_1 denotes the blending function which is designed to be a value of one in the near-wall region and zero far from the wall.

3.2. Model setup

3.2.1. CAD design of a pre-aligned blade

Griffiths et al. [46] developed a methodology to design a blade with a 100-meter length, used in the SANDIA SNL100-00 wind turbine, to serve as a baseline for future researches. This blade was employed to model and simulate a pre-aligned rotor in a study by Loth et al. [1], which is the validation reference of the current study. The structural properties of SANDIA are given in Table 1.

3.2.2. CAD modeling of the coned blade (verification blade)

Re-simulation of one of the previous studies as the reference frame was required to validate the results of the current research. To this end, the 112.7 m length blade of a Downwind Pre-Aligned wind turbine (D2PAL) introduced by Loth et al. [1] was modeled in CATIA. The dimensions, as well as the coning angle of this blade, are presented in Figure 4.

Table 1. Blade geometry and properties of SANDIA SNL100-00

Section	Blade fraction	Chord (m)	Twist (deg)	Pitch axis (fraction)	Distance from pitch axis (m)	Transition	Airfoil description
1	0	5.694	13.308	0.5	0	0	Cylinder
2	0.005	5.694	13.308	0.5	0	0	Cylinder
3	0.007	5.694	13.308	0.5	0	99.25	Trans 99.25 %
4	0.009	5.694	13.308	0.5	0	98.5	Trans 98.5 %
5	0.011	5.694	13.308	0.5	0	97.75	Trans 97.75 %
6	0.013	5.64	13.308	0.5	0	97	Ellipse 97 %
7	0.024	5.792	13.308	0.499	0.0058	93.1	Ellipse 93.1 %
8	0.026	5.811	13.308	0.498	0.0116	92.5	Ellipse 92.5 %
9	0.047	6.058	13.308	0.483	0.103	84	Trans 84 %
10	0.068	6.304	13.308	0.468	0.2017	76	Trans 76 %
11	0.089	6.551	13.308	0.453	0.3079	68	Trans 68 %
12	0.114	6.835	13.308	0.435	0.4443	60	Trans 60 %
13	0.146	7.215	13.308	0.41	0.6494	51	Trans 51 %
14	0.163	7.407	13.177	0.4	0.7407	47	Trans 47 %
15	0.179	7.552	13.046	0.39	0.8307	43.5	Trans 43.5 %
16	0.195	7.628	12.915	0.38	0.9154	0	Du99-w-405
17	0.222	7.585	12.133	0.378	0.9254	38	Du99-w-405 (38 %)
18	0.249	7.488	11.35	0.377	0.921	36	Du99-w-350 (36 %)
19	0.276	7.347	10.568	0.375	0.9184	34	Du99-w-350 (34 %)
20	0.358	6.923	9.166	0.375	0.8654	0	Du97-w-300
21	0.439	6.942	7.688	0.375	0.8678	26	Du91-w2-250 (26 %)
22	0.52	5.915	6.18	0.375	0.7394	23	Du93-w-210 (23 %)
23	0.602	5.417	4.743	0.375	0.6771	0	Du93-w-210
24	0.667	5.019	3.633	0.375	0.6274	19	Naca-64-618 (19 %)
25	0.683	4.92	3.383	0.375	0.615	18.5	Naca-64-618 (18.5 %)
26	0.732	4.621	2.735	0.375	0.5776	0	Naca-64-618
27	0.764	4.422	2.348	0.375	0.5528	0	Naca-64-618
28	0.846	3.925	1.38	0.375	0.4906	0	Naca -64-618
29	0.894	3.619	0.799	0.375	0.4524	0	Naca -64-618
30	0.943	2.824	0.28	0.375	0.353	0	Naca -64-618
31	0.957	2.375	0.21	0.375	0.2969	0	Naca -64-618
32	0.972	1.836	0.14	0.375	0.2295	0	Naca -64-618
33	0.986	1.208	0.07	0.375	0.151	0	Naca -64-618
34	1	0.1	0	0.375	0.0125	0	Naca -64-618

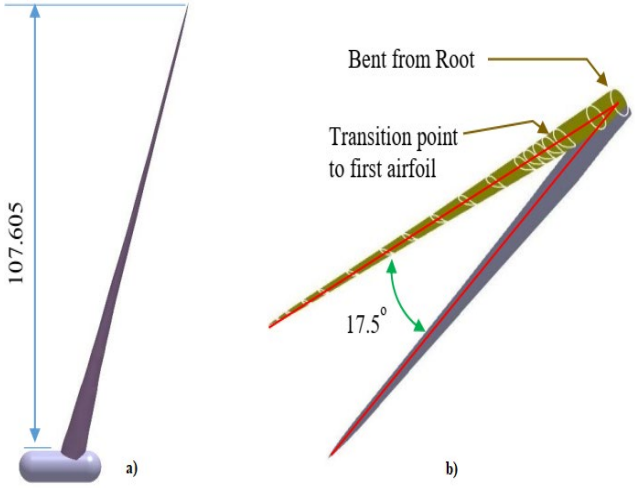

Figure 4. Geometry and dimensions of D2PAL blade: a) side view and b) isometric view

3.2.3. Modeling the bent blade in CATIA

The proposed blade in the present study is of the same length and airfoil sections as the verification blade, but the distinctive difference is contemplated in the bending location. While the D2PAL blade is angled from the hub root, the bent blade has a 17.5° bend in the transition area between the cylindrical section and the elliptic airfoil. The final designed model is shown in Figure 5.

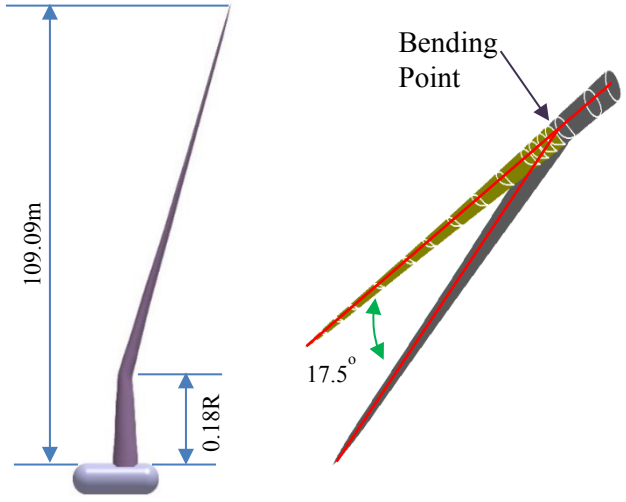

Figure 5. Geometry and dimensions of the proposed blade designed in CATIA

3.2.4 Computational setup

The computational domain and subsequently, the associate mesh are divided into two sections thanks to the solution domain's symmetric geometry. Thus, the flow analysis was performed only in one of the halves. The most prominent step in pre-processing is the generation of grids. It is crucial to employ accurate grids in the solver to acquire precise results.

In the present simulation, an unstructured triangular mesh of average orthogonal quality of 0.90 and a total number of 20 million cells and 4,340,843 nodes was applied to the geometry. To ensure that the blade surface is pinpointed within the viscous sublayer, the very first elements should be close enough to the wall so as to yield y pluses ideally close to 1. Therefore, 20 inflation layers with a growth rate of 1.2 were applied to the blade surface. It must be noted that the first elements next to the blade surface have a thickness of only 2.7 × 10−5 meters. Figure 6 illustrates the applied mesh on the two more challenging regions of the blade geometry.

y+ indicates the dimensionless distance from the wall measured in terms of viscous length on the boundary layer. y+ can be calculated using Equation (11) in which y is the distance from the wall, u_t the friction velocity, and ν the kinematic viscosity.

$$y^+ = \frac{yu_t}{\nu} \quad (11)$$

According to Figure 7, y+ values lie within 0 to 5 in the generated mesh in all three directions. This is enough to fulfill the near-wall requirement, which states that y+ should be kept under 5 for the SST k-ω model [47].

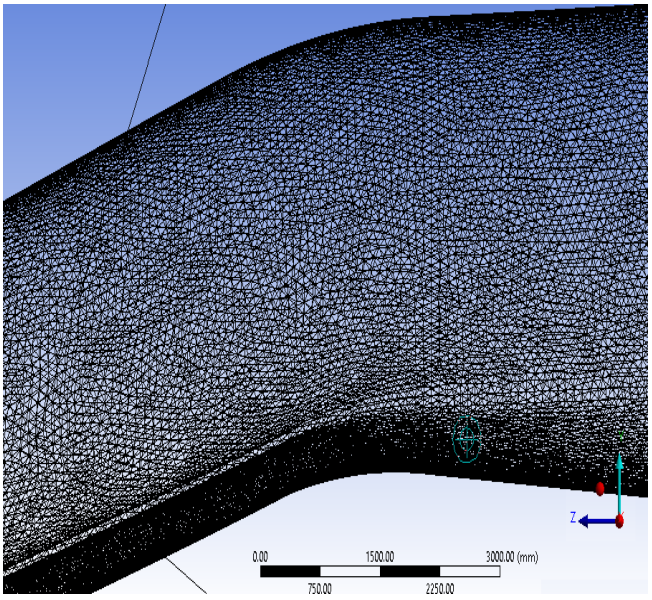

(a)

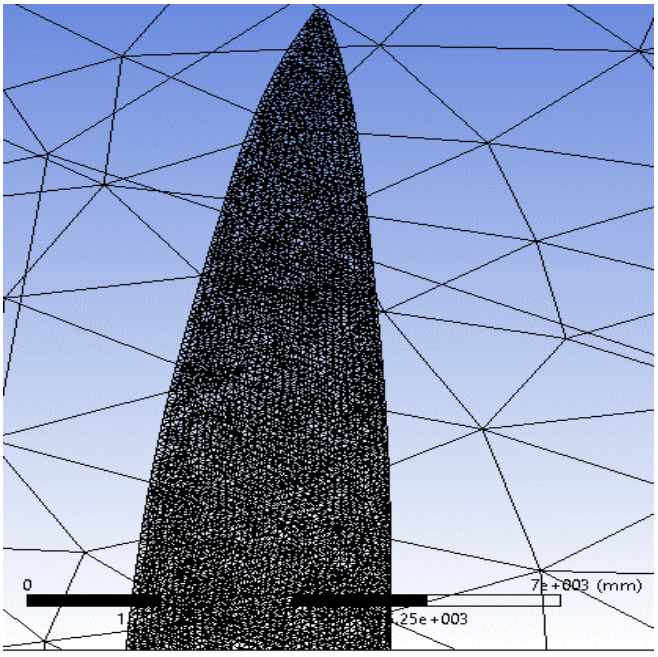

(b)

Figure 6. Applied unstructured triangular mesh on the blade geometry at a) bending point and b) blade tip

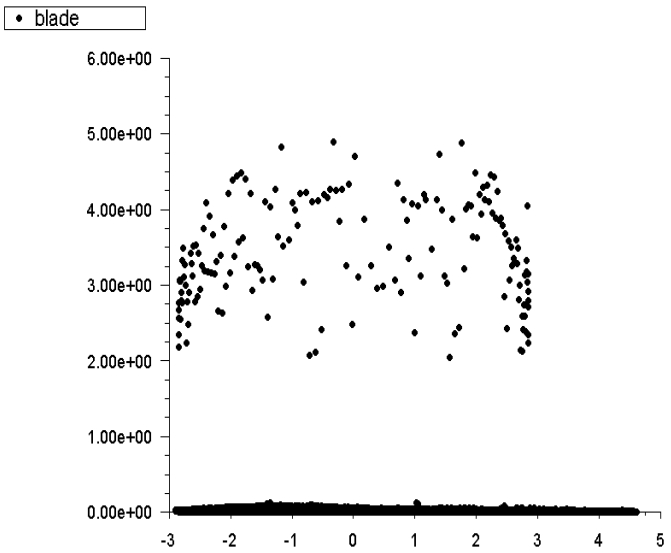

Figure 7. y^+ values of the designed blade in the chord-wise direction

Once the 3D model of the turbine's rotor and the solution domain are created, their corresponding Boundary Conditions (BC) must be defined. The boundary conditions must be accurately specified to secure a reliable simulation. The solution domain and applied boundary conditions are illustrated in Figure 8.

According to Figure 8, the velocity-inlet condition is assigned to face A. With reference to the study of Loth et al. [1], the input velocity for the turbine in the rated conditions is decided to be 14.125 m/s. Further simulations are also conducted at different freestream velocities ranging between 7-24 m/s, equivalent to the tip speed ratio (λ) of 4-15 in which λ is defined through Equation (12). The pressure outlet condition was selected for face C.

A: Velocity inlet
B: Symmetry
C: Pressure outlet
D: Periodic
E: Periodic
F: Body-sizing
G: Blade

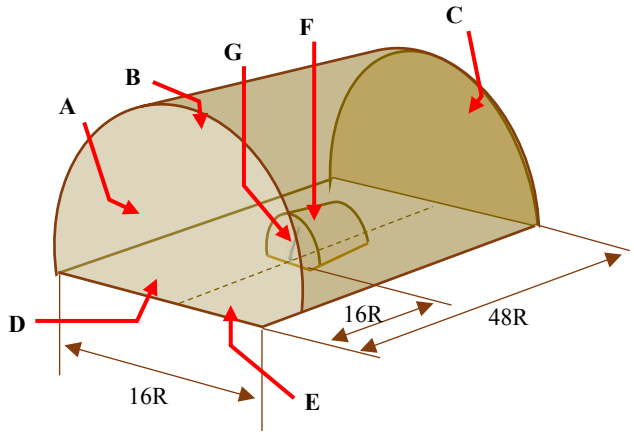

Figure 8. Dimensions and Boundary conditions of the computational domain (R is blade radius)

This is because this boundary condition is applied only to the flow exits, where the flow velocity and/or the pressure details are unknown. The no-slip or the wall condition set for face G is employed to capture solid and fluid regions, which are the surfaces of the blade and the surrounding air. The symmetry boundary condition was selected for face B because its corresponding physical geometry was somehow mirrored in symmetry. As in the current study, the tower effect is neglected and the geometry of each blade is identical. The physical geometry and the flow pattern seem to have a periodically repeating cycle. Therefore, the periodic boundary condition is attributed to the faces D and E. All the interior surfaces including face F that are not part of the rigid geometry and are only designated to refine the grid mesh around the blades are set as interior boundary conditions.

$$\lambda = \frac{R\Omega}{V} \tag{12}$$

where Ω is the angular speed of the rotor, R the blade radius, and V the incident free-stream airflow speed.

4. RESULTS AND DISCUSSION

To assess the performance of the proposed blade by this research, as the first step, the blade geometry used in the study of Loth et al. [1], named D2PAL, was modeled in a CAD software named CATIA, which would be considered as the reference model for further comparisons. Then, by considering identical conditions of Loth et al. [1], CFD simulation of flow around this CAD modeled blade was carried out. Finally, to attempt to implement data validation, several parameters including the turbine's power coefficient (Cp), thrust force, and the applied torque on blades were extracted and compared with the actual D2PAL [1].

4.1. Validation of the reference model

4.1.1. Evaluation of the developed torque

Figure 9 shows the generated torque at different wind speeds for the original D2PAL and its CAD modeled blade. As shown in the graph, the highest error occurs at a wind speed of 20 m/s and is reported to be 7-8 %, while the lowest deviation is reported in the rated condition of 14.125 m/s, with only 1.39 % error. Also, the mean error percentage is found to be almost 4.

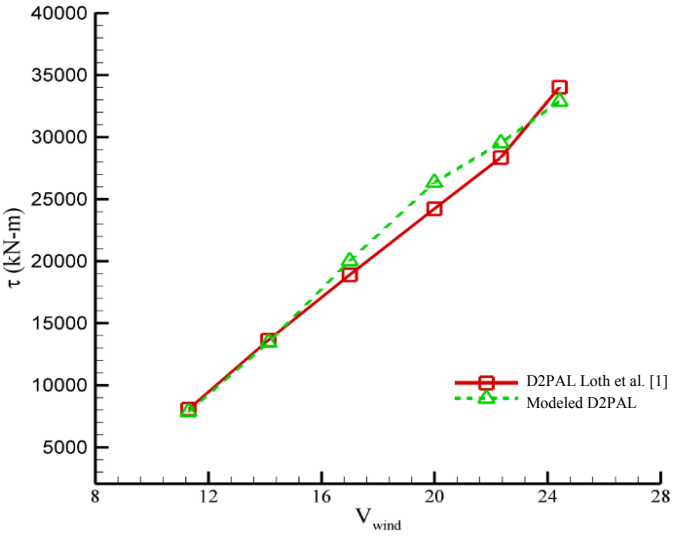

Figure 9. Developed torque as a function of wind speed

4.1.2. Evaluation of power coefficient

Evaluation of power coefficient (Cp) for the actual D2PAL and the CAD modeled blade is presented in Figure 10. With respect to the graph, generally, it can be pointed out that the

results from the modeled blade are in good agreement with the simulation results of the study established by Loth et al. [1].

In addition, Table 2 provides data regarding the deviance percentage of the calculated power coefficient for the actual D2PAL [1] and its CAD modeled rotor at the tip speed ratio of 11. According to Table 2, the lowest and highest deviations are observed at $\lambda = 14$ and 5, respectively, where computed results via FLUENT were overestimated about 0.29 % for the former and 8.78 % for the latter, compared to the experimental values. In addition, the average deviation percentage was reported to be almost 3.0 %.

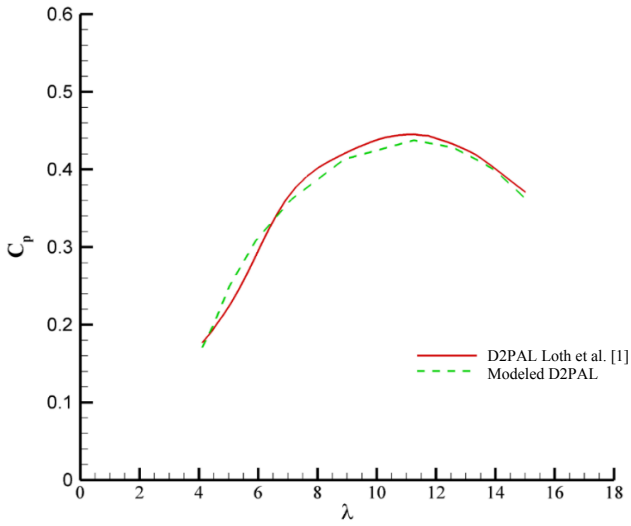

Figure 10. Power coefficient at different tip speed ratios

Table 2. Deviation percentage of calculated power coefficient at different tip speed ratios

Deviation	C_p presented by Loth et al. [1]	Calculated C_p with Fluent	(λ)
3.37 %	0.176	0.171	4.12
4.16 %	0.192	0.20	4.5
8.78 %	0.23	0.25	5
5.99 %	0.29	0.308	5.9
1.4 %	0.366	0.361	7.1
2.4 %	0.423	0.412	8.9
1.73 %	0.445	0.437	11.25
1.52 %	0.434	0.428	12.57
1.13 %	0.414	0.409	13.51
0.29 %	0.399	0.398	14
2.27 %	0.37	0.362	15

Acknowledging the precision of the above results, modeling and CFD simulations of the proposed concept, which is a bent blade with a coning angle of 17.5°, could be safely and consistently proceeded further along.

4.2. Simulation results of the proposed model

4.2.1. Assessment of performance parameters

4.2.1.1. Thrust force

A comparison between the total thrust force as a function of wind speed for the D2PAL and the bent blade is shown in Figure 11. This figure indicates that the thrust force in the D2PAL rotor is always lower than that in the bent blade for all wind speeds.

4.2.1.2. Thrust coefficient

The diagram in Figure 12 illustrates the thrust coefficient (C_T) as a function of the wind velocity for both the D2PAL and the bent blade. With a glimpse into the graph, it is worth mentioning that although the thrust coefficient has a direct linear relationship with the thrust force, changes in flow velocity have a stronger effect. This is because the thrust force has an inverse relationship with the square of the free stream velocity. Therefore, the thrust coefficient declines as the free stream speed increases.

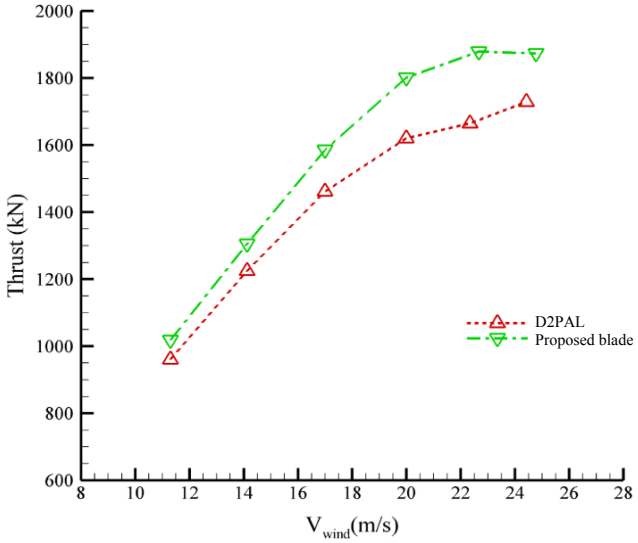

Figure 11. Total thrust force as a function of wind speed for the modeled D2PAL and the proposed blade

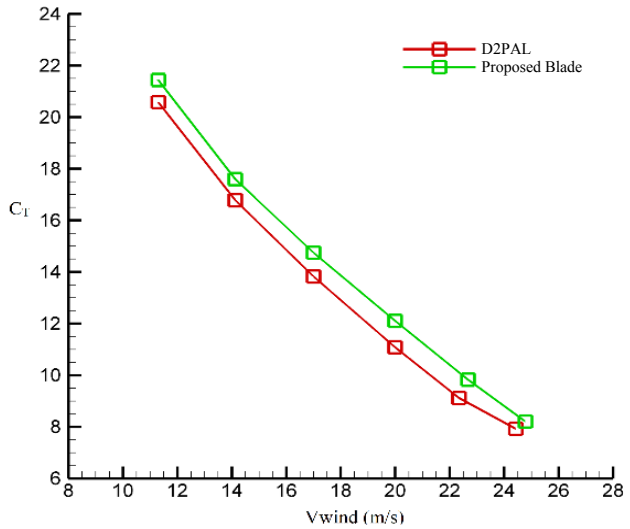

Figure 12. Thrust coefficient as a function of wind speed for the modeled D2PAL and the proposed blade

4.2.1.3. Rotor's torque

The torque developed by the proposed rotor concept as a function of wind speed is shown in Figure 13. As in the figure, as the wind speed increases, the torque exerted on the rotor also increases; however, the striking point here is that the greatest generated torque belongs to the bent blade, which in

turn can result in a higher power coefficient. The position and the magnitude of the coned angle in the bent blade geometry, which provided a longer moment arm than that of the D2PAL blade, is one of the main contributors to this increase.

4.2.1.4. Power coefficient

Figure 14 displays the results of the captured power coefficients for both of the proposed blade and the modeled D2PAL along with the D2PAL data set given by Loth et al. [1]. According to the graph in Figure 14, the proposed blade presented in this study has considerably enhanced the power coefficient compared to the D2PAL blade. The simulation results have exhibited increase rates of 13.21 % and 12.79 % in the mean power coefficient of the bent blade compared to the actual D2PAL and its modeled blade, respectively. The growth of the bent blade's swept area due to its unique bending point is responsible for this increase. Another contributing factor could be the enhancement of the airfoils' alignment with the wind flow, compared to the D2PAL blade.

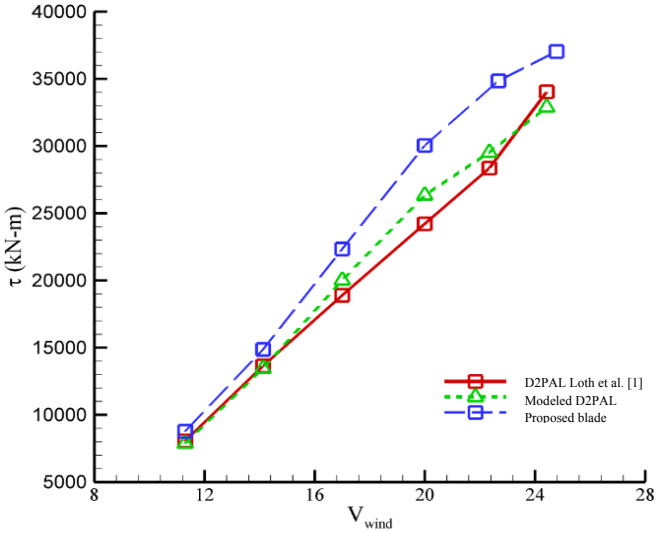

Figure 13. Developed torque as a function of wind speed for both D2PALs and the proposed blade

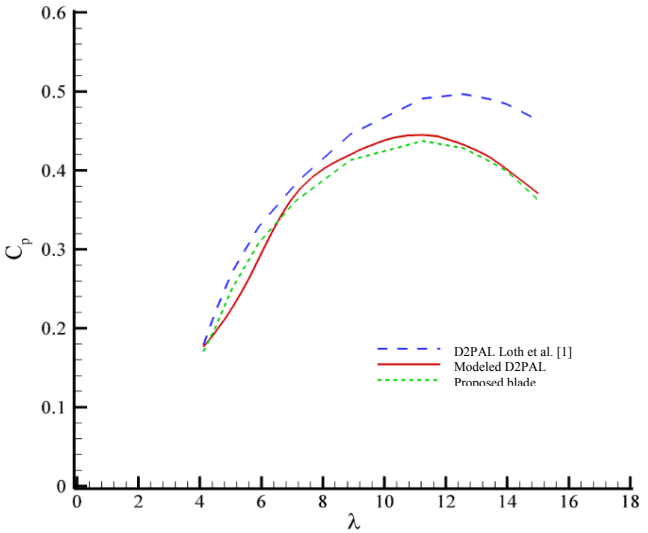

Figure 14. Power coefficient for both D2PALs and the proposed blade concept

4.2.2. Simulation of the flow field around blades

4.2.2.1. Flow velocity pattern

The flow velocity behind the two-bladed configurations is shown in Figure 15. The simulation results revealed that the decline in the flow velocity behind the proposed bent blade is, to some extent, greater than that of the coned blade. This means that the bent wind turbine is more capable of harnessing the kinetic energy of the wind based on Betz's law, which in turn results in a higher power coefficient.

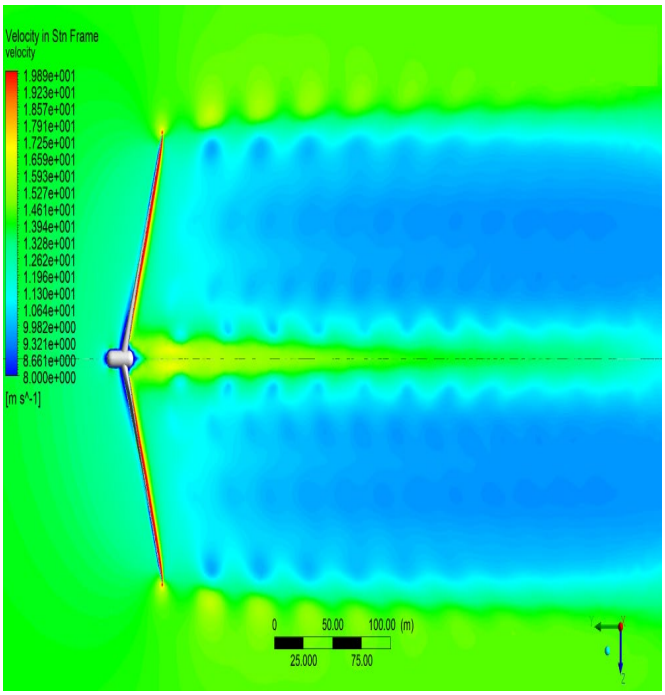

(a)

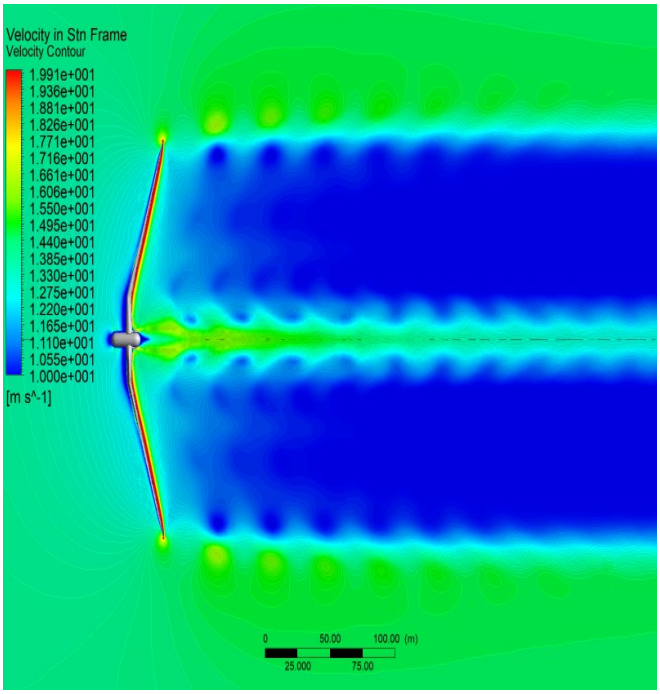

(b)

Figure 15. Comparison of flow velocity around the rotor in the rated condition (14/125 m/s) for a) the modeled D2PAL blade and b) the proposed blade

Figure 16 represents the tangential velocity vectors for both the coned and bent blades. The greatest velocity magnitude occurs at the blade's tip, while the lowest occurs at its root.

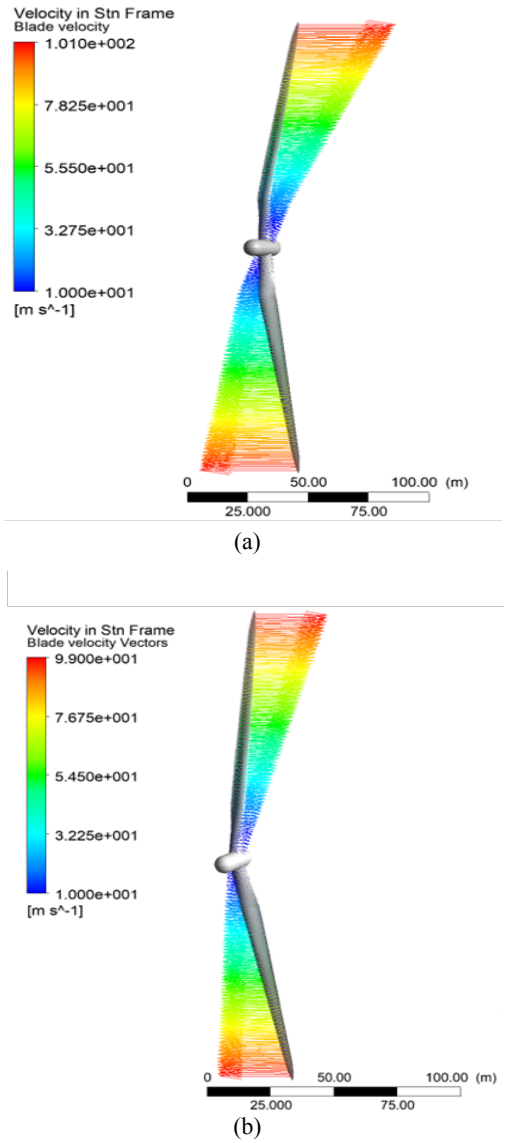

Figure 16. Comparison of tangential velocity vectors for a) the proposed blade and b) the modeled D2PAL blade

4.2.2.2. Streamlines and wake simulation

This section discusses the wake simulation results and the flow streamlines of the two different rotor configurations in rated conditions (14.125 m/s) and the rotational speed of 8.93 rpm for the rotor. In the case of wind turbines, flow streamlines twist after they collide with blades and hub. An illustration of this phenomenon for both coned and bent rotors is given in Figure 17. According to this figure, the swirling streamlines not only are formed earlier around the bent blade but also are more intense, closely tight, and tangled together. The main reason for this distinction might be the difference in the bending point of the two blades' configurations.

A comparison of the generated downstream vortices and the wakes behind the two coned and bent rotors is made, as given in Figure 18. Wake simulation results have shown that the wakes behind the bent rotor are formed closer to the rotation plane for identical free-stream velocity and rotational speed. This phenomenon is ascribed to different geometries of the two blades. As shown in Figure 18, the initial wakes form right at the tip of the blade. On the other hand, the blade tip in the proposed rotor is positioned closer to the rotation plane because the bending point in the bent blade is designed at the end of its cylindrical cross-section, while the conventional pre-aligned configuration starts right from the hub. This structure delays the formation of wakes and vortices behind the turbine.

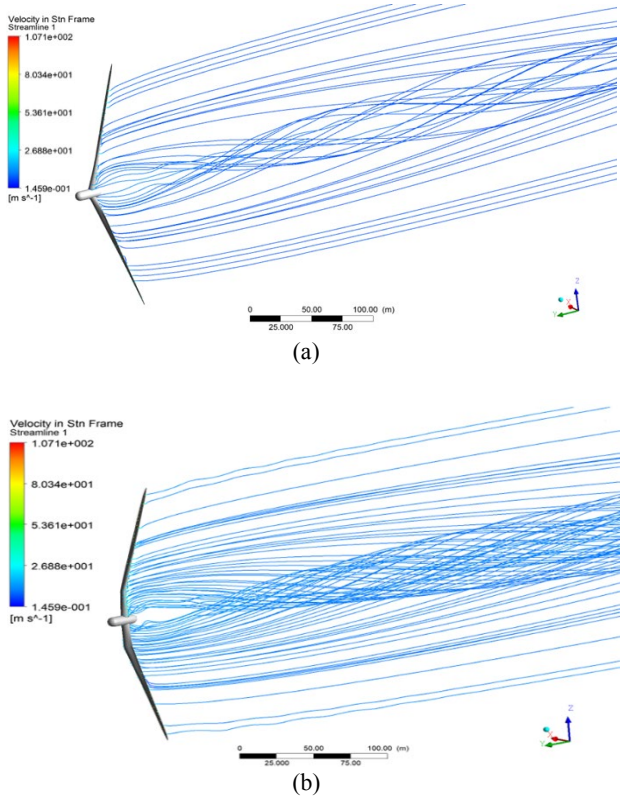

Figure 17. Comparison of streamlines behind the rotor in a) the D2PAL and b) proposed blade concept

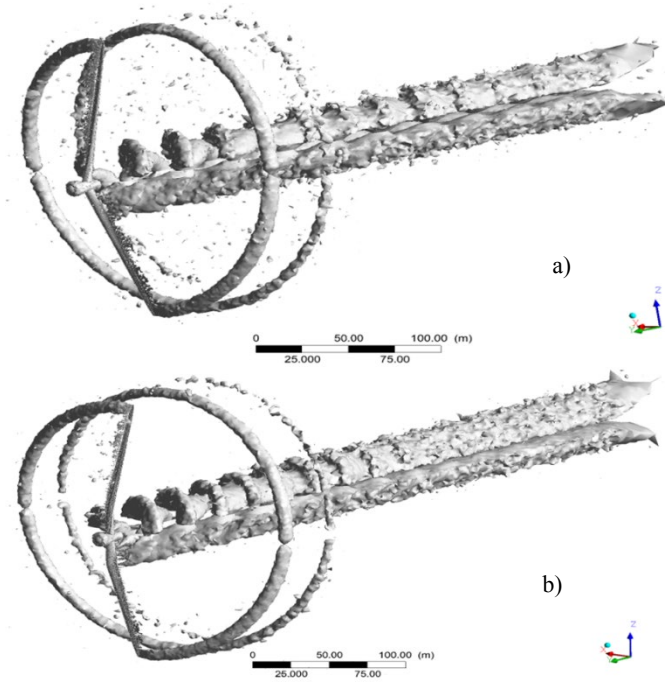

Figure 18. Isometric view of the generated wake behind the rotor at rated condition for a) Rotor with the modeled D2PAL blade, b) Rotor with the proposed blade

5. CONCLUSIONS

In this study, modeling and CFD simulation of two downwind pre-aligned turbines with different blade concepts were conducted. The first concept used as a reference model for data validation was a coned blade with a fixed downwind conceptual angled from the blade root, while the second design was a blade bent lengthwise concept proposed in this study. The latter had a coning angle of 17.5° at a particular point in the transition area between the cylindrical section and the blade's first airfoil. Both of the rotors were compared in terms of several performance parameters including power coefficient, thrust force, and applied torque on the blades.

Increased swept area led to a considerable improvement in the mean power coefficient. It was also found that the thrust force of the proposed bent blade was greater than that of the coned blade under all wind speeds. The simulation results revealed that the mean produced power by the bent rotor increased by 13.21 % compared to the reference coned rotor designs. Analyzing the induction area in front of the rotor plane displayed a greater drop in the flow velocity streaming to the bent rotor, which in turn could lead to a more efficient energy conversion for harnessing the wind power based on Betz's law. The wake simulation captured a delay in the formation of vortices behind the turbine with a coned blade, which is due to its geometrical structure.

The lengthwise bent blade rotor enjoys a higher capability to harvest wind energy at low upstream wind speeds, as the root portion of straight wind turbine blades has the main role in wind turbine power production at lower wind speeds because of the twist arrangement design.

6. ACKNOWLEDGEMENT

I would like to express my special thanks of gratitude to Shahrood University of Technology, Department of Mechanical Engineering, which supported us with high speed computers in our research process.

NOMENCLATURE

a	Axial induction factor
a'	Tangential induction factor
A , A_d	Rotor disk area
B	Number of blades
c	Chord
C , F_C	Centrifugal force
C_d	Drag coefficient
C_P	Power coefficient
C_T	Thrust coefficient
D	Drag force
F_1	Blending function
F_Q	Torque-wise force
F_R	Resultant force
G , F_G	Gravitational force
k	Turbulent kinetic energy
L	Lift force
M	Mach number
p	Pressure
P	Power
Q	Torque
R	Blade radius
t	Time
T , F_T	Thrust force
u	Flow velocity
V , U_∞	Wind speed
W	Relative wind velocity
Greek letters	
ν	Kinematic viscosity
ν_t	Kinematic eddy viscosity
μ_t	Eddy viscosity
β	Load-path angle
φ	Blade azimuthal angle
λ	Tip-speed ratio
ρ	Density
τ	Torque moment
ω	Turbulent frequency
τ_{ij}	Turbulent Reynolds stress tensor
$\dot{\beta}$	Turbulence modeling constant
β^*	Turbulence modeling constant
σ	Turbulence modeling constant
γ	Turbulence modeling constant
Ω	Angular speed of rotor
Subscripts	
3D	Three dimensional
BC	Boundary condition
BEM	Blade element momentum theory
CAD	Computer-aided design
CFD	Computational Fluid Dynamics
D2PAL	Downwind 2-Bladed Pre-Aligned Lengthened
DPAR	Downwind Pre-Aligned Rotor
LCOE	Levelized Cost of Energy
MDAR	Morphing Downwind-Aligned Rotor
SST	Shear Stress Transport
SUMR	Segmented Ultralight Morphing Rotors
SUPAR	Segmented Ultralight Pre-Aligned Rotors
WTCFD	Wind Turbine Computational Fluid Dynamics

REFERENCES

1. Loth, E., Steele, A., Qin, C., Ichter, B., Selig, M.S. and Moriarty, P., "Downwind pre-aligned rotors for extreme-scale wind turbines", ***Wind Energy***, Vol. 20, No. 7, (2017), 1241-1259. (https://doi.org/10.1002/we.2092).
2. Wingerden, J.V., Hulskamp, A., Barlas, T.K., Marrant, B., Kuik, G.V., Molenaar, D.P. and Verhaegen, M., "On the proof of concept of a smart wind turbine rotor blade for load alleviation", ***Wind Energy***, Vol. 11, (2008), 265-280. (https://doi.org/10.1002/we.264).
3. Chetan, M., Sakib, M.S., Griffith, D.T. and Yao, S., "Aero-structural design study of extreme-scale segmented ultralight morphing rotor blades", ***Proceedings of AIAA AVIATION 2019 Forum***, Dallas, Texas, (2019). (https://doi.org/10.2514/6.2019-3347).
4. Fischer, G.R., Kipouros, T. and Savill, A.M., "Multi-objective optimisation of horizontal axis wind turbine structure and energy production using aerofoil and blade properties as design variables", ***Renewable Energy***, Vol. 62, (2014), 506-515. (https://doi.org/10.1016/j.renene.2013.08.009).
5. Sartori, L., Bellini, F., Croce, A. and Bottasso, C., "Preliminary design and optimization of a 20 MW reference wind turbine", ***Journal of Physics: Conference Series***, Vol. 1037, (2018). (https://doi.org/10.1088/1742-6596/1037/4/042003).
6. Griffith, D.T. and Richards, P.W., "The SNL100-03 blade: Design studies with flatback airfoils for the Sandia 100-meter blade", Sandia National Labs, Technical report SAND2014-18129, (2014). (http://energy.sandia.gov/wp-content/gallery/uploads/dlm_uploads/1418129.pdf).
7. Deshmukh, A.P. and Allison, J.T., "Multidisciplinary dynamic optimization of horizontal axis wind turbine design", ***Structural and Multidisciplinary Optimization***, Vol. 53, (2016), 15-27. (https://doi.org/10.1007/s00158-015-1308-y).
8. Fingersh, L.J., Hand, M.M. and Laxson, A.S., "Wind turbine design cost and scaling model", National Renewable Energy Lab (NREL), Golden, Colorado, USA, (2006). (https://doi.org/10.2172/897434).
9. Loth, E., Steele, A., Ichter, B., Selig, M. and Moriarty, P., "Segmented ultralight pre-aligned rotor for extreme-scale wind turbines", ***Proceedings of AIAA Aerospace Sciences Meeting***, Nashville, Tennessee, USA, (2012). (https://doi.org/10.2514/6.2012-1290).
10. Thomsen, O.T., "Sandwich materials for wind turbine blades - Present and future", ***Journal of Sandwich Structures & Materials***, Vol. 11, (2009), 7-24. (http://dx.doi.org/10.1177/1099636208099710).
11. Thirumalai, R. and Prabhakaran, D., "Future materials for wind turbine blades - A critical review", ***Proceedings of International Conference on Wind Energy: Materials, Engineering and Policies***, Hyderabad, India, (2012).

(https://www.inderscienceonline.com/doi/abs/10.1504/IJMATEI.2014.060339).

12. Konga, C., Banga, J. and Sugiyamab, Y., "Structural investigation of composite wind turbine blade considering various load cases and fatigue life", ***Energy***, Vol. 30, (2005), 2101-2114. (http://dx.doi.org/10.1016/j.energy.2004.08.016).
13. Liao, C.C., Zhao, X.L. and Xu, J.Z., "Blade layers optimization of wind turbines using FAST and improved PISO algorithm", ***Renewable Energy***, Vol. 42, (2012), 227-233. (http://dx.doi.org/10.1016/j.renene.2011.08.011).
14. Rasmussen, F., Petersen, J.T., Vølund, P., Leconte, P., Szechenyi, E. and Westergaard, C., "Soft rotor design for flexible turbines- Final report", (1998), 1-19. (https://cordis.europa.eu/docs/projects/files/JOR/JOR3950062/47698171-6_en.pdf).
15. Tong, W., Wind power generation and wind turbine design, WIT Press, (2010). (https://www.witpress.com/books/978-1-84564-205-1).
16. Loth, E., Selig, M. and Moriarty, P., "Morphing segmented wind turbine concept", ***Proceedings of 28th AIAA Applied Aerodynamics Conference***, Chicago, Illinois, USA, (2010). (https://doi.org/10.2514/6.2010-4400).
17. Daynes, S. and Weaver, P.M., "Design and testing of a deformable wind turbine blade control surface", ***Smart Materials and Structures***, Vol. 21, No. 10, (2012). (https://doi.org/10.1088/0964-1726/21/10/105019).
18. Neal, D.A., Good, M.G. and Johnston, C.O., "Design and wind-tunnel analysis of a fully adaptive aircraft configuration", ***Proceedings of 45th AIAA/ASME/ASCE/AHS/ASC Structures, Structural Dynamics & Materials Conference***, Palm Springs, California, USA, (2004). (https://doi.org/10.2514/6.2004-1727).
19. Buhl, T., Bak, D.C., Gaunaa, M. and Andersen, P.B., "Load alleviation through adaptive trailing edge control surfaces: Adapwing overview", ***Proceedings of European Wind Energy Conference and Exhibition***, Milan, Italy, (2007). (https://www.semanticscholar.org/paper/Load-alleviation-through-adaptive-trailing-edge-Buhl-Bak/a8af7c1327cbac0796888a3aeca3d48de7dc2cf6).
20. Lachenal, X., Daynes, S. and Weaver, P.M., "Review of morphing concepts and materials for wind turbine blade applications", ***Wind Energy***, Vol. 16, (2013), 283-307. (https://doi.org/10.1002/we.531).
21. Wang, W., Caro, S.E. and Bennis, F., "Optimal design of a simplified morphing blade for fixed-speed horizontal axis wind turbines", ***Proceedings of the ASME 2012 International Design Engineering Technical Conferences & Computers and Information in Engineering Conference***, Chicago, Illinois, USA, (2012), 233-242. (https://doi.org/10.1115/DETC2012-70225).
22. Lackner, M.A. and Kuik, G.V., "A comparison of smart rotor control approaches using trailing edge flaps and individual pitch control", ***Wind Energy***, Vol. 13, (2010), 117-134. (https://doi.org/10.1002/we.353).
23. Griffith, D.T., "Structural design of the SUMR-13 wind turbine blade-Technical report M2.5.9", Advanced Research Projects Agency - Energy, (2017). (https://arpa-e.energy.gov/technologies/projects/ultra-large-wind-turbine).
24. Steele, A., Ichter, B., Qin, C., Loth, E., Selig, M. and Moriarty, P., "Aerodynamics of an ultralight load-aligned rotor for extreme-scale wind turbines", ***Proceedings of 51st AIAA Aerospace Sciences Meeting Including the New Horizons Forum and Aerospace Exposition***, Grapevine, Texas, USA, (2013). (https://doi.org/10.2514/6.2013-914).
25. Yao, S., Chetan, M. and Griffith, D.T., "Structural design and optimization of a series of 13.2 MW downwind rotors", ***Wind Engineering***, Vol. 45, No. 6, (2021), 1459-1478. (https://doi.org/10.1177/0309524X20984164).
26. Ananda, G.K., Bansal, S. and Selig, M.S., "Aerodynamic design of the 13.2 MW SUMR-13i wind turbine rotor", ***Proceedings of Wind Energy Symposium, American Institute of Aeronautics and Astronautics***, Kissimmee, Florida, USA, (2018). (https://m-selig.ae.illinois.edu/pubs/AnandaBansalSelig-2018-AIAA-Paper-2018-0994-SUMR-13i.pdf).
27. Noyes, C., Qin, C. and Loth, E., "Pre-aligned downwind rotor for a 13.2 MW wind turbine", ***Renewable Energy***, (2018), 749-754. (https://doi.org/10.1016/j.renene.2017.10.019).
28. Zalkind, D.S., Ananda, G.K. and Chetan, M., "System-level design studies for large rotors", ***Wind Energy Science***, Vol. 4, (2019), 595-618. (https://doi.org/10.5194/wes-4-595-2019).
29. Noyes, C., Qin, C. and Loth, E., "Ultralight morphing rotor for extreme-scale wind turbines", ***Proceedings of AIAA SciTech Forum***, (2017), 1-6. (https://doi.org/10.2514/6.2017-0924).
30. Ichter, B., Steele, A., Loth, E., Moriarty, P. and Selig, M., "A morphing downwind-aligned rotor concept based on a 13 MW wind turbine", ***Wind Energy***, Vol. 19, (2016), 625-637. (https://doi.org/10.1002/we.1855).
31. Noyes, C., Qin, C. and Loth, E., "Analytic analysis of load alignment for coning extreme-scale rotors", ***Wind Energy***, Vol. 23, (2020), 357-369. (https://doi.org/10.1002/we.2435).
32. Qin, C., Loth, E., Zalkind, D.S., Pao, L.Y., Yao, S., Griffith, D.T., Selig, M.S. and Damiani, M.S., "Downwind coning concept rotor for a 25 MW offshore wind turbine", ***Renewable Energy***, Vol. 156, (2020), 314-327. (https://doi.org/10.1016/j.renene.2020.04.039).
33. Yao, S., Chetan, M., Griffith, D.T., Mendoza, A.S., Selig, M.S. and Martin, D., "Aero-structural design and optimization of 50 MW wind turbine with over 250 m blades", ***Wind Engineering***, (2021). (https://doi.org/10.1177/0309524X211027355).
34. Bortolotti, P., Kapila, A. and Bottasso, C.L., "Comparison between upwind and downwind designs of a 10 MW wind turbine rotor", ***Wind Energy Science***, Vol. 4, (2019), 115-125. (https://doi.org/10.5194/wes-4-115-2019).
35. Ichter, B., Steele, A., Loth, E. and Moriarty, P., "Structural design and analysis of a segmented ultralight morphing rotor (SUMR) for extreme-scale wind turbines", ***Proceedings of 42nd AIAA Fluid Dynamics Conference***, New Orleans, Louisiana, USA, (2012). (https://doi.org/10.2514/6.2012-3270).
36. Crawford, C., "Parametric variations of a coning rotor wind turbine", ***Proceedings of 46th AIAA Aerospace Sciences Meeting and Exhibit***, Reno, Nevada, USA, (2008). (https://doi.org/10.2514/6.2008-1340).
37. Ning, A. and Petch, D., "Integrated design of downwind land-based wind turbines using analytic gradients", ***Wind Energy***, Vol. 19, (2016), 2137-2152. (https://doi.org/10.1002/we.1972).
38. Tossas, L.M. and Leonardi, S., "Wind turbine modeling for computational fluid dynamics", National Renewable Energy Laboratory, Technical report No. NREL/SR- 5000-55054, (2013). (https://www.nrel.gov/docs/fy13osti/55054.pdf).
39. Réthoré, P., "Thrust and wake of a wind turbine: Relationship and measurements", Master's Thesis, Technical University of Denmark, (2006). (https://www.mek.dtu.dk/-/media/Institutter/Mekanik/Sektioner/FVM/uddannelse/eksamensprojekt/mastertheses-fm/pierrerethore2006.ashx?hash=4E37E5F71D60845E67D3A018D7373297BA54C4E3&la=da).
40. Burton, T., Sharpe, D., Jenkins, N. and Bossanyi, E., Wind energy handbook, John Wiley & Sons, (2001). (https://books.google.com/books/about/Wind_Energy_Handbook.html?id=4UYm893y-34C).
41. Chu, Y.J., Lam, H.F. and Peng, H.Y., "Numerical investigation of the power and self-start performance of a folding-blade horizontal axis wind turbine with a downwind configuration", ***International Journal of Green Energy***, Vol. 19, No. 1, (2021), 28-51. (https://doi.org/10.1080/15435075.2021.1930003).
42. Betz, A., "The maximum of the theoretically possible exploitation of wind by means of a wind motor", ***Wind Engineering***, Vol. 37, (2013), 441-446. (https://www.jstor.org/stable/43857254).
43. Menter, F.R., "Two-equation eddy-viscosity turbulence models for engineering applications", ***AIAA Journal***, Vol. 32, (1994), 1598-1605. (https://doi.org/10.2514/3.12149).
44. Wilcox, D.C., Turbulence modeling for CFD, Second edition, DCW Industries, (1994). (https://books.google.com/books?id=VwlRAAAAMAAJ&q).
45. Launder, B.E. and Spalding, D.B., Lectures in mathematical models of turbulence, Academic Press, (1972). (https://books.google.com/books?id=61iqAAAAIAAJ&dq).
46. Griffith, D.T. and Ashwill, T.D., "The Sandia 100-meter all-glass baseline wind turbine blade:SNL100-00", Sandia National Laboratories, Albuquerque, report No. SAND2011-3779, (2011). (https://energy.sandia.gov/wp-content/gallery/uploads/SAND2011-3779.pdf).
47. ANSYS. 12.0 user's guide, Ansys Incorporayion, (2009). (https://www.afs.enea.it/project/neptunius/docs/fluent/html/ug/main_pre.htm), (Accessed: 16 July 2009).

JREE: Vol. 9, No. 4, (Autumn 2022) 76-84

Journal of Renewable Energy and Environment

Journal Homepage: www.jree.ir

Materials and Energy Research Center

MERC

Research Article

Methyl-Esters from Ternary Oil Blend Using Catalyst Synthesized from Mixed Agro-Wastes

Ayowumi Rita Soji-Adekunle [a*], Eriola Betiku [b], Abraham A. Asere [c]

[a] *Department of Mechanical Engineering, Faculty of Engineering, Adeleke University, P.M.B. 250, Ede, Osun State, Nigeria.*
[b] *Department of Chemical Engineering, Faculty of Technology, Obafemi Awolowo University, P.M.B. 13, Ile-Ife, Osun State, Nigeria.*
[c] *Department of Mechanical Engineering, Faculty of Technology, Obafemi Awolowo University, P.M.B. 13, Ile-Ife, Osun State, Nigeria.*

PAPER INFO

Paper history:
Received: 07 December 2021
Revised in revised form: 07 February 2022
Scientific Accepted: 27 February 2022
Published: 20 September 2022

Keywords:
Non-Edible,
Biodiesel,
Catalyst,
Transesterification,
Microwave,
Irradiation

ABSTRACT

This study used ternary substrates consisting of honne, neem, and yellow oleander (HONOYO) oil blend to produce methyl-esters for sustainability of raw materials for biodiesel synthesis. A biomass-based catalyst from calcined mixed agro-wastes consisting of kolanut pod, cocoa pod, and plantain peel ash was employed to transesterify the blend. A two-step method was adopted to convert HONOYO into methyl-esters. Taguchi L9 experimental design tool was used to ascertain the interactive effects of microwave irradiation power (W), Methanol/oil ratio (MeOH), time (min), and agro-wastes synthesized catalyst ASC (wt %) on the yield of methyl-esters from HONOYO. Results demonstrated that at 3:1 MeOH, microwave power of 150 W, ASC of 1.5 wt %, and reaction time of 1 minute, a yield of 80.96 % was achieved. HONOYOB satisfied ASTM D6751 and EN 14214 standards. Performance evaluation of the process input variables suggests weight of ASC as the most significant process parameters for HONOYOB yield. This work authenticates that biomass catalyst from agricultural wastes can adequately be applied to synthesis biodiesel effectively from blends of non-edible oils to supplement fossil diesel.

https://doi.org/10.30501/jree.2022.317615.1294

1. INTRODUCTION

There is a continuous demand for low-cost and eco-friendly fuel both for domestic and industrial purposes in the developed and developing countries. The quest for sustainable energy source is a main concern for the present and future needs. Efforts made by various research works suggest that renewable energies from biomass, hydropower, wind, geothermal, solar, and tidal waves are among the suggested alternatives to combustion of fossil-diesel, although these choices suffer one form of disadvantage or others ranging from initial costs (solar) to restriction of efficiency due to geographical location (geothermal) and need for appropriate head and water conservation during drought (hydropower) [1]. Despite the suggested alternatives, it has been projected that fossil fuel would still supply almost 80 % of the world's energy requirement for more than the next three decades [2]. One major alternative fuel suggested as a supplement for the transportation industry is biofuel, which a non-petroleum natural recyclable liquid fuel. This fuel type is obtained by the combined chemical activity of catalyst and alcohol on oil from plant origin or fats from animals via transesterification. Biofuels possess properties suitable to be applied in the automotive gas engine directly or mixed with automotive gas oil to obtain a blend [3]. The consideration of biofuel as a supplement or supernumerary for fossil fuel is directly concomitant with some benefits, including energy safety, biological advantage, direct application in diesel engines, and related socio-economic reasons [4]. Among several existing biofuel alternatives, bioethanol and biodiesel are the most extensively renowned biofuels appropriate for transportation purposes, especially biodiesel [5]. This is because biodiesel is characterized by additional advantages including non-toxicity, low level of polycyclic aromatic hydrocarbons and their nitrate derivatives, its direct use in unmodified diesel engines as fuel, and its miscibility with automotive gas oil in different proportions [6]. It is nearly sulfur-free and possesses the ability to cut down on the amount of SOx, besides other products of combustion [7]. However, the production cost is directly related to feedstock, that is, a major concern that hinders its commercialization [2]. There is an indication that biofuels may eventually become a globally recognized substitute for fossil diesel both in unindustrialized and developed countries if low-cost and accessible feedstock can be adopted. Furthermore, synthesis of biodiesel from edible oil is discouraged due to other applications including contest with food as well as pharmaceutical and cosmetic purposes that these oils serve [8, 9].

*Corresponding Author's Email: soji-adekunle.ayowunmi@adelekeuniversity.edu.ng (A.R. Soji-Adekunle)
URL: https://www.jree.ir/article_157727.html

Please cite this article as: Soji-Adekunle, A.R., Betiku, E. and A.A. Asere, "Methyl-esters from ternary oil blend using catalyst synthesized from mixed agro-wastes", ***Journal of Renewable Energy and Environment (JREE)***, Vol. 9, No. 4, (2022), 76-84. (https://doi.org/10.30501/jree.2022.317615.1294).

Transesterification is a catalyzed chemical interaction between molecules of triglycerides and alcohol. Such catalysts could be acid, base or both, and the reactions could be done either in a single step or two steps depending on the acid value of the substrates which is directly linked to the percentage of free fatty acid [10, 11]. At present, the two forms of catalyst used for transesterification are homogeneous and heterogeneous catalysts. Heterogeneous catalyst types have been found to be containing more than one active element and they are used for the transesterification process successfully [11, 12].

The key element in producing biodiesel is feedstock, which is vegetable oil. A major hitch in adopting biodiesel as fuel in the transportation industry is the need for sustainable feedstock, which will not hamper food, drug, pharmaceutical, or other purposes. Current research has shifted to the use of nonedible and waste oils as well as catalysts made from biowastes for producing biodiesel to prevent the crisis of edible vegetable oil shortage in the future and possibly reduce the cost of production [13, 14]. Waste from the agro and bio sectors, threatening the environment, can be used in a single or mixed fashion and used to produce catalysts capable of transesterifying vegetable oil. Heterogeneous catalysts were processed from different biowaste materials such as peels of plantain peel [15], kolanut pud [16], egg shell [17], banana trunk [18], bagasse from sugarcane, and oil palm trunk [19].

Agro-wastes can also be mixed to investigate the possibility of improving its elemental composition potency for transesterification of a combination of oils at different volumetric ratios. As shown earlier, when a biowaste-based catalyst is used for transesterification, the yield is comparable to that of the homogeneous catalyst and the time of reaction is very short, meaning that this method could be more cost-effective [20]. In addition, the application of catalysts synthesized from agrowastes in synthesizing oils is an emerging technology. Nonedible oil types can be blended based on types or volumetric ratios to alter physicochemical properties to facilitate applicability to transesterification. Similarly, previous research studies have revealed that the time required for transesterification when microwave irradiation is adopted is quite shorter than that when the hot plate is used (Table 1). Thus, there is still a wider gap in exploration in biodiesel synthesis from different oil blends to be breached in terms of the characteristic feature of oil, volumetric ratio and whether the transesterification process is aided or not.

An important issue which cannot be overlooked is that no research has discovered any seed with hundred percent oil yield so far, thereby putting a limit on the quantity of oil that can be extracted per given species of oil seed. It has also been found that there are nonedible oils having a substantial oil percentage but cannot be used alone due to the limited and peculiar characteristics of such oils [21]. There is a need for research interest in the combination of different nonedible oil samples to discover the combinations, which will have substantial yield, especially when transesterified using different blends of biowaste catalysts.

1.1. Objectives and novelty

This study explored the effect of blend of ternary oil samples including honne (Calophyllum inophyllum), neem (Azadirachta indica), and yellow oleander (Thevetia peruviana) in equal proportion using ASC as an agrowaste synthesized catalyat on the yield of biodiesel via microwave irradiation assisted transesterification process. Times for reaction, weight of ASC, MeOH, and irradiation power were optimized using the L9 Taguchi tool for experimental design to obtain optimum yield. The process parameter with premier effect on biodiesel yield was also determined and the biodiesel produced was analyzed for fuel properties. The experiment was carried out to:

i. determine the physiochemical properties of the oil mixture (HONOYO) to ascertain suitability for biodiesel production;
ii. use agro-waste materials plantain peel, cocoa, and kolanut husk to make catalysts (ASC), thus finding a useful purpose for the waste materials;
iii. investigate the influence of microwave irradiation on the time required for completion of the transesterification process;
iv. study the effect of four process parameters namely microwave irradiation power, MeOH, ASC, and time on biodiesel yield using the Taguchi L9 design tool; and
v. characterize the biodiesel produced code named HIONOYOB to verify its properties with ASTM D6751 and EN 14214 standards and ascertain its suitability as fuel.

Table 1. Biodiesel synthesized from oil blends via homogeneous and bio-based catalysts

Oil blend	Volumetric ratio	Method	Time	Catalyst type	Optimum yield (wt %)	Reference
Soybean and rape seed	50:50	Hot plate	2 h	Homogeneous	94.00	[22]
Pongamia and Neem	70:30	Hot plate	77 min	Homogeneous	86.3	[23]
Waste cooking/Honne	70:30	Microwave	7.15 min	Homogeneous	97.65	[24]
Pongamia, Jatropha, and honne	Equal	Hot plate	95 min	Homogeneous	98.00	[25]
Rubber seed and Neem	40:60	Microwave	5.88 min	Heterogeneous	98.77	[26]
Castor oil and waste fish	50:50	Hot plate	39 min	Homogeneous	95.2+2.5	[27]
Soybean/castor	25:75			Homogeneous	87.00	
Palmoil/Rubber seed	50:50	Hot plate	1 h	Homogeneous	97.00	[28]
Honne rubber seed and yellow oleander	20:20:60	Microwave	6 min	Heterogeneous	98.45	[20]

2. MATERIALS AND METHODS

2.1. Material procurement

The honne and yellow oleander seeds were collected from Obafemi Awolowo University Ile-Ife Nigeria compound, processed, and taken to the Faculty of Pharmacy, Obafemi Awolowo University, Ile-Ife for oil extraction via Soxhlet apparatus using n-hexane to obtain Honne Oil (HO) and yellow oleander oil (YO) oils, while Neem Oil (NO) was purchased from National Research Institute of Chemical Technology (NARICT) Zaria, Nigeria. The three oils were blended at equal volumetric ratios to obtain HONOYO. Reagents and chemicals including di-ethyl ether, ethanol, methanol, potassium iodide, starch solution, cyclohexane, sulphuric acid, sodium sulphate, phenolphthalein, potassium hydroxide, and Wij's solution of analytical grade were used for the study.

2.2. Blended agro-wastes synthesized catalyst (ASC) preparation

The obtained agro-wastes were cut into tiny pieces, washed 3 times with distilled water and sundried for 2 weeks, and then dried in the oven at 80 ^{o}C until constant weight was achieved. These wastes were separately charred into ashes in the open air, after which each ash was manually minced to a fine powder using porcelain mortar and pestle. The resulting powdered samples were weighed in equal proportion, mixed, and calcined in a muffle furnace at 300, 500, 700, 900, and 1100 °C for four hours to determine the best calcination temperature. The produced calcined ASC ash was then stored in corked plastic vessels.

2.3. Determination of characteristic features of ASC

The ASC was characterized using Energy Dispersive X-ray Spectroscopy (EDX), Fourier Transform Infrared (FT-IR), XRD chromatograms, and Scanning Electron Microscopy (SEM). The Cambridge S200 SEM equipped with an energy dispersive X-ray analyzer system was employed to investigate the surface morphology of ASC, as represented in Figure 1. The EDX was used to analyze the elemental composition of the ASC sample. The active surface functional groups of the ash sample were also determined by FT-IR spectral studies using Perkin Elmer Spectrum 100 FT-IR spectrophotometer in the wavelength range of 4000-400 cm^{-1} (Figure 2). XRD chromatograms reveal the crystalline compounds present in ASC at 500 °C (Figure 3). In addition, the residual gases in the ASC were eliminated at 150 °C for 16 h to eliminate moisture and atmospheric vapor by heating and evacuation.

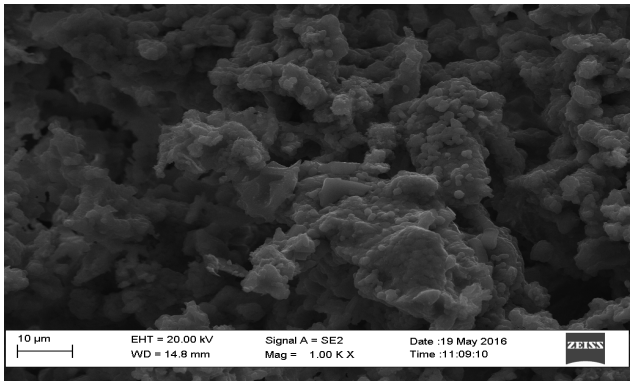

Figure 1. SEM image of calcined ASC

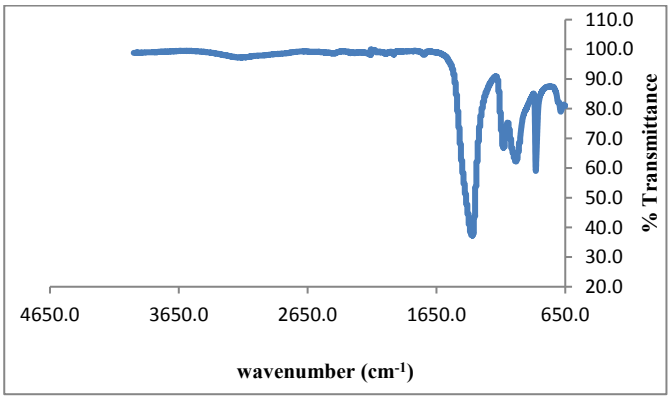

Figure 2. FTIR spectra of calcined ASC at 500 °C

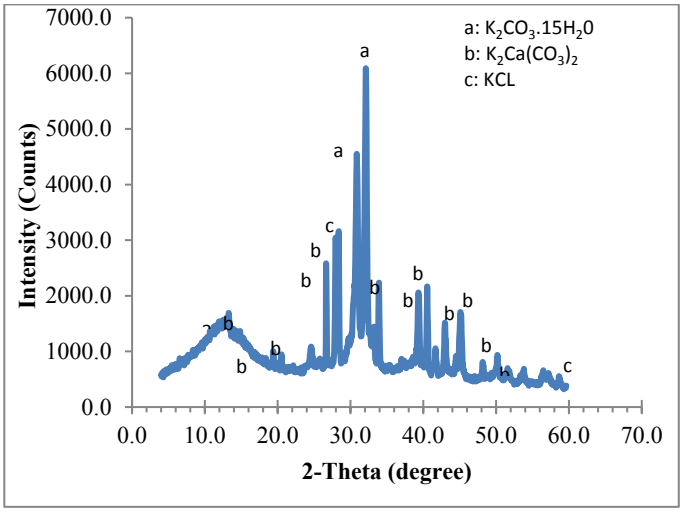

Figure 3. XRD chromatogram calcined ASC at 500 °C

2.4. Blending of honne, neem, and yellow oleander (HONOYO) oils

This study mixed an equal volume of honne, neem, and yellow oleander seed oils by first heating them separately in a 500 ml conical flask at 60 °C for 15 minutes and then, decanted one after the other into a 1000 ml flat bottom flask placed on a hot plate equipped with a stirrer having magnetic property for agitation and proper fraternization at 60 °C for another 30 minutes to obtain HONOYO.

2.5. Experimental design for transesterification

The acid value of HONOYO was determined to be 37.5 mg of KOH/g of oil, corresponding to FFA of 18.84. This was reduced to < 2 mg KOH/g oil via sulphuric acid pretreatment to prevent the formation of soap during transesterification.

2.5.1. Acid catalyzed esterification of HONOYO

A known amount of HONOYO was measured into a 500 ml two-necked glass reactor. The esterification process was carried out using MeOH 25:1, H_2SO4 1 wt %, microwave power 300 w, and reaction time of 15 minutes. The reaction took place in a glass reactor placed in the microwave oven. Following the completion of the reaction, the mixture was allowed to be separated by gravity and the residual methanol was removed by heating off on the hot plate before determining the acid value of the esterified oil.

A known quantity of esterified HONOYO was measured into a two-necked glass reactor. A known volume of methanol

was added to a certain amount of ASC. This was placed in a pre-timed microwave and the reaction was stopped based on the time specified by the experimental design, as given in Table 3. MeOH, reaction time, microwave irradiation power, and weight of ASC were combined at three levels to generate an orthogonal array of nine experimental conditions using the Taguchi L9 experimental design tool to model the production of HONOYO methyl-esters, as depicted in Table 2. The genera of process parameters considered for the transesterification process of pretreated HONOYO are presented in Table 3.

Table 2. Factors and levels for design of experiment for transesterification of pretreated HONOYO

Factors	Unit	Level for factors		
		-1	0	1
MeOH	v/v	3	9	15
Catalyst amount	wt %	1.5	3.0	4.5
Microwavw power	Watt	150	300	450
Reaction time	Mins	1	3	5

Table 3. Transesterification of the pretreated HONOYO

Run	MeOH	ASC (wt.%)	Power (W)	Time (min)	Actual yield (wt%)	Predicted yield (wt%)	Residuals (wt %)
1	9	3	450	1	62.70	61.20	1.50
2	15	1.5	450	3	75.71	77.22	-1.51
3	15	3	150	5	65.20	65.19	0.013
4	3	3	300	3	42.36	43.87	-1.51
5	9	4.5	150	3	81.86	83.37	-1.51
6	3	1.5	150	1	80.96	79.46	1.50
7	9	1.5	300	5	90.30	90.29	0.013
8	3	4.5	450	5	49.00	48.99	0.013
9	15	4.5	300	1	65.29	63.79	1.50

Upon the completion of the reaction, the resulting product was allowed to separate; glycerol was tapped off; and the HONOYOB was washed with distilled water at 50 °C to get rid of residual catalyst, glycerol, methanol, and soap. The washed HONOYOB was dried over heated anhydrous sodium sulphate powder and the HONOYOB yield was determined gravimetrically according to Equation 1.

$$\text{HONOYOB yield (wt.\%)} = \frac{\text{weight of oil sample}}{\text{weight of biodiesel sample}} \times 100 \quad (1)$$

The most significant factor was evaluated using Equation 2 where SSf is the sum of the square of the individual parameters and SST is the total sum of squares of all the parameters obtained for the model (Dhawane et al., 2016b).

$$\text{C. F. (\%)} = \frac{SS_f}{SS_T} \text{ x } 100 \quad (2)$$

2.6. Determination of HONOYOB properties

The physicochemical properties of the produced HONOYOB considered. The determined properties include kinematic viscosity, density, moisture content, acid value, saponification value (sv), iodine value, higher heating value, cetane number diesel, and index AOAC (Chemists and Horwitz, 1990) [22, 23].

3. RESULTS AND DISCUSSION

3.1. Characterization of ASC

It was revealed by the EDS study that the active elemental compositions of ASC were significantly affected by the temperature of calcination (Table 4). The result shows Magnessium (Mg), phosphorous (P), calcium (Ca), and potassium (K) as the metallic element in ASC and that K has the highest mass fraction (47.67 wt % and 47.93 wt %) at 500 °C and 700 °C, respectively, suggesting that it is the main active element responsible for transesterification of HONOYO. Similar results were found in the research finding in which cocoa pod husk was used to produce CCPHA bio-based catalyst [2]. The SEM image at a resolution of 1000X reveals that the morphology of ASC is composed of disjointed clusters of granules that are glossy, porous, and spongy, suggesting better permeability to moisture as well as improved surface area. This property is preferred for conversion of pretreated oil or feedstock which may likely contain traces of moisture to methyl-esters. The XRD pattern of ASC shows peaks in the plot, corresponding to various components such as KCl (Sylvite), $K_2Ca(CO_3)_2$ (Fairchildite), and $K_2CO_3.5H_2O$ (potassium carbonate) as the prominent crystalline compounds present in the calcined ASC. It was equally observed that increase in calcination temperature results in decomposition of $CaCO_3$ to CaO and quartz to SiO_2. Similar peaks were observed for ash samples of waste rubber seed shell [30] and banana peel [31, 20]. The elemental analysis data and the XRD studies establish that a significant amount of potassium present in the characterized calcined ASC ash exists in its chloride form. The FT-IR results for the ASC ash reveal various adsorption bands, as shown in (Figure 2). The IR spectrum consists of 673, 876, 1020, 1410, 2160, 3120, and 3640 per cm bands. The bands from 3134-673 per cm indicate the expanse hydrogen-bonded vibration of O-H functional group and unseparated water molecules forming the

surface hydrated layer. This correlates with the report by [33] and [34]. Characteristic bands between the regions of 1410-3120 cm^{-1} indicate the symmetric and asymmetric elongation and vibration of the CH3 group [35]. The elongation and vibrations of the C–O bond are observed near 1020–876 cm^{-1}, indicating the presence of CO_3. This band is peculiar to K_2CO_3 and prominent in the XRD spectral.

3.2. Transformation of HONOYO to HONOYOB

The biodiesel production-related properties were determined for HO, NO, and YO as well as HONOYO (Table 5). The acid values were found to be 40.28, 14.57, 61.49, and 37.5 mg KOH/g oil, respectively. This corresponds to an FFA of 18.84 % for the HONOYO. The acid value of HONOYO shows a need to reduce the acid value to prevent saponification.

3.2.1. Pretreatment of HONOYO

The acid value of HOMOYO was reduced from 37.5 to < 2 % via acid esterification. Thus, the tendency of soap formation was eliminated.

3.2.2. Modeling and parameter optimization for transesterification of pretreated HONOYO

The result of predicted and experimental yields of HONOYOB via ASC catalyzed methanolysis of HONOYO to HONOYOB using an orthogonal array of nine experiments is shown in Table 3. The mathematical expression for the reaction is represented by Equation 3.

$$N = +68.15 - 10.71A1 + 10.13A2 + 14.17B1 - 11.40B2 + 7.85C1 - 2.17C2 \quad (3)$$

The terms A, B, and C are the molar ratio of methanol to prtreated HONOYO (MeOH), amount of agrowastes synthesized catalyst (ASC), and microwave irradiation power, respectively, and N is the biodiesel (HONOYOB) yield. The yield varied between 42.36 wt % and 90.30 wt %. The minimum and maximum yields were obtained at fourth and seventh experimental runs, respectively. These correspond to 3 min, 3 wt %, 300 W, 3:1 and 5 min, 1.5 wt %, 300 W, 9:1, respectively. The fuel properties of HONOYOB are presented in Table 6. HONOYOB improved cetane number, implying better fuel strength; the iodine value is very low, signifying good cold flow properties. The viscosity is a tad higher than specified; therefore, HONOYOB may require blending with AGO to be fit for use in an unmodified IC engine to secure engine life for long-term usage. The regression analysis for this study tested by means of ANOVA shows that $p < 0.05$ as revealed in Table 7 for all model terms, meaning that the result is statistically significant at a 95 % level of confidence and that the most influential parameter affecting the yield of HONOYOB is ASC. The F value of 48.29 and p-value of 0.0204 of the models confirm that all the model terms are significant, as shown in Table 7.

Table 4. Elemental composition of ASC

Temperature (°C)	Elements (mass %)											
	O	Mg	Si	P	S	Cl	K	Ca	Fe	Zn	Na	Al
300	40.43	4.06	0.90	1.74	1.41	1.97	43.99	5.50	0.00	0.00	0.00	0.00
500	37.21	4.21	0.56	1.65	1.26	1.88	47.67	5.56	0.00	0.00	0.00	0.00
700	41.20	3.05	0.79	1.61	0.92	1.88	47.93	3.93	0.00	0.00	0.00	0.00
900	41.59	1.85	1.41	1.77	1.29	1.43	45.55	4.68	0.64	0.00	0.00	0.00
1100	45.30	0.81	2.82	5.20	1.17	1.03	43.90	0.00	0.00	0.00	0.00	0.75

Table 5. Properties of oil samples

Parameters	Values			
	HO	NO	YO	HONOYO
Physical state at 25 °C	Liquid/dark green	Liquid/dark brown	Liquid/golden yellow	Liquid/dark brown
Moisture content (%)	0.640 ± 0.001	0.050 ± 0.001	0.342 ± 0.001	ND
Specific gravity	0.901 ± 0.005	0.961 ± 0.001	0.908 ± 0.017	0.967 ± 0.00
Kinematic viscosity (mm^2/s) at 40 °C	37.01 ± 0.76	124.43 ± 0.04	35.47 ± 0.27	72.22 ± 0.00
Refractive index at 25 °C	1.475 ± 0.00	1.4764 ± 0.001	1.464 ± 0.00	1.47 ± 0.00
Density (kg/m^3) at 25 °C	901 ± 0.014	964 ± 0.001	909 ± 0.001	967 ± 0.00
% FFA (as oleic acid)	20.24 ± 0.35	7.32 ± 0.91	30.90 ± 0.35	18. 84 ± 0.53
Acid value (mg KOH/g oil)	40.28 ± 0.00	14.57 ± 0.00	61.49 ± 0.00	37.5 + 0.00
Iodine value (g I_2/100 g oil)	80.44 ± 0.65	84.53 ± 0.74	87.37 ± 0.96	ND
Saponification value (mg KOH/g oil)	226.5 ± 0.94	178.86 ± 0.81	174.74 ± 0.61	ND
Higher heating value (MJ/kg)	51.69 ± 0.00	49.39 ± 0.00	57.04 ± 0.00	50.71 ± 0.00
Cetane number	52.29 ± 0.00	58.00 ± 0.00	57.87 ± 0.00	56.05 ± 0.00
ND: means not done				

Table 6. Fuel properties of HONOYOB

Properties	HONOYOB	ASTM D6751	EN 14214
Physical state and colour	Liquid/golden yellow	NS	NS
Kinematic viscosity(mm^2/s) at 40 °C	6.83	1.9 - 6.0	3.5 - 5.0
Density at 25 °C (kg/m^3)	868.	NS	860 – 900
Moisture content (%)	0.025	<0.03	0.02 max
Acid value (mg KOH/g oil)	0.20	0.50 max	0.50 max
SV (mg KOH/g oil)	212	-	-
Iodine value (g I_2/100 g oil)	33. 18	NS	120 max
Higher heating value (MJ/kg)	40.00	NS	NS
Flash point	ND	130 minimum	120 minimum
Pour point	ND	NS	NS
API gravity (deg.)	ND	39.95	NS
Diesel index	72.6	331.00	NS
Aniline point	ND	NS	NS
Cloud point	ND	NS	NS
Cetane number	62.57	47 mi	51 min
aNS = not specified bNS = not specified			

Table 7. Significance result for modeling of methanolysis of HONOYO

Source of variance	Sum of squares	Degree of freedom	Mean square	F-value	p-value
Model	1964.71	6	327.45	48.29	0.0204
A- MeOH:HONOYO	653.39	2	326.69	48.18	0.0203
B - ASC	1015.27	2	507.63	74.87	0.0132
C - Power	296.05	2	148.03	21.83	0.0438
Standard Deviation	2.60				
Mean of response	68. 15				
Coefficient of Variation (%)	3.82				
R^2	0.9931				
Adequate Precision	20.212				

The model terms were developed by eliminating the term that is not significant in the response. Only the reaction time is insignificant on the yield of HONOYOB being the reason why it was not contained in the model terms. ASC catalyst has the most prominent effect on HONOYOB yield when placed side by side with other significant factors. From the value of the R^2 (0.9931), the model can explicate 99.31 % of the changeability of the process [2] (Table7). For the signal of the design process to be strong enough, the adequate precision must be > 4. Thus, 20.212 denotes a strong signal of the design of this study. Similarly, the adeptness of the model is reflected in its percentage Coefficient of Variation (CV), which is required to be less than ten. The CV for this study is 3.82 %. This substantiates the finding that the model is fit to describe this process adequately. The lack-of-fit F-value of 0.0204 implies that the model is 99.97 % fit to predict this process. The model predicted data by equation and the data obtained from the experiment were plotted to obtain Figure 4. Plot 4a reflects the adequacy of the model equation in predicting the yield of HONOYOB. The closeness to the linearity of both the model-predicted and experimental values is proof that the untainted error is minimal and that there is agreement between the model predicted and experimental data. Thus, the model is adequate for predicting this process [36]. Figure 4b shows the normal distribution pattern for the plot of the studentized residuals, showing that the experimental errors were random. The scattering of data points in Figure 4c plot which is a plot of studentized residuals against the data predicted by the model implies evenness in variation for response values, thus confirming that the model is suitable. The outlier t plot for all studentized residuals is depicted in Figure 4d. The plot reveals that all data values lie within ± 3.0. This further establishes the fitness of the model [37, 20].

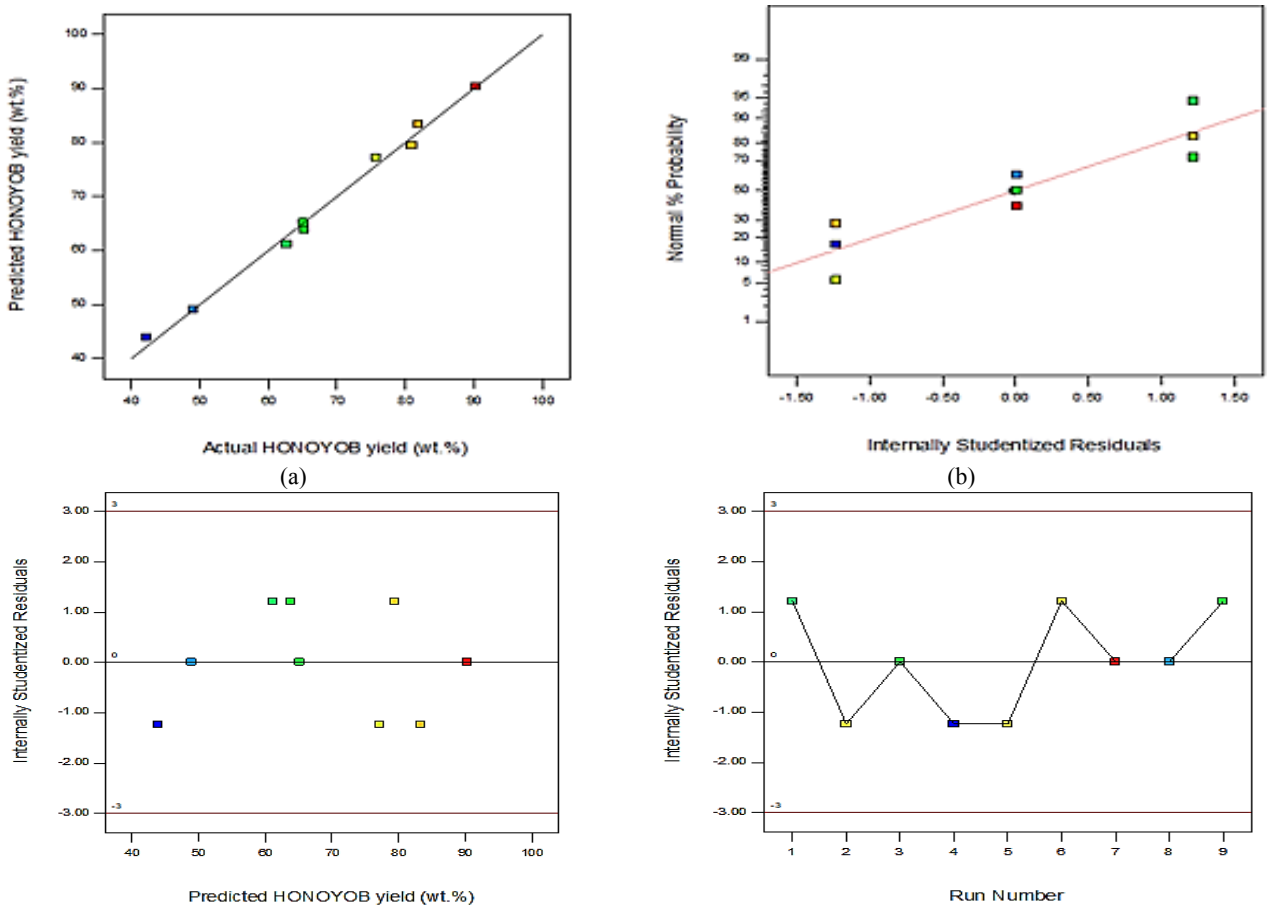

Figure 4. Analytical plot of the surface model for HONOYOB formation

3.3.1. Effect of MeOH on HONOYOB yield

Transesterification is a reversible reaction. As reported by various researchers, 1 mole of oil is to be reacted with 3 mole of alcohol stoichiometrically for transesterification. The equilibrium of the reaction can be driven to the product side if the excess amount of alcohol is present in the reaction [13, 32, 38, 39]. However, caution should be exercised in the quantity of alcohol used to prevent dilution; otherwise, there will be a reduction in the expected yield of the methyl-esters [32]. In this study, the molar proportion of methanol to oil at three levels i.e., 3:1, 9:1, and 15:1, was adopted to investigate its influence on HONOYOB yield while keeping other parameters constant (Table 2). The effect of these ratios is represented in Figure 5a. HONOYOB yield increased from 3:1 and reached the peak at 9:1. The ratio that favoured HONOYOB yield most was 9:1 with a significant yield of 90.30 wt %.

3.3.2. Effect of microwave power on HONOYOB yield

Microwave power is one of the key factors that facilitates biodiesel production. The raised temperature at the reaction sites may favor the antiphon rate [40]. Microwave powers at 150 W, 300 W, and 450 W were investigated to study their effect on the yield of HONOYOB while keeping other parameters constant (Table 2). This is represented in Figure 5b. The yield was significantly higher for 150 W. The reduction in the yield at the other investigated power may result from the possibility of drying-off of the alcohol in the reaction mixture because of the intensity of heat generated in the microwave.

3.3.3. Effect of ASC loading on HONOYOB Yield

Catalyst loading at three levels, 1.5, 3, and 5 wt %, were investigated to study the influence of the amount of catalyst on HONOYOB yield while keeping other parameters constant (Table 2). The graph obtained by plotting HONOYOB yield against catalyst amount in weight percentage is shown in Figure 5c. At the methanol-to-oil molar ratio of 9:1, 1.5 wt % catalyst loading, microwave power of 150 W, and reaction time of 1-minute, maximum HONOYOB yield was observed to be 80.96 wt %. Further increase in the amount of catalyst in the reaction does not favor the yield of HONOYOB. This is a advantage for the ASC catalyst used because a small quantity of it is required for transesterification, thus lowering the production cost of HONOYOB. Researchers also reported similar observations on the amount of biowastes catalyst required for transesterification in their study [2].

3.4. Model validation

The optimization of each parameter was performed to determine the best combination to give the optimum HONOYOB yield based on the mathematical model developed. The optimum values of the process parameters and the biodiesel yield obtained from this study for the conversion of HONOYO into HONOYOB using ASC catalyst were methanol to oil molar ratio of 9:1, catalyst loading of 1.5 wt %, microwave power of 150 W, and reaction time of 1 minute. The optimum HONOYOB yield projected in this condition was 100 wt % with desirability of one. The optimum condition forecast by the regression model equation was validated through experimentation in triplicates. It was

observed that the results of the experimental and predicted were close, implying that the chosen model was appropriate for predicting the optimum condition for HONOYOB production. The average HONOYOB yield observed was 98.57 ± 0.58 wt % (Figure 5 a, b, and c).

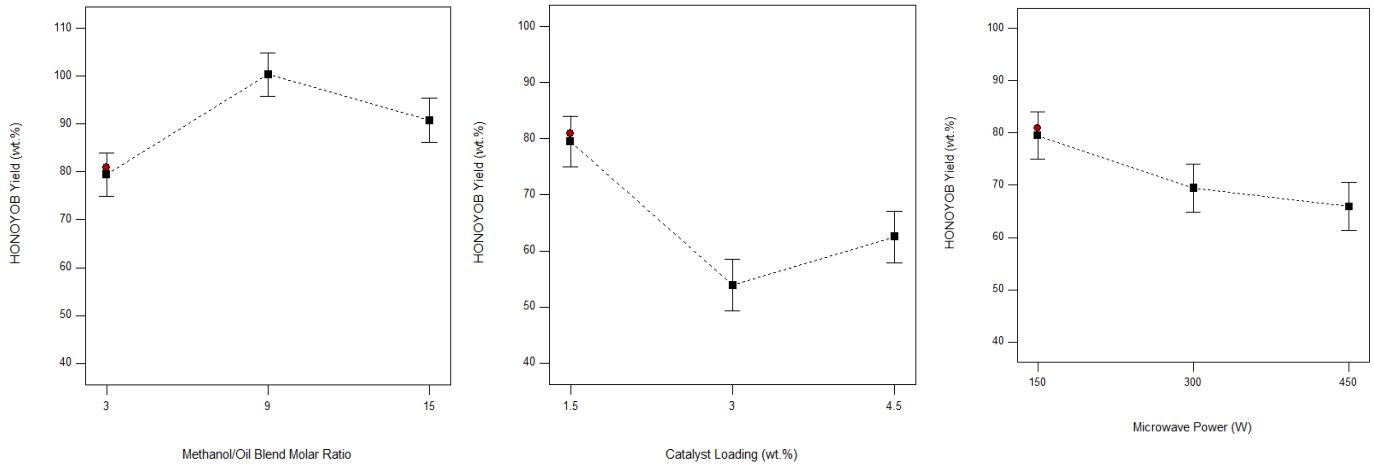

Figure 5. Plot of model validation

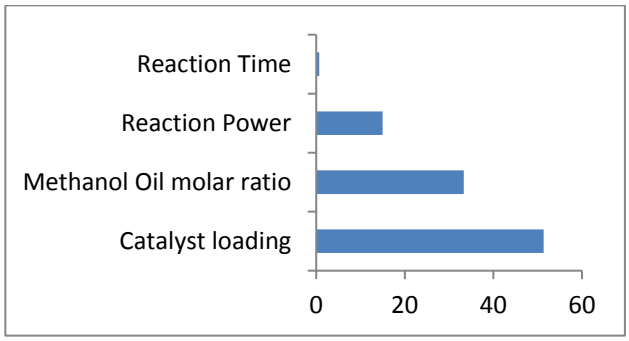

Figure 6. Level of contribution of process parameters intransesterification process

4. CONCLUSIONS

This work investigated the combination of three oil types in equal proportion to obtain HONOYO. The HONOYO was used to synthesize biodiesel by two steps. Calcined agrowastes ash ASC was used as a catalyst for the transesterification process. Microwave irradiation was employed to aid the production process. The physicochemical properties of HONOYO demonstrateed that it was a feasible feedstock for biodiesel production, but required acid pre-treatment prior to transesterification. ASC catalyst was heterogeneous in nature containing potssium, calcium, Magnessium, and Phosphorus as active metallic elements. The optimal condition for synthesizing biodiesel from pretreated HONOYO was MeOH of 3:1, microwave power of 150 W, ASC of 1.5 wt %, and reaction time of 1 minute. An optimum yield of 80.96 % was achieved. ASC was found to be the process parameter with peak effect on the yield (Figure 6). The application of microwave irradiation to the transesterification process reduced the production time drastically. The produced biodiesel (HONOYOB) is of high quality since most of its properties are considered to be satisfactory in line with biodiesel standard specifications (ASTM D6751 and EN 14214).

5. AKNOWLEDGEMENT

The authors approvingly acknowledge biochemical engineering laboratory Obafemi Awowolo University Ile-Ife Nigeria'.

NOMENCLATURE

ASC	Agro-waste Catalyst
HONOYO	Honne, Neem and Yello Oleander Blend
HONOYOB	Methyl eters from HONOYO
ASTM D	American
EN141214	European
MeOH	Methanol to oil ratio
CV	coefficient of Variation
SV	Saponification Value
FFA	Free Fatty Acid
ANOVA	Analysis of Variance
AGO	Automotive Gas Oil

REFERENCES

1. Azarpour, A., Suhaimi, S., Zahedi, G. and Bahadori, A., "A review on the drawbacks of renewable energy as a promising energy source of the future", ***Arabian Journal for Science and Engineering***, Vol. 38, (2013), 317-328. (https://doi.org/10.1007/s13369-012-0436-6).
2. Betiku, E., Etim, A.O., Pereao, O. and Ojumu, T.V., "Two-step conversion of neem (*Azadirachta indica*) seed oil into fatty methyl esters using a heterogeneous biomass-based catalyst: An example of cocoa pod husk", ***Energy & Fuels***, Vol. 31, (2017a), 6182-6193. (https://doi.org/10.1021/acs.energyfuels.7b00604).
3. Chavan, S.B., Kumbhar, R.R. and Deshmukh, R.B., "Callophyllum inophyllum linn ("honne") oil, a source for biodiesel production", ***Research Journal of Chemical Sciences***, Vol. 3, No. 11, (2013), 24-31. (http://www.isca.in/rjcs/Archives/v3/i11/4.ISCA-RJCS-2013-068.php).
4. Demirbas, A., "Progress and recent trends in biodiesel fuels", ***Energy Conversion and Management***, Vol. 50, (2009), 14-34. (https://doi.org/10.1016/j.enconman.2008.09.001).
5. Manivannan, A., Prabu, R. and Kumar, K.,'"Investigation on influence of blending Jatropha biofuel with diesel to improve fuel quality", ***Australian Journal of Mechanical Engineering***, (2009). (https://doi.org/10.1080/14484846.2019.1567029).
6. Knothe, G., "Analytical methods used in the production and fuel quality assessment of biodiesel", ***Transactions of the ASAE***, Vol. 44, No. 2, (2001), 193-200. (https://doi.org/10.13031/2013.4740).
7. Albuquerque, M., Machado, Y., Torres, A., Azevedo, D., Cavalcante Jr., C., Firmiano, L. and Parente Jr., E., "Properties of biodiesel oils formulated using different biomass sources and their blends", ***Renewable Energy***, Vol. 34, (2009), 857-859. (https://doi.org/10.1016/j.renene.2008.07.006).
8. Akella, A., Saini, R. and Sharma, M.P., "Social, economical and environmental impacts of renewable energy systems", ***Renewable Energy***, Vol. 34, (2009), 390-396. (https://doi.org/10.1016/j.renene.2008.05.002).

9. Wakil, M., Kalam, M., Masjuki, H., Atabani, A. and Fattah, I.R., "Influence of biodiesel blending on physicochemical properties and importance of mathematical model for predicting the properties of biodiesel blend", ***Energy Conversion and Management***, Vol. 94, (2015), 51-67. (https://doi.org/10.1016/j.enconman.2015.01.043).
10. Ma, F. and Hanna, M.A., "Biodiesel production: A review", ***Bioresource Technology***, Vol. 70, No. 1, (1999), 1-15. (https://doi.org/10.1016/S0960-8524(99)00025-5).
11. Leung, D.Y., Wu, X. and Leung, M., "A review on biodiesel production using catalyzed transesterification", ***Applied Energy***, Vol. 87, (2010), 1083-1095. (https://doi.org/10.1016/j.apenergy.2009.10.006).
12. Balbaşi, M., Bartan, A., Ar, İ. and Gürü, M., "Development of low cost heterogeneous catalysts for biodiesel processes", ***Energy Sources, Part A: Recovery, Utilization, and Environmental Effects***, Vol. 33, No. 11, (2011), 1035-1047. (https:/doi.org/10.1080/15567030903330736).
13. Dhawane, S.H., Kumar, T. and Halder, G., "Biodiesel synthesis from Hevea brasiliensis oil employing carbon supported heterogeneous catalyst: Optimization by Taguchi method", ***Renewable Energy***, Vol. 89, (2016a), 506-514. (https://doi.org/10.1016/j.renene.2015.12.027).
14. Soji-Adekunle, A.R., Asere, A.A., Ishola, N.B., Oloko-Oba, I.M. and Betiku, E., "Modelling of synthesis of waste cooking oil methyl esters by artificial neural network and response surface methodology", ***International Journal of Ambient Energy***, Vol. 40, (2019), 716-725. (https://doi.org/10.1080/01430750.2017.1423378).
15. Betiku, E. and Ajala, S.O., "Modeling and optimization of *Thevetia peruviana* (yellow oleander) oil biodiesel synthesis via *Musa paradisiacal* (plantain) peels as heterogeneous base catalyst: A case of artificial neural network vs. response surface methodology", ***Industrial Crops and Products***, Vol. 53, (2014), 314-322. (https://doi.org/10.1016/j.indcrop.2013.12.046).
16. Refaat, A., "Biodiesel production using solid metal oxide catalysts", ***International Journal of Environmental Science & Technology***, Vol. 8, (2011), 203-221. (https://doi.org/10.1007/bf03326210).
17. Viriya-empikul, N., Krasae, P., Puttasawat, B., Yoosuk, B., Chollacoop, N. and Faungnawakij, K., "Waste shells of mollusk and egg as biodiesel production catalysts", ***Bioresource Technology***, Vol. 101, (2010), 3765-3767. (https://doi.org/10.1016/j.biotech.2009.12.079).
18. Deka, D.C. and Basumatary, S., "High quality biodiesel from yellow oleander (*Thevetia peruviana*) seed oil", ***Biomass and Bioenergy***, Vol. 35, (2011), 1797-1803. (https://doi.org/10.1016/j.biombioe.2011.01.007).
19. Ezebor, F., Khairuddean, M., Abdullah, A.Z. and Boey, P.L., "Oil palm trunk and sugarcane bagasse derived heterogeneous acid catalysts for production of fatty acid methyl esters", ***Energy***, Vol. 70, (2014b), 493-503. (https://doi.org/10.1016/j.biortech.2014.01.110).
20. Falowo, O.A., Ojumu, T.V., Pereao, O. and Betiku, E., "Sustainable biodiesel synthesis from honne-rubber-neem oil blend with a novel mesoporous base catalyst synthesized from a mixture of three agrowastes", ***Catalysts***, Vol. 10, No. 2, (2020), 190. (https://doi.org/10.3390/catal10020190).
21. Atabani, A., Silitonga, A., Ong, H., Mahlia, T., Masjuki, H., Badruddin, I.A. and Fayaz, H., "Nonedible vegetable oils: A critical evaluation of oil extraction, fatty acid compositions, biodiesel production, characteristics, engine performance and emissions production", ***Renewable and Sustainable Energy Reviews***, Vol. 18, (2013), 211-245. (https://doi.org/10.1016/j.rser.2012.10.013).
22. A.O.A.C. International, Official Methods of Analysis, 15th Edition, Association of Official Analytical Chemist, Washington DC, (1990).
23. Betiku, E., Okunsolawo, S.S., Ajala, S.O. and Odedele, O.S., "Performance evaluation of artificial neural network coupled with generic algorithm and response surface methodology in modeling and optimization of biodiesel production process parameters from shea tree (*Vitellaria paradoxa*) nut butter", ***Renewable Energy***, Vol. 76, (2015), 408-417. (https://doi.org/10.1016/j.renene.2014.11.049).
24. Qiu, F., Li, Y., Yang, D., Li, X. and Sun, P., "Biodiesel production from mixed soybean oil and rapeseed oil", ***Applied Energy***, Vol. 88, (2011), 2050-2055. (https://doi.org/10.1016/j.apenergy.2010.12.070).
25. Vinayaka, A.S., Mahanty, B., Rene, E.R. and Behera, S.K., "Biodiesel production by transesterification of a mixture of pongamia and neem oils", ***Biofuels***, (2018). (https://doi.org/10.1080/17597269.2018.1464874).
26. Milano, J., Ong, H.C., Masjuki, H.H., Silitonga, A.S., Chen, W.-H., Kusumo, F., Dharma, S. and Sebayang, A.H., "Optimization of biodiesel production by microwave irradiation-assisted transesterification for waste cooking oil-*Calophyllum inophyllum* oil via response surface methodology", ***Energy Conversion and Management***, Vol. 158, (2018), 400-415. (https://doi.org/10.1016/j.enconman.2017.12.027).
27. Miraculas, G.A., Bose, N. and Raj, R.E., "Process parameter optimization for biodiesel production from mixed feedstock using empirical model", ***Sustainable Energy Technologies and Assessments***, Vol. 28, (2018), 54-59. (https://doi.org/10.1016/j.seta.2018.06.004).
28. Falowo, O.A., Oloko-Oba, M.I. and Betiku, E., "Biodiesel production intensification via microwave irradiation-assisted transesterification of oil blend using nanoparticles from elephant-ear tree pod husk as a base heterogeneous catalyst", ***Chemical Engineering and Processing-Process Intensification***, Vol. 140, (2019), 157-170. (https://doi.org/10.1016/j.cep.2019.04.010).
29. Fadhil, A.B., Al-Tikrity, E.T. and Albadree, M.A., "Biodiesel production from mixed nonedible oils, castor seed oil and waste fish oil", ***Fuel***, Vol. 210, (2017), 721-728. (http://doi.org/10.1016/j.fuel.2017.09.009).
30. Onoji, S.E., Iyuke, S.E., Igbafe, A.I. and Daramola, M.O., "Transesterification of rubber seed oil to biodiesel over a calcined waste rubber seed shell catalyst: Modeling and optimization of process variables", ***Energy & Fuels***, (2017), (https://doi.org/10.1021/acs.energfuels.7b00331).
31. Betiku, E., Akintunde, A.M. and Ojumu, T.V., "Banana peels as a biobase catalyst for fatty acid methyl esters production using Napoleon's plume (*Bauhinia monandra*) seed oil: A process parameters optimization study", ***Energy***, Vol. 103, (2016), 797-806. (https://doi.org/10.1021/j.energy.2016.02.138).
32. Etim, A.O., Betiku, E., Ajala, S.O., Olaniyi, P.J. and Ojumu, T.V., "Potential of ripe plantain fruit peels as an ecofriendly catalyst for biodiesel synthesis: Optimization by artificial neural network integrated with genetic algorithm", ***Sustainability***, Vol. 10, No. 3, (2018), 707. (https://doi.org/10.3390/su10030707).
33. Singh, A., He, B., Thompson, J. and Van Gerpen, J., "Process optimization of biodiesel production using alkaline catalysts", ***Applied Engineering in Agriculture***, Vol. 22, (2006), 597-600. (https://doi.org/10.13031/2013.21213).
34. Olutoye, M., Lee, S. and Hameed, B., "Synthesis of fatty acid methyl ester from palm oil (*Elaeis guineensis*) with $K_y(MgCa)_{2x}O_3$ as heterogeneous catalyst", ***Bioresource Technology***, Vol. 102, No. 23, (2011), 10777-10783. (https://doi.org/10.1016/j.biortech.2011.09.033).
35. Alhassan, Y. and Kumar, N., "Single step biodiesel production from *pongamia pinnata* (Karanja) seed oil using deep eutectic solvent (DESs) catalysts", ***Waste and Biomass Valorization***, Vol. 7, (2016), 1055-1065. (https://doi.org/10.1007/s12649-016-9529-x).
36. Ezebor, F., Khairuddean, M., Abdullah, A.Z. and Boey, P.L., "Esterification of oily-FFA and transesterification of high FFA waste oils using novel palm trunk and bagasse-derived catalysts", ***Energy Conversion and Management***, Vol. 88, (2014a), 1143-1150. (https://doi.org/10.1016/j.enconman.2014.04.062).
37. Mendonça, I.M., Machado, F.L., Silva, C.C., Junior, S.D., Takeno, M.L., de Sousa Maia, P.J., Manzato, L. and de Freitas, F.A., "Application of calcined waste cupuaçu (*Theobroma grandiflorum*) seeds as a low-cost solid catalyst in soybean oil ethanolysis: statistical optimization", ***Energy Conversion and Management***, Vol. 200, (2019), 112095. (https://doi.org/10.10.16/j.enconman.2019.112095).
38. Abu-Jrai, A.M., Jamil, F., Ala'a, H., Baawain, M., Al-Haj, L., Al-Hinai, M., Al-Abri, M. and Rafiq, S., "Valorization of waste date pits biomass for biodiesel production in presence of green carbon catalyst", ***Energy Conversion and Management***, Vol. 135, (2017), 236-243. (https://doi.org/10.10.16/j.enconman.2016.12.083).
39. Betiku, E., Etim, A.O., Pereao, O. and Ojumu, T.V., "Two-step conversion of Neem (*Azadirachta indica*) seed oil into fatty methyl esters using a heterogeneous biomass-based catalyst: An example of cocoa pod husk", ***Energy & Fuels***, Vol. 31, No. 6, (2017), 6182-6193. (https://doi.org/10.1021/acs.energyfuels.7b00604).
40. Azcan, N. and Danisman, A., "Alkali catalyzed transesterification of cottonseed oil by microwave irradiation", ***Fuel***, Vol. 86, (2007), 2639-2644. (https://doi.org/10.1016/j.fuel.2007.05.021).

JREE: Vol. 9, No. 4, (Autumn 2022) 85-100

Journal of Renewable Energy and Environment

Journal Homepage: www.jree.ir

Materials and Energy Research Center

MERC

Review Article

Maiden Application and Control Parameter Sensitivity Analysis of Fractional Order Tilt Integral Derivative Controller in Standalone Solar Photovoltaic System

Anupama Subhadarsini*, Babita Panda, Byamakesh Nayak

Department of Electrical Engineering Technology, School of Electrical Engineering, KIIT deemed to be University, Bhubaneswar, India.

PAPER INFO

Paper history:
Received: 31 October 2021
Revised in revised form: 12 February 2022
Scientific Accepted: 27 February 2022
Published: 08 October 2022

Keywords:
Fractional Order Controller,
Optimal Performance,
Error Minimization,
HGPSJO,
FOTIDC

ABSTRACT

The solar photovoltaic system is modeled in Simulink using Matlab. Boost converter, FOTIDC controller, and Reduced Switch Multilevel Inverter are all included in this PV system (RSMLI). With regard to solar photovoltaic systems, the focus of this study is on the Fractional Order Tilt Integral Derivative Controller (FOTIDC). In the suggested control technique, Hybrid Genetic Particle Swarm Jaya Optimization is used to optimize the control parameters (HGPSJO). Jaya Optimization (JO) is a hybrid of the Particle Swarm Optimization (PSO), Genetic Algorithm (GA), and GA/PSO algorithm optimization techniques, combining the best of each for improved control executions. Control performance is enhanced using a fractional calculus-based technique to redesign the Tilt Integral Derivative Controller (TIDC) in order to reduce noise and harmonic distortions. Harmonic distortion and voltage magnitude are reduced by applying the proposed control method to the PV system. Simulated Matlab environments are used to test the stability, robustness, and stability of the proposed system as well as its capacity to reduce harmonic distortions. It is also compared to other well-known control techniques in order to ensure that the real-time implementation is properly validated.

https://doi.org/10.30501/jree.2022.312874.1274

1. INTRODUCTION

Depleting reserves of conventional resources have forced researchers to focus on the renewable form of energy as an alternative [1]. Rapid developments in the field of solar energy have appeared recently. Over the years, numerous control methods such as Proportional Integral Derivative Controller (PIDC), fuzzy, adaptive, neuro, optimal, and fractional controllers have been studied [2-7].

The use of fractional order calculus in control theory has led to the advent of fractional order controllers. The basic reason for choice of fractional order controllers is because it is seen to demonstrate capabilities of suppressing chaotic behavior of mathematical models. A fractional-order calculus controller creates a distribution of time constant. This implies that there is no particular time constant or resonating frequency which, in turn, improves system responses. Fractional order controllers are seen to demonstrate the capabilities of suppressing chaotic behavior in mathematical models [8-12]. While being used as controllers, they serve various purposes. The basic purposes include the overall stability system enhancement [13, 14], robustness promotion [15], disturbance rejection ability against parameter uncertainties [16], voltage and current stabilization [17-20], enhanced dynamic response of the system [21], optimal dynamic performance [22], power flow control between source and load, ripple rejection [23], better performance under abnormal operating condition [24], computational burden reduction [25-30], flexibility of system [31], frequency stabilization, harmonic minimization [32], changing operating conditions [33], multi-criteria control of parameters, maintainance of average voltage across load under various operating conditions, hunting reduction, efficient transient tracking, regulation of output voltage, maintaining constant Direct Current (DC) link voltage, power factor control, and improved power quality [34]. Use of a prefilter in the controller enhances the controller response compared to traditional controller and it will give less overshoot to the system. PIDC suffers from large time delay and poor control for an integrating process forced to look for an alternative. TIDC is a great viable alternative. In TIDC, the proportional gain of PIDC is replaced by a tilted component. The tilted component is having a transfer function of s^n. The resultant transfer function of TIDCF represents an optimal transfer function which improves the feedback response of the controller [35, 36]. TIDC has better disturbance rejection ability, precise tuning, robustness, minimizes the impact of parameter deviations, better stabilization from internal and external disturbances, and enhances the feedback control as compared to PIDC. The control parameters (Tilt Gain (K_t), Integral Gain (K_i), Derivative Gain (K_d), Coefficient of tilt (n), angle of Integral (α), and angle of derivative (β) of FOTIDC

*Corresponding Author's Email: anupamasubhadarsini@gmail.com (A. Subhadarsini)
URL: https://www.jree.ir/article_158613.html

Please cite this article as: Subhadarsini, A., Panda, B. and Nayak, B., "Maiden application and control parameter sensitivity analysis of Fractional Order Tilt Integral Derivative Controller in standalone solar photovoltaic system", ***Journal of Renewable Energy and Environment (JREE)***, Vol. 9, No. 4, (2022), 85-100. (https://doi.org/10.30501/jree.2022.312874.1274).

are tuned for a better response. There are many tuning methods like Ziegler Nichols method of tuning, time domain tuning, and frequency domain tuning. The advent of optimization algorithms provides better tuning methods.

Genetic Algorithm (GA), Particle Swarm Optimization (PSO) and JO Algorithm are the optimization algorithms employed. The convergence rate of GA and PSO is low, while the convergence rate of JO is higher, since GA has the ability to get stuck at local minima and PSO has the ability to get trapped at global maxima. In order to overcome the primary shortcomings of GA, PSO, and JO, it is necessary to combine all three optimization algorithms to establish an approach that enjoys efficiency and robustness.

It is critical to boost the voltage generated by the solar panels after selecting and fine-tuning the controller. Because the voltage generated by solar panels is so low, it cannot be used directly; instead, a boost converter is used to boost it [37-40]. An inverter is used to transform this stepped-up voltage into Alternating Current (AC). By employing a Reduced Switch Multilevel Inverter (RSMLI), which uses the same number of sources as a cascaded h-bridge multilevel inverter, it employs less switches [41], which can be achieved. These switches are triggered by a performance-improving technology known as Third Harmonic Injected Sinusoidal Pulse Width Modulation (THISPWM). To achieve the intended objective, an attempt was made to devise a new strategy, which is formulated as follows:

- Designing a single-phase PV model in a MATLAB/SIMULINK environment.
- Designing a novel control strategy HGPSJO-tuned FOTIDC with THISPWM for the PV system in order to improve the system performance and reduce harmonic distortions.
- Employing harmonic distortion analysis of a suggested PV system to support its superior performance.
- Improvement of the proposed PV model's robustness.
- Performing comparative analysis to certify the superiority of the proposed approach.
- Conducting sensitivity analysis on FOTIDC parameters.

According to this plan, Section 2 gives mathematical models for boosting converters, THISPWM, and RSMLI. The filter design of the proposed model is also examined in this section. Section 3 provides a more in-depth explanation of FOTIDC. Section 4 focuses on results and performance analysis in great detail. Section 5 is a conclusion that takes the future potential into account.

2. FORMULATION OF THE PROBLEM

The major components of the FOTIDC-based photovoltaic system are photovoltaic cell, non-ideal boost converter, FOTIDC, THI-SPWM, and RSMLI. Figure 1(a-f) represents the basic circuit of photovoltaic cell, non-ideal boost converter, averaging model of boost converter, model of RSMLI, model of FOTIDC-based photovoltaic system, and block diagram of the overall proposed photovoltaic system. The inputs to the solar cell are irradiance and temperature. This generated voltage is DC in nature and is very low in magnitude; hence, it is fed to step-up converter to step up its magnitude. THISPWM-based triggering circuit provides the switching pulses to RSMLI. The PV system's detailed model is examined in the following sections.

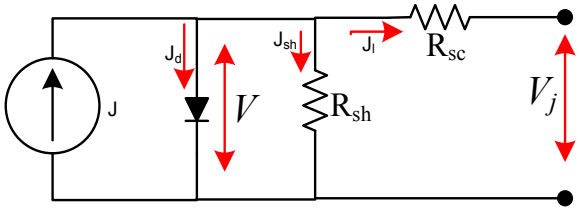

(a)

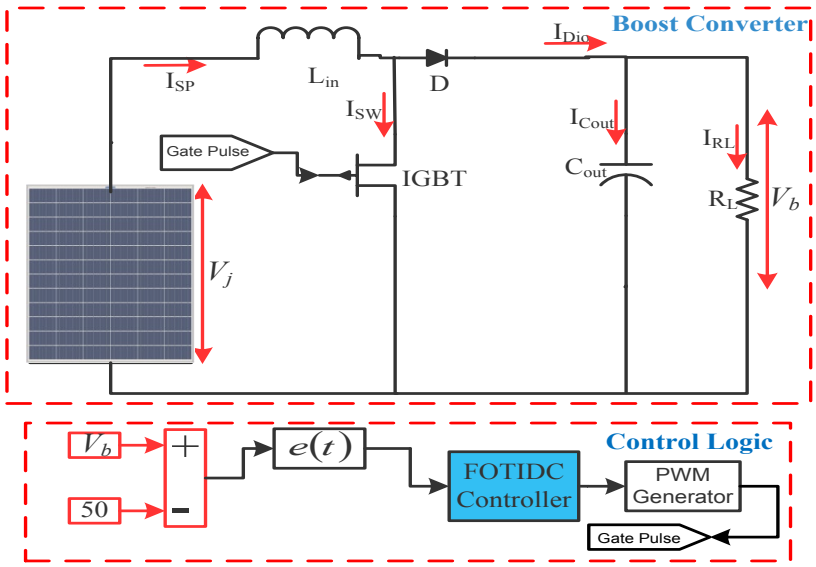

(b)

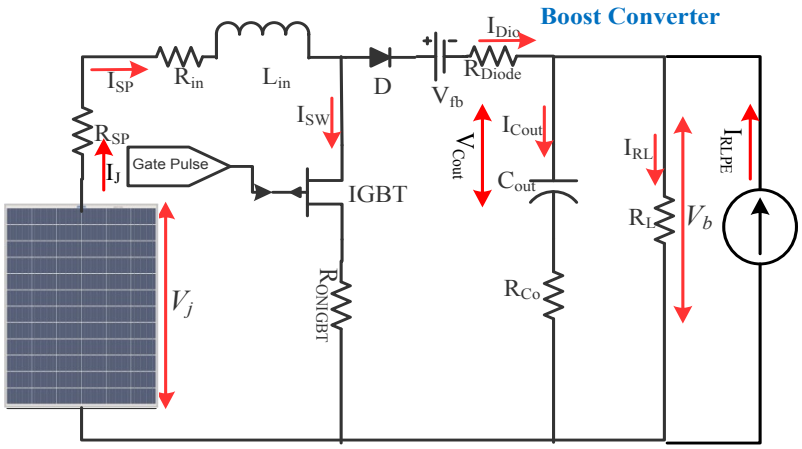
Boost Converter
I_{Dio}
I_{SP}
R_{in}
L_{in}
D
V_{fb}
R_{Diode}
I_{SW}
R_{SP}
I_J
Gate Pulse
IGBT
V_{Cout}
I_{Cout}
C_{out}
I_{RL}
I_{RLPE}
R_L
V_b
V_j
R_{ONIGBT}
R_{Co}

(c)

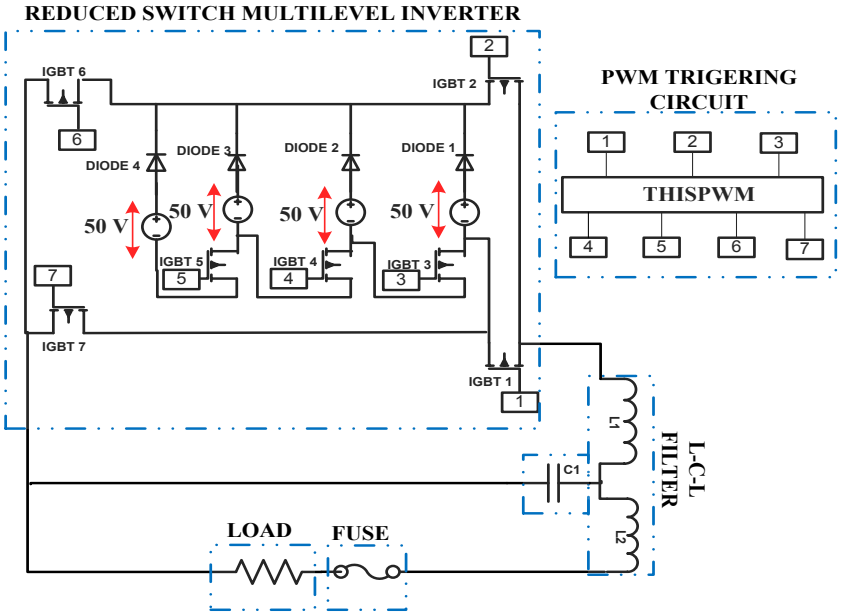
REDUCED SWITCH MULTILEVEL INVERTER
IGBT 6
IGBT 2
DIODE 4
DIODE 3
DIODE 2
DIODE 1
50 V
50 V
50 V
50 V
IGBT 5
IGBT 4
IGBT 3
IGBT 7
IGBT 1
PWM TRIGERING CIRCUIT
THISPWM
L1
L2
C1
L-C-L FILTER
LOAD
FUSE

(d)

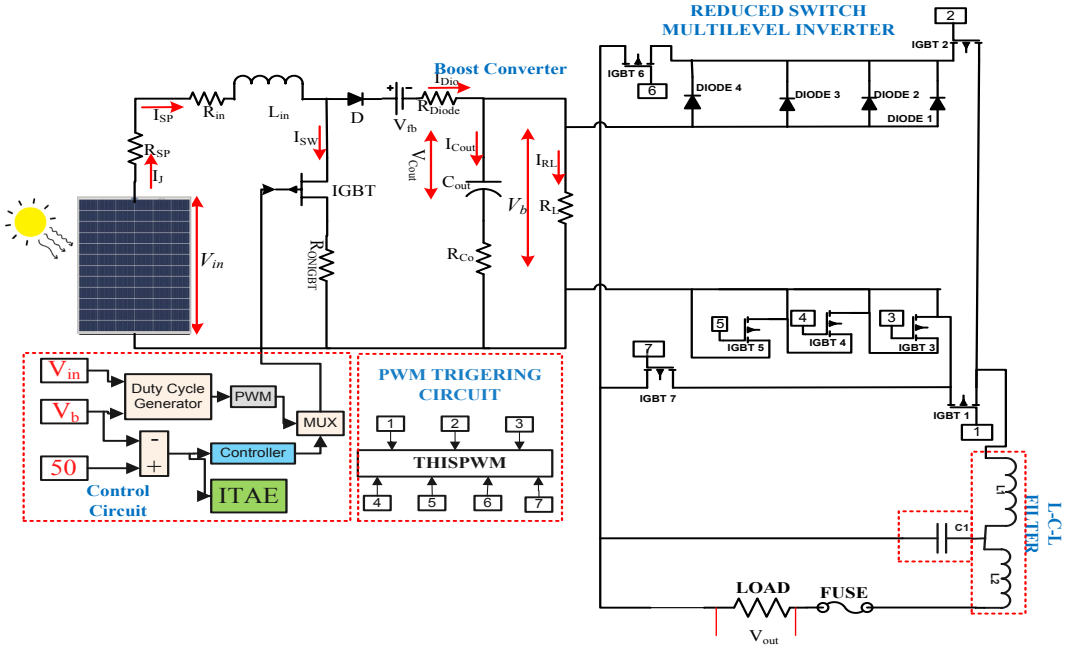
REDUCED SWITCH MULTILEVEL INVERTER
Boost Converter
I_{SP}
R_{in}
L_{in}
D
V_{fb}
R_{Diode}
I_{SW}
R_{SP}
I_J
IGBT
V_{Cout}
I_{Cout}
C_{out}
I_{RL}
V_b
R_L
R_{Co}
R_{ONIGBT}
V_{in}
IGBT 6
IGBT 2
DIODE 4
DIODE 3
DIODE 2
DIODE 1
IGBT 5
IGBT 4
IGBT 3
IGBT 7
IGBT 1
V_{in}
V_b
50
Duty Cycle Generator
PWM
MUX
Controller
ITAE
Control Circuit
PWM TRIGERING CIRCUIT
THISPWM
L1
L2
C1
L-C-L FILTER
LOAD
FUSE
V_{out}

(e)

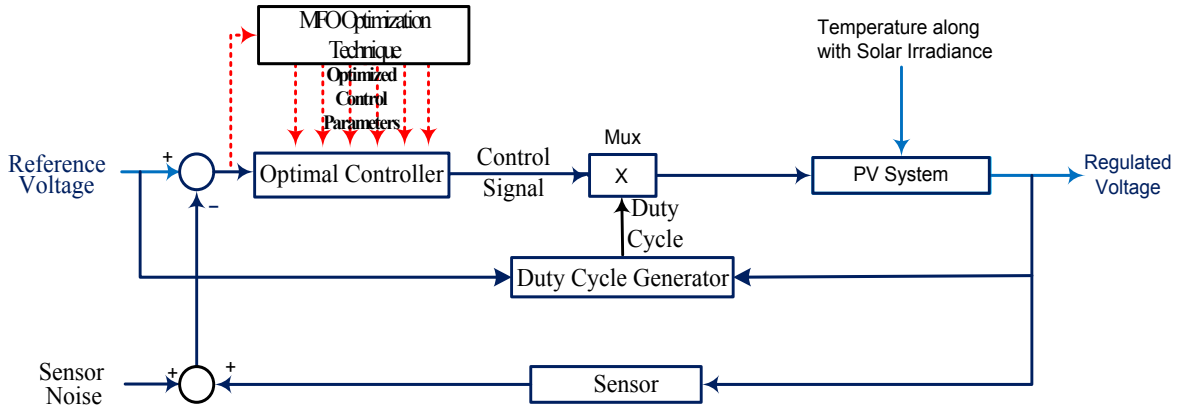

(f)

Figure 1. (a) Single diode model of solar PV cell, (b) Circuit diagram of boost converter, (c) Non-ideal model of boost converter, (d) Simulation model of the reduced switch multilevel inverter, (e) Model of FOTIDC-based photovoltaic system, and (f) Block Diagram of FOTIDC-based photovoltaic system

2.1. Photovoltaic cell

The photovoltaic cell is based on photo-electric effect which in turn depends on the presence of solar irradiance. Short-circuit current, open-circuit voltage, and maximum power point are the characteristics required for the design of photovoltaic cell. Figure 1(a) represents the equivalent circuit of the photovoltaic cell. Mathematically, the solar cell current can be represented as follows:

$$I = I_{pv} - I_O\left[\exp\left(\frac{qV}{akT}\right)\right] \tag{1}$$

Equation (1) fails to represent the characteristics of a photovoltaic array as there are several photovoltaic cells connected to form an array and it also requires additional parameters. This is achieved in Equation (2). The modified expression for the current generated by the photovoltaic cell is expressed as follows:

$$I = \frac{R_p}{R_s + R_p}\left(I_{PV} - I_0\left[\exp\left(\frac{V + R_s}{aV_t}\right) - 1\right] - \left(\frac{V}{R_p}\right)\right) \tag{2}$$

The summation of all structural resistances of the photovoltaic cell is represented by R_S. In order to compensate for the presence of leakage current in photovoltaic cell and different fabrication methods used by photovoltaic cell manufacturers, R_p is used. When the photovoltaic cell operates in the voltage source region, the influence of R_S is greater. Conversely, if the photovoltaic cell operates in the current source region, then the effect of R_p is greater. The value of R_S is lower than R_p. The standard value of R_S is taken in the range of 0.5-1.3 Ωcm^2. The standard value of R_p is taken in the range of 1-1000 $K\Omega cm^2$.

The energy generated by the photovoltaic cell is affected directly by the number of charge carriers present, which in turn depends upon the magnitude of solar irradiance incidences on the photovoltaic cell surface. I_{PV} in idyllic conditions is very difficult to determine as datasheets only inform about I_{SC}. Hence, it is assumed that for all photovoltaic cells, $I_{SC} \approx I_{PV}$. This assumption also holds ground as the value of R_S is lower than R_p. I_{PV} at (25 °C & 1 KW/m^2) depends upon solar irradiance and temperature and is mathematically expressed as:

$$I_{PV} = \left(\frac{R_S + R_P}{R_P} I_{SC} + K_I \Delta T\right)\frac{G}{G_n} \tag{3}$$

Mathematically, I_O can be represented as:

$$I_O = \frac{I_{SC} + K_I \Delta T}{\exp\left(\frac{V_{OC} + K_V \Delta T}{aV_t}\right) - 1}\left(\frac{T_n}{T}\right)^3 \exp\left[\frac{qE_g}{ak}\left(\frac{1}{T_n} - \frac{1}{T}\right)\right] \tag{4}$$

The diode identity factor is taken as 1.3. Upon substituting the values of I_{PV} and I_O into Equation (1), the modified expression for the current from photovoltaic cell is as follows:

$$I = \frac{R_p}{R_s + R_p}\left(\left(\frac{R_S + R_P}{R_P} I_{SC} + K_I \Delta T\right)\frac{G}{G_n} - \frac{I_{SC} + K_I \Delta T}{\exp\left(\frac{V_{OC} + K_V \Delta T}{aV_t}\right) - 1}\left(\frac{T_n}{T}\right)^3 \exp\left[\frac{qE_g}{ak}\left(\frac{1}{T_n} - \frac{1}{T}\right)\right]\left[\exp\left(\frac{V + R_s}{aV_t}\right) - 1\right] - \left(\frac{V}{R_p}\right)\right) \tag{5}$$

2.2. Boost converter

Boost converter steps up the magnitude of DC voltage. It is essential that the low voltages generated by solar arrays are in order of 20-25 volts and cannot be converted to alternating current quantities. Figure 1 (b) represents the model for boost converter. The boost converter consists of a diode (D), an Insulated Gate Bipolar Transistor (IGBT), a capacitor (C_{out}), and an inductor (L_{in}). In order to investigate the steady state and dynamical behaviour, it is essential to model the boost

converter dynamically. There are many methods to mathematically model the boost converter. Some of the populous methods include switching flow graph, averaging technique, state space technique, current injection technique, and bond graph method. All of these methods have their share of advantages and disadvantages. However, in most of these techniques, all elements of boost converter are considered ideal. Hence, an ideal control strategy is never formulated. When the elements are not considered ideal, then an effective and ideal switching technique is formulated. The boost converter is modeled by using a non-ideal state space averaging technique.

2.2.1. Non-ideal boost converter

The non-ideal model of boost converter is represented in Figure 1(c). The parasitic resistance and equivalent resistances are also represented in the circuit. R_{SP} represents the internal resistance of the PV system. R_{in} represents the Equivalent Series Resistance (ESR) of inductor. ESR value of the inductor is less than 1 Ω. The internal resistance of IGBT is represented by R_{ONIGBT}. The ESR resistance connected in series with C_{out} is R_{Co}. The typical value of R_{Co} is less than 1 Ω. The resistance of diode D is represented by R_{Diode}. The forward voltage drop of diode is represented by a voltage source, named as V_{fb}. The switching operation of IGBT present in boost converter is divided into two time frames. The time frames are on time and off time. The analysis is done separately for both on time and off time [3].

2.2.2. During IGBT on time

The input loop equation of the boost converter is represented by:

$$L_{in}\frac{dI_{SP}(t)}{dt} = -(R_{lin} + R_{ONIGBT} + R_{SP})I_{SP}(t) + V_j(t) \quad (6)$$

In order to analyse the non-ideal modelling of the boost converter, small perturbation is applied to the boost converter. This current perturbation is I_{RLPE}. The non-ideal model of the boost converter is represented in Figure 1(c, d). The current across capacitor C_{out} is represented in Equation (7).

$$I_{Cout}(t) = \frac{C_{out}dV_{Cout}(t)}{dt} = \frac{(R_L \| R_{Co})}{(R_L + R_{Co})}V_{Cout}(t) - \frac{(R_L \| R_{Co})}{R_{Co}}I_{RLPE}(t) \quad (7)$$

The output voltage is represented by Equation (8).

$$V_b(t) = \frac{(R_L \| R_{Co})}{(R_{Co})}V_{Cout}(t) - (R_L \| R_{Co})I_{RLPE}(t) \quad (8)$$

Equations (6-8) can be written in a state space equation form. The state variables are $Z_2(t) = |I_{SP}(t)\ V_{Cout}(t)|^T$, $u(t) = |V_b(t)\ I_{RLPE}(t)|^T$, and $y(t) = |V_b(t)\ I_J(t)|^T$.

$$\left.\begin{aligned} \dot{z}_2(t) &= A_{w1}z_2(t) + B_{w1}u(t) + G_{w1}V_{fb} \\ y(t) &= C_{w1}z_2(t) + E_{w1}u(t) + H_{w1}V_{fb} \end{aligned}\right\} \quad (9)$$

The state space matrices are represented below.

$$A_{w1} = \begin{vmatrix} \frac{-(R_{ONIGBT} + R_{in} + R_{SP})}{L_{in}} & 0 \\ 0 & -\frac{(R_L \| R_{Co})}{(C_{out}R_L R_{Co})} \end{vmatrix};$$

$$G_{w1} = |0 \quad 0|^T; \quad H_{w1} = |0 \quad 0|^T; \quad C_{w1} = \begin{vmatrix} 0 & \frac{(R_L \| R_{Co})}{(R_{Co})} \\ 1 & 0 \end{vmatrix};$$

$$B_{w1} = \begin{vmatrix} \frac{1}{L_{in}} & 0 \\ 0 & -\frac{(R_L \| R_{Co})}{(C_{out}R_{Co})} \end{vmatrix}; \quad E_{w1} = \begin{vmatrix} 0 & -(R_L \| R_{Co}) \\ 0 & 0 \end{vmatrix} \quad (10)$$

2.2.3. During IGBT off time

When IGBT is turned off and diode D is conducting, the input equation of boost converter is represented by:

$$L_{in}\frac{dI_{SP}(t)}{dt} = -\left((R_L + R_{Diode} + R_{SP}) + (R_L \| R_{Cout})\right)I_{SP}(t) - \frac{(R_L \| R_{Cout})}{R_{Cout}}V_{Cout}(t) + V_j(t) + (R_L \| R_{Cout})I_{RLPE}(t) - V_f \quad (11)$$

The current across capacitor C_{out} is represented in Equation (12).

$$I_{Cout}(t) = \frac{C_{out}dV_{Cout}(t)}{dt} = \frac{(R_L \| R_{Co})}{(R_{Co})}I_{RL}(t) - \frac{(R_L \| R_{Co})}{R_L R_{Co}}V_{Cout}(t) - \frac{(R_L \| R_{Co})}{(R_{Co})}I_{RLPE}(t) \quad (12)$$

The output voltage is represented by Equation (13).

$$V_b(t) = \frac{(R_L \| R_{Co})}{(R_{Co})}V_{Cout}(t) - (R_L \| R_{Co})I_{RLPE}(t) + (R_L \| R_{Co})I_{RL}(t) \quad (13)$$

Equations (11-13) can be written in the state space equation form. The state variables are $Z_2(t) = |I_{SP}(t)\ V_{Cout}(t)|^T$, $u(t) = |V_b(t)\ I_{RLPE}(t)|^T$, and $y(t) = |V_b(t)\ I_J(t)|^T$.

$$\left.\begin{aligned} \dot{z}_2(t) &= A_{w2}z_2(t) + B_{w2}u(t) + G_{w2}V_{fb} \\ y(t) &= C_{w2}z_2(t) + E_{w2}u(t) + H_{w2}V_{fb} \end{aligned}\right\} \quad (14)$$

The state space matrices are represented below.

$$A_{w2} = \begin{vmatrix} \frac{-(R_{Diode}+R_{SP}+R_L)+((R_L \| R_{Co}))}{L_{in}} & 0 \\ 0 & -\frac{(R_L \| R_{Co})}{(C_{out}R_L R_{Co})} \end{vmatrix};$$

$$B_{w2} = \begin{vmatrix} \frac{1}{L_{in}} & \frac{(R_L \| R_{Co})}{L_{in}} \\ 0 & -\frac{(R_L \| R_{Co})}{(C_{out}R_{Co})} \end{vmatrix}; \quad C_{w2} = \begin{vmatrix} (R_L \| R_{Co}) & \frac{(R_L \| R_{Co})}{(R_{Co})} \\ 1 & 0 \end{vmatrix};$$

$$E_{w2} = \begin{vmatrix} 0 & -(R_L \| R_{Co}) \\ 0 & 0 \end{vmatrix} \quad G_{w2} = \begin{vmatrix} \frac{-1}{L_{in}} & 0 \end{vmatrix}^T; \quad H_{w2} = \begin{vmatrix} 0 & 0 \end{vmatrix}^T; \quad (15)$$

The overall averaged non-ideal state space model of the boost converter is obtained by using Equations (9 and 14). The overall averaged non-ideal state space matrices are represented by Equation (16).

where D is duty cycle and $\tilde{D}$ = 1-D. The overall state space matrices of the averaged non-ideal model of the boost converter are represented by Equation (17).

$$\left.\begin{aligned} A_{avg} &= DA_{w1} + \tilde{D}A_{w2} \quad B_{avg} = DB_{w1} + \tilde{D}B_{w2} \quad C_{avg} = DC_{w1} + \tilde{D}C_{w2} \\ E_{avg} &= DE_{w1} + \tilde{D}E_{w2} \quad G_{avg} = DG_{w1} + \tilde{D}G_{w2} \quad H_{avg} = DH_{w1} + \tilde{D}H_{w2} \end{aligned}\right\} \quad (16)$$

$$A_{avg} = \begin{vmatrix} \frac{-\left(\left(DR_{ONIGBT} + \tilde{D}R_{Diode} + R_{SP} + R_{in}\right)\left(R_L + R_{Cout}\right) + D\tilde{D}R_L R C_{out}\right)}{L_{in}} & \frac{\tilde{D}\left(R_L \| R_{Co}\right)}{\left(L_{in}R_{Co}\right)} \\ \frac{\tilde{D}\left(R_L \| R_{Co}\right)}{\left(C_{out}R_{Co}\right)} & -\frac{\left(R_L \| R_{Co}\right)}{\left(C_{out}R_L R_{Co}\right)} \end{vmatrix}; \quad B_{avg} = \begin{vmatrix} \frac{1}{L_{in}} & \frac{\tilde{D}\left(R_L \| R_{Co}\right)}{L_{in}} \\ 0 & -\frac{\left(R_L \| R_{Co}\right)}{\left(C_{out}R_{Co}\right)} \end{vmatrix};$$

$$C_{avg} = \begin{vmatrix} \tilde{D}\left(R_L \| R_{Co}\right) & \frac{\left(R_L \| R_{Co}\right)}{\left(R_{Co}\right)} \\ 1 & 0 \end{vmatrix}; \quad E_{avg} = \begin{vmatrix} 1 & -\left(R_L \| R_{Co}\right) \\ 0 & 0 \end{vmatrix}; \quad G_{avg} = \begin{vmatrix} -\frac{\tilde{D}}{L_{in}} \\ 0 \end{vmatrix}; \quad H_{avg} = \begin{vmatrix} 0 \\ 0 \end{vmatrix} \quad (17)$$

The Transfer Function is defined as the ratio of Laplace transform of output to Laplace transform of input. The transfer function for the non-ideal boost converter is the ratio of output voltage to input voltage. This can be obtained by conducting small signal analysis of the non-ideal boost converter. Mathematically, it is expressed through Equation (18).

$$TF(s) = \frac{V_b(s)}{V_j(s)} = C_{avg}\left(sI - A_{avg}\right)^{-1}B_{avg} + E_{avg} \quad (18)$$

I is the unitary matrix and S is the Laplace operator.

2.3. Reduced switch multilevel inverter (RSMLI)

The stepped-up DC voltage from boost converter is fed to the inverter circuit to convert into AC. The choice of the inverter is the reduced switch multi-level inverter which is an improvised version of the cascaded h-bridge multilevel inverter. The improvisation made in cascaded h-bridge multilevel inverter technology is the reduction of effective switch count while keeping the number of sources the same [31-34]. The RSMLI is represented by Figure 1(d). The choice of RSMLI is listed out as follows:

- RSMLI manages to reduce voltage stress as compared to other inversion techniques.
- The use of transformers is naturally eliminated by choosing RSMLI.
- Total Harmonic Distortion (THD) values are lower.
- RSMLI has high-quality output with better electromagnetic compatibility.

Mathematically, the number of switches and sources required is dependent on the number of levels of RSMLI. The RSMLI used in this proposed manuscript is a 9-level RSMLI. Nine-level RSMLI is chosen because below 9-level harmonic distortion is dominant and above the 9-level mode, the triggering mechanism is becoming very complex, which tends to make the circuit redundant and often to reduce efficiency. Equations (19 and 20) give mathematical expressions for the quantity requirement of source and switches for the 9-level RSMLI.

$$\text{Number of sources} = \frac{\text{Level}-1}{2} \quad (19)$$

$$\text{Number of Controlled Switching devices} = \frac{\text{Level}+5}{2} \quad (20)$$

Level indicates the level of RSMLI. In this proposed manuscript from Equations (19 & 20) for 9-level RSMLI, the number of sources and controlled switches is 4 and 7, respectively. The switches include IGBT 1, IGBT 2, IGBT 3, IGBT 4, IGBT 5, IGBT 6, and IGBT 7. IGBT 1, IGBT 5,

IGBT 6, and IGBT 7 form the basis of bridge circuit of RSMLI. IGBT 1 and IGBT 5, IGBT 6, and IGBT 7 are connected as complimentary pairs. IGBT 1 and IGBT 5 are used to provide the negative half cycle, while the positive half cycle is provided by IGBT 6 and IGBT 7. IGBT 2, IGBT 3, and IGBT 4 are used when there is a need to supply the peak voltage. The reason for choosing 9-level RSMLI is:

- Below 9-level mode, harmonic disturbance is quite dominant making it difficult to operate;
- Above 9-level mode, the triggering mechanism becomes more complex;
- Soft switching technique is applicable to tuning of RSMLI; and
- In the case of higher level RSMLI, there is no sufficient reduction in harmonic.

2.3.1. Harmonics in RSMLI

Harmonic distortions present in electrical signals affect the power systems in many possible ways like heating effects, electromagnetic emissions, and an irritant trip of circuit breakers and reduction of power factors amongst many others [36]. A harmonic distortion present in electrical signals is measured by Total Harmonic Distortion (THD). THD is expressed mathematically through the expression Equation (21).

$$THD = \sqrt{\frac{((i_2)^2 + (i_3)^2 .....(i_n)^2)}{i_1}} \times 100\% \quad (21)$$

where the fundamental component is i_1, while i_2, i_3 … i_n represent the harmonic components. This situation calls for maintaining lower values of harmonics as lower value points to higher values of efficiency, power factor, and lower value of peak current.

2.4. Third harmonic injected sinusoidal pulse width modulation (THISPWM)

The triggering pulses for RSMLI are generated by PWM technique. The choice of PWM is taken as Third Harmonic Injected Sinusoidal Pulse Width Modulation (THI-SPWM) [35]. THI-SPWM as the name suggests that the third harmonic component is added to the sinusoidal reference. The addition of the third harmonic component to the sinusoidal reference improves the response of RSMLI. With reference to the sinusoidal signal, the harmonic injected is one-sixth of the amplitude. The peak magnitude of the carrier wave and modified sinusoidal reference are denoted by V_{car} and V_{ref}, respectively. The modified reference is represented mathematically by Equation (22).

$$V_{ref} = V_1 c_{max} \text{ Sin } (\omega t) + V_3 c_{max} \text{ Sin } (3\omega t) \quad (22)$$

where the fundamental component is represented by $V_1 c_{max}$ and injected third harmonic component is represented by $V_3 c_{max}$. The intersection of the carrier wave with the modified reference sets the operating point of THI-SPWM. The triggering pulse is generated after comparing the magnitudes of the carrier wave and the modified sinusoidal reference. If the magnitude of the modified wave is greater than that of carrier wave, then a positive trigger wave is generated, and vice versa. The extent to which modulation is done with a carrier signal is called as modulation index (m_a). Alternatively, m_a is defined as the relation between the ratios of modified reference voltages to carrier voltage. m_a is represented mathematically by Equation (23).

$$m_a = \frac{V_{ref}}{V_{car}} \quad (23)$$

The input voltage to RSMLI is V_b, while the Root Mean Square (RMS) value of the output of RSMLI is represented by V_{out} volts. The relationship between V_b and V_{out} is represented by Equation (24).

$$V_{out} = V_b \sqrt{\left(\sum_{b=1}^{2n} \frac{2T_{on}}{T \times \pi} \right)} \quad (24)$$

The time period is represented by T. The width of the n^{th} pulse is denoted by T_{on}.

2.5. Filter

The current and voltage signals from micro inverters often contain disturbances and harmonic components. The purpose of filter is to filter out unwarranted disturbances coming from micro inverter. A L-C-L type filter remains in the scope of this paper. The proposed filter has a better response than other types of filter. The base impedance (Z_b) for the proposed L-C-L type filter is expressed by Equation (25). Equation (26) and Equation (27) represent the mathematical formularies for base capacitance (C_b) and maximum values of load current (I_{max}), respectively.

$$z_b = V_{bn}{}^2 p_l^{-1} \quad (25)$$

$$C_b = (\omega_g Z_b)^{-1} \quad (26)$$

$$I_{max} = 0.333 * P\sqrt{2} * \left(V_f\right)^{-1} \quad (27)$$

The active power and the filter voltage are represented by P_l and V_f, respectively. A tolerance of 10 % is accommodated in the values of design parameters for robustness purposes. The change in load current accommodating 10 % variation and the value of inverter side inductance are given by Equations (28 and 29) separately. The switching frequency and DC link voltage are represented by f_{sw} and V_b, respectively.

$$\Delta I_{max} = 0.10 \times I_{max} \quad (28)$$

$$L_1 = \frac{V_b}{6 \times f_{sw} \times \Delta I_{max}} = \frac{V_b}{0.6 \times f_{sw} \times I_{max}} \quad (29)$$

A 10 % variation in the capacitance of the filter is allowed. Equation (30) represents the capacitance of the filter. The DC link side inductor is having a value of L_2 and is expressed mathematically by Equation (31).

$$C_f = 0.05 \times C_b \quad (30)$$

$$L_2 = \frac{\sqrt{\left(k_a^{-2}+1\right)}}{C_f \times \left(f_{sw}\right)^2} \quad (31)$$

The attenuation factor is represented by k_a. In order to compensate for the ripple effects, electromagnetic interference and resonance in a resistor with resistance (R_f) is inserted in series with a filter capacitor. The resonant frequency is denoted by f_{res}. The value of R_f is expressed mathematically by Equation (32).

$$R_f = (3C_f \times \omega_{res})^{-1} \quad (32)$$

Equations (25-32) help formulate a filter strategy for photovoltaic system, which is established in the simulation model, as shown in Figure 1(d, e).

2.6. Open loop analysis of photovoltaic system

The performance analysis of the open-loop model of the proposed PV system is analysed in the subsequent sub-sections.

2.6.1 Open-loop PV system's boost converter performance analysis

In the open-loop mode of the proposed PV system, the triggering pulse is provided through the pulse generator. IGBT is switched at 30 kHz. The voltage input is 20 volts. This value may increase up to 50 volts. The output voltage waveform for boost converter is represented in Figure 2. The output of the boost converter is fed as input to the inverter.

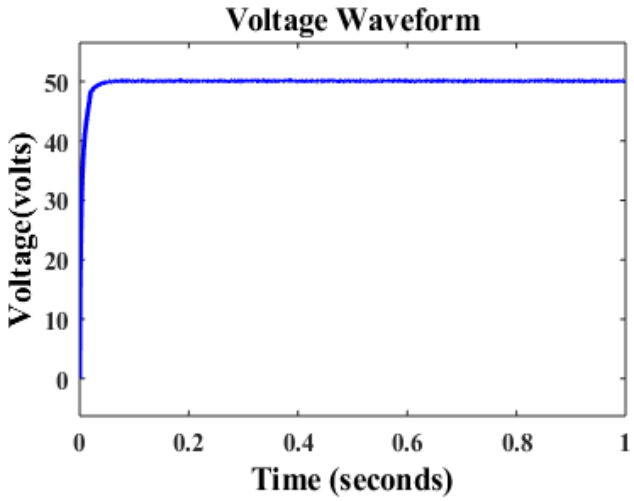

Figure 2. Boost converter response voltage waveform for the open-loop mode

2.6.2. Reduced switch multilevel inverter (RSMLI) performance analysis

The magnitude of the output voltage is 260 volts; this is represented in Figure 3(a). Figure 3(b) represents output current whose magnitude is 2.54 ampere. The load used is Resistive-Inductive (RL) load. The power is represented in Figure 3(c) having a magnitude of 670 watts. The waveform is not perfectly sinusoidal in nature and this loss in the waveform is due to nonlinearities present in the circuit. THD is a measure of the performance of the proposed circuit. The Voltage Total Harmonic Distortion (THD_V) was found to be 23.65 %, as depicted in Figure 4(a). However, Current Total Harmonic Distortion (THD_i) was found to be 23.07 %, as depicted in Figure 4(b).

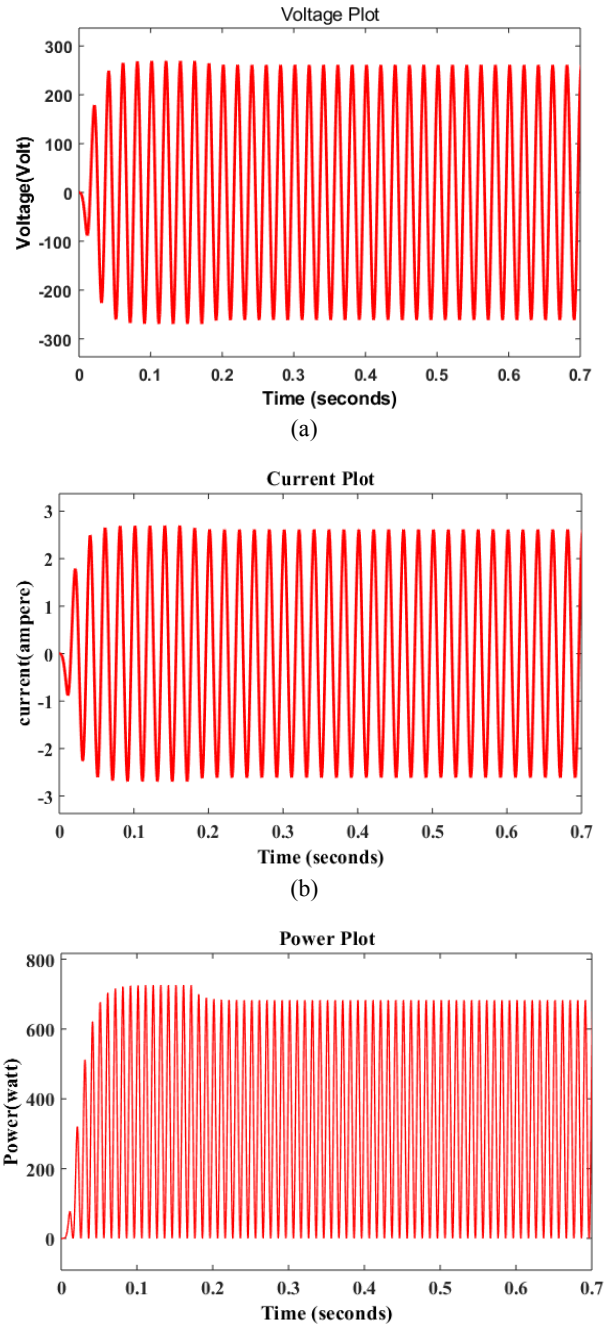

Figure 3. Responses of RSMLI of open-loop PV system: (a) Output voltage; (b) Output current; (c) Output power.

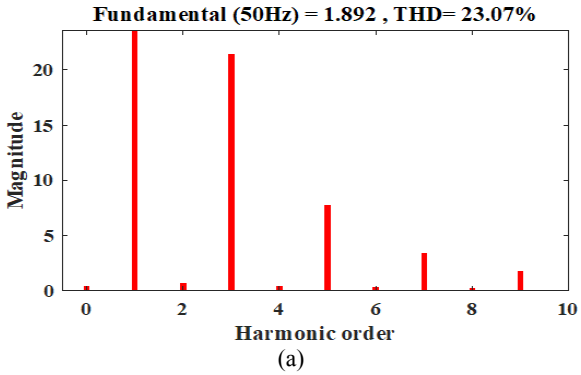

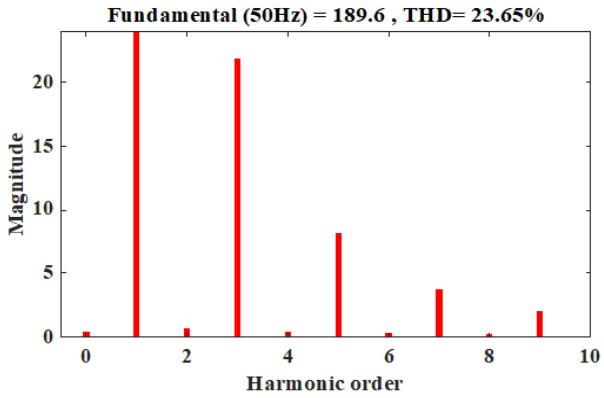

(b)

Figure 4. Performance plots for open-loop PV system: (a) Voltage harmonic analysis plot; (b) Current harmonic analysis plot.

According to Figures 3 and 4, the response of open-loop PV is not optimal and it requires an implementation of a controller. The FOTIDC is explained in the next section.

3. CONTROL ALGORITHM

The proposed control approach uses Tilt Integral Derivative Controller with Filter (TIDCF).

3.1. FOTIDC

FOTIDC is similar to PID controller. The major difference lies in the proportional gain of a compensator having a transfer function represented by $K_t s^{-n}$. For FOTIDC, the suitable value of n is taken between 2 and 3. It is chosen as 3 in this paper. This controller belongs to the family of fractional order controllers. The tilted behaviour provides a feedback gain as a function of frequency, which is tilted with respect to the gain of conventional compensator. The control signal ($U_{TID}(S)$) for the FOTIDC can be generated using the transfer function of the gain of the FOTIDC ($G_{TID}(S)$), error signal ($E_{TID}(S)$), reference signal ($R_{TID}(S)$), and output signal ($Y_{TID}(S)$). This is explained by Equations (33-35).

$$U_{TID}(S) = G_{TID}(S)E_{TID}(S) \tag{33}$$

$$E_{TID}(S) = R_{TID}(S) - Y_{TID}(S) \tag{34}$$

where

$$G_{TID(s)} = \frac{C_{OUT(s)}}{E_{TID(s)}} = K_t \times S^n + \frac{K_i}{S^\alpha} + K_d \times S^\beta \tag{35}$$

The control parameters (Tilt Gain(K_t), Integral Gain (K_i), Derivative Gain(K_d), Coefficient of tilt (n), angle of Integral (α), and angle of derivative (β)) of FOTIDC are tuned for better response. FOTIDC produces a higher degree of freedom in control parameters. FOTIDC is a Fractional Order controller. This serves good in eliminating disturbances quickly and efficiently. There is a need to optimize the control parameters of the controller. This is achieved through the application of a proper optimization algorithm.

3.2. Optimization algorithm

The advent of optimization algorithms provides better tuning methods. The optimization algorithms used are Genetic Algorithm (GA), Particle Swarm Optimization (PSO), and Jaya Algorithm (JA). These algorithms are hybridized and are applied to the parameter optimization of TIDCF. This is explained in sections appended below.

3.2.1. Genetic algorithm

Genetic Algorithm is a metaheuristically inspired process of natural selection that belongs to a larger class of evolutionary algorithms [3]. It obtains a high-quality solution to optimize and search problems using biological operators like mutation, crossover, and selection. A genetic algorithm requires a genetic representation of the solution and a fitness function to the solution domain.

3.2.2. Particle swarm optimization

PSO algorithm is one of the optimization techniques and a kind of evolutionary computation technique. It iteratively tries to improve or find a better solution with respect to a given measure of quantity [4]. PSO is a metahuristic as it makes no or the least number of assumptions about the problem being optimized and can search large spaces.

3.2.3. Jaya algorithm

Jaya algorithm always tries to get closer to success while avoiding failures. It tries to get closer to an optimal solution without being struck at any local minima and maxima [5]. The JA variables include population size, number of design variables, and termination criteria (iterations). The entire JAYA algorithm is based on Equation (23). The objective function is either to be minimized or maximized depending upon the proposed criteria for optimization. For any iteration i, it is assumed that m is the number of design variables and n is the number of candidates in a population. The best and worst solutions are represented by $X_{j,best,i}$ and $X_{j,worst,i}$ respectively. If $X_{j,k,i}$ is the value for the j^{th} variable, the k^{th} candidate of population during the i^{th} iteration is obtained. Then, the value is given by Equation (36).

$$X'_{l,n,i} = X_{l,n,i} + r_{1l,i}(X_{l,best,i} - |X_{l,n,i}|) - r_{2l,i}(X_{l,worst,i} - |X_{l,n,i}|) \tag{36}$$

where, $X'_{l,n,i}$ represents the new value of the controller parameter to be determined and $X_{l,n,i}$ represents the previously calculated value. $X_{l,best,i}$ and $X_{l,worst,i}$ represent the best and worst solutions of the optimization problem. $r_{1l,i}$ and $r_{2l,i}$ are two random variables for the l^{th} variable at the i^{th} iteration which have values between [0, 1], respectively.

3.2.4. Hybrid genetic particle swarm jaya algorithm (HGPSJA)

Hybrid Genetic Particle Swarm Jaya Algorithm (HGPSJA), as the name indicates, is a combination of 3 optimization algorithms. It combines the benefits of GA, PSO, and JA. This algorithm solves the problem of solution being struck at local minima or maxima. At first, PSO algorithm is employed to find the initial fit for the control parameters. Then, GA is applied to find intermediate fit of control parameter values. In the final step, JA is applied to find an optimal solution for the control parameters. The process is very swift and reduces the value of performance index to a very low value.

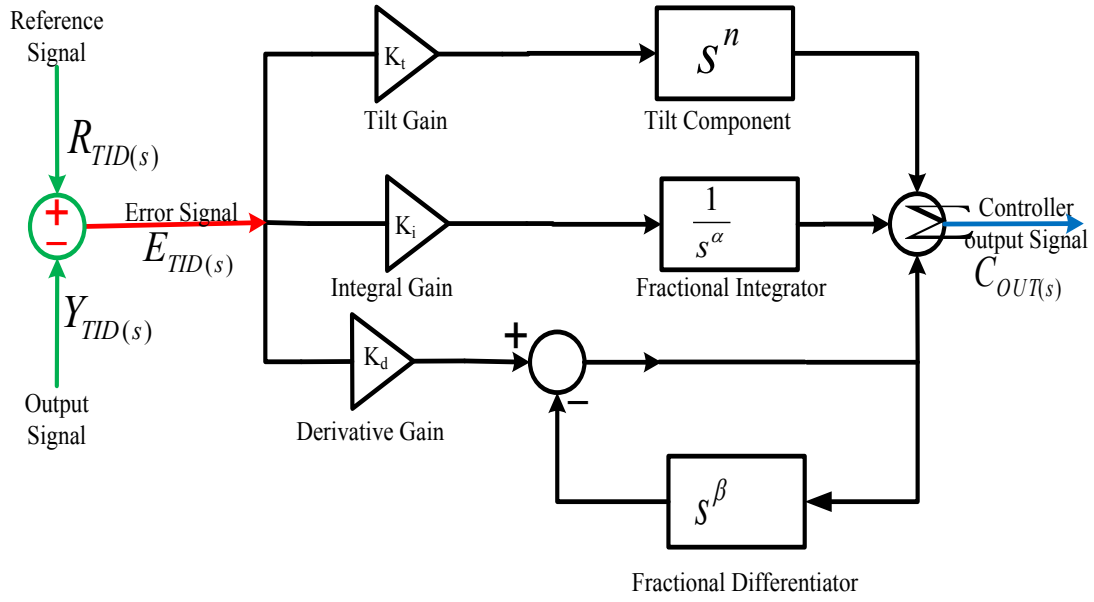

(a)

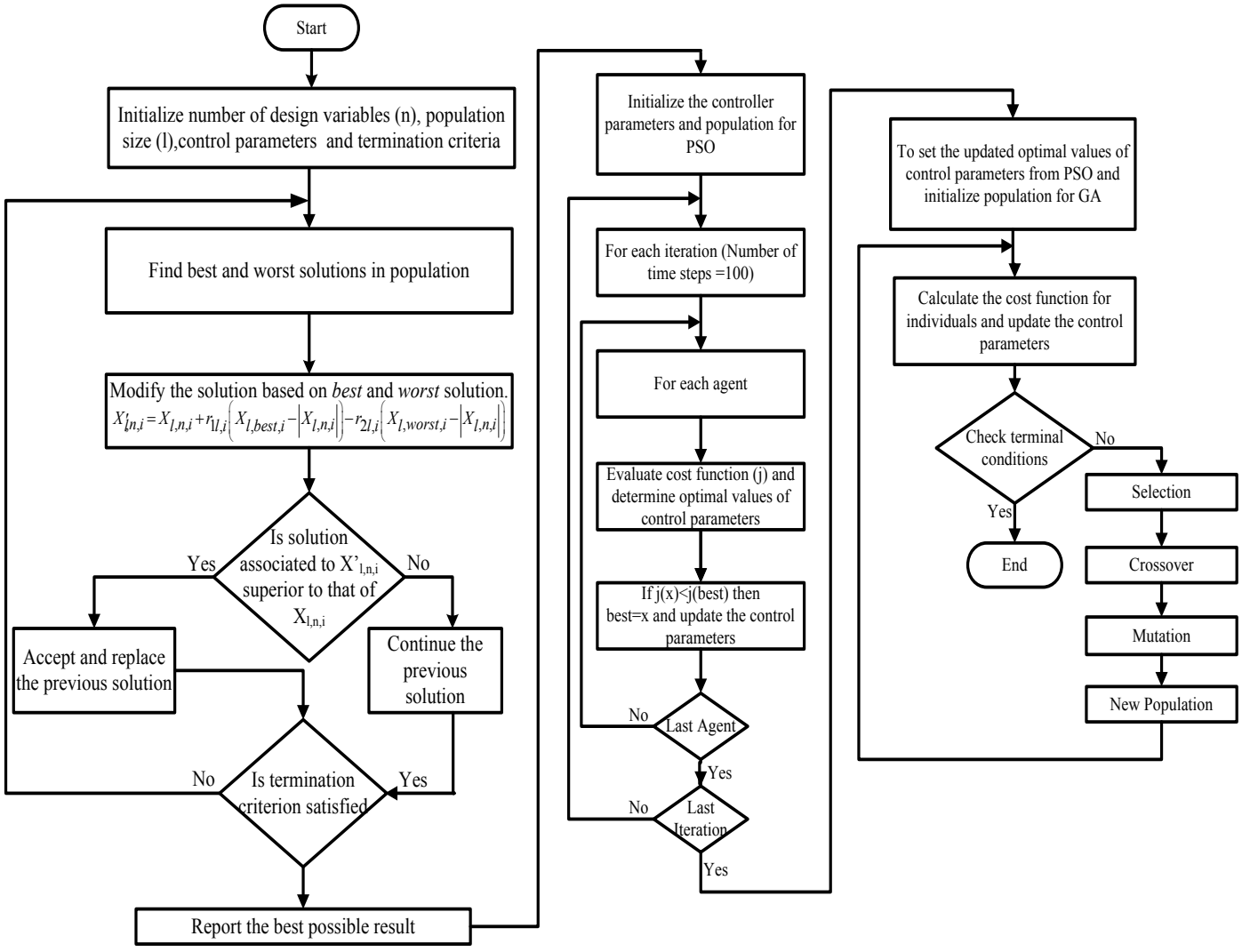

(b)

Figure 5. (a) Model of tilt integral derivative controller with filter (TIDCF), (b) Hybrid genetic particle swarm jaya algorithm (HGPSJA)

3.3. Cost function

A number of performance evaluation measures like maximum overshoot, peak time, settling time, rise time and damping ratio, etc. must be checked while designing a complex control system. However, it is not only a time consuming but also a hit-and-trial-based procedure. When input and operational conditions vary, it is cumbersome to analyse this measure. Performance index analysis has a selectivity feature which enables it to differentiate between optimal and non-optimal responses. Hence, the performance index criteria are good evaluation tools. Sensitivity of a controller can easily be predicted through analysis of its performance indexes. Performance index can be used as standard for controller design and optimization. Cost function and minimization or maximization function are closely related to each other. Hence, the cost function does play a role in designing and optimization of controllers. Broadly speaking, there are three performance indexes. They are Integral Time Absolute Error (ITAE), Integral Square Error (ISE), Integral Absolute Error (IAE). The mathematical equivalence is represented in Equation (37).

$$\left.\begin{aligned} \text{ITAE} &= \int t.\,|\,e(t)\,|\,dt \\ \text{IAE} &= \int |\,e(t)\,|\,dt \\ \text{ISE} &= \int |\,e(t)\,|^2\,dt \end{aligned}\right\} \quad (37)$$

ISE and IAE are less sensitive and computationally not compatible owing to these conditions; and ITAE is chosen as a performance index criterion. The parameters for different optimization algorithms are summarized in Table 1.

Table 1. Parameters of HGPSJO algorithm

Parameters	HGPSJO
No. of iterations	100
Mutation factor	0.7
Crossover factor	0.9
No. of population	200
No. of design variables	6
Cognitive factor	1.4
Social factor	1.4
Inertia weight	0.785
Random variable-1	1
Random variable-2	1

4. RESULT AND DISCUSSION

The detailed analysis of HGPSJA-tuned FOTIDC based closed-loop system is discussed in the appending sub-sections.

4.1. Closed loop response

The closed-loop or FOTIDC-based response of the proposed photovoltaic system is discussed in the sections appended below. The system is analysed in terms of performance, stability, and robustness.

4.1.1. Boost converter

The voltage generated by solar panels is so small that it is useless. As a result, the voltage must be increased in magnitude. A boost converter is employed to do this. In order to increase the voltage, it is escalated to 50 volts. Figure 6 depicts the situation.

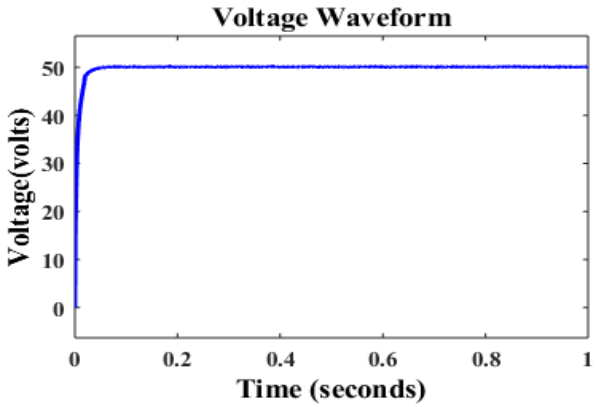

Figure 6. DC voltage output of the boost converter

4.1.2. RSMLI

RSMLI receives this boosted voltage. This, then, converts the voltage to an alternating one. This induced voltage has a magnitude of 254 volts. It is represented in Figure 7. The inverter is connected to a load of $100 + 240e^{-3}$ j Ω. The steady-state current generated by the load is 2 amperes, as given in Figure 8. As shown in Figure 9, the load draws 508 watts of electricity.

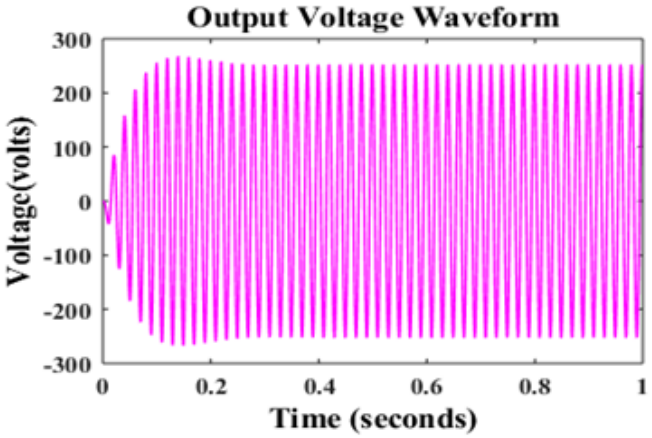

Figure 7. Output voltage of RSMLI

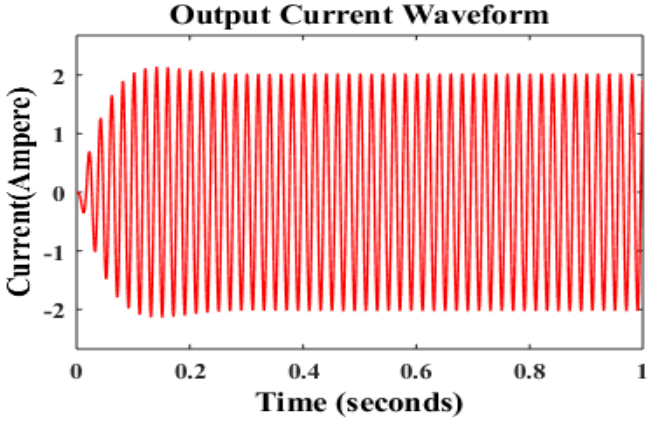

Figure 8. Output current of RSMLI

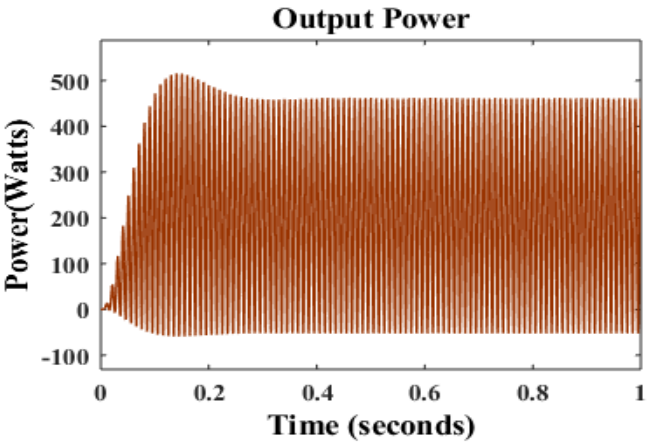

Figure 9. Output power of RSMLI

4.1.3. Robustness

Figure 10 (a-d) represents the variation in temperature, irradiance, fluctuation of boost converter output voltage, and fluctuation of RSMLI (inverter) output voltage. Boost converter output voltage fluctuates from 49 volts at 800 watt/m^2 to 53 at 1150 watt/m^2. Inverter voltage fluctuates from 249 volts to 256 volts. Solar power generation can be fluctuatory in nature. Hence, a power system frequency response plot indicates the efficacy and effectiveness of the proposed model.

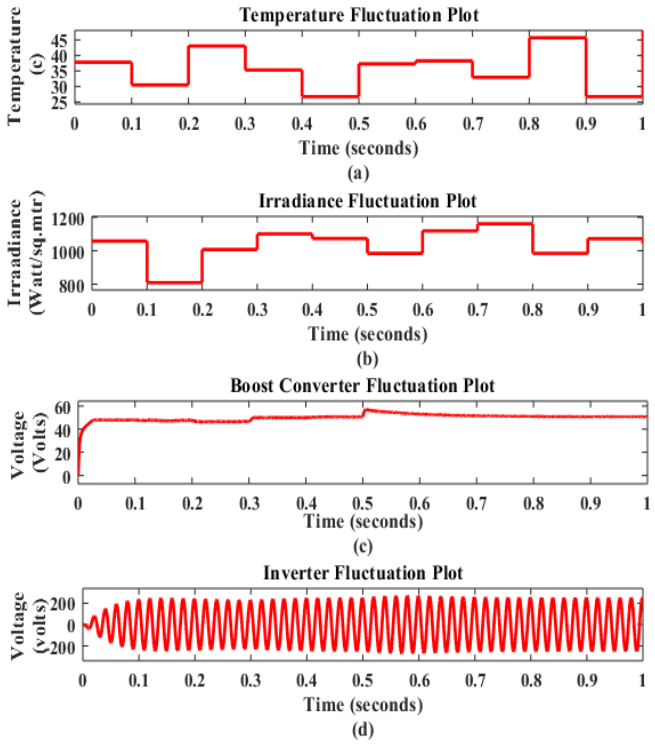

Figure 10. (a) Variation of temperature with time; (b) Variation of irradiance with time; (c) fluctuation of boost converter output voltage with change in irradiance and temperature; (d) fluctuation of RSMLI (inverter) output voltage with fluctuation in irradiance and temperature

4.1.4. Stability

Stability of any controller or for the matter of the entire proposed PV system is essential to any validation of the model. The proposed model is analysed for a wide range of frequency spectra. The proposed model is analysed for stability based on Matignon stability theorem. Dynamic system stability analysis of linear time invariant system suggests that the all roots of the characteristic equation should lie on the left and side of s-plane and should be away from origin [44]. However, it is not the case in fractional order controllers. The stability of fractional order system is based on Matignon stability theorem, stating that a fractional order system G(s) is stable if it satisfies Equation (38). In this equation, σ is seen as a symbol for the Laplace variable s. i represents the ith root of characteristic equation and q is the order of integral. Figure 11 represents the stability curve for fractional-order (FOTIDC) closed-loop system.

$$\left|\arg\left(\sigma_i\right)\right| = q\frac{\pi}{2}, \left\{\sigma = s^q : q \ni \left(0 \le q \le 2\right) : \forall \sigma_i \in C\right\} \quad (38)$$

As shown in Figure 11, the suggested model is able to handle higher-order frequency responses with ease.

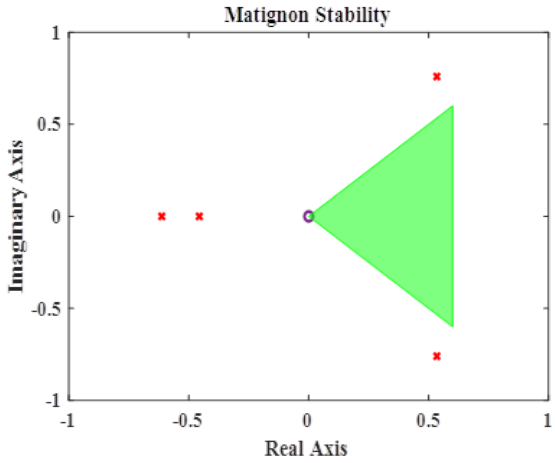

Figure 11. Stability (Matignon stability plot) of the proposed system

4.2. Harmonic analysis

Components of frequency other than fundamental component form the harmonic. This harmonic causes the irrational behaviour of the proposed system. The harmonic induced in system is current harmonic (THD$_i$) and it induces harmonic disturbance in voltage component, which is known as voltage harmonic (THD$_v$). THD$_i$ and THD$_v$ for the proposed system are represented in Figure 12 (a, b), respectively.

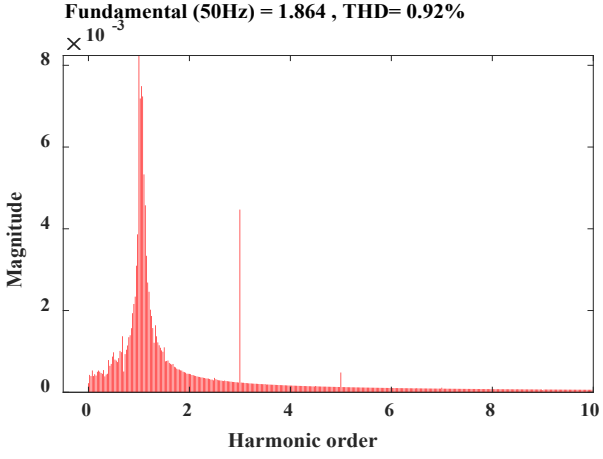

(a)

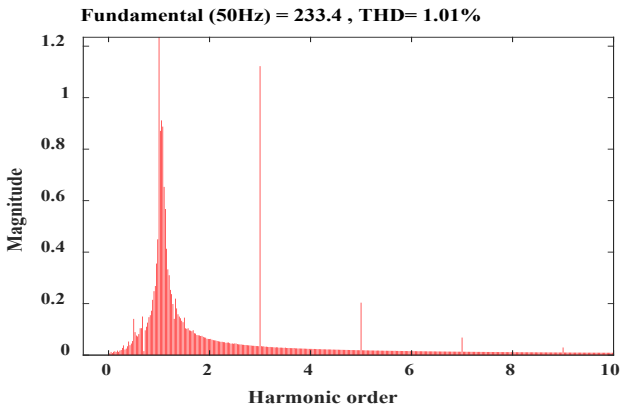

(b)

Figure 12. Total harmonic distortion curve for RSMLI: (a) THD_i and (b) THD_v plots

4.3. Frequency control

The proposed model also provides frequency control apart from making the system robust and stable. Figure 13 (a, b) represents frequency and angular frequency plot along time. Less fluctuations in frequency appear with a peak of 50.23 Hz. This, in turn, indicates that the proposed model maintains good power quality even when the system in itself is projected to fault.

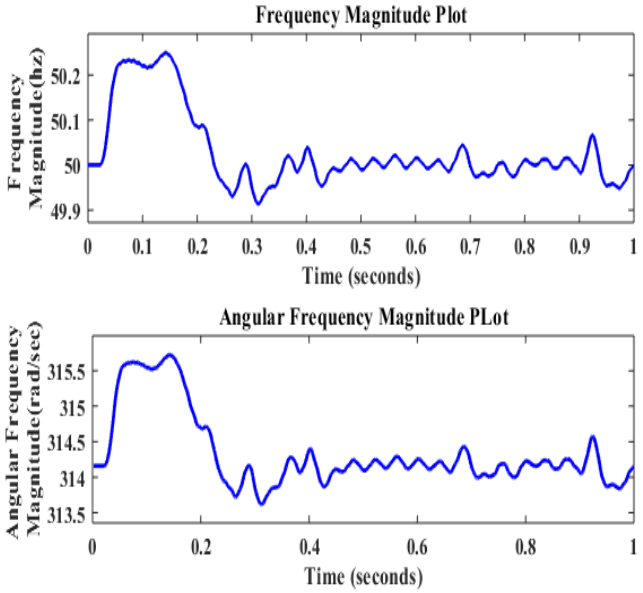

Figure 13. (a) Magnitude of frequency variation with respect to time; (b) Magnitude of angular frequency variation with respect to time

5. SENSITIVITY ANALYSIS

The model is a mathematical approximation of actual system. The controllers designed for the nominal model often provide suitable performance as per nominal model requirements. However, they may not satisfy the control objective of the actual system. Sensitivity analysis is performed on the performance of the controller in the presence of model uncertainties. The use of sensitivity analysis is to evaluate how the parameters of the proposed model influence the model output or model design requirements. Sensitivity analysis is defined as the study of how uncertainty in the output of a model can be attributed to different sources of uncertainty in the model input. Mathematically, the sensitivity of the cost function with respect to certain parameters is equal to the partial derivative of the cost function with respect to those parameters. There are two types of sensitivity analysis. They are local sensitivity analysis and global sensitivity analysis. Local sensitivity analysis is a One-At-a-Time (OAT) technique. OAT techniques analyse the effect of one parameter on the cost function at a time, thus keeping the other parameters fixed.

They explore only a small fraction of the design space, especially when there are many parameters. Also, they do not provide an insight into how the interactions between parameters influence the cost function. Global sensitivity analysis is often implemented using Monte Carlo techniques. This approach uses a representative (global) set of samples to explore the design space. The objective of the sensitivity analysis for the proposed model is to reduce THD and maximize output voltage while reducing cost function (ITAE). The control parameter variation plot is represented in Figure 14(a), and Figure 14(b) represents the THD variation plot. It is evident that in order to minimize THD, the optimized values of control parameters are not prone to sensitivity fluctuations. This is evident from 0.0008 variations in THD value.

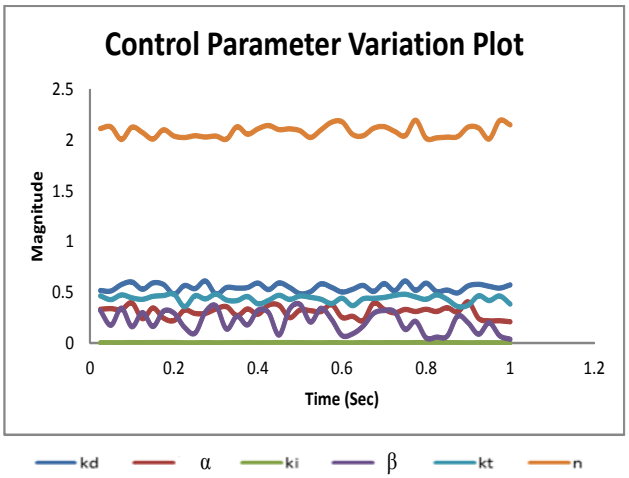

(a)

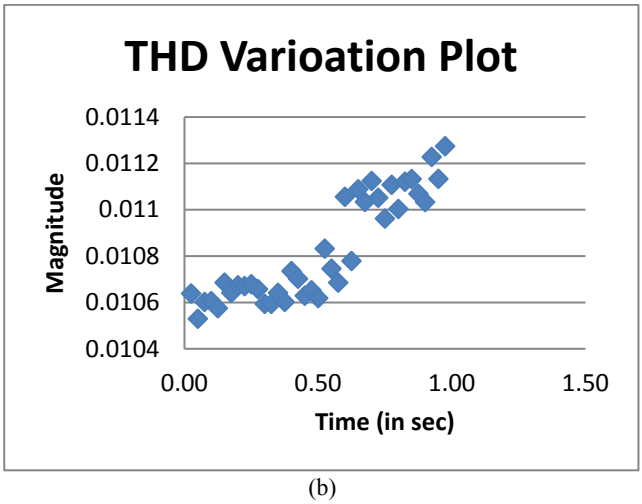

(b)

Figure 14. (a) FOTIDC control parameter variation plot; (b) THD variation with fluctuation of control parameter

5.1. Comparative study

The performance of the proposed system is compared with those of other controllers and from Table 2, it is evident that

the proposed system has outperformed all state-of-the-art controllers. The proposed system is compared with others in terms of harmonic, system stability, robustness, and frequency control.

Table 2. Comparative analysis

Parameter	Fractional proportional-resonant current controllers [19]	Adaptive PI controller [28]	Adaptive PI controller [17]	Fuzzy logic based PV system [5]	PR controller based PV system [15]	Proposed model
THD_i in %	7.2	5.06	4.27	3.37	1.19	1.02
THD_v in %	3.2	2.86	-	-	-	0.91
Stability	Less	Less	Less	Less	Less	More
Robust	Less	Less	Less	Less	Less	More
Frequency control	No	No	No	No	No	Yes

6. CONCLUSIONS

In the proposed PV system, the total harmonic distortion was reduced due to the application of HGPSJO-tuned FOTIDC in a PV system, thus resulting in improvements in its accuracy, stability, and robustness. The proposed model was tested against sudden changes in solar irradiance. The performance was as expected. The proposed work was seen to reduce harmonic distortion. The use of THISPWM in the implementation of HGAPSO-tuned FOTIDC-based PV system enhanced its overall performance by facilitating the suppression of harmonic distortions and there by improvement of stability and robustness. The concomitant enhanced performance of the proposed HGPSJO-tuned FOTIDC-based PV system enjoyed better accuracy, more robustness, and higher stability through the capability to bear irradiance fluctuations as validated in real time.

7. ACKNOWLEDGEMENT

The authors would like to thank Prof. Chinmaya Kumar Panigrahi for his comments and insightful suggestions about the manuscript. This research was supported by the School of Electrical Science, Kalinga Institute of Industrial Technology, Bhubaneswar, India.

NOMENCLATURE

I	Solar cell current (Ampere)
I_{PV}	Photo current (Ampere)
I_0	Cell reverse saturation current (Ampere)
a	Diode identity factor
q	Charge of electron (coloumb)
K	Boltzmann constant (joule per kelvin)
ΔT	Change in temperature (K)
G_n	Solar nominal irradiation (KW/m^2)
G	Solar actual irradiation (KW/m^2)
V_{OC}	Nominal open circuit voltage (volt)
T	Temperature (K)
V_t	Terminal voltage $V_t = \frac{kT}{q}$ (volt)
R_p	Shunt resistance (Ω)
R_s	Series resistance (Ω)
I_{SC}	Short- circuit current (Ampere)
K_I	Short- circuit temperature (Ampere)
K_v	Voltage/temperature coefficient (ppm/°C)
N_s	Series-connected cells
T_n	Nominal temperature (K)
J_O	Current density of the semiconductor (ampere/m^2)

Subscript

PV	Photovoltaic Cell
n	Nominal
SC	Short circuit
p	Shunt
I	Short circuit temperature
OC	Open circuit
O	Output
t	Terminal voltage
s	Series
V	Voltage coefficient

REFERENCES

1. Shakouri, M., Ghadamian, H. and Noorpoor, A., "Quasi-dynamic energy performance analysis of building integrated photovoltaic thermal double skin façade for middle eastern climate case", ***Applied Thermal Engineering***, Vol. 179, (2020), 115724. (https://doi.org/10.1016/j.applthermaleng.2020.115724).
2. Gopal, Y., Birla, D. and Lalwani, M., "Reduced switches multilevel inverter integration with boost converters in photovoltaic system", ***SN Applied Sciences***, Vol. 2, No. 1, (2020), 1-15. (https://doi.org/10.1007/s42452-01).
3. Janardhan, K., Mittal, A. and Ojha, A., "A symmetrical multilevel inverter topology with minimal switch count and total harmonic distortion", ***Journal of Circuits, Systems and Computers***, Vol. 29, No. 11, (2020). (https://doi.org/10.1142/S0218126620501741).
4. Mukundan, C.N., Jayaprakash, P., Subramaniam, U. and Almakhles, D.J., "Binary hybrid multilevel inverter-based grid integrated solar energy conversion system with damped SOGI control", ***IEEE Access***, Vol. 8, (2020), 37214-37228. (https://doi.org/10.1109/ACCESS.2020.2974773).
5. Gopal, Y., Birla, D. and Lalwani, M., "Selected harmonic elimination for cascaded multilevel inverter based on photovoltaic with fuzzy logic control maximum power point tracking technique", ***Technologies,*** Vol. 6, No. 3, (2018), 62-79.(https://doi.org/10.3390/technologies6030062).
6. Babkrani, Y., Naddami, A. and Hilal, M., "A smart cascaded H-bridge multilevel inverter with an optimized modulation techniques increasing the quality and reducing harmonics", ***International Journal of Power Electronics and Drive Systems***, Vol. 10, No. 4, (2019), 1852-1862. (https://doi.org/10.11591/ijpeds.v10.i4.1852-1862).
7. Mhiesan, H., Wei, Y., Siwakoti, Y.P. and Mantooth, H.A., "A fault-tolerant hybrid cascaded H-bridge multilevel inverter", ***IEEE Transactions on Power Electronics***, Vol. 35, No. 12, (2020), 12702-12715. (https://doi.org/10.1109/TPEL.2020.2996097).
8. Doostinia, M, Beheshti, M.T.H., Alavi, S.A. and Guerrero J.M., "Distributed control strategy for DC microgrids based on average consensus and fractional-order local controllers", ***IET Smart Grid***, Vol. 4, No. 8, (2021),1-12. (https://doi.org/10.1049/stg2.12038).
9. Guha, D.R., Banerjee, P.K., Padmanaban, S., Blaabjerg, S. and Chittathuru, D., "Small-signal stability analysis of hybrid power system with quasi-oppositional sine cosine algorithm optimized fractional order PID controller", ***IEEE Access***, Vol. 8, (2020), 155971-155986. (https://doi.org/10.1109/ACCESS.2020.3018620).
10. Djebbri, S., Ladaci, S., Metatla, A. and Balaska, H., "Fractional-order model reference adaptive control of a multi-source renewable energy

system with coupled DC/DC converters power compensation", ***Energy Systems***, Vol. 11, No. 2, (2020), 315-355. (https://doi.org/10.1007/s12667-018-0317-5).

11. Shakouri, M., Noorpoor, A. and Ghadamian, H., "Quantification of thermal energy performance improvement for building integrated photovoltaic double-skin façade using analytical method", ***Journal of Renewable Energy and Environment (JREE)***, Vol. 7, No. 3, (2020), 56-66. (https://dx.doi.org/10.30501/jree.2020.228559.1105).
12. Shakoori, M., Noorpoor, A., Golzari, S. and Zamen, M., "Energy simulation and parametric analysis of water cooled photovoltaic/thermal system", ***Amirkabir Journal of Mechanical Engineering***, Vol. 50, No. 6, (2019), 1361-1374. (https://dx.doi.org/10.22060/mej.2017.12703.5402).
13. Ramadan, H.S., "Optimal fractional order PI control applicability for enhanced dynamic behavior of on-grid solar PV systems", ***International Journal of Hydrogen Energy***, Vol. 42, No. 7, (2017), 4017-4031. (https://doi.org/10.1016/j.ijhydene.2017.01.122).
14. Shakouri, M., Ebadi, H. and Gorjian, S., "Solar photovoltaic thermal (PVT) module technologies", In ***Photovoltaic Solar Energy Conversion***, Academic Press, Vol. 1, No. 1, (2020), 79-116. (https://doi.org/10.1016/B978-0-12-819610-6.00004-1).
15. Fallah Ardashir, J., Mohammadpour, S.A., Khoun-Jahan, H. and Sabahi, M.,"Fractional PR control of a grid tied flying capacitor inverter for PV applications", ***Journal of Energy Management and Technology***, Vol. 3, No. 2, (2019), 58-64. (https://dx.doi.org/10.22109/jemt.2019.143673.1116).
16. Yousef, A.M., Abo-Elyousr, F.., Elnozohy, A., Mohamed, M. and Abdelwahab, S.A.M., "Fractional order PI control in hybrid renewable power generation system to three phase grid connection", ***International Journal on Electrical Engineering and Informatics***, Vol. 12, No. 3, (2020), 470-493. (https://dx.doi.org/10.15676/ijeei.2020.12.3.5).
17. Merai, M., Naouar, M.W., Slama-Belkhodja, I. and Monmasson, E., "An adaptive PI controller design for DC-link voltage control of single-phase grid-connected converters", ***IEEE Transactions on Industrial Electronics***, Vol. 66, No. 8, (2018), 6241-6249. (https://doi.org/10.1109/TIE.2018.2871796).
18. Swarnakar, J., Sarkar, P. and Singh, L.J., "Direct discretization method for realizing a class of fractional order system in delta domain–a unified approach", ***Automatic Control and Computer Sciences***, Vol. 53, No 2, (2019), 127-139. (https://doi.org/10.3103/S014641161902007X).
19. Heredero-Peris, D., Chillón-Antón, C., Sánchez-Sánchez, E. and Montesinos-Miracle, D., "Fractional proportional-resonant current controllers for voltage source converter", ***Electric Power Systems Research***, Vol. 168, (2019), 20-45. (https://doi.org/10.1016/j.epsr.2018.09.014).
20. Zhang, S., Wei, J., Xu, Z., Tang, B. and Niu, R., "Research on the influence of system parameters on the electromechanical dynamics of a large wind turbine drivetrain", ***Energy Reports***, Vol. 7, (2021), 7835-7851. (https://doi.org/10.1016/j.egyr.2021.11.020).
21. Ahmed, T., Waqar, A., Elavarasan, R.M., Imtiaz, J., Premkumar, M. and Subramaniam, U., "Analysis of fractional order sliding mode control in a D-STATCOM integrated power distribution system", ***IEEE Access***, Vol. 9, (2021), 70337-70352. (https://doi.org/10.1109/ACCESS.2021.3078608).
22. Nicola, M. and Nicola, C.I., "Fractional-order control of grid-connected photovoltaic system based on synergetic and sliding mode controllers", ***Energies***, Vol. 14, No. 2, (2021), 510-535. (https://doi.org/10.3390/en14020510).
23. Darvish, F.A., "Optimal fractional order BELBIC to ameliorate small signal stability of interconnected hybrid power system", ***Environmental Progress and Sustainable Energy***, Vol. 38, No. 5, (2019), 13208, 1-23. (https://doi.org/10.1016/j.est.2021.102983).
24. Kakkar, S., Maity, T., Ahuja, R.K., Walde, P., Saket, R.K., Khan, B. and Padmanaban, S., "Design and control of grid-connected PWM rectifiers by optimizing fractional order PI controller using water cycle algorithm", ***IEEE Access***, Vol. 9, (2021), 125941-125954. (https://doi.org/10.1109/ACCESS.2021.3110431).
25. Zamee, M.A. and Dongjun W., "A novel plant propagation-based cascaded fractional order PI controller for optimal operation of grid-connected single-stage three-phase solar photovoltaic system", ***Applied Sciences***, Vol. 9, No, 20, (2019), 4269-4290. (https://doi.org/10.3390/app9204269).
26. Ozan, G.Ü.L. and Nusret, T.A.N., "Voltage control at building integrated photovoltaic and wind turbine system with PI-PD controller", ***Avrupa Bilim ve Teknoloji Dergisi***, Vol. 18, (2020), 992-1003. (https://doi.org/10.31590/ejosat.668427).
27. Guel-Cortez, A.J., Méndez-Barrios, C.F., González-Galván, E.J., Mejía-Rodríguez, G. and Félix, L., "Geometrical design of fractional PDμ controllers for linear time-invariant fractional-order systems with time delay", ***Proceedings of the Institution of Mechanical Engineers, Part I: Journal of Systems and Control Engineering***, Vol. 233, No. 7, (2019), 815-829. (https://doi.org/10.1177%2F0959651818823450).
28. Lai, J., Yin, X., Yin, X. and Jiang, L., "Fractional order harmonic disturbance observer control for three-phase LCL-type inverter", ***Control Engineering Practice***, Vol. 107, (2021), 1-13. (https://doi.org/10.1016/j.conengprac.2020.104697).
29. Shakouri, M. and Ghadamian, H., "A energy and exergy quasi-dynamic analysis of building integrated photovoltaic system using data analytics", ***Journal of Solar Energy Research***, Vol. 4, No. 4, (2019), 273-279. (https://dx.doi.org/10.22059/jser.2020.295324.1136).
30. Mousavi, Y., Bevan, G., Küçükdemiral, I.B. and Fekih, A., "Maximum power extraction from wind turbines using a fault-tolerant fractional-order nonsingular terminal sliding mode controller", ***Energies***, Vol. 14, No. 18, (2021), 5887-5903. (https://doi.org/10.3390/en14185887).
31. Pazhanimurugan, R., Bensraj R. and Balamurugan. C.R., "Time response of FOPID controlled PV based cascaded landsman converter-inverter fed induction motor and electric drives applications", ***International Journal of Power Electronics and Drive Systems***, Vol. 11, No. 3, (2020), 1379-1387. (https://doi.org/10.11591/ijpeds.v11.i3.pp1379-1387).
32. Prasad, P., Bhaskara, P.L.M., and Sarvesh, B., "Fractional order PID controlled cascaded re-boost seven level inverter fed induction motor system with enhanced response", ***International Journal of Power Electronics and Drive Systems***, Vol. 9, No. 4, (2018), 1784-1791. (https://doi.org/10.11591/ijpeds.v9.i4.pp1784-1791).
33. Long, B., Lu, P.J., Chong, K.T., Rodriguez, J. and Guerrero, J.M., "Robust fuzzy-fractional-order nonsingular terminal sliding-mode control of a LCL-type grid-connected converter", ***IEEE Transactions on Industrial Electronics***, (2021). (https://doi.org/10.1109/TIE.2021.3094411).
34. Yousef, A.M., Abo-Elyousr, F.K., Elnozohy, A., Mohamed, M. and Abdelwahab, S.A.M., "Fractional order PI control in hybrid renewable power generation system to three phase grid connection", ***International Journal on Electrical Engineering and Informatics***, Vol. 12, No. 3, (2020), 470-493. (https://doi.org/10.15676/ijeei.2020.12.3.5).
35. Ahmed, E.M., Mohamed, E.A., Elmelegi, A., Aly, M. and Elbaksawi, O., "Optimum modified fractional order controller for future electric vehicles and renewable energy-based interconnected power systems", ***IEEE Access***, Vol. 9, (2021), 29993-30010. (https://doi.org/10.1109/ACCESS.2021.3058521).
36. Priyadarshani, S, Subhashini, K.R. and Satapathy, J.K., "Pathfinder algorithm optimized fractional order tilt-integral-derivative (FOTID) controller for automatic generation control of multi-source power system", ***Microsystem Technologies***, Vol. 27, No. 1, (2021), 23-35. (https://doi.org/10.1007/s00542-020-04897-4).
37. Banaei, M.R. and Hossein A.F.B., "A high efficiency nonisolated buck–boost converter based on ZETA converter", ***IEEE Transactions on Industrial Electronics***, Vol. 67, No. 3 (2019), 1991-1998. (https://doi.org/10.1109/TIE.2019.2902785).
38. Padmanaban, S., "An original transformer and switched-capacitor (T and SC)-based extension for DC-DC boost converter for high-voltage/low-current renewable energy applications: Hardware implementation of a new T and SC boost converter", ***Energies***, Vol. 11, No. 4, (2018), 783-806. (http://dx.doi.org/10.3390/en11040783).
39. Leyva-Ramos, J., Mota-Varona, R., Ortiz-Lopez, M. G., Diaz-Saldierna, L.H. and Langarica-Cordoba, D., "Control strategy of a quadratic boost converter with voltage multiplier cell for high-voltage gain", ***IEEE Journal of Emerging and Selected Topics in Power Electronics***, Vol. 5, No. 4, (2017), 1761-1770. (https://doi.org/10.1109/JESTPE.2017.2749311).
40. Zhang, Y., Liu, H., Li, J., Sumner, M. and Xia, C., "DC–DC boost converter with a wide input range and high voltage gain for fuel cell vehicles", ***IEEE Transactions on Power Electronics***, Vol. 34, No. 5, (2018), 4100-4111. (https://doi.org/10.1109/TPEL.2018.2858443).
41. Premkumar, K. and Shyam, D., "Design and development of N-level symmetrical multilevel inverter topology with reduced switches", ***Journal of Circuits, Systems and Computers***, Vol. 30, No. 11, 2150197.(https://doi.org/10.1142/S0218126621501978).

42. Davis, T.T. and Dey, A., "Enhanced floating capacitor voltage balancing schemes for single-source seven-level inverters with capacitor fed H-bridge units", ***IEEE Transactions on Industrial Electronics***, Vol. 67, No. 8, (2019), 6227-6236. (https://doi.org/10.1109/TIE.2019.2939976).

43. Motamarri, R. and Bhookya, N., "JAYA algorithm based on Lévy flight for global MPPT under partial shading in photovoltaic system", ***IEEE Journal of Emerging and Selected Topics in Power Electronics***, Vol. 9, No. 4, (2020), 4979-4991. (https://doi.org/10.1109/JESTPE.2020.3036405).

44. Monteghetti, F., Ghislain, H., and Matignon, D., "Stability of linear fractional differential equations with delays: A coupled parabolic-hyperbolic PDEs formulation", ***IFAC-PapersOnLine***, Vol. 50, No. 1, (2017), 13282-13288. (https://doi.org/10.1016/j.ifacol.2017.08.1966).

JREE: Vol. 9, No. 4, (Autumn 2022) 101-108

Journal of Renewable Energy and Environment

Journal Homepage: www.jree.ir

Materials and Energy Research Center

MERC

Research Article

Bio-Based Lubricant Synthesis by Chemical Modification of Linoleic and Oleic Acid Mixture

Sharareh Esmaeili [a], Kambiz Tahvildari [a*], Barat Ghobadian [b], Masoud Dehghani-Soufi [c*], Sanaz Mohammadzadeh Koumleh [d], Tirth Panchal [e]

[a] *Young Researchers and Elites Club, North Tehran Branch, Islamic Azad University, Tehran, Tehran, Iran.*
[b] *Department of Biosystems Engineering, School of Agriculture, University of Tarbiat Modares, P. O. Box: 14115-111, Tehran, Tehran, Iran.*
[c] *School of Environment, College of Engineering, University of Tehran, P. O. Box: 1417853111, Tehran, Tehran, Iran.*
[d] *Faculty of Chemistry, Shahroud University of Technology, P. O. Box: 3619995161, Shahroud, Semnan, Iran.*
[e] *C1 Water Industries LLC, Dubai Industrial City, Dubai, United Arab Emirates.*

PAPER INFO

Paper history:
Received: 18 January 2022
Revised in revised form: 05 May 2022
Scientific Accepted: 21 May 2022
Published: 11 December 2022

Keywords:
Biolubricant,
Epoxidation,
Esterification,
Linoleic Acid,
Oleic Acid

ABSTRACT

The presence of increasing concerns and enforcement of growing regulations over environmental pollution are nowadays at play. The pollution arising from mineral oils is among the major concerns. With the gradual reducation of the world oil reserves, an increasing pressure comes into play for finding sustainable alternatives. Being appealing alternatives, vegetable oils consist of different fatty acids; however, they cannot be applied directly to internal combustion engines owing to their poor oxidation stability and high pour point value. Biolubricants are considered to be a new generation of lubricants, which are renewable and biodegradable and are produced from the chemical modification of vegetable oils. There are few studies investigating the feasibility of using the mixture of fatty acids as biolubricant feedstock. In this study, epoxidation, oxirane ring opening with palmitic acid and p-Toluenesulfonic acid, esterification reaction with octanol, and reaction of the remaining hydroxyl group with stearic acid were applied to modify the mixture of oleic and linoleic fatty acids and produce biolubricant. For this purpose, the IR spectrums of each epoxide, monoester, diester, and triester products were obtained and analyzed. At the end of the experiments, monoester, diester, and triester were obtained with 94 % yield, with 96 % yield, and with 98 % yield, respectively. Eventually, the final product was found with physicochemical properties comparable with the physicochemical properties of the lubricant standard ISO VG10.

https://doi.org/10.30501/jree.2022.316482.1282

1. INTRODUCTION

Nowadays, some phenomena like reduction of oil reserves and the increasing rate of energy price have made economic consumption of energy and its optimization in energy consumptive systems an indispensable task. Thus, renewable energy sources, including wind, solar energy, and biofuels (e.g., biodiesel and bioethanol) have attracted the attention of researchers and scientists. In this regard, the biggest quota of energy use is attributed to internal combustion engines, which are considered to be among the highest energy consumers. Accordingly, it is very important to devise various methods for reducing energy consumption by such engines. It is noteworthy that a third of the energy consumed by these engines is attributable to frictional losses; therefore, it seems reasonable to opt for the lubrication of different parts of such engines for the sake of reducing the degree of friction and abrasion in their moving parts. This can exert an enormous effect on the reduction of energy and fuel consumption [1]. In fact, engine oil is an integral fluid for engines whose role can be likened to that of blood in the body system in which engine oil accomplishes this important task by lubricating the moving parts of engine. In addition, this fluid is petroleum-based, similar to other oils employed in engine and is also dependent upon costly and non-renewable sources. This has made it unreliable to be used in the long run. On the other hand, vast amounts of lubricants are used every year and their disposal as burned oils to nature brings about environmental pollution [2]. In addition to the harmful effects and air pollution caused by burning the lubricant of the engine fuel, this pollution also arises. Thus, lubricants are nowadays generated from renewable and eco-friendly resources such as vegetable oils, which are referred to as biolubricants and are dependent upon renewable vegetable resources. The desirable biodegradation of such oil ensures that no environmental pollution comes into play by these vegetable oils [3]. The materials existing in vegetable oils are both sustainable and biodegradable in a way

*Corresponding Authors' Email: k_tahvildari@iau-tnb.ac.ir (K. Tahvildari) and dehghanisoufi@ut.ac.ir (M. Dehghani-Soufi)
URL: https://www.jree.ir/article_162705.html

Please cite this article as: Esmaeili, Sh., Tahvildari, K., Ghobadian, B., Dehghani-Soufi, M., Mohammadzadeh Koumleh, S. and Panchal, T., "Bio-based lubricant synthesis by chemical modification of linoleic and oleic acid mixture", ***Journal of Renewable Energy and Environment (JREE)***, Vol. 9, No. 4, (2022), 101-108. (https://doi.org/10.30501/jree.2022.316482.1282).

that may lead to the decrease of global warming. Accordingly, such materials are becoming popular in the market from different perspectives, especially due to their availaibility, economic aspect, and environmentally friendliness [4]. Figure 1 shows different applications of biolubricants in different parts of a vehicle and values of their physicochemical properties including pour point, flash point, and Viscosity Index (VI) [5].

Biolubricants, which are made from chemical modification of vegetable oils, enjoy a good potential to act as an alternative to petroleum-based lubricants [6]. Vegetable oils are available in two types of edible and non-edible oils. The edible oils like canola, soybean, and sunflower oils are utilized for foods and the production of biodiesel and biolubricants. The non-edible oils like kitchen waste cooking oils and seed oils like Jatropha and castor are used for producing biofuels and biodiesels. It should be mentioned that the majority of vegetable oils are obtained from Triacylglycerol, which is a glycerol triester where ester linkage to three glycerol hydroxyl groups links three fatty acids together (Figure 2).

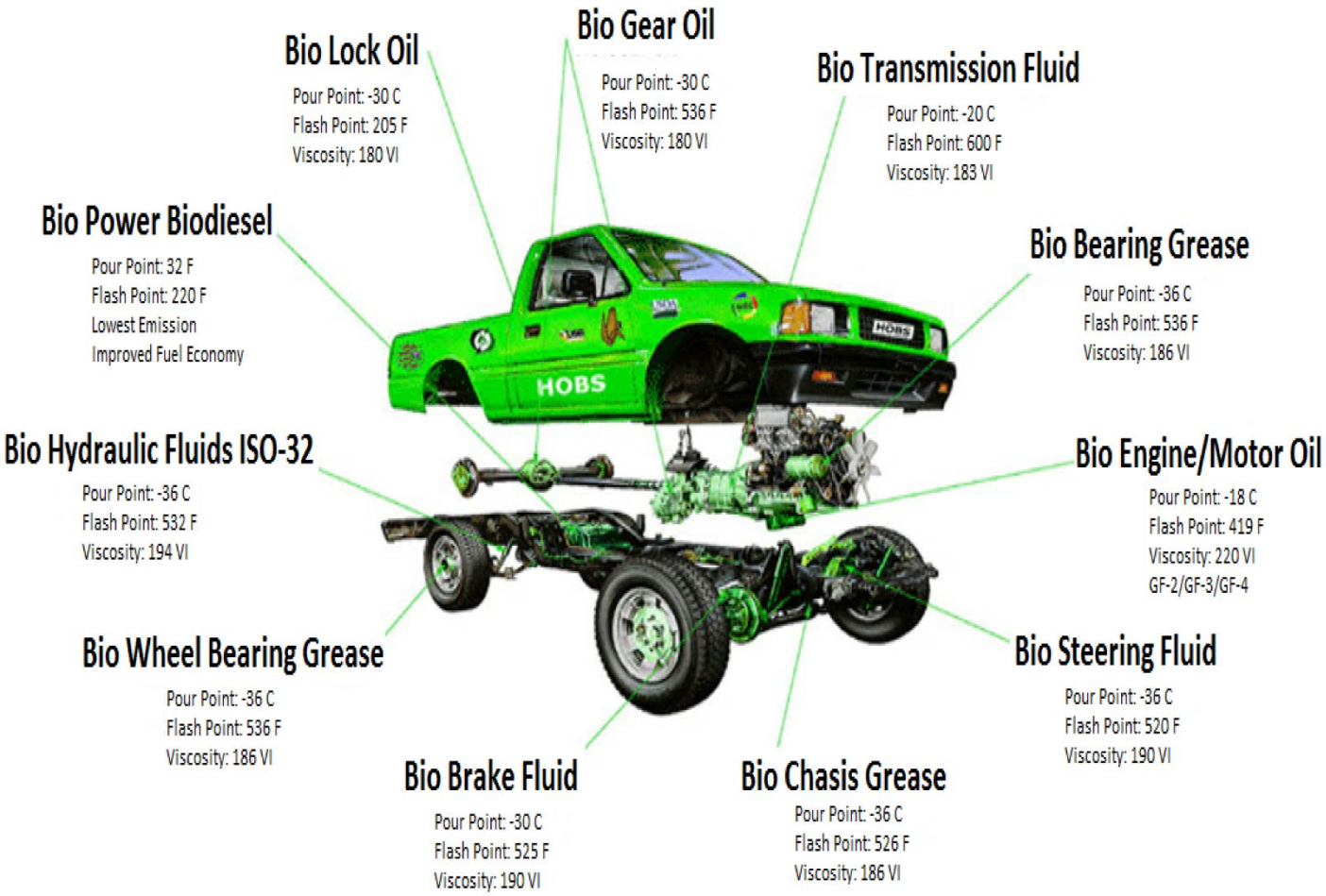

Figure 1. Different applications of biolubricants in various parts of a vehicle [5]

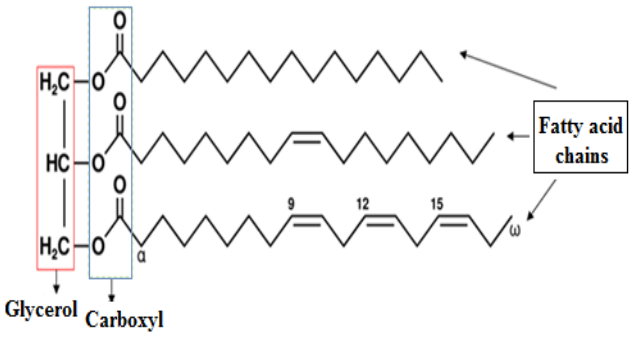

Figure 2. Triacylglycerol structure of vegetable oils

Two main factors, including the glycerol structure of Triacylglycerol and the composition and distribution of fatty acids are determinnets of the chemical and physical properties of vegetable oils [7]. Indeed, the Triacylglycerol structure is approparite for lubrication because combination of carboxyl group and long-chain fatty acids with each other leads to highly strong lubrication. The presence of 14 to 22 carbon atoms with varying saturations in the majority of fatty acids of vegetable oils is evident. The delineation of higher interaction of triacylglycerol molecules with metal surfaces compared to that of hydrocarbons has made triacylglycerol molecules a highly strong lubricant to metal surfaces. Therefore, they contribute to the reduction of abrasion and friction [8].

However, it is not possible to use vegetable oils as lubricants without any intermediacy. As shown in Figure 3, it is evident that double bonds in the fatty acids of triacylglycerol are prone to reaction with oxygen in the air. Thus, some oxidation comes into play and as a result, it makes the insoluble materials deposited and the value of acid and oil viscosity raise. In the same way, it is possible to conveniently separate β hydrogen in glycerol section from the molecule structure and convert ester into acid and olefin. Low stability against oxidation and low pour point can be enumerated as the

negative effects of direct employment of vegetable oils as lubricants [9].

To date, different methods have been used by researchers to see whether or not vegetable oils can be used as lubricants. In this regard, some reserachers have examined polyols like Trimethylolpropane having a vegetable oil base and glycerol structure as an alternative to raise the stability of oxidation [10-13]. Some others have employed epoxidation as an alternative to stabilizing vegetable oils against oxidation [6, 14]. The hydrogenation, transesterification reaction, and genetic change of vegetable oils with long-chain alcohols, that is, 8-15 carbon atoms, were examined, as well [1, 15-17]. As a major additive reaction with double bonds, epoxidation results in forming oxirane rings and consequently, the oxidation stability of vegetable oils increases (Figure 3).

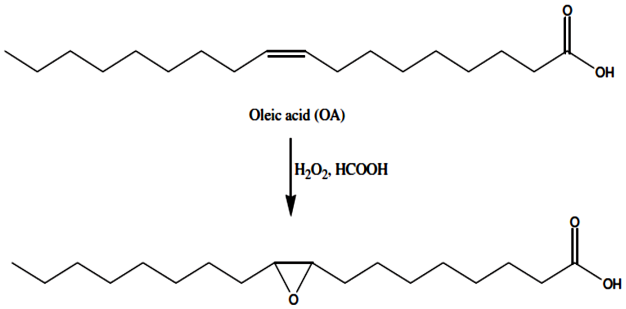

Figure 3. Epoxidation reaction

Considering the fact that natural compounds are available as fatty acid mixtures, conducting a survey on applied reactions in the mixture of these compounds supplies less expense for initial consumable ingredients than purified fatty acids and their following reactions. Therefore, a mixture of oleic and linoleic acid was used in this study. Through a chain of reactions, such as epoxidation, oxirane ring opening, and the esterification of epoxide, monoester, diester, and triester compounds were synthesized and analyzed by the functional FTIR spectroscopy. Indeed, most of previous research studies have focused on transesterification reaction as the most common route for biolubricant production. However, this paper addresses a multi-stage production process including the above-mentiond stages.

2. EXPERIMENTAL

2.1. Meterial

The mixture of oleic and linoleic acids was purchased from Alandshimi Company, Iran. Magnesium sulfate 97 %, sodium chloride 99 %, para toluene sulfonic acid 98 %, and octanol 99 % were purchased from Sigma Company, while formic acid 88 %, hydrogen peroxide 30 %, palmitic acid 99 %, and stearic acid 99 % were provided from Merck Company. Antonpaar viscometer SVM-3000, ignition point determiner (Model: P611A, Analysis Company, Belgium), rotary evaporator (Model: STRIKE 202, Italy), and overhead mixer (Wreke Eurostar Digital (S1), IKA Germany) in the speed range of 50-2000 rpm were also applied in this study. Similarly, the cloud and pour point refrigerator (Model: STEA assembled in England), spectroscope (FTIR) (Model: Tensor 27, Brucker Germany) were employed in the course of this study.

2.2. Procedure

2.2.1. Preparation of epoxide from mixed fatty acids (oleic acid and linoleic acid)

In order to prepare epoxide, 30 g of mixed fatty acids was poured into a beaker (100 ml), which had been placed in an ice bath until it reached 4 °C. Then, 28 ml of formic acid 88 % was gradually added. About 16 ml of hydrogen peroxide 30 % was slowly added using a burette at 0-4 °C. Next, the mixing process began at a speed of 800 rpm for 2-5 hours till a white precipitate was formed. To extract formic acid, the resulting precipitate was washed five times with the distilled water (50 ml) and was then filtered using a vacuum filter. After filtration, the precipitate was placed in a vacuum desiccator to dry and allow for the discharge of the extra formic acid.

2.2.2. Preparation of monoester from fatty acid epoxide

To perform this examination, 31 g of fatty acid epoxide, 6 g of palmitic acid, and 5 g of para toluene sulfonic acid were dissolved in 70 ml of toluene. This mixture was, then, poured into a two-necked flask (capacity: 250 ml). The reaction took place through stirring at 70-80 °C for 90 minutes. Thereafter, the temperature was raised to 90-100 °C and the admixture of the compounds was refluxed and mixed for 3 hours. When the reaction was over, the flask contents were replaced into a separatory funnel and remained there for 12 hours at ambient temperature. Next, the funnel's contents were washed 5 times using 50 ml of distilled water until the wash water had a neutral pH. The organic phase was, first, dehydrated using magnesium sulfate and was then filtered via vacuum filtration. Following the filtration, toluene was separated from the admixture using rotary evaporator (temperature: 90 °C; speed: 100 rpm).

2.2.3. Preparation of diester from fatty acid monoester

First, 10 g of fatty acid monoester and 27.8 g of octanol were poured into a two-necked flask (capacity: 100 ml), while 4 drops of sulfuric acid (10 %) were added as a catalyst. The reaction lasted for 10 hours (temperature: 60 °C). When the reaction was over, the flask contents were replaced into a separatory funnel (capacity: 250 ml). Then, 50 ml of normal hexane was added to separate and purify the product. Following the separation of the aqueous phase from the organic phase, 5 ml of saturated solution of sodium hydrogen carbonate was added to the organic layer to separate the lower phase (pH = 10). After that, 10 ml of saturated solution of sodium chloride (2 times) was added to the organic layer and the lower phase was separated once more (pH = 8). Finally, the organic phase was dehydrated using magnesium sulfate and was filtered by vacuum filtration. After being filtered, normal hexane was extracted from the recent admixture using rotary evaporator (temperature: 80 °C; speed: 100 rpm).

2.2.4. Preparation of triester from fatty acid diester

At the outset, 5 g of fatty acid diester and 5 g stearic acid were poured into a two-necked flask (capacity:100 ml), while 2 drops of sulfuric acid (10 %) were added as a catalyst. The reaction took place, while the mixture was being mixed and refluxed for 10 hours at 100-110 °C. At the end of the reaction, the flask contents were placed into a separatory funnel (250 ml) and 20 ml of normal hexane was added to it so as to separate and purify the product. After the separation

of the aqueous phase from the organic phase, 5 ml of the saturated solution of sodium hydrogen carbonate (2 times) was added to the organic layer so as to separate the lower phase (pH = 10). Afterwards, 10 ml of the saturated solution of sodium chloride (2 times) was added to the organic layer in order to separate the lower phase (pH = 7). At the end, the organic phase was dehydrated and filtered using magnesium sulfate and vacuum filtration, respectively. After filtration, normal hexane was extracted from the recent admixture using rotary evaporator (temperature: 80 °C; speed: 100 rpm).

The synthesis process of triester from oleic acid and linoleic acid is given in Figures 4 and 5.

2.3. Standard tests to identify lubricant physicochemical properties

2.3.1. Flash point

Flash point is the lowest temperature at which the sample is evaporated adequately and the combination of evaporated sample and air produces a flammable admixture. Thus, when the flame is drawn to this gas, it ignites for a moment and then, dies out. The flash point should be high so as to lower the risk of volatility at high temperatures and increase the level of safety [18, 19]. During this examination, the flash point was measured by a flash point apparatus in accordance with ASTM D-93 standards.

2.3.2. Pour point

Pour point was measured using specific equipment in accordance with ASTM D-79. In order to measure the cloud point, the sample was poured into a test tube and placed in the measuring instrument. The contents were refrigerated in butyl glycol bath gradually. As soon as the sample got opaque or a milky cloud appeared, the temperature displayed on the monitor was written down. If the sample gets cooler, the process of freezing starts and the temperature in this state is defined as the freezing point. If the tube is taken out and held in a horizontal position, after some time, the sample gets warmer and begins to flow. The temperature in this state is defined as the pour point, which is a few grades above the freezing point.

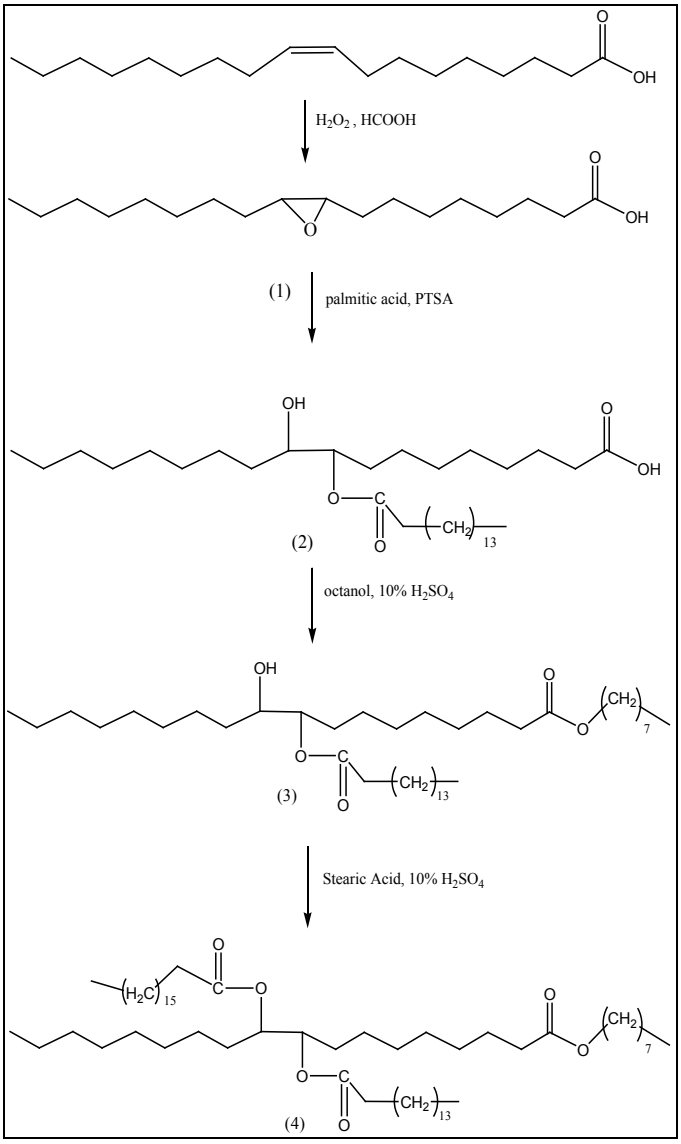

Figure 4. The process of preparing triesters from oleic acid: step (1): epoxidation, step (2): oxirane ring opening, step (3): esterification using octanol and step, (4): esterification using stearic acid

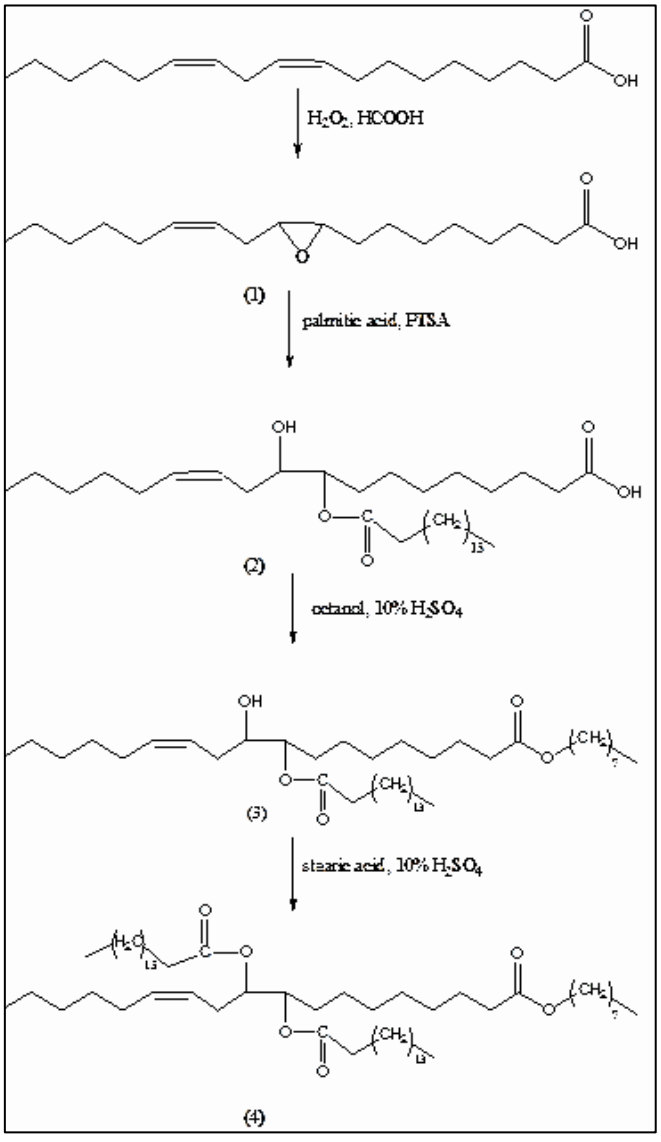

Figure 5. The process of preparing triester from linoleic acid, step (1): epoxidation, step (2): oxirane ring opening, step (3): esterification using octanol, and step (4): esterification using stearic acid

2.3.3. Viscosity index

Viscosity is defined as the resistance of fluid to moving and flowing. In order to produce a lubricant film with desired width, viscosity should be high; otherwise, it increases friction. Consequently, the dissipation power and abrasion grow.

Viscosity index is a dimensionless contract parameter that identifies the extent of kinematic viscosity which depends on the temperature. Low viscosity index represents wide fluctuations in viscosity in response to temperature changes, bringing about a steep slope in the viscosity-temperature curve. The more the viscosity index is, the less the viscosity fluctuates will be in response to temperature changes. Under these conditions, the slope of the viscosity-temperature curve remains constant and the lubricant provides a better function [18].

3. RESULTS AND DISCUSSION

3.1. IR spectrum analysis

In this study, 863 negligible cm^{-1} and 924 cm^{-1} peaks in mixed fatty acid (oleic acid and linoleic acid) epoxide correlated with oxirane ring carbons and 2927 cm^{-1} and 2852 cm^{-1} peaks correlated with the stretching vibration of CH_2 (aliphatic carbons). Analysis of epoxide spectrum also indicates that 1711 cm^{-1} and 1466 cm^{-1} peaks correlated with the stretching vibration of carbonyls and the flexion vibration of CH_2, respectively. Also, 721 cm^{-1} , 1412 cm^{-1}, and 3343 cm^{-1} peaks belonged to the oscillation vibration of CH_2, flexion, and stretching vibrations of O-H, respectively (Figure 6).

Regarding monoesters, 2924 cm^{-1} and 2854 cm^{-1} peaks were related to the stretching vibration of CH_2, while 1709 cm^{-1} and 1726 cm^{-1} peaks correlated with the stretching vibration of carbonyl ester group and carboxylic acid section, which represented the oxirane ring opening phenomenon. In monoester spectrums, 1098 cm^{-1} and 1175 cm^{-1} peaks correlated with the stretching vibration of C-O section of an ester; and 1290 cm^{-1}, 1376 cm^{-1}, and 1464 cm^{-1} peaks correlated with the stretching vibration of C-O section of acid, symmetric flexion vibration of CH_3, and flexion vibration of CH_2, respectively (Figure 7).

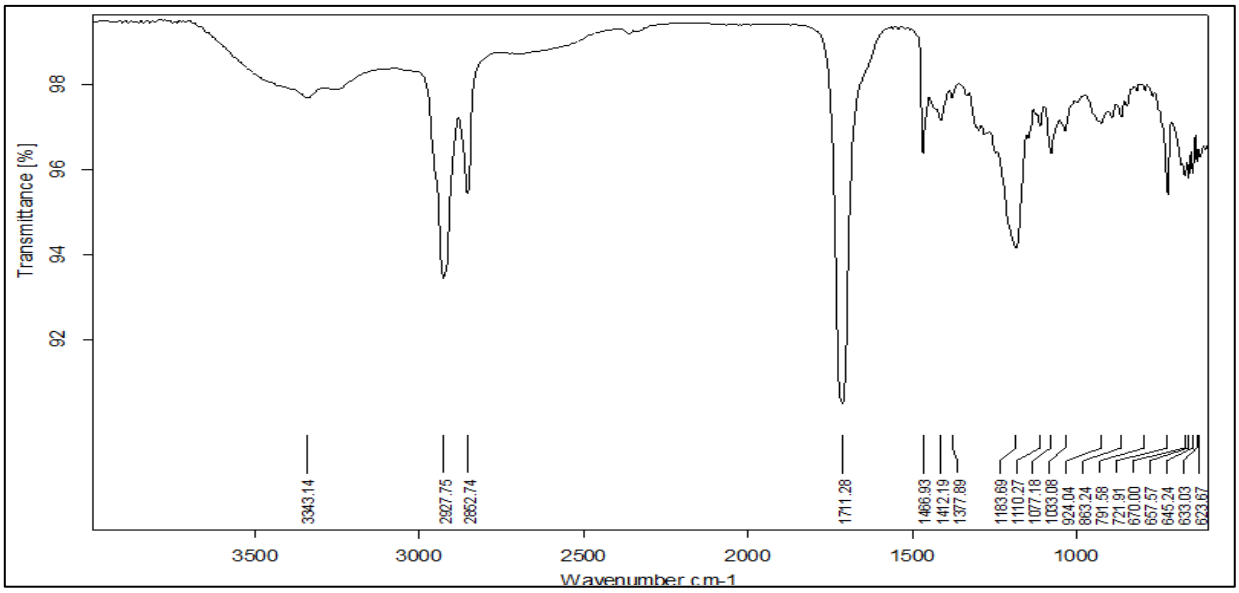

Figure 6. IR spectrum for the mixed fatty acid epoxide

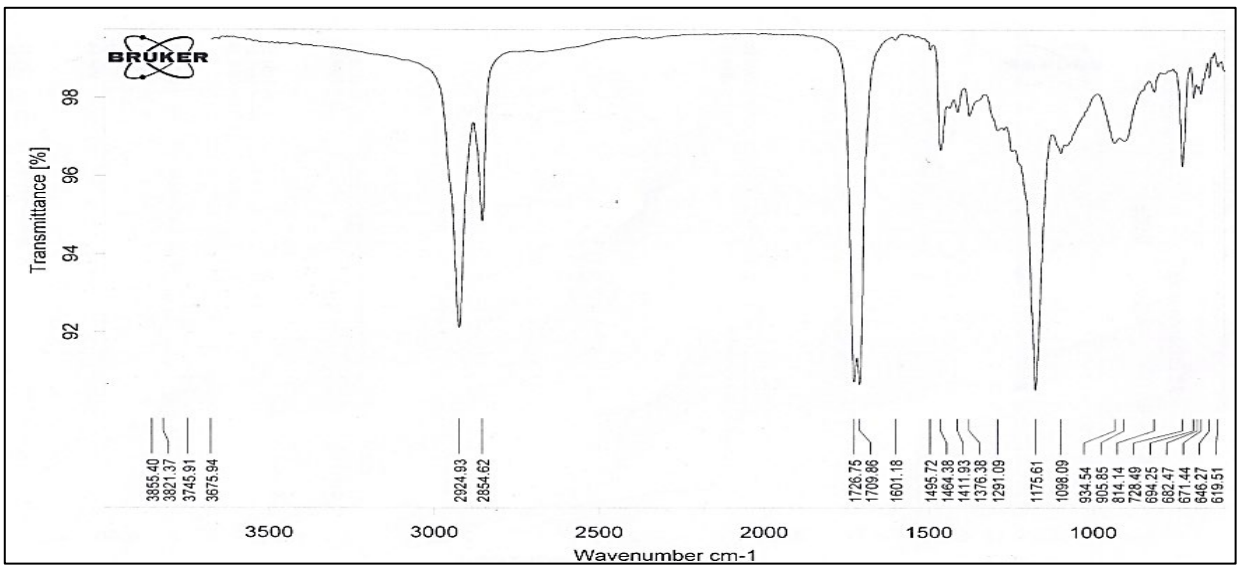

Figure 7. IR spectrum for fatty acid monoester

The analysis of the diester spectrums indicates that 3350 cm^{-1} peaks belonged to OH stretching vibration, 2925 cm^{-1} and 2855 cm^{-1} peaks correlated with CH_2 stretching vibration, and 1737 cm^{-1} peak correlated with carbonyl stretching vibration. Moreover, 1117 cm^{-1}, 1174 cm^{-1}, and 1246 cm^{-1} peaks correlated with the stretching vibrations of C-O part of an ester. Considering this spectrum, 1465 cm^{-1}, 1377 cm^{-1}, and 722 cm^{-1} peaks correlated with the flexion vibration of CH_2, symmetric flexion vibration of CH_3, and oscillation vibration of CH_2, respectively (Figure 8).

In triester spectrums, 1738 cm^{-1} peak belonged to carbonyl stretching vibration and the absence of OH peak in 3400 cm^{-1} area indicated the triester structure. On the other hand, 2923 cm^{-1} and 2853 cm^{-1} peaks correlated with the stretching vibrations of CH_2, and 1465 cm^{-1} and 1377 cm^{-1} peaks correlated with the flexion vibration of CH_2 and symmetric flexion vibration of CH_3, respectively. Peaks in 1116 cm^{-1}, 1170 cm^{-1}, and 1245 cm^{-1} areas correlated with the stretching vibration of C-O section of an ester (Figure 9) [6, 16].

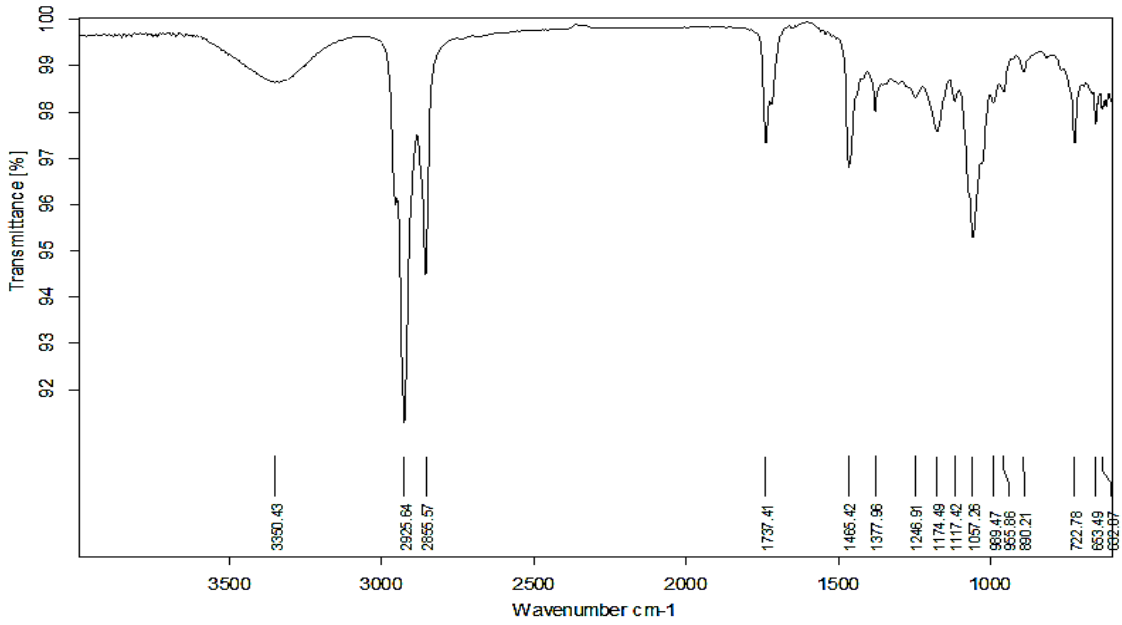

Figure 8. IR spectrum for fatty acid diester

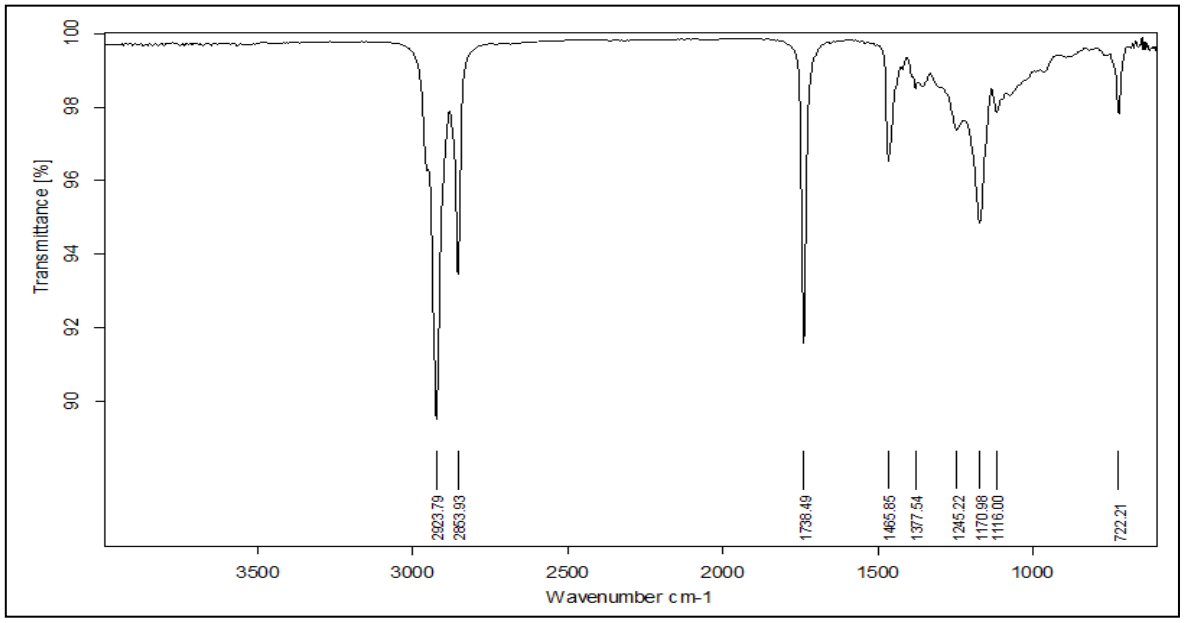

Figure 9. IR spectrum for fatty acid triester

Based on these spectrums, it can be concluded that the elimination of 863 cm^{-1} peak in Figure 6 was related to oxirane ring opening and the formation of 1709 cm^{-1} and 1726 cm^{-1} peaks in Figure 7 was related to the production of ester groups. In Figure 8, the 3350 cm^{-1} peak was related to the formation of an OH group, which was eliminated during the production process of the triester (Figure 9). The results obtained in this section are comparable with findings obtained by Bashiri et al. [6].

3.2. Physicochemical test results

The physical properties of the synthetized diester and triester and their comparison with lubricant ISO standard are presented in Table 1. The ISO VG standard is an international

standard for lubricants classification and indicates the main physicochemical qualifications of a standard lubricant. It can be observed that the physicochemical properties of the obtained biolubricant (triester) are compatible with the ISO VG 10 standard and the triester has better values in some features like VI and flash point, while there is a negligible difference between pour point values of the triester and the ISO standard.

Table 1. Physical properties of synthetized diester and triester

	Viscosity, 40 °C, cSt	Viscosity 100 °C, cSt	VI	Pour point °C	Flash point °C
Diester	9.89	2.63	90.27	-24	153
Triester	12.50	3.3413	138.77	-27	238
ISO VG10	> 9	> 2.68	104	-30	154

According to the results of lubricant standard tests, esters exhibited better lubricant behavior than diesters at low temperatures. There are two possible reasons for this phenomenon:

1- The presence of side chains attached to the main fatty acid skeleton prevents the individual molecules from accumulation. In the presence of stearic acid side chains in triester structure, spatial steric hindrance is greater compared to diesters. As a result, the pour point of fatty acid triester is lower than that of diester.

2- Diesters have one hydroxyl group less than monoesters and the absence of a hydroxyl group in triester's structure results in the reduction of hydrogen bond quantity and pour point value.

Lubricant performance, as a friction reducer, greatly depends on its viscosity. In fact, lubricant viscosity should be high; otherwise, it leads to an increased friction; as a result, greater abrasion and dissipation may occur.

Moreover, to ensure the safety and lower the possibility of evaporation at high temperatures, the flash point should be high. The flash points of diesters and triesters are 153 °C and 238 °C respectively. Triester compounds own a higher flash point than diesters since they consist of one more side chain.

4. CONCLUSIONS

In this paper, a multi-step synthesis process through a chain of reactions including epoxidation, oxirane ring opening, and the esterification of epoxide was applied to biolubricant (triester) production and the final product was analyzed by the functional FTIR spectroscopy. The calculated efficiencies of epoxidation reactions, oxirane ring opening, esterification by octanol, and esterification by fatty acids were 96.6, 94, 96, and 98 %, respectively. These values clarify the fact that applying mixed fatty acids can be more cost-effective. Moreover, considering the low cost of linoleic and oleic acid mixtures compared with mineral lubricants and the fact that these products are biodegradable and generate lower environmental pollution, their production was found to be justifiable.

According to kinematic viscosity values for diesters and triesters at 40 °C and 100 °C, the viscosity indexes for diesters and triesters were determined as 90.27 and 138.77, respectively. These values describe a negligible viscosity fluctuation in response to temperature changes. Finally, it can be concluded that triester derived from fatty acids, due to their greater viscosity index than diesters, can act as an ideal substitute for petroleum-based lubricants.

5. ACKNOWLEDGEMENT

The authors express their thankful regrads to the authorities of Rnewable Energies Resrach Institute, Tarbiat Modares University for their technical support.

REFERENCES

1. Zulkifli, N.W.M., Kalam, M.A., Masjuki, H.H., Shahabuddin, M. and Yunus, R., "Wear prevention characteristics of a palm oil-based TMP (trimethylolpropane) ester as an engine lubricant", ***Energy***, Vol. 54, (2013), 167-173. (https://doi.org/10.1016/j.energy.2013.01.038).
2. Salimon, J., Salih, N. and Yousif, E., "Biolubricants: Raw materials, chemical modifications and environmental benefits", ***European Journal of Lipid Science and Technology***, Vol. 112, No. 5, (2010), 519-530. (https://doi.org/10.1002/ejlt.200900205).
3. Almasi, S., Ghobadian, B., Najafi, G. and Dehghani-Soufi, M., "A review on bio-lubricant production from non-edible oil-bearing biomass resources in Iran: Recent progress and perspectives", ***Journal of Cleaner Production***, (2021), 125830. (https://doi.org/10.1016/j.jclepro.2021.125830).
4. Dehghani-Soufi, M., Ghobadian, B., Atashgaran, M., Mousavi, S.M. and Najafi, G., "Biolubricant production from edible and novel indigenous vegetable oils: Mainstream methodology, and prospects and challenges in Iran", ***Biofuels, Bioproducts and Biorefining***, Vol. 13, No. 3, (2019), 838-849. (https://doi.org/10.1002/bbb.1953).
5. Mobarak, H.M., Mohamad, E.N., Masjuki, H.H., Kalam, M.A., Al Mahmud, K.A.H., Habibullah, Md. and Ashraful, A.M., "The prospects of biolubricants as alternatives in automotive applications", ***Renewable and Sustainable Energy Reviews***, Vol. 33, (2014), 34-43. (https://doi.org/10.1016/j.rser.2014.01.062).
6. Bashiri, S., Ghobadian, B., Dehghani-Soufi, M. and Gorjian, S., "Chemical modification of sunflower waste cooking oil for biolubricant production through epoxidation reaction", ***Materials Science for Energy Technologies***, Vol. 4, (2021), 119-127. (https://doi.org/10.1016/j.mset.2021.03.001).
7. Gunstone, F., Rapeseed and canola oil production, processing, properties and uses, CRC Press, (2004). (https://www.wiley.com/en-us/exportProduct/pdf/9781405147927).
8. Fox, N.J. and Stachowiak, G.W., "Vegetable oil-based lubricants-a review of oxidation", ***Tribology International***, Vol. 40, No. 7, (2007), 1035-1046. (https://doi.org/10.1016/j.triboint.2006.10.001).
9. Mehdi, S., Asghari, A., Ghobadian, B. and Dehghani-Soufi, M., "Conversion of Pistacia atlantica mutica oil to trimethylolpropane fatty acid triester as a sustainable lubricant", ***Biomass Conversion and Biorefinery***, Vol. 10, No. 1, (2020), 139-148. (https://doi.org/10.1007/s13399-019-00452-y).
10. Rudnick, L.R., Synthetics, mineral oils, and bio-based lubricants: chemistry and technology, CRC Press, (2020). (https://doi.org/10.1201/9781315158150).
11. Honary, L. and Richter, E., Biobased lubricants and greases: Technology and products, Vol. 17., John Wiley & Sons, (2011). (https://media.wiley.com/product_data/excerpt/89/04707415/0470741589-42.pdf).
12. Almasi, S., Ghobadian, B., Najafi, G. and Dehghani-Soufi, M., "A novel approach for bio-lubricant production from rapeseed oil-based biodiesel using ultrasound irradiation: Multi-objective optimization", ***Sustainable Energy Technologies and Assessments***, Vol. 43, (2021), 100960. (https://doi.org/10.1016/j.seta.2020.100960).
13. Dehghani-Soufi, M., Ghobadian, B., Mousavi, S.M., Najafi, N. and Aubin, J., "Valorization of waste cooking oil based biodiesel for

biolubricant production in a vertical pulsed column: Energy efficient process approach", ***Energy***, Vol. 189, (2019), 116266. (https://doi.org/10.1016/j.energy.2019.116266).

14. Sharma, R.V. and Dalai, A.K., "Synthesis of bio-lubricant from epoxy canola oil using sulfated Ti-SBA-15 catalyst", ***Applied Catalysis B: Environmental***, Vol. 142, (2013), 604-614. (https://doi.org/10.1016/j.apcatb.2013.06.001).
15. Chowdhury, A., Debarati M. and Biswas, D., "Biolubricant synthesis from waste cooking oil via enzymatic hydrolysis followed by chemical esterification", ***Journal of Chemical Technology & Biotechnology***, Vol. 88, No. 1, (2013), 139-144. (https://doi.org/10.1002/jctb.3874).
16. Salimon, J., Salih, N. and Yousif, E., "Biolubricant basestocks from chemically modified ricinoleic acid", ***Journal of King Saud University-Science***, Vol. 24, No. 1, (2012), 11-17. (https://doi.org/10.1016/j.jksus.2010.08.008).
17. Sabzimaleki, M., Ghobadian, B., Farsibaf, M.M., Najafi, G., Dehghani-Soufi, M. and Ardebili, S.M.S., "Optimization of biodiesel ultrasound-assisted synthesis from castor oil using response surface methodology (RSM)", ***Chemical Product and Process Modeling***, Vol. 10, No. 2, (2015), 123-133. (https://doi.org/10.1515/cppm-2014-0013).
18. Biermann, U. and Metzger, J.O., "Synthesis of alkyl-branched fatty acids", ***European Journal of Lipid Science and Technology***, Vol. 110, No. 9, (2008), 805-811. (https://doi.org/10.1002/ejlt.200800033).
19. Salimon, J., Salih, N. and Yousif, E., "Synthetic biolubricant basestocks from epoxidized ricinoleic acid: Improved low temperature properties", ***Kemija u Industriji: Journal of Chemists and Chemical Engineers***, Vol. 60, No. 3 (2011), 127-134. (https://www.researchgate.net/publication/50247430_Synthetic_Biolubricant_Basestocks_from_Epoxidized_Ricinoleic_Acid_Improved_Low_Temperature_Properties).

JREE: Vol. 9, No. 4, (Autumn 2022) 109-121

Journal of Renewable Energy and Environment

Journal Homepage: www.jree.ir

Materials and Energy Research Center

MERC

Research Article

Multiobjective Design Optimization of a Multi-Phase Outer-Rotor Permanent Magnet Wind Generator

Ali Ebadi *, Ali Akbar Abdoos, Mohammad Ebrahim Moazzen, Sayyed Asghar Gholamian

Department of Electrical and Computer Engineering, Babol Noshiravani University of Technology, P. O. Box: 47148-71167, Babol, Mazandaran, Iran.

PAPER INFO

Paper history:
Received: 28 February 2022
Revised in revised form: 02 June 2022
Scientific Accepted: 20 June 2022
Published: 18 December 2022

Keywords:
Optimization,
Permanent Magnet Generator,
Wind Power,
Genetic Algorithm

ABSTRACT

Nowadays, the Permanent Magnet (PM) generator has become an instrumental tool for wind power generation due to its high performance. In this study, an optimal design is established to provide a cost-effective multiphase outer-rotor PM wind generator (OR-PMWG). The cost of the generation system (generator and power converter) as well as the annual energy output must be optimized to ensure cost-effective PM wind generation. In fact, the main novelty of this paper lies in the presentation of an accurate model of OR-PMWG and the investigation of the design variables affecting annual energy output and the generation system cost (GSC). In this respect, a multi-objective framework is presented to make satisfactory agreement among all objectives. At first, the main optimal design objectives namely generation system cost and annual energy output are optimized separately and then, a multi-objective optimization is established, in which all the objectives are considered simultaneously. In order to tackle these optimization problems, Genetic Algorithm (GA) is adopted herein to determine the design variables. It is also shown that simultaneous optimization with 71.39 (MWh) AEO and 2651.51 (US$) GSC leads to a more optimal design for a PM wind generation system. In addition, the effectiveness of the presented optimal design is demonstrated by making a comparison between a prototype outer-rotor PM wind generator and the theoretical counterpart. Finally, a finite element analysis (FEA) is carried out for the validation of the outcomes obtained from the proposed optimal design.

https://doi.org/10.30501/jree.2022.317176.1287

1. INTRODUCTION

In recent years, due to the precipitous depletion of fossil fuels, increased energy costs, and environmental issues, the demand for a reliable and sustainable alternate source of energy has been highlighted. Potentially, renewable energy resources are becoming more viable technology to resolve this concern. Among renewable resources, wind energy generation has exhibited dramatic development, which can be attributed to infinite resources, low production cost, and environmentally-friendliness. Moreover, in comparison with other renewable resources, the scope of wind power market is growing substantially [1, 2]. In fact, the global-scale installed capacity of wind power has grown swiftly during the past two decades, from 18 GW in 2000 to 743 GW at the end of 2019 [3]. There is an increasing interest in the development of a small-scale wind power system because large-scale wind farms do not represent a sustainable alternative for renewable power generation. Therefore, the best available option is the installation of decentralized wind power systems that comprise small-scale wind farms. The unit installation costs and the expenses for production per power unit for small-scale wind power generation, among other wind power generation systems, are smaller than those for solar power generation with the same capacity [4]. Generally, a wind turbine according to the construction of drive trains can be classified into direct-drive and geared-drive concepts. Low maintenance, high efficiency, energy efficiency, and reliability requirements for wind power generation tend to use gearless concept [5, 6]. Furthermore, among different types of electrical generators available for converting the wind power, the permanent magnet synchrounes generator (PMSG) has huge potential for this application because of its higher efficiency, torque density, reliability, and lower maintenance [6, 7]. Polinder et al. [8] compared different well-known types of employable generator systems for wind turbines in view of annual energy output and cost for a given wind climate. They concluded that the direct-drive PM wind generator (DD-PMWG) was the best choice on account of the above-mentioned advantages as well as the elimination of brushes or gearbox. This machine can be divided into two categories from the viewpoint of the rotor-stator structure including inner and outer rotor types, in which the second one has a better performance in terms of cooling and saturatio [9].

Based on the above descriptions, designing high-performance PM generators and wind turbines optimally has become more important day by day. In [10], the Lagrange

*Corresponding Author's Email: ebadi.power@gmail.com (A. Ebadi)
URL: http://www.jree.ir/article_155019.html

Please cite this article as: Ebadi, A., Abdoos, A.A., Moazzen, M.E. and Gholamian, S.A., "Multiobjective design optimization of a multi-phase outer-rotor permanent magnet wind generator", ***Journal of Renewable Energy and Environment (JREE)***, Vol. 9, No. 4, (2022), 109-121. (https://doi.org/10.30501/jree.2022.317176.1287).

multiplier as a simple analytical optimization method was employed to maximize the air-gap apparent power of the PMSG under tangential stress constraint. A combination of the simple magnetic equivalent circuit approach and the finite-element method was established in [11] to achieve an optimum design of an outer-rotor PM wind generator using a high-energy neodymium-iron-boron magnet. Based on the results of an optimal design presented by Li et al. [12], the multi-bird concept of PM generator was more cost-effective than the direct-drive one. The cogging torque and total harmonic distortion (THD) of back electromotive force of the small-scale outer-rotor PM wind generator were minimized by a multi-objective optimization design method proposed by Lee et al. [13]. Bazzo et al. [14] presented a multi-physics design of a PM generator so that the cost and losses of the grid side power electronic converters could be taken into account. In [15], the optimization of the direct drive PM generators was accomplished to reduce the cost of energy in offshore wind turbines. Asef et al. combined the modified Booth's algorithm and a dual-response surface method for the purpose of multi-objective design optimization of a PMSG [16]. The output power maximization and manufacturing cost minimization were considered as two main objectives to improve the performance of power generation under a number of design constraints. In some papers, the main focus of design optimization of PM wind generators is to reduce the cogging torque [17, 18]. In [19], a compact BEM (blade element momentum) analysis was derived to design optimal blades for continuously variable speed horizontal axis wind turbines. The present BEM modeling may be useful to reduce the computational effort of iterative numerical methods used in determining off-design power performance of conventional wind turbines with constant speed. In [20], the circulating aerofoil for use in Magnus-type wind turbine was introduced which utilized the treadmill motion in a simple and easy manner to manufacture aerofoil surfaces. It is proved here that the concept of generating Magnus lift from circulating aerofoil surface is computationally valid. In [21], artificial neural network (ANN) modeling was employed to investigate the effects of various environmental and machine factors on the energy gain from wind farm systems. It was demonstrated that ANN was a better statistical predictor based on numerical comparison with non-linear regression. Since the gearless wind generators operate at relatively low speeds, they are known by their large dimensions, volume, and heavy weight. In practical applications, low system cost and high annual output energy are two main advantages for a cost-effective wind power system.

In this paper, a multi-objective framework is oriented to minimize the cost of generation system and to maximize annual the output energy of the generation system. The global cost of a wind power system includes the costs of production, transportation, and installation of all components, like electrical generator, power electronic converter, and turbine blades and tower. Also, the operational as well as maintenance costs of the system should be calculated [22]. The calculation of these costs is difficult and is often estimated by adopting several assumptions. Hence, this research only considers the PM generator and power converter costs. The six-phase PM wind generator is proposed to increase the reliability of the wind power generation. It is noteworthy to mention that this type of generator can continue operating during faults using the remaining healthy phases. Reducing the torque pulsation amplitude and reducing the current phase amplitude of armature without increasing the phase voltage are the other advantages of multiphase machines [23]. In this study, the six phases of the generator are arranged as a two-star configuration. For more reliability, each three-phase set is supplied by a back-to-back power converter and the converters are connected as parallel. Figure 1 indicates a schematic view of the grid-connected DDPMWG.

This paper is organized as follows. In Section 2, the modeling of the OR-PMWG concept is described. The design variables are presented in Section 3. Optimal design results are presented in Section 4, and also the results are compared with a prototype. Then, the design validity is verified by 3D finite element analysis in Section 5. Finally, conclusions are given in Section 6.

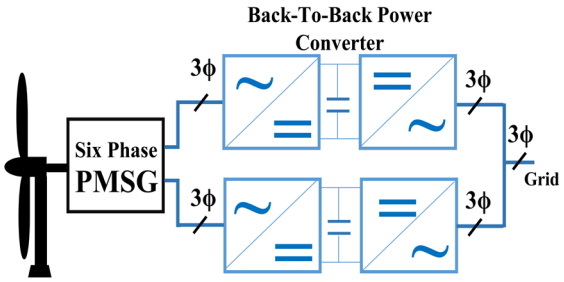

Figure 1. Configuration of the multiphase DD-PMWG system

2. MODELING THE OR-PMWG CONCEPTS

The generator specifications and explanation of its structure are described at the beginning of this section. Thereafter, geometrical relationships of the generator are outlined. The calculation of the generator losses and OR-PMWG costs comes after that. Next, the wind turbine modeling and annual energy output calculation in this case study are described. Finally, the overview of the design model is presented as a flowchart.

2.1. PMSG specifications

There are various types of PM machines that can be employed in the low-speed, gearless large wind turbines. However, because of high torque density, simple structure, and suitable reliability, the radial-flux concept with surface-mounted PMs can be counted as a better option [5, 22]. Generally, there are two configurations of the radial-flux PMSG: inner outer rotor types. In the case of the outer rotor structure, the outer part is rotor, and the stator is inside of machine, as shown in Figure 2a. Figure 2b illustrates the main geometrical parameters of a radial-flux, surface-mounted outer-rotor PMSG (OR-PMSG). The inner rotor type is mostly used, whereas the outer rotor structure is having few applications. However, in order to cope with the various difficulties in designing a DD-PMWG, the outer rotor configuration was adopted in this paper. Following are the several advantages of OR-PMSG [7, 9, 11, 13]:

(a) The hub of the turbine blades can be conveniently fixed to the exterior rotor; therefore, this structure can be well adapted to wind power application.

(b) Unlike the inner rotor type, the cooling condition for the PMs is improved, because the outer rotor is directly exposed to the wind.

(c) Regarding the large rotor diameter, multi-pole magnets can be applied in order to generate power at low speeds.

(d) The multi-pole structure leads to (1) the reduction of the total length of the magnetic flux path and a noticeable decrease in the volume and weight of the rotor back iron and (2) shorter coil pitch and resulting end-winding than the inner rotor. Therefore, the copper loss is lower.

The six-phase stator winding is divided into two star-connection and three-phase sets, i.e., winding sets of ABC and XYZ (see Figure 3). According to this figure, the proposed generator has symmetrical 60° displacement windings. It should be noted that the neutral points of the two star-connection winding sets are considered not to be connected together. By doing so, a winding becomes immune to physical fault events on the other winding, leading to higher reliability. Consequently, the flow of triplen harmonics in line-to-line voltage is prevented [24]. Specific parameters of OR-PMSG are listed in Table 1. The following assumptions are made in the OR-PMSG design optimization:

(1) In order to provide an almost sinusoidal induced voltage, the stator winding is a two-layer distributed winding. Moreover, to minimize both the 5th and 7th time harmonics, the coil span is equal to 5/6 of the pole pitch.

(2) The air-gap is one thousandth of the outer diameter of stator [6, 25].

(3) The NdFeB35 is selected as PM material with remanent flux density B_r = 1.23 T.

(4) Since the PM wind generator is connected to grid via power electronic converter, it is assumed that the PMSG runs at the unity power factor and at all wind speeds [26].

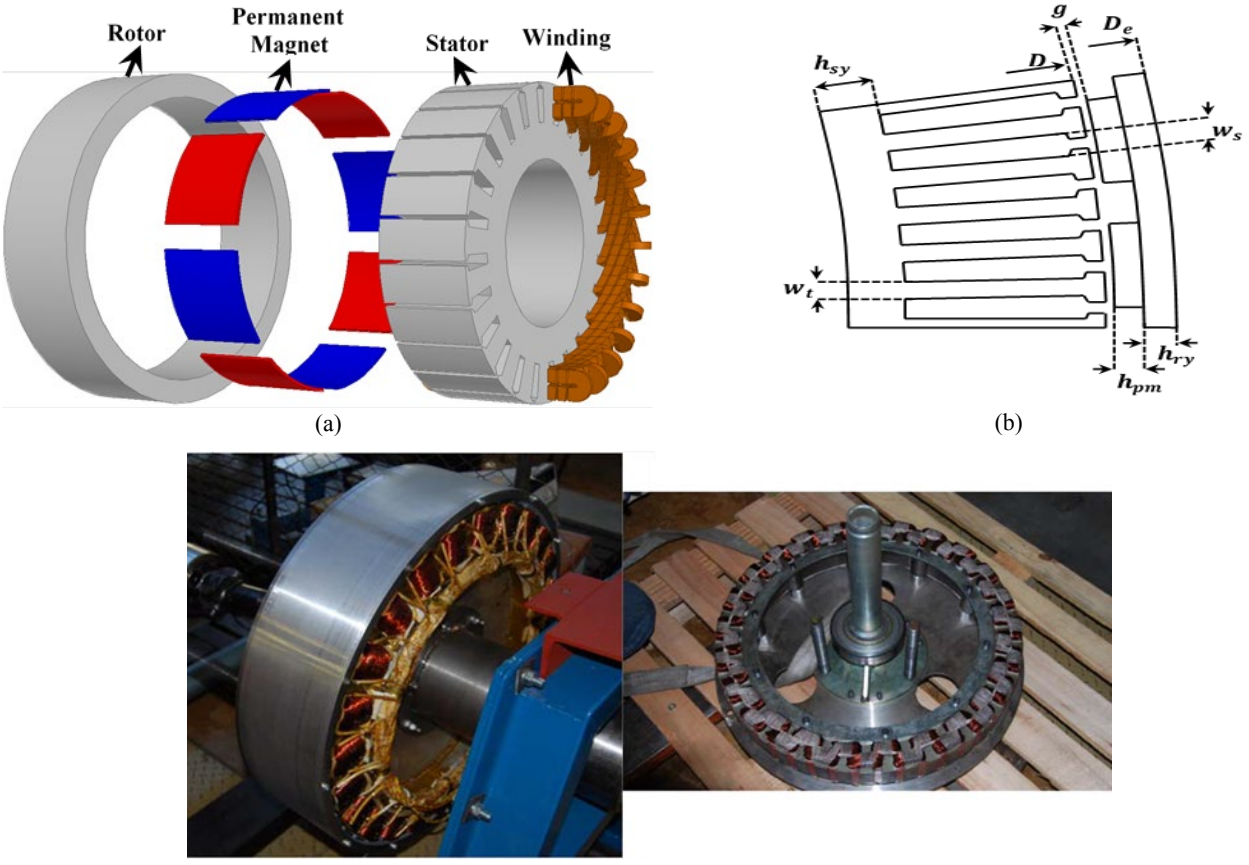

Figure 2. (a) Radial-flux PM machine construction with outer rotor, (b) Typical cross section of the OR-PMSG, (c) The real configuration of OR-PMSG [17]

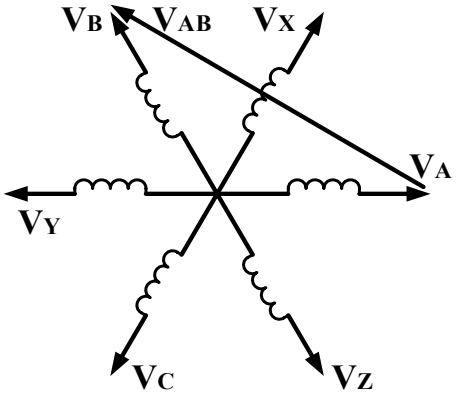

Figure 3. Phasor diagram of the six-phase winding connections

Table 1. Modeling constants and generator main parameters

Parameters and constants	Value
Main design parameters	
Nominal output power (W)	15000
Nominal Line voltage (V)	400
Nominal shaft speed (rpm)	150
Number of slots per pole per phase	2
Current density (A/mm^2)	5
Iron core specifications	
ρ_h (W/kg)	2
ρ_e (W/kg)	0.5
Cost modeling constants	
Copper cost (US$/kg)	9.61
Permanent magnet cost (US$/kg)	220.31
Iron core cost (US$/kg)	2.62
Reference structure cost (US$)	3250

2.2. Generator geometrical modeling

In this subsection, the analytical models are established to calculate various dimensions of the generator. To extract an analytic relationship between the geometric dimensions and magnetic parameters, the air-gap apparent power is developed in terms of the current and induced voltages of the stator winding. The induced voltage by air-gap flux density can be presented as follows:

$$e(t) = \sqrt{2}\, E_{rms} \sin(2\pi ft) \quad (1)$$

where f is frequency. The rms value of the induced voltage E_{rms} as a function of the generator dimensions can be calculated as follows [8, 12]:

$$E_{rms} = \frac{\sqrt{2}}{2} N_{ph} \omega_m D L B_{mg1} k_{w1} \quad (2)$$

wherein N_{ph}, ω_m, and k_{w1} are the winding turns per phase, the mechanical angular speed of the rotor, and fundamental winding factor, respectively. Also, L and D are the machine length and stator outer diameter, respectively, and B_{mg1} is the highest fundament harmonic value of the air-gap flux density due to the PMs, which is obtained as follows [8, 27]:

$$B_{mg1} = \frac{4}{\pi} B_{mg} \sin\left(\frac{\pi}{2}\alpha_i\right) \quad (3)$$

where the air-gap flux density peak value B_{mg} and the pole-arc to pole-pitch ratio α_i are illustrated in Figure 4. B_{mg} in PM machines depends on the PM material properties and allowable flux density in the machine teeth. To reduce the amount of needed copper as well as the volume and weight of the machine, the magnetic air gap flux density for low- and medium-speed applications must be high enough. Because of its high residual flux density and energy generation, the NdFeB magnet is technically the best choice for this machine [28]. Therefore, for the sizing procedure of PM machine using NdFeB, the value of the air-gap flux density peak is initially chosen to be 60-80 % for Br [27]. The range of values for α_i as one of the design variables is chosen to be 0.6-0.9 [6]. By introducing the peak value expression of stator linear current density, A_m, the current waveform rms value is as follows [10, 12]:

$$I_{rms} = \frac{\pi D A_m}{2m\sqrt{2}\, N_{ph}} \quad (4)$$

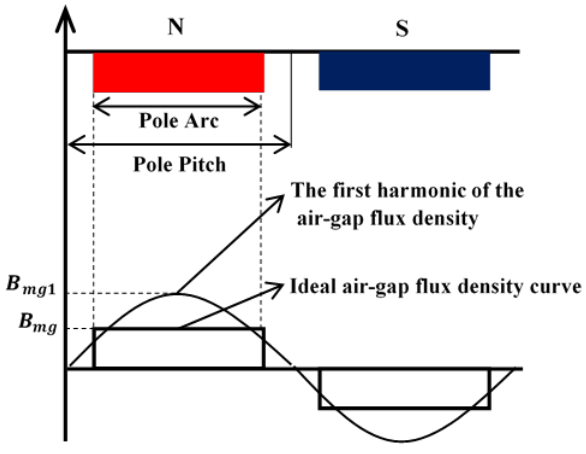

Figure 4. The ideal curve of the air-gap magnetic flux density distribution above the magnets in an electric period

where m stands for the number of phases. The specific electric loading is determined based on the machine cooling system and efficiency [28]. The amplitude of the specific electric loading ranges from 10000 to 55000 A/m for medium power machines [27]. Therefore, the current expression takes the following form:

$$i(t) = \sqrt{2} I_{rms} \sin(2\pi ft) \quad (5)$$

The average apparent power crossing the air-gap over one period of the power source can be expressed as:

$$S_g = \frac{m}{T}\int_0^T e(t).i(t)\, dt \quad (6)$$

By substituting Eqs. (1) and (5) into Eq. (6), the air-gap apparent power in terms of the generator main dimensions can be written as follows:

$$S_g = 0.5\pi^2 k_{w1} n_s D^2 L A_m B_{mg1} \quad (7)$$

where n_s is the rotational speed of the rotor in rev/sec. (since). Then, the output power is calculated as follows:

$$P_{out} = \frac{1}{\epsilon} S_g \cos(\phi) \quad (8)$$

The generator main dimensions in terms of the output power can be expressed as follows:

$$D^2 L = \frac{P_{out}.\epsilon}{0.5\pi^2 A_m B_{mg1} n_s k_{w1} \cos(\phi)} \quad (9)$$

In which P_{out} denotes the nominal output power of the PMSG. ϵ is the ratio of the induced voltage to the full load terminal voltage. In addition, $\cos(\phi)$ stands for the load power factor. In the electrical machine design, the relative apportionment of the machine length and air-gap diameter depends on its application. For the direct-drive radial-flux PM wind generator, the suitable range for the ratio of the generator length to air-gap diameter is 0.14-0.5 [29]. Based on Ampere's circuital law, the BH characteristic of a PM material, magnetic flux continuity, and geometry are shown in Figure 2 and the PM height as a function of magnetic air-gap flux density can be expressed as [6, 12]:

$$h_{pm} = \frac{B_{mg}}{B_r} \mu_{rec} g_{eff} \quad (10)$$

where g_{eff} is the effective air-gap length and μ_{rec} is the PM recoil line relative permeability. The stator teeth, rotor, and stator yoke provide the return paths for flux between poles. Therefore, dimensions of these parts are calculated by the allowed magnetic flux densities. The stator tooth width w_t, rotor, and stator yoke height h_y can be presented by [6, 30]:

$$w_t = \frac{\pi D}{k_{st} Q} . \frac{B_{mg}}{B_t} \quad (11)$$

$$h_y = \frac{D}{k_{st} P} . \frac{B_{mg}}{B_y} \quad (12)$$

where k_{st}, Q, and P denote the stacking factor for the stator core, number of slots, and poles, respectively. Also, B_t and B_y are the maximum tooth and yoke flux density, respectively.

2.3. OR-PMWG losses modeling

The considered losses in this study are the basic losses of the OR-PMWG, i.e., the stator iron losses P_{Fe}, the generator copper losses P_{Cu}, and the back-to-back power converter losses P_{BPC}. In fact, the generator total losses are the sum of P_{Fe} and P_{Cu}. Also, the sum of these losses with power converter losses is called total generation loss. The rotor iron losses are negligible in the surface-mounted PM machine due to their large effective air-gap [27]. The mechanical losses in the electrical machines consist of friction in couplings and bearings and windage losses. Here, the mechanical losses will not be considered because they are usually small [31]. Therefore, the total generation losses are determined as follows:

$$P_{loss} = P_{Fe} + P_{Cu} + P_{BPC} \quad (13)$$

The iron losses can be calculated approximately using Steinmetz formula as follows [8, 15]:

$$P_{Fe} = 2m_{Fe}\rho_h \frac{f}{50}\left(\frac{B_{Fe}}{1.5}\right)^2 + 2m_{Fe}\rho_e \left(\frac{f}{50}\right)^2 \left(\frac{B_{Fe}}{1.5}\right)^2 \quad (14)$$

where f, B_{Fe}, and m_{Fe} are the frequency of the field in the iron, stator teeth or yoke flux density, and iron weight, respectively. ρ_e is the specific eddy current loss and ρ_h is the specific hysteresis loss w/kg at flux density 1.5 T and frequency 50 Hz [8, 16]. For the calculation of total iron losses, the hysteresis and eddy current losses in various parts (teeth and yokes) are determined and then added. The iron core specifications are given in Table 1. The peak magnetic flux densities in the teeth and stator and rotor yoke are of the most important limitations in designing an electrical machine and also chosen as design variables. The copper losses are given by:

$$P_{Cu} = mR_s {I_{rms}}^2 \quad (15)$$

Various ways to estimate the power converter losses are presented. In this study, the losses of each three-phase back-to-back power converter are calculated as [5, 8]:

$$P_{BPC} = \frac{P_{CN}}{31}\left(1 + 10\frac{I_P}{I_{PN}} + 5\left(\frac{I_P}{I_{PN}}\right)^2 + 10\frac{I_G}{I_{GN}} + 5\left(\frac{I_G}{I_{GN}}\right)^2\right) \quad (16)$$

where P_{CN} denotes the converter loss at the nominal power which is 3 % of it, I_P denotes the PMSG side current, and I_{PN} is the PMSG side converter nominal current. I_G and I_{GN} are the grid side current and nominal current of the grid side converter, respectively.

2.4. OR-PMWG cost modeling

The proposed model considers the generator cost and costs of power electronic converters to estimate the cost of a generation system. The OR-PMWG cost C_{OP} can be calculated by summing up the active material and generator structure costs. The cost of the back-to-back power converter (BPC) for different power ratings includes OR-PMWG side power converter (OSPC), grid side power converter (GSPC), capacitors, drivers, protections, and heat-sink system [14]. The cost of active materials (C_{act}) based on the relevant specific cost (c_{Cu}, c_{PM}, and c_{Fe}) can be expressed by the sum of the copper, PM, and core weights (w_{Cu}, w_{PM}, and w_{Fe}) in the following:

$$C_{act} = w_{PM}c_{PM} + w_{Cu}c_{Cu} + w_{Fe}c_{Fe} \quad (17)$$

Furthermore, an approximate model is used for the structure cost C_{str}; thereafter, it is calculated based on the rotor outer diameter D_e and length of the generator as follows [6, 19]:

$$C_{st} = \frac{c_{str}}{2}\left[\left(\frac{D_e}{D_{ref}}\right)^a + \left(\frac{L}{L_{ref}}\right)^a\right] \quad (18)$$

where c_{str} denotes a reference machine specific cost with the diameter (D_{ref}) of 1.0 m and the length (L_{ref}) of 0.3 m. The exponent a (set to 3) describes how fast the structure cost increases with increasing rotor outer diameter and length of generator. The BPC cost of each three-phase power converter is calculated as follows [14]:

$$C_{BPC} = 725.\, e^{0.0145\, I_{rms}} \quad (19)$$

Finally, the total cost that is obtained by summing up the OR-PMSG and the BPC costs can be written as follows:

$$C_t = C_{OP} + C_{BPC} \quad (20)$$

Table 1 presents the costs of different components.

2.5. Modeling of wind turbine

The wind turbine shaft speed as a function of wind speed, available nominal power on the shaft, and annual energy output (AEO) of generation systems should be calculated using this sub-model. In this paper, the wind turbine with a horizontal axis is used and it enjoys a number of advantages over vertical axis type including higher aerodynamic efficiency and higher tip-speed ratio.

2.5.1. Power absorption and shaft speed

The nominal speed of the OR-PMSG, which has direct impact on the overall size, can be estimated from the wind energy equations. The wind turbine absorbs power P_T as a function of the wind speed v and it can be calculated as follows [14, 32, 33]:

$$P_T = 0.5C_p\rho_{air}\pi R^2 v^3 \quad (21)$$

where ρ_{air} is the air density and R is the radius of the turbine blade. C_p is the aerodynamic efficiency with typical values between 0.3 and 0.45, which is a function of the tip speed ratio λ. Furthermore, λ can be expressed as [32, 33]:

$$\lambda = \frac{\omega_r R}{v} \quad (22)$$

wherein $\omega_r = 2\pi n_r/60$ is the angular shaft speed rad/s and n_r denotes the rotational speed rpm. The range of the values for the tip-speed ratio is 6-8 [1], or 5-7 [22]. Finally, by combining Eqs. (21) and (22), one can obtain an estimation of the operating shaft speed as a function of the generator output power [29, 32]:

$$\omega_r = \sqrt{\frac{0.5C_p\rho_{air}\pi\lambda^2 v^5\eta_g}{P_{out}}} \quad (23)$$

where η_g is the efficiency of the generator, which is assumed to be 0.9 for shaft speed estimation [5]. The wind speed is one

of the important input parameters for the calculation of the nominal shaft speed. In this study, its range is considered 5-10.2 m/s. It should be noted that this range of wind speeds has been reported for Hamoon region in Iran [33]. Therefore, OR-PMSG is designed to operate at a wind speed of 10 m/s. The characteristics of the wind turbine as well as the wind site are summarized in Table 2. Assuming a 10 m/s wind speed and using the characteristics given in Table 2, the nominal shaft speed can be estimated at 150 rpm or 2.5 rev/s. The small-scale PM wind generators frequency has a normal range that is reported to be 10-70 Hz [29] or 30-80 Hz [11]. Thus, for the purpose of this paper, the generator pole number as an optimization variable varies from 8 to 64.

2.5.2. Annual energy output calculation

To assess the economic feasibility of the wind turbine installation at a specific site, the estimation of the annual output energy is very important. The AEO estimation depends on many parameters, e.g., average wind speed and operational and power characteristics of the wind turbine. The operating and power characteristics of the wind turbines at different wind speeds can be described conventionally as a power curve, which is shown in Figure 5. It has three zones based on the velocity scale [2, 19]:

Zone A: The power extracted from the wind turbine is zero, because the wind is very light for useful energy production.

Zone B: The lower limit of this zone is the cut-in wind speed v_i. The wind turbine commences power production Above v_i. In this zone, the control system of the wind turbine to capture the maximum wind power regulates the shaft speed for each wind speed.

Zone C: In this zone, the wind speeds are above nominal value v_r. The rotational speed and power are kept constant Above v_r, and the maximum power output of the electrical generator is obtained. Beyond the cut-out wind speed v_o, the wind turbine shuts off.

By integrating the product of the probability density function $f(v_j)$ of wind speed with the generation system output power, the AEO of the generation system (generator and power converter) can be approximately estimated as follows [12]:

$$AEO_G = 24 \times 365 \int_{v_i}^{v_o} \eta_{gs}(v).P_T(v).f(v)dv = 8760 \sum_{j=1}^{n} \eta_{gs}(v_j).P_T(v_j).f(v_j)\Delta v \quad (24)$$

where η_{gs} is the efficiency of the generation system. The wind data can be well fitted into the Rayleigh distribution function. The expression of Rayleigh distribution function, which describes the probability of having a wind speed during the year, is expressed as follows [31, 31]:

$$f(v_j) = \frac{\pi}{2}\frac{v_j}{(\bar{v})^2} e^{-\frac{\pi}{4}(\frac{v_j}{\bar{v}})^2} \quad (25)$$

where v_j is the particular wind speed and $\bar{v}$ is the average wind speed.

Table 2. Wind turbine and wind site specifications

Specifications	Value
Nominal wind speed (m/s)	10
Average wind speed (m/s)	8.7
Cut-in wind speed (m/s)	4
Cut-out wind speed (m/s)	25
Nominal turbine shaft speed (rpm)	150
C_p	0.42
λ	7

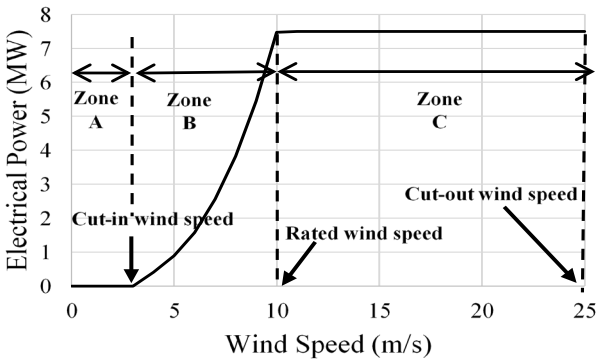

Figure 5. Operational zones of a wind power generation

2.6. Design flow chart

Figure 6 shows the proposed design procedure. As introduced earlier, the design variables are determined by the GA to achieve the minimal generation system cost and maximum AEO. Afterwards, different generator parameters are calculated. Accordingly, the magnetic air gap flux density and the terminal voltage at nominal load are computed. If one of the termination criteria is satisfied, the optimization procedure stops; if else, it will cease to operate.

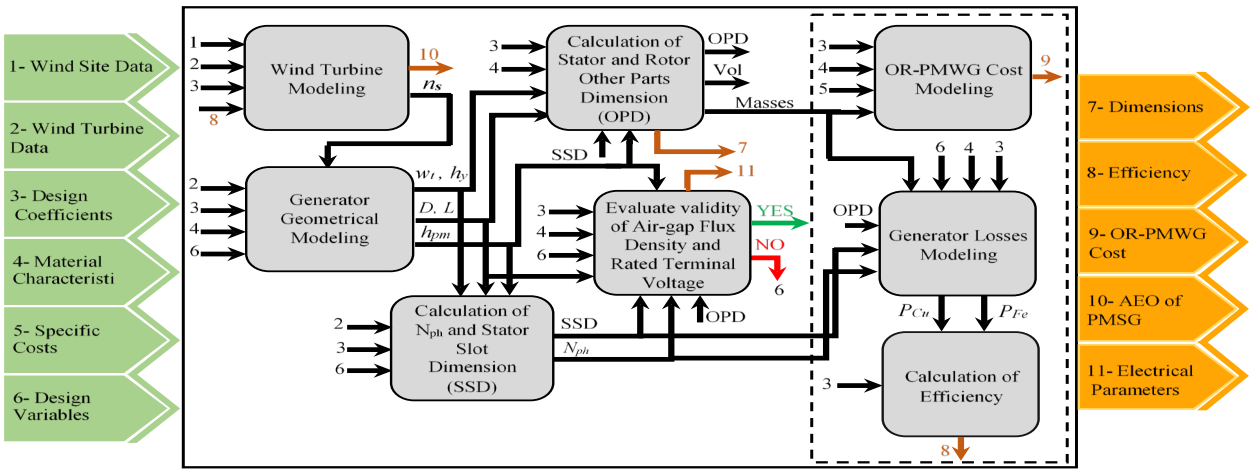

Figure 6. Design flowchart of the OR-OMWG

3. The design variables

In order to obtain an optimal design, the design variables are determined first. Then, their impacts on the GSC and AEO are investigated. The design variables are presented in Table 3. Two effective parameters within the optimal design process are Am and Bmg and their impact alongside the other parameters are shown in Figures 7 and 8.

Table 3. The design variables and their boundaries

Design variables	Range	
	Min	Max
A_m (kA/m)	10	55
B_{mg} (T)	0.738	0.984
L/D	0.14	0.5
ϵ	1	1.4
α_i	0.6	0.9
P	8	64
B_y Stator (T)	1.1	1.5
B_y Rotor (T)	1.3	1.6
B_t (T)	1.5	2

To provide a better visual representation of the impact of the design variables, the GSC and AEO are shown in Figure 7 in separate 3D subplots, while the A_m and another effective parameter are considered as two variables. It can be seen from Figure 7a that maximum AEO can be achieved when A_m varies between 20 and 30 kA/m and B_{mg} ranges between 0.8 and 0.9 T. Moreover, Figure 7b shows that the lowest GSC occurs at A_m and B_{mg}. According to Figure 7c, when A_m varies between 20 and 40 kA/m and the pole-arc to pole-pitch ratio α_i is in the range of 0.8 to 0.9, the maximum AEO is delivered. According to Figure 7d, the generation system cost is minimum when α_i=0.6 and A_m=60 kA/m. Figure 7e shows that when A_m and L/D ratio ranges between 30-50 kA/m and 0.14-0.2, respectively, the AEO can be maximum. According to Figure 7f, the lowest cost is obtained when L/D=0.14 and A_m=60 kA/m. The impacts of A_m and pole number P on GSC and AEO are investigated, as shown in Figures 7g and 7h, respectively. The lowest generation system cost is achieved when A_m varies between 20 and 30 kA/m and the pole number is 20. Moreover, minimum GSC is related to A_m and maximum pole number is found in Figure 7h. Figure 7i shows that the maximum AEO is restricted to A_m in the range of 20 to 30 kA/m, while the ratio of induced voltage to full load terminal voltage ϵ is minimum. According to Figure 7j, the minimum cost is computed when ϵ =1 and A_m=60 kA/m. Furthermore, according to Figure 7k, maximum AEO belongs to the area with A_m at about 25 kA/m, while the peak tooth flux density B_t varies from 1.6 to 1.75 T. As shown in Figure 7l, minimum GSC occurs at A_m and B_t does not have a significant effect on it.

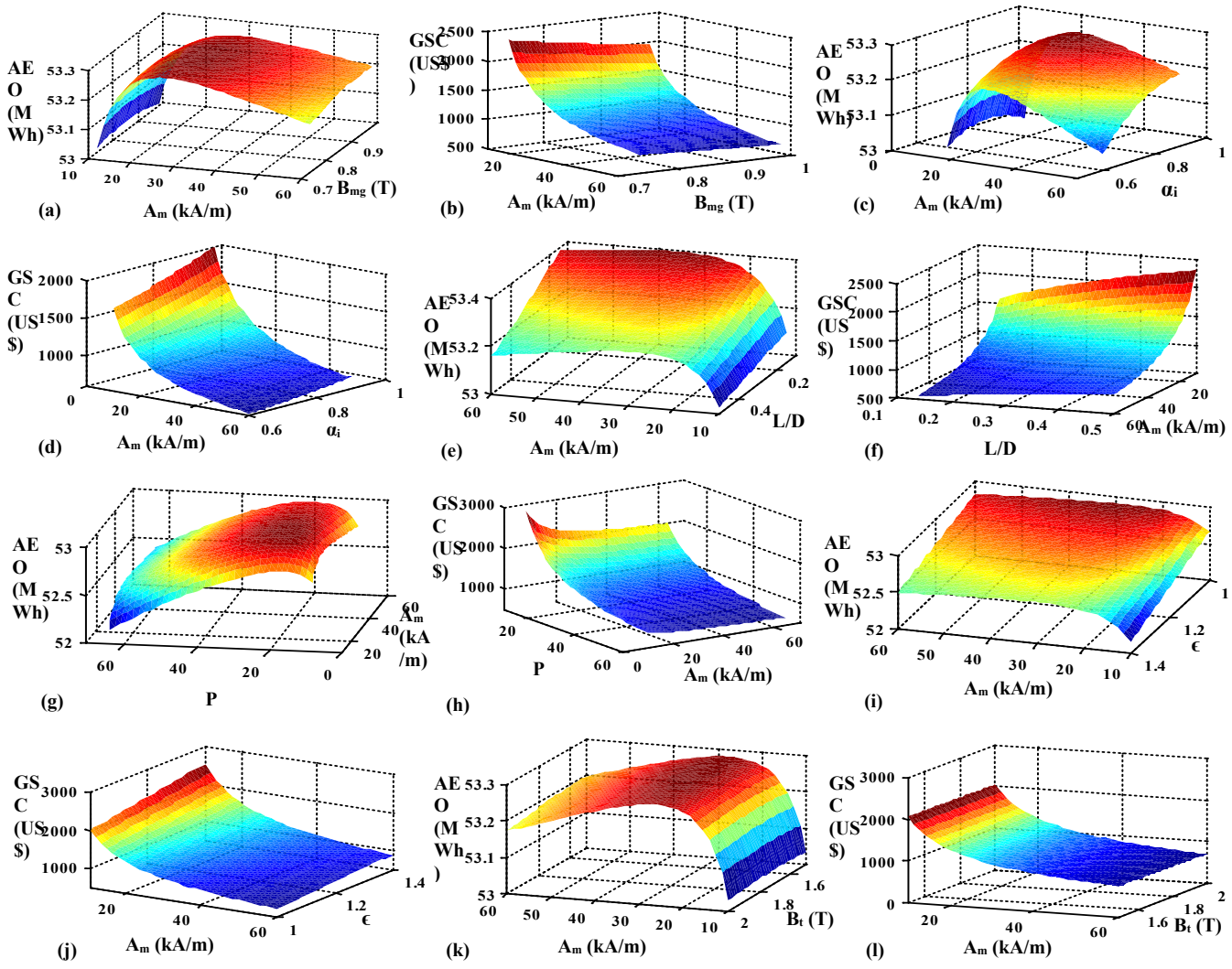

Figure 7. Impacts of A_m and other design variables on GSC and AEO

Similarly, in Figure 8, the impact of maximum air gap flux density and other optimization variables on the generation system cost and AEO is shown. It is clearly observed from Figure 8a that the maximum AEO is obtained when α_i is in the range of 0.75-0.85 and B_{mg}=0.984 T. According to Figure 8b, the minimum GSC value is computed when B_{mg}=0.738 T and α_i=0.9. The impact of B_{mg} and the ratio of L/D on AEO are depicted in Figure 8c where its maximum values are available where L/D varies between 0.35 and 0.45 and B_{mg}=0.738 T. Figure 8d shows that the lowest GSC occurs at B_{mg}=0.738 T and L/D =0.5. In Figures 8e and 8f, the impact of B_{mg} and pole number on GSC and AEO is investigated. The maximum P as well as the maximum value of B_{mg} result in the minimum generation system cost. Besides, the maximum AEO is obtained when pole number is 20 and B_{mg}=0.984 T. It is seen in Figure 8g that when B_{mg} ranges between 0.85 and 0.95 T and ϵ=1, the maximum AEO is obtained. According to Figure 8h, the minimum GSC belongs to B_{mg}=0.984 T and ϵ=1. The impact of B_t and B_{mg} on AEO is shown in Figure 8i. It is observed that the maximum AEO is when B_{mg} and B_t are in the range of 0.8-0.85 T and 1.85-1.95 T, respectively. Also, as depicted in Figure 8j, the minimum generation system cost is observed at B_{mg}=0.984 T and B_t=2 T.

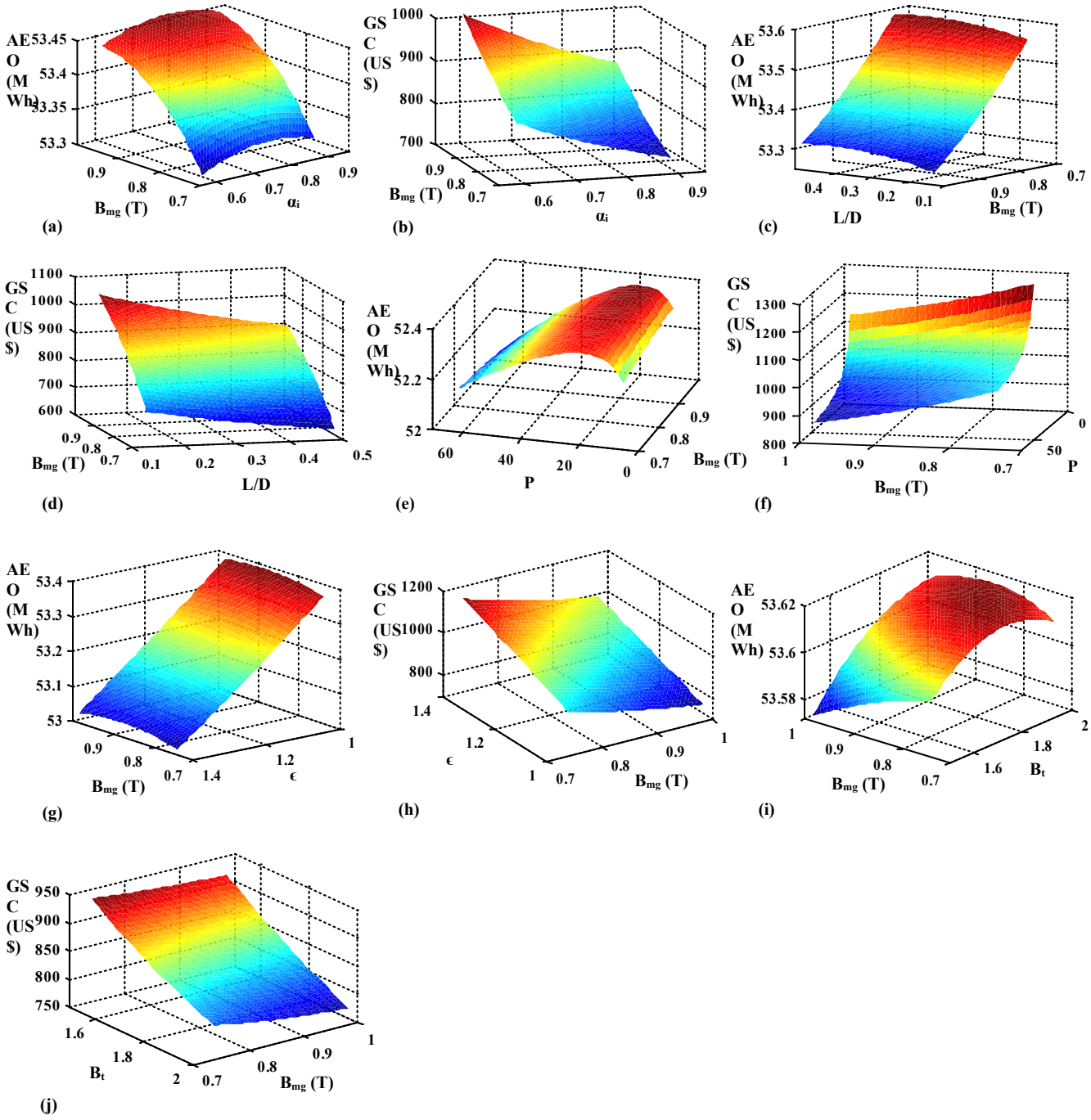

Figure 8. Impacts of B_{mg} and other design variables on GSC and AEO

4. Design optimization and results

The aim of this paper is to make a viable agreement between the cost and the AEO of generation system. In fact, the optimization procedure is considered in two parts, single-objective and multi-objective methods. In the case of single-objective method, the OR-PMWG cost and the AEO of

generation system are optimized separately. In the multi-objective method, these requirements are optimized simultaneously. The Lower Boundaries (LB) and the Upper Boundaries (UB) of design variables are listed in Table 3. To this point, three optimization cases have been employed:

Case A: The objective minimizes the OR-PMWG cost using Eq. (26).

Case B: The objective maximizes the AEO of generation system using Eq. (27).

Case C: The objective is used to optimize the multi-objective function given by Eq. (28).

$$F_1 = C_t \tag{26}$$

$$F_2 = \frac{1}{AEO_G} \tag{27}$$

$$F_3 = \frac{AEO_{G,ref}}{AEO_G} + \frac{C_t}{C_{t,ref}} \tag{28}$$

where $C_{t,ref}$ is the minimum value of the OR-PMWG cost and $AEO_{G,ref}$ is the maximum value of the AEO of generation system, which will be obtained by optimizing F_1 and F_2, respectively. Optimization results of different objective functions are listed in Table 4. It can be observed that Case B is more expensive, but gives more energy (AEO_G) than Case A. In comparison to Case A, Case B presents the increase of US$2096.44 (84.57 %) in the OR-PMWG cost corresponding to an increase in the AEO_G of 2.52 MWh (3.56 %). Consequently, Case A is a poor choice in terms of AEO of generation system, and the Case B is a poor choice in terms of manufacturing cost. It is clear that any attempt to achieve a high AEO for the generation system or a low OR-PMWG cost deteriorates other requirement. Therefore, a multi-objective optimization is required to make a satisfactory compromise between the OR-PMWG cost and the AEO of generation system. To this end, a flexible multi-objective function is defined as Eq. (28). According to Table 4, it is seen that compared to Case B, Case C (C_t= US$2651.51) presents a considerable reduction in the OR-PMWG cost and a moderate reduction in the AEO of the generation system. Also, compared to Case A, the AEO_G of Case C is 657.75 kWh higher with the moderate increase of US$172.53 (6.96 %) in the OR-PMWG cost. Thus, it yields a good compromise between the OR-PMWG cost and AEO of the generation system. The improvement of the multi-objective function F_3 in iterations of the optimization process is shown in Figure 9. Finally, the probability function of the Rayleigh distribution at an average wind speed of 8.7 m/s is seen in Figure 10a and the annual energy output of the generation system as a function of discrete wind speed is shown in Figure 10b.

Table 4. The optimization results for different objectives

Parameters	Range		The optimized values for different objectives		
	LB	UB	Case A	Case C	Case B
Am (kA/m)	10	55	47.86	36.21	11.93
Bmg (T)	0.738	0.984	0.982	0.983	0.981
L/D	0.14	0.5	0.16	0.17	0.21
ϵ	1	1.4	1.33	1.15	1.09
αi	0.6	0.9	0.77	0.83	0.88
P	8	64	12	12	14
By Stator (T)	1.1	1.5	1.49	1.35	1.1
By Rotor (T)	1.3	1.6	1.59	1.59	1.42
Bt (T)	1.5	2	1.55	1.51	1.75
AEOG (MWh)			70.73	71.39	73.25
OR-PMWG cost (US$)			2478.98	2651.51	4575.42
Generator full-load efficiency (%)			94.01	95.11	96.27
Generator full-load total losses (W)			955.45	771.01	579.94
g (mm)			0.56	0.58	0.73
f			15	15	17.5
Line-to-line Erms (V)			546.25	463.3	445.22

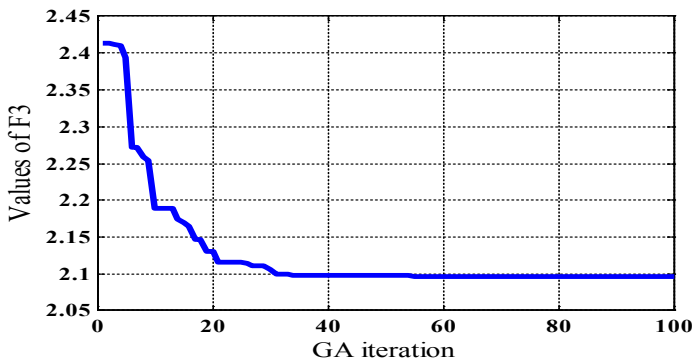

Figure 9. The improved values of F3 for the first 100 iterations

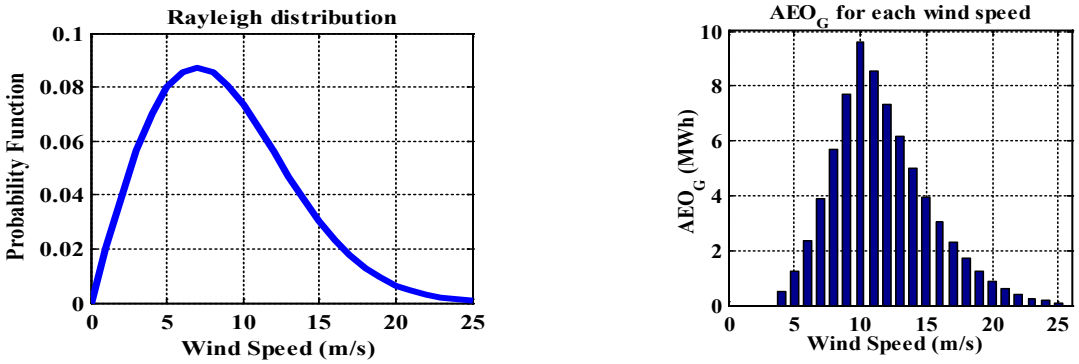

(a) (b)

Figure 10. (a) Rayleigh distribution at an average wind speed of 8/7 m/s, (b) AEO of the generation system as a function of discrete wind speed

4.1. Comparison with prototype generator

As shown in Table 5, the optimized generator parameters are presented and compared with a three-phase 15 kW direct-drive outer rotor permanent magnet wind power generator prototype, which was built and tested. It was found that the proposed optimization design achieved lower total volume and higher efficiency. On the other hand, the optimized generator is characterized by a six-phase configuration, which make it superior to the three-phase prototype generator in terms of reliability.

Table 5. Comparison of the optimized generator and prototype generator characteristics

Design parameters	OR-PMSG optimized parameters	PM generator grototype parameters [17]
Total volume (cm^3)	33094.1	33541.39
Efficiency	95.11	94.4
Stator outer diameter (D) (mm)	581.41	623
Generator outer diameter (D_e) (mm)	650.63	653.5
Magnet thickness (mm)	3.33	6
Stator stack length (mm)	99.54	100
Nominal line voltage (V)	408	408
Magnet to pole pitch ratio (α_i)	0.83	0.73
Frequency (Hz)	15	50
Number of poles	12	40
Nominal rotational speed (rpm)	150	150

5. FEA verification

In this section, the 3D FEA simulation method is used for verifying the effectiveness of the analytical design procedure (ADP) presented in this study. To do this, the Ansoft-MAXWELL® v.16 software package is employed. In the generator simulation process, resistive load is used because of a unitary PF considered in the design model. The evaluation is performed by a comparison of the optimized generator parameters and the FEA results, which can be seen in Table 6. It is observed that the difference between the ADP and FEA results is less than 2 %. Figure 11a depicts the mesh diagram of the generator finite element model, and Figure 11b shows the flux density distribution in various parts of the machine.

Table 6. Comparison between ADP and FEM results

PMSG parameters	ADP results	FEA results	Error (%)
Line-to-line E_{rms} (V)	463.3	461.7	0.34
V_L (V)	400	398.3	0.42
B_{mg1} (T)	1.21	1.19	1.65
P_{out} (W)	15000	14965	0.23
P_{in} (W)	15771	15748	0.14
B_y Stator (T)	1.35	1.33	1.5
B_y Rotor (T)	1.59	1.56	1.9
B_t (T)	1.51	1.5	0.66

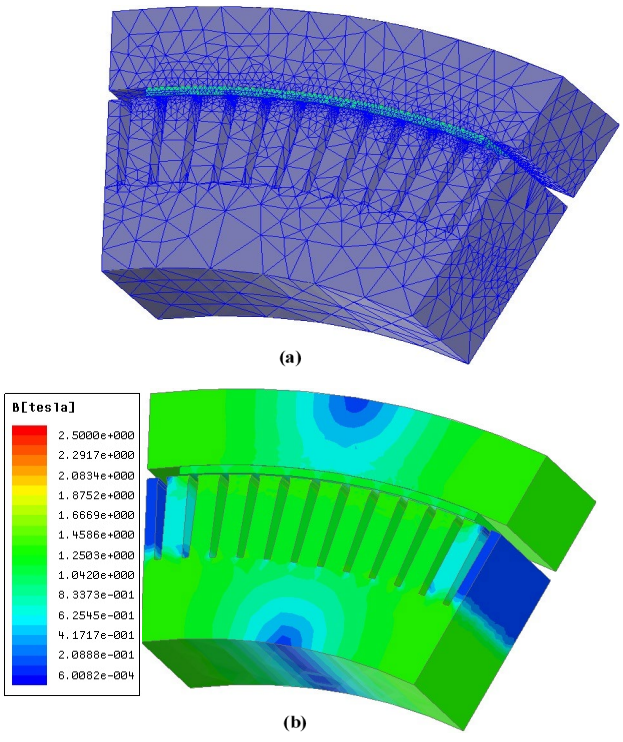

Figure 11. (a) The finite element mesh of the generator, (b) The magnetic flux density distribution of the generator

The curve of magnetic air gap flux density distribution is shown by Figure 12a under no-load conditions, in which the fundamental air gap flux density highest value (B_{mg1}) is measured 1.19 (T). Figure 12b shows the line-induced voltage waveforms in the no-load condition (line-to-line E_{rms}). The fundamental rms value E_{rms} is computed 461.7 (V) and the total harmonic distortion (THD) of voltage is 4.21 %. The waveforms of full-load terminal line voltages (V_L) are shown in Figure 12c. Fundamental rms value of these voltages is 398.3 V and their THD = 0.72 %. The waveform of the output power (P_{out}) in the full-load condition is given in Figure 12d. Its average value in steady state conditions is measured at about 14965 (W). Figure 12e shows the input power (P_{in}) waveform of the generator in the full-load condition. The average value of the measured input power is about 15748 W in steady-state conditions.

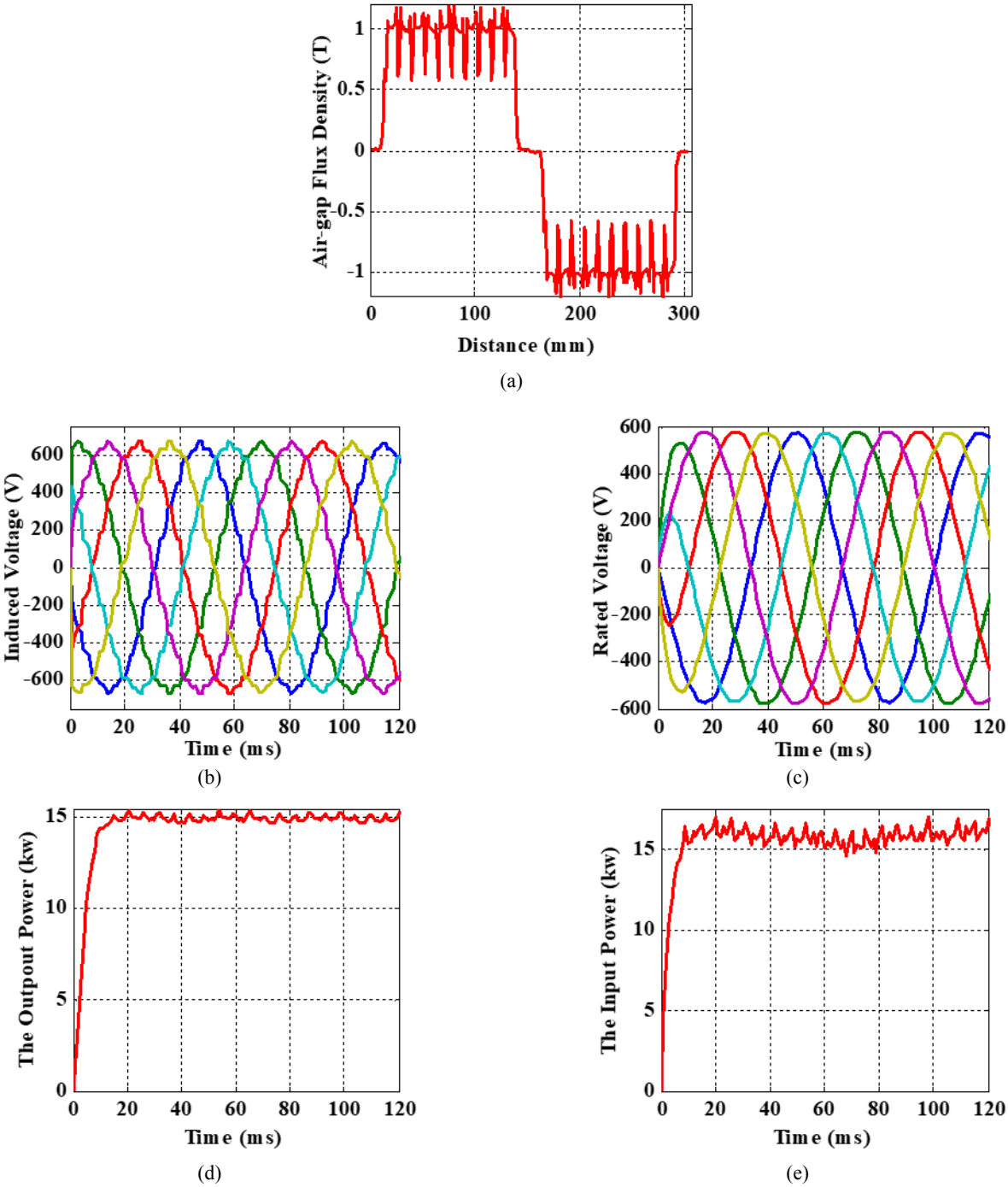

Figur 12. (a) Air-gap flux density curve, (b) No-load terminal line voltages, (c) Nominal line voltages, (d) The waveform of the generator full-load output power, (e) The waveform of the generator input power in the full-load condition

6. CONCLUSIONS

This study made an attempt to establish a multi-objective optimal design for a small-scale direct-drive wind power system in accordance with a PM synchronous generator with outer-rotor. This optimization problem was aimed at obtaining an optimum cost-effective OR-PMWG, i.e., high AEO and low cost of generation systems. The presented accurate model and design flowchart of OR-PMWG were the main novelties of this paper. In this regard, the generation system was firstly optimized for each of the objectives independently. Then, a multi-objective optimization design considering all the objectives was provided. It was also demonstrated that the

proposed multi-objective optimization afforded reliable performance in view of OR-PMWG design. It was shown that the AEOG was 657.75 (KWh) higher and GSC was 1923.91 (US$) lower than single-objective functions. To this end, the GA was applied to handling the optimization process. Furthermore, a comparison was made between the influential characteristics of the optimized generator and a prototype outer-rotor PM generator, indicating that the performance of the optimized PMSG was superior to that of the prototype generator in terms of efficiency as well as total volume. Moreover, as demonstrated by the results, the six-phase OR-PMWG was found to be more reliable. Eventually, the three-dimensional Finite Element Analysis (FEA) justifies the results obtained from the numerical optimization.

7. ACKNOWLEDGEMENT

The authors gratefully acknowledge the funding support obtained from Babol Noshirvani University of Technology with grant program numbers BNUT/370509/00 and BNUT/390066/00.

REFERENCES

1. Eterafi, S., Gorjian, S. and Amidpour, M., "Effect of covering aperture of conical cavity receiver on thermal performance of parabolic dish collector: Experimental and numerical investigations", ***Journal of Renewable Energy and Environment (JREE)***, Vol. 8, No. 4, (2021), 29-41. (https://dx.doi.org/10.30501/jree.2021.275871.1194).
2. Hosseini, E., Behzadfar, N., Hashemi, M., Moazzami, M. and Dehghani, M., "Control of pitch angle in wind turbine based on doubly fed induction generator using fuzzy logic method", ***Journal of Renewable Energy and Environment (JREE)***, Vol. 9, No. 2, (2022), 1-7. (https://dx.doi.org/10.30501/jree.2021.293546.1226).
3. Global Wind Energy Council, "Global wind report: Annual market update 2021", (2021). (https://gwec.net/wp-content/uploads/2021/03/GWEC-Global-Wind-Report-2021.pdf), (Accessed: 11 March 2021).
4. Abdoos, A.A, "A new intelligent method based on combination of VMD and ELM for short term wind power forecasting", ***Neurocomputing***, Vol. 203, (2016), 111-120. (https://doi.org/10.1016/j.neucom.2016.03.054).
5. Abdoos, A.A., Moazzen, M.E. and Hosseini, S.M., "Optimal design of an exterior-rotor permanent magnet generator for wind power applications", ***Journal of Operation and Automation in Power Engineering (JOAPE)***, Vol. 9, No. 3, (2021), 193-202. (https://doi.org/10.22098/JOAPE.2021.7337.1532).
6. Grauers, A., "Design of direct-driven permanent-magnet generators for wind turbines", Doctoral Thesis at School of Electrical and Computer Engineering, Chalmers University of Technology, (1996), 76-79. (https://www.osti.gov/etdeweb/servlets/purl/442505).
7. Hailemariam, Z.M., Leidhold, R. and Tesfamariam, G.T., "Real-time dc-link voltage control of 5-kW PMSG-based wind turbine generator through a test-rig", ***Electrical Engineering (EE)***, Vol. 103, (2021), 1869-1880. (https://doi.org/10.1007/s00202-020-01176-3).
8. Polinder, H., Pijl, F., Vilder, G. and Tavner, P., "Comparison of direct-drive and geared generator concepts for wind turbines", ***IEEE Transactions on Energy Conversion (IEEETEC)***, Vol. 23, No. 3, 725-733, (2006). (https://doi.org/10.1109/TEC.2006.875476).
9. Puri, V., Chauhan, Y.K. and Singh, N., "A comparative design study and analysis of inner and outer rotor permanent magnet synchronous machine for power generation in vertical axis wind turbine using GSA and GSA-PSO", ***Sustainable Energy Technologies and Assessments (SETA)***, Vol. 23, (2017), 136-148. (https://doi.org/10.1016/j.seta.2017.09.008).
10. Tapia, J., Pyrhönen, J., Puranen, J., Lindh, P. and Nyman, S., "Optimal design of large permanent magnet synchronous generators", ***IEEE Transactions on Magnetics (IEEETM)***, Vol. 49, No. 1, (2013), 642-650. (https://doi.org/10.1109/TMAG.2012.2207907).
11. Chen, J., Nayar, C.V. and Xu, L., "Design and finite-element analysis of an outer-rotor permanent-magnet generator for directly coupled wind turbines", ***IEEE Transactions on Magnetics (IEEETM)***, Vol. 36, No. 5, (2000), 3802-3809. (https://doi.org/10.1109/20.908378).
12. Li, H., Chen, Z. and Polinder, H., "Optimization of multibrid permanent- magnet wind generator systems", ***IEEE Transactions on Energy Conversion (IEEETEC)***, Vol. 24, No. 1, (2009), 82-92. (https://doi.org/10.1109/TEC.2008.2005279).
13. Lee, S., Kim, Y., Lee, K. and Kim, S., "Multiobjective optimization design of small-scale wind power generator with outer-rotor based on box–behnken design", ***IEEE Transactions on Applied Superconductivity (IEEETASC)***, Vol. 26, No. 4, (2016), 605-609. (https://doi.org/10.1109/TASC.2016.2524620).
14. Bazzo, T.P.M., Kolzer, J.F., Carlson, R., Wurtz, F. and Gerbaud, L., "Multiphysics design optimization of a permanent magnet synchronous generator", ***IEEE Transactions on Industrial Electronics (IEEETIE)***, Vol. 64, No. 12, (2017), 9815-9823. (https://doi.org/10.1109/TIE.2017.2726983).
15. McDonald, A. and Bhuiyan, N., "On the optimization of generators for offshore direct drive wind turbines", ***IEEE Transactions on Energy Conversion (IEEETEC)***, Vol. 32, No. 1, (2017), 348-358. (https://doi.org/10.1109/TEC.2016.2624219).
16. Asef, P., Perpiñà, R.B., Barzegaran, M.R., Lapthorn, A. and Mewes, D., "Multiobjective design optimization using dual-level response surface methodology and booth's algorithm for permanent magnet synchronous generators", ***IEEE Transactions on Energy Conversion (IEEETEC)***, Vol. 33, No. 2, (2018), 652-659. (https://doi.org/10.1109/TEC.2017.2777397).
17. Potgieter, J.H.J. and Kamper, M.J., "Torque and voltage quality in design optimization of low-cost non-overlap single layer winding permanent magnet wind generator", ***IEEE Transactions on Industrial Electronics (IEEETIE)***, Vol. 59, No. 5, (2012), 2147-2156. (https://doi.org/10.1109/TIE.2011.2159955).
18. Öztürk, N., Dalcalı, A., Çelik, E. and Sakar, S., "Cogging torque reduction by optimal design of PM synchronous generator for wind turbines", ***International Journal of Hydrogen Energy (IJHE)***, Vol. 42, (2017), 17593-17600. (https://doi.org/10.1016/j.ijhydene.2017.02.093).
19. Sedaghat, A., El Haj Assad, M. and Gaith, M., "Aerodynamics performance of continuously variable speed horizontal axis wind turbine with optimal blades", ***Energy***, Vol. 77, (2014), 752-759. (https://doi.org/10.1016/j.energy.2014.09.048).
20. Sedaghat, A., Samani, I., Ahmadi-Baloutaki, M., El Haj Assad, M. and Gaith, M., "Computational study on novel circulating aerofoils for use in Magnus wind turbine blades", ***Energy***, Vol. 91, (2015), 393-403. (https://doi.org/10.1016/j.energy.2015.08.058).
21. Abidoye, L.K., Bani-Hani, E., El Haj Assad, M., AlShabi, M., Soudan, B. and T Oriaje, A., "Effects of environmental and turbine parameters on energy gains from wind farm system: Artificial neural network simulations", ***Wind Engineering (WE)***, Vol. 44. No. 2, (2019), 181-195. (https://doi.org/10.1177/0309524X19849834).
22. Bazzo, T.P.M., Kolzer, J.F., Carlson, R., Wurtz, F. and Gerbaud, L., "Multidisciplinary design optimization of direct-drive PMSG considering the site wind profile", ***Electric Power Systems Research (EPSR)***, Vol. 141, (2016), 467-475. (http://dx.doi.org/10.1016/j.epsr.2016.08.023).
23. Li, F. and Zhu, X., "Comparative study of stepwise optimization and global optimization on a nine-phase flux-switching PM generator", ***Energies***, Vol. 14, No. 16, (2021), 4754. (https://doi.org/10.3390/en14164754).
24. Singh, G., Kumar, A. and Saini, R., "Performance evaluation of series compensated self-excited six-phase induction generator for stand-alone renewable energy generation", ***Energy***, Vol. 35, No. 1, (2010), 288-297. (https://doi.org/10.1016/j.energy.2009.09.021).
25. Pyrhönen, J., Jokinen, T. and Hrabovcová, V., Design of rotating electrical machines, Wiley, USA, (2009), 512-519. (https://doi.org/10.1002/9781118701591).
26. Boldea, I., Variable speed generators, CRC Press, (2005), 420-423. (https://doi.org/10.1201/b19293).
27. Gieras, J.F., Permanent magnet motor technology, design and applications, CRC Press, (2010), 100-102. (https://doi.org/10.1201/9780429292736).
28. Kurt, E, Gör, H. and Çelik, K., "Optimization of a 3-kW axial flux permanent magnet generator with variable air gap", ***International Transactions on Electrical Energy Systems (ITEES)***, Vol. 31, No. 11, (2021), e13074. (https://doi.org/10.1002/2050-7038.13074).

29. Khan, A. and Pillay, P., "Design of a PM wind, optimized for energy capture over a wide operating range", ***IEEE International Conference on Electrical Machines and Drives***, San Antonio, TX, USA, (2005), 1501-1506. (https://doi.org/10.1109/IEMDC.2005.195919)

30. Wang, T. and Wang, Q., "Optimization design of a permanent magnet synchronous generator for a potential energy recovery system", ***IEEE Transactions on Energy Conversion (IEEETEC)***, Vol. 27, No. 4, (2012), 856-863. (https://doi.org/10.1109/TEC.2012.2211080).

31. Eriksson, S. and Bernhoff, B., "Loss evaluation and design optimization for direct driven permanent magnet synchronous generators for wind power", ***Applied Energy (AE)***, Vol. 88, No. 1, (2011), 265-271. (https://doi.org/10.1016/j.apenergy.2010.06.010).

32. Jagau, H., Khan, M.A. and Barendse, P., "Design of a sustainable wind generator system using redundant material", ***IEEE Transactions on Industry Applications (IEEETIA)***, Vol. 23, No. 6, (2012), 1827-1837. (https://doi.org/10.1109/TIA.2012.2221672).

33. Iranian Renewable Energy Organization Magazine, (2010). (In Farsi). (http://www.satba.gov.ir/suna_content/media/image/2015/11/4222_orig.pdf), (Accessed: 15 July 2010).

34. Abdoos, A.A., Moazzen, M.E. and Ebadi, A., "Optimal design of a radial-flux permanent magnet generator with outer-rotor for direct-drive wind turbines", ***Computational Intelligence in Electrical Engineering (CIEE)***, Vol. 11, No. 4, (2020), 51-64. (In Farsi). (https://dx.doi.org/10.22108/isee.2020.117057.1227).

ABSTRACTS

Development of Rural Tourism in Iran Using PV-Based System: Finding the Best Economic Configuration

Mehdi Jahangiri [a*], Farhad Raeiszadeh [a], Reza Alayi [a,b], Atabak Najafi [c], Ahmad Tahmasebi [d]

[a] *Energy Research Center, Shahrekord Branch, Islamic Azad University, Shahrekord, Iran.*
[b] *Department of Mechanics, Germi Branch, Islamic Azad University, Germi, Iran.*
[c] *Department of Electrical Engineering, Eskisehir Osmangazi University, Eskisehir, Turkey.*
[d] *Department of Research and Development, Pars Regulator Company, Tehran, Iran.*

PAPER INFO

Paper history:
Received: 03 August 2021
Revised in revised form: 09 January 2022
Scientific Accepted: 18 January 2022
Published: 19 July 2022

Keywords:
Rural Tourism,
HOMER Software,
Sustainable Development,
Electricity Cost,
Total NPC

ABSTRACT

Rural tourism is an important factor in achieving economic, social, and cultural development. Given that villages in Iran do not have access to permanent electricity or are associated with high power outages, the provision of sustainable electricity through renewable energy can cause more tourists to choose these villages as their ultimate goal. Therefore, in this paper, for the first time, a hybrid system has been evaluated based on solar energy in 10 tourism target villages in Iran using HOMER software. This study investigated the design of the system with real and up-to-date data on equipment and fossil fuel prices taking into account transportation costs as well as a comprehensive study of energy-economic-environmental with electricity generation approach to the development of rural tourism. The results demonstrated that for the studied stations, the LCOE parameter was in the range of $ 0.615-0.722, the percentage of power supply by solar cells was in the range of 90-99 %, and the prevention of pollutants was 33.9-277 kg/year. According to the results, Meymand village is the most suitable and Mazichal village is the unsuitable station in the field of energy supply required by solar cells. The production pollution in the studied stations is mainly CO_2 and results from the operational phase of the project and its amount is 979.5 kg/year. Given that the rural tourism has grown and become a solution for development, the authors hope that the present work results can be used as a perspective to help energy and rural tourism decision-makers.

https://doi.org/10.30501/jree.2022.298089.1234

چکیده

گردشگری روستایی به‌عنوان ابزاری برای دستیابی به توسعه اقتصادی، اجتماعی، فرهنگی کارآفرینی می‌باشد. باتوجه به اینکه در ایران، روستاها دسترسی به برق دائمی ندارند و یا با قطعی برق زیاد همراه هستند، لذا تأمین برق پایدار توسط انرژی‌های تجدیدپذیر، می‌تواند سبب شود تا گردشگران بیشتری این روستاها را به‌عنوان هدف نهایی خود انتخاب کنند. لذا در کار حاضر برای نخستین بار یک سیستم هیبریدی مبتنی بر انرژی خورشیدی در ۱۰ روستای هدف گردشگری در ایران با استفاده از نرم‌افزار HOMER مورد ارزیابی قرار گرفته است. طراحی سیستم با داده‌های واقعی و به روز تجهیزات و قیمت سوخت فسیلی با لحاظ نمودن هزینه حمل و نقل و همچنین بررسی جامع انرژی-اقتصادی-زیست‌محیطی با رویکرد تولید برق بمنظور توسعه گردشگری روستایی، برای نخستین بار است که در کار حاضر انجام شده‌اند. نتایج بررسی‌ها نشان داد که برای ایستگاه‌های مورد بررسی، پارامتر LCOE در محدوده ۰/۷۲۲-۰/۶۱۵ دلار بوده، درصد تأمین برق توسط سلول‌های خورشیدی در محدوده ۹۹-۹۰ درصد بوده و جلوگیری از انتشار آلاینده‌ها ۲۷۷-۳۳/۹ کیلوگرم در سال بوده است. بر اساس نتایج، روستای میمند مناسب‌ترین و روستای مازیچال نامناسب‌ترین ایستگاه در زمینه تأمین انرژی مورد نیاز توسط سلول‌های خورشیدی هستند. آلودگی تولیدی مورد بررسی در ایستگاه های مورد مطالعه، عمدتاً CO_2 بوده و ناشی از مرحله عملیاتی پروژه است و مقدار آن سالیانه ۹۷۹/۵ کیلوگرم می‌باشد. با توجه به اینکه گردشگری روستایی رشد یافته و به یک راه‌حل برای توسعه تبدیل شده است، نویسندگان مقاله حاضر امیدوارند تا نتایج این کار بتواند به‌عنوان یک چشم‌انداز به کمک تصمیم‌گیران حوزه انرژی و گردشگری روستایی بیاید.

Development of a Solar Energy Operated Weeder for Wetland Paddy Crop

Gunasagar Sahu, Hifjur Raheman *

Department of Agricultural and Food Engineering, Indian Institute of Technology Kharagpur, Kharagpur, West Bengal, P. O. Box: 721302, India.

P A P E R I N F O

Paper history:
Received: 10 September 2021
Revised in revised form: 25 January 2022
Scientific Accepted: 23 November 2021
Published: 25 July 2022

Keywords:
Solar Photovoltaic,
Weeding Wheel,
Weeding Efficiency,
Cost of Weeding,
Brake-Even Point

A B S T R A C T

A solar energy operated two-row weeder was developed for weeding in wetland paddy crop. Its major components are power source, power transmission system, weeding wheels, and a float. The power source comprised a DC motor, solar panel, and power storage unit with maximum power point tracker and motor controller. Solar panel/power storage unit through a motor controller supplied power to the DC motor and it was transmitted to the shaft of the weeding wheel through a dog clutch. A pair of wheels attached with jaw tooth and plane blades at wheel circumference was used for carrying out weeding and movement of the weeder in the field. A float was used to prevent sinkage of the weeder in soft soil which, in turn, ensured stability during operation. The developed weeder could do weeding at a rate of 0.06 ha per hour with field efficiency, weeding efficiency, and plant damage of 83.3 %, 83 % and 2-3 %, respectively. As compared to cono-weeder, the cost of weeding was 41.2 % lower due to higher field capacity and fewer labor requirements. Annual use less than 4.13 ha for the developed weeder was found uneconomical for carrying out weeding. The developed powering system comprising solar photovoltaic panels could supply power to do weeding continuously for 2 hours with a maximum discharge of 20 % from the battery.

https://doi.org/10.30501/jree.2022.304080.1255

چکیده

یک دستگاه وجین‌کن دو ردیفه که از انرژی خورشیدی تغذیه می‌کند، جهت حذف علفزارها در نمزارهای شالیزار توسعه داده شد. اجزای اصلی این دستگاه: منبع نیرو، سیستم انتقال نیرو، چرخ‌های وجین و شناور است. منبع نیرو شامل یک موتور DC، پنل خورشیدی، واحد ذخیره‌سازی حداکثر نیرو با ردیاب نقطه توان و کنترل‌کننده موتور است. پنل خورشیدی/ واحد ذخیره انرژی از طریق یک موتور کنترل‌کننده، برق را به موتور DC می‌رساند و از طریق یک کلاچ دندانه‌ای به محور چرخ وجین منتقل می‌شود. یک جفت چرخ متصل به دندانه فک و تیغه‌های صفحه در محیط چرخ برای انجام وجین و حرکت علف هرز در مزرعه استفاده شد. یک شناور برای جلوگیری از فرو رفتن دستگاه علف‌زنی در خاک نرم استفاده شد که به نوبه خود پایداری را در طول عملیات تضمین می‌کرد. وجین‌کن توسعه‌یافته وجین علف‌های هرز را به میزان ۰/۰۶ هکتار در ساعت با بازده مزرعه، راندمان وجین علف هرز و مقدار خسارت به گیاه به ترتیب معادل ۸۳/۳، ۸۳ و ۳-۲ درصد انجام داد. در مقایسه با وجین‌کن یک ردیفه، هزینه وجین کردن به دلیل ظرفیت مزرعه بالاتر و نیاز به نیروی کار کمتر، ۴۱/۲ درصد کمتر بود. استفاده سالانه به میزان کمتر از ۴/۱۳ هکتار برای وجین‌کن توسعه‌یافته غیراقتصادی تشخیص داده شد. سیستم تغذیه توسعه‌یافته متشکل از پانل‌های فتوولتائیک خورشیدی می‌تواند انرژی لازم را برای انجام وجین علفهای هرز به‌مدت ۲ ساعت با حداکثر تخلیه ۲۰ درصد از باتری تأمین کند.

Energy Demand of Supplementary Lighting in Agricultural Greenhouses: Solar Energy Utilization

Iman Ayoobi, Ramin Roshandel *

Department of Energy Engineering, Sharif University of Technology, P. O. Box: 11365-9567, Tehran, Tehran, Iran.

P A P E R I N F O

Paper history:
Received: 17 September 2021
Revised in revised form: 05 February 2022
Scientific Accepted: 10 February 2022
Published: 25 July 2022

Keywords:
Greenhouse,
Natural Light,
Artificial Light,
Greenhouse Locations,
Greenhouse Shapes,
Photovoltaic Panel

A B S T R A C T

Light is a critical parameter for plant growth such that providing enough light for the plant can ensure better quality and higher yield in greenhouses. In many areas, in the cold seasons of the year, not enough natural light reaches the plant. Thus, to compensate for the natural light deficit, artificial light is used. Since the use of artificial light leads to energy consumption, effective parameters in the energy consumption of the lighting system such as available natural light, greenhouse shape, and the on-off plan of the lighting system should be considered. In this paper, available natural light is estimated based on greenhouse structure in five cities of Iran. Then, the natural light deficit was investigated. Finally, to achieve clean cultivation, the utilization of photovoltaic panels is investigated to compensate for the electrical energy needed for supplementary lighting. The results show that although Iran is recognized as a region with high solar energy potential, natural light is not enough for optimum tomato lighting demand. Using supplementary lighting in greenhouses could compensate for the lack of natural light in proportion to the capacity of the lighting system. In 73.22 % to 91.32 % of days in the period of September to April, the natural light is not sufficient for optimum lighting. Therefore, 98 ($kWh\ m^{-2}\ y^{-1}$) to 377 ($kWh\ m^{-2}\ y^{-1}$) electricity is needed to supply power for supplementary lighting system. Accordingly, the photovoltaic area and its associated with costs to compensate electrical energy consumption for the supplementary lighting is estimated to be 0.47 m^2_{PV} to 2.58 m^2_{PV} per m^2 of greenhouse area, which is equal to $ 171.08 to $ 939.12 per m^2 of greenhouse area, respectively.

https://doi.org/10.30501/jree.2022.305230.1258

چکیده

نور یک پارامتر حیاتی برای رشد گیاه است و اطمینان از دریافت نور کافی منجر به بهبود کیفیت و افزایش محصولات گلخانه می‌شود. در بسیاری از مناطق، در فصول سرد سال، نور طبیعی کافی به گیاه نمی‌رسد، بنابراین برای جبران کمبود نور طبیعی از نور مصنوعی استفاده می‌شود. از آن جایی که نور مصنوعی منجر به مصرف انرژی می‌شود، پارامترهای کلیدی مؤثر بر مصرف انرژی سیستم روشنایی نظیر نور طبیعی موجود در منطقه مورد نظر، شکل گلخانه و برنامه روشن و خاموش کردن سیستم روشنایی باید بررسی گردد. در این مقاله، نور طبیعی در دسترس بر اساس ساختار گلخانه در پنج شهر ایران تخمین زده شده است. در ادامه کمبود نور طبیعی موجود در شهرهای مذکور بررسی شده است. در انتها به منظور دستیابی به کشت پاک، استفاده از پنل فوتوولتائیک برای جبران مصرف انرژی سیستم روشنایی بررسی شده است. نتایج نشان می‌دهد که ایران با وجود آنکه به عنوان یک منطقه با پتانسیل بالای انرژی خورشیدی شناخته می‌شود، نور طبیعی مطلوب برای تأمین تقاضای گیاهانی نظیر گوجه فرنگی از مهر ماه تا فروردین ماه کافی نیست. استفاده از نور مصنوعی متناسب با ظرفیت آن، می‌تواند کمبود نور طبیعی را تا حدی جبران کند. درصد روزهایی که طی دوره کشت (۲۴ سپتامبر تا ۲۰ آپریل) نور کافی به گیاه نمی‌رسد، از ۷۳/۲۲ درصد تا ۹۱/۳۲ درصد تغییر می‌کند. به همین ترتیب، مساحت پنل فوتوولتائیک برای جبران تقاضای انرژی الکتریکی سیستم روشنایی از ۰/۴۷ مترمربع تا ۲/۵۸ مترمربع در هر مترمربع مساحت کشت گلخانه، تخمین زده می‌شود که به ترتیب معادل ۱۷۱/۰۸ دلار تا ۹۳۹/۱۲ دلار به ازای هر مترمربع از گلخانه است.

The Problem of Resilient Stochastic Unit Commitment with Consideration of Existing Uncertainties Using the Rate of Change of Frequency

Moslem Geravandi, Hassan Moradi CheshmehBeigi *

Department of Electrical Engineering, Faculty of Engineering, Razi University, P. O. Box: 67144-14971, Kermanshah, Iran.

P A P E R I N F O

Paper history:
Received: 24 September 2021
Revised in revised form: 09 December 2021
Scientific Accepted: 08 January 2022
Published: 16 August 2022

Keywords:
Resilience,
Unit Commitment,
Uncertainty,
Wind and Solar Power Plants,
Load Interruption Contracts,
Adaptive Frequency Load Shedding

A B S T R A C T

The ability of power systems against severe events shows their increased resilience, which in turn reduces the operation costs and recovery time of the system. This study presents a new resilient stochastic unit commitment model using the frequency change rate as a new index of system resilience. Furthermore, uncertainties of wind and solar power plants and demanded load are considered simultaneously. In the proposed method that considers the occurrence of a destructive incident in important production units in the worst-case scenarios and by using the generation capacity, adaptive frequency load shedding, and interrupting contracts, an effective strategy was provided to solve the unit commitment problem of thermal units to prevent instability in system frequency and to minimize unwanted load shedding. The proposed model was tested and evaluated on the IEEE 39-bus system with a wind power plant and a solar power plant. Moreover, the results obtained from simulation were reported. The effectiveness of this innovative approach in increasing the resilience of the power system against different degrees of uncertainty was confirmed based on the results.

https://doi.org/10.30501/jree.2022.306473.1262

چکیده

توانایی سیستم‌های قدرت در مقابله با حوادث شدید منجر به افزایش تاب‌آوری، کاهش هزینه‌ها و زمان بازیابی سیستم می‌شود. در این مقاله، با استفاده از نرخ تغییر فرکانس به‌عنوان شاخصی جدید برای تاب‌آوری سیستم، یک مدل جدید به‌مدار آمدن واحد تصادفی تاب‌آور ارائه شده است. علاوه بر این، عدم قطعیت‌های نیروگاه‌های بادی و خورشیدی و بار مورد نیاز، به‌طور همزمان درنظر گرفته می‌شود. در مدل پیشنهادی با وقوع یک حادثه مخرب در واحدهای تولیدی مهم در بدترین سناریوها، با استفاده از ظرفیت تولید، کاهش بار فرکانسی تطبیقی و قراردادهای قطع، یک استراتژی مؤثر برای حل مسئله به‌مدار آمدن واحدهای حرارتی برای جلوگیری از بی‌ثباتی در فرکانس شبکه و حداقل شدن میزان حذف بار ناخواسته، فراهم شده است. مدل پیشنهادی بر روی سیستم ۳۹ باسه IEEE همراه با یک نیروگاه بادی و یک نیروگاه خورشیدی آزمایش و ارزیابی شده و نتایج به دست آمده از شبیه‌سازی گزارش شده است. اثربخشی این روش ابتکاری در افزایش تاب‌آوری سیستم قدرت در حضور عدم قطعیت‌های مختلف، توسط نتایج تأیید شده است.

Sustainable Backup Power Supply of a Hospital by Designing a Hybrid Renewable Energy System

Setare Peirow, Fateme Razi Astaraei *, Amir Ali Saifoddin Asl, Hossein Yousefi

Department of Renewable Energies and Environment, Faculty of New Sciences and Technologies, University of Tehran, P. O. Box: 14399-56191, Tehran, Tehran, Iran.

P A P E R I N F O

Paper history:
Received: 13 September 2021
Revised in revised form: 18 June 2022
Scientific Accepted: 20 May 2022
Published: 22 August 2022

Keywords:
Hospital's Energy System,
Design-Builder Software,
Photovoltaic Panel,
PVsyst Software,
Economic and Environmental Assessment,
HOMER Pro Software

A B S T R A C T

The issue of power supply in hospitals is of special importance because of its direct effect on people's health conditions and vital treatment and care measures. Hospitals are among buildings with high energy consumption. The possibility of using renewable sources in their energy supply is one of the issues and challenges that specialists encounter. This paper discusses the possibility of installing a small solar power generation unit on a hospital rooftop to improve the quality of power supply systems. The case study is a hospital located in Tehran, Iran. For this purpose, the hospital energy system was modeled with the Design-Builder software. The obtained results were validated based on the actual consumption of the model specified in the hospital energy bills. According to the modeling step results, the annual consumption of the current energy system was 3.08 GWh of electricity and 4.23 GWh of gas. In the second step, a renewable power generation unit consisting of photovoltaic panels and battery was designed for the hospital's roof using PVsyst software. The designed power generation unit could produce 132 MWh of solar energy per year, of which 85 MWh may be sold to the main grid. The techno-economic and environmental feasibility study for the proposed system was performed using HOMER Pro software. The evaluation results revealed that considering the 20-year lifetime of the project, the proposed system achieved a lower energy cost and lower net present cost than the current system. Environmental assessment of the model by considering emission penalty indicated that the proposed system emitted fewer pollutant gases into the environment than the current system. Sensitivity analysis was also applied to investigate the effect of discounting and diesel fuel price variation on the system's energy cost. According to the results, a 4 % increase in the discount rate leads to a 14 % growth in the cost of energy for the project. Also, there was a direct relation between enhancement of the expected inflation rate and raising the net present cost of the project.

https://doi.org/10.30501/jree.2022.304704.1257

چکیده

موضوع تأمین توان در بیمارستان‌ها، به دلیل تأثیر مستقیم آن بر سلامت مردم و اقدامات مراقبتی و درمانی، از اهمیت بالایی برخوردار است. از طرف دیگر بیمارستان‌ها جزء ساختمان‌هایی با مصرف انرژی بالا می‌باشند و امکان بهره گیری از منابع تجدیدپذیر در تأمین انرژی آن‌ها، از موضوعات و چالش‌های پیش روی متخصصان می‌باشد. این مقاله به بررسی امکان نصب یک واحد کوچک تولید توان خورشیدی بر روی بام یک بیمارستان، به منظور ارتقاء کیفیت سیستم تأمین توان می‌پردازد. مورد مطالعه یک بیمارستان واقع در شهر تهران می‌باشد. برای این هدف، سیستم انرژی بیمارستان در نرم‌افزار دیزاین بیلدر مدل‌سازی شده و نتایج بدست آمده بر اساس مصرف واقعی مدل که در قبض‌های انرژی مشخص شده، اعتبارسنجی گردیده است. با توجه به نتایج مرحله‌ی مدل‌سازی، مصرف سالانه سیستم انرژی فعلی ۳/۰۸ GWh الکتریسیته و ۴/۲۳ GWh گاز می‌باشد. در مرحله بعدی، یک واحد تولید توان تجدیدپذیر که شامل پنل‌های فوتوولتاییک و باتری می‌باشد، بر روی بام بیمارستان با استفاده از نرم‌افزار پی‌وی‌سیست طراحی شده است. سیستم تولید توان طراحی شده، قابلیت تولید سالانه ۱۳۲ MWh توان را دارا می‌باشد که ۸۵ MWh از آن به شبکه‌ی اصلی فروخته می‌شود. امکان‌سنجی فنی- اقتصادی و زیست‌محیطی سیستم پیشنهادی با استفاده از نرم‌افزار هومر انجام گرفته است. نتایج ارزیابی آشکار کرد که با در نظر گرفتن طول عمر ۲۰ ساله برای پروژه، سیستم پیشنهادی نسبت به سیستم فعلی هزینه انرژی پایین‌تر و هزینه خالص فعلی کمتری دارد. ارزیابی زیست‌محیطی مدل با در نظر گرفتن جریمه‌ی انتشار، نشان داد که سیستم پیشنهادی در مقایسه با سیستم فعلی گازهای آلاینده کمتری وارد محیط‌زیست می‌کند. آنالیز حساسیت نیز به منظور تشخیص تأثیر تغییرات نرخ تنزیل و قیمت سوخت بر هزینه انرژی سیستم، اعمال شد. با توجه به نتایج بدست آمده، ۴ درصد افزایش نرخ تنزیل منجر به رشد ۱۴ درصدی هزینه‌ی انرژی پروژه می‌گردد. همچنین رابطه‌ی مستقیمی بین افزایش نرخ تورم و بالارفتن هزینه خالص فعلی پروژه وجود دارد.

Numerical Modeling and Evaluation of a Downwind Pre-Aligned Wind Turbine with an Innovative Blade Geometry Concept

Amir Hossein Zare [a,b], Esmail Mahmoodi [c*], Mohsen Boojari [a], Ali Sarreshtehdari [a]

[a] *Department of Mechanical Engineering, Shahrood University of Technology, P. O. Box: 3619995161-316, Shahrood, Semnan, Iran.*
[b] *Fars Power Generation Management Company, Shiraz, Fars, Iran.*
[c] *Department of Mechanical Engineering of Biosystem, Shahrood University of Technology, P. O. Box: 3619995161-316, Shahrood, Semnan, Iran.*

PAPER INFO

Paper history:
Received: 03 October 2021
Revised in revised form: 27 January 2022
Scientific Accepted: 27 February 2022
Published: 04 September 2022

Keywords:
Extreme-Scale Wind Turbines,
Pre-Aligned Rotor,
CFD Simulation,
Wake Simulation

ABSTRACT

Significant growth of the wind power market has led to a dramatic increase in the scale and capacity of wind turbines over the past decades. As these extreme-scale structures are expected to pose a wide range of challenges, an innovative concept which both lightens blade's mass and improves their aerodynamic performance, is vital for the future of rotor's design. In the present study, modeling and evaluating of an innovative pre-aligned rotor design based on SANDIA SNL100-00 wind turbine blade were accomplished. To evaluate the aerodynamic performance of the proposed rotor, CFD simulation was used as a well-developed technique in fluid mechanic. In the new rotor design, the swept area was increased using an equal blade length and the blade sections were more appropriately aligned with the wind flow compared to the reference model. This enhancement attained due to transferring the bending position from the root to a certain point alongside the length of blade. According to simulation assessments, this modification led to the overall improvement of main performance parameters in terms of the mean power and the applied torque on the blades. The simulation revealed that the novel concept is capable of increasing the mean power coefficient by 13.21 % compared to the conventional rotor designs. Analysis of the axial induction in front of the rotor plane displayed a greater drop in the flow velocity streaming up to the rotor, which could lead to have a more efficient configuration for harnessing the upcoming wind's power.

https://doi.org/10.30501/jree.2022.306692.1264

چکیده

رشد قابل توجه بازار انرژی بادی در دهه‌های اخیر، منجر به افزایش چشمگیر ابعاد و ظرفیت توربین‌های بادی شده است. باتوجه به آنکه انتظار میرود این سازه‌های عظیم با طیف وسیعی از چالش‌ها مواجه شوند، ارائه یک ایده نوین طراحی که منجر به کاهش وزن پره‌ها و بهبود عملکرد آیرودینامیکی آن‌ها بشود، ضروری می‌باشد. در این پژوهش، مدلسازی و اعتبارسنجی یک روتور پیش-تنظیم شده با طراحی نوین که براساس توربین بادی پروژه SANDIA SNL100-00 می‌باشد، صورت پذیرفته است. بررسی و اعتبارسنجی عملکرد آیرودینامیکی روتور پیشنهادی توسط شبیه‌سازی دینامیک سیالات محاسباتی (CFD) که یک رهیافت توسعه یافته در علم مکانیک سیالات است، انجام گرفت. در طراحی جدید این روتور، مساحت جاروب باوجود پره‌های با طول برابر با طرح اصلی، افزایش یافت؛ همچنین همراستایی سطح مقطع‌های مختلف پره در جریان باد نسبت به مدل مرجع بهبود یافت. علت این بهبود، تغییر محل خمش پره از ریشه به نقطه‌ای دیگر در طول پره می‌باشد. طبق نتایج شبیه‌سازی، اصلاحات انجام شده منجر به بهبود کلی مشخصه‌های عملکردی اصلی از جمله توان متوسط و گشتاور اعمالی بر پره‌ها شد. نتایج شبیه‌سازی‌ها نشانگر امکان افزایش ۱۳/۲۱ ٪ ضریب توان متوسط توربین‌ها با ایده نوین، در قیاس با روتورهای با طراحی متداول بود. آنالیز الگوی ضریب القای محوری در مقطع جلوی روتور با طراحی نوین، حاکی از افت بیشتر سرعت جریان آزاد بود که طبق قانون بتز این امر منجر به تشکیل یک پیکره‌بندی بهینه‌تر برای روتور جهت استخراج توان جریان باد می‌شود.

Methyl-Esters from Ternary Oil Blend Using Catalyst Synthesized from Mixed Agro-Wastes

Ayowumi Rita Soji-Adekunle [a*], Eriola Betiku [b], Abraham A. Asere [c]

[a] *Department of Mechanical Engineering, Faculty of Engineering, Adeleke University, P.M.B. 250, Ede, Osun State, Nigeria.*
[b] *Department of Chemical Engineering, Faculty of Technology, Obafemi Awolowo University, P.M.B. 13, Ile-Ife, Osun State, Nigeria.*
[c] *Department of Mechanical Engineering, Faculty of Technology, Obafemi Awolowo University, P.M.B. 13, Ile-Ife, Osun State, Nigeria.*

PAPER INFO

Paper history:
Received: 07 December 2021
Revised in revised form: 07 February 2022
Scientific Accepted: 27 February 2022
Published: 20 September 2022

Keywords:
Non-Edible,
Biodiesel,
Catalyst,
Transesterification,
Microwave,
Irradiation

ABSTRACT

This study used ternary substrates consisting of honne, neem, and yellow oleander (HONOYO) oil blend to produce methyl-esters for sustainability of raw materials for biodiesel synthesis. A biomass-based catalyst from calcined mixed agro-wastes consisting of kolanut pod, cocoa pod, and plantain peel ash was employed to transesterify the blend. A two-step method was adopted to convert HONOYO into methyl-esters. Taguchi L9 experimental design tool was used to ascertain the interactive effects of microwave irradiation power (W), Methanol/oil ratio (MeOH), time (min), and agro-wastes synthesized catalyst ASC (wt %) on the yield of methyl-esters from HONOYO. Results demonstrated that at 3:1 MeOH, microwave power of 150 W, ASC of 1.5 wt %, and reaction time of 1 minute, a yield of 80.96 % was achieved. HONOYOB satisfied ASTM D6751 and EN 14214 standards. Performance evaluation of the process input variables suggests weight of ASC as the most significant process parameters for HONOYOB yield. This work authenticates that biomass catalyst from agricultural wastes can adequately be applied to synthesis biodiesel effectively from blends of non-edible oils to supplement fossil diesel.

https://doi.org/10.30501/jree.2022.317615.1294

چکیده

این مطالعه از بسترهای سه تایی متشکل از ترکیب روغن هون، چریش و خرزهره زرد (HONOYO) برای تولید متیل استرها جهت مواد خام پایدار و سنتز بیودیزل استفاده کرده است. مخلوطی از ضایعات کشاورزی کلسینه شده متشکل از مغز قهوه ی سودانی، غلاف کاکائو و خاکستر پوست درخت چنار بعنوان کاتالیزور زیستی برای ترانس استری کردن ترکیب، مورد استفاده قرار گرفت. یک روش دو مرحله‌ای برای تبدیل HONOYO به متیل استر استفاده شد. از روش طراحی آزمایش تاگوچی L9 برای تعیین اثرات متقابل توان تابش امواج مایکروویو (W)، نسبت متانول به روغن، زمان (دقیقه) و ضایعات کشاورزی سنتزشده کاتالیزور (درصد وزنی) بر روی بازده متیل استرهای HONOYO استفاده شد. نتایج نشان داد که با نسبت روغن به متانول ۳:۱، توان مایکروویو ۱۵۰ وات، ۱/۵ درصد وزنی کاتالیست و زمان واکنش ۱ دقیقه، بازده‌ای به مقدار ۸۰/۹۶ درصد حاصل می‌شود. متیل استر HONOYOB از استانداردهای ASTM D6751 و EN 14214 برخوردار است. ارزیابی عملکرد متغیرهای ورودی فرآیند، وزن کاتالیست را به عنوان مهم‌ترین پارامتر فرآیند برای بازده HONOYOB نشان می‌دهد. این نتیجه تأیید می‌کند که کاتالیزور زیست‌توده از ضایعات کشاورزی می‌تواند به بطور مؤثر برای سنتز بیودیزل از مخلوط روغن‌های غیر خوراکی استفاده شود.

Maiden Application and Control Parameter Sensitivity Analysis of Fractional Order Tilt Integral Derivative Controller in Standalone Solar Photovoltaic System

Anupama Subhadarsini *, Babita Panda, Byamakesh Nayak

Department of Electrical Engineering Technology, School of Electrical Engineering, KIIT deemed to be University, Bhubaneswar, India.

P A P E R I N F O

Paper history:
Received: 31 October 2021
Revised in revised form: 12 February 2022
Scientific Accepted: 27 February 2022
Published: 08 October 2022

Keywords:
Fractional Order Controller,
Optimal Performance,
Error Minimization,
HGPSJO,
FOTIDC

A B S T R A C T

The solar photovoltaic system is modeled in Simulink using Matlab. Boost converter, FOTIDC controller, and Reduced Switch Multilevel Inverter are all included in this PV system (RSMLI). With regard to solar photovoltaic systems, the focus of this study is on the Fractional Order Tilt Integral Derivative Controller (FOTIDC). In the suggested control technique, Hybrid Genetic Particle Swarm Jaya Optimization is used to optimize the control parameters (HGPSJO). Jaya Optimization (JO) is a hybrid of the Particle Swarm Optimization (PSO), Genetic Algorithm (GA), and GA/PSO algorithm optimization techniques, combining the best of each for improved control executions. Control performance is enhanced using a fractional calculus-based technique to redesign the Tilt Integral Derivative Controller (TIDC) in order to reduce noise and harmonic distortions. Harmonic distortion and voltage magnitude are reduced by applying the proposed control method to the PV system. Simulated Matlab environments are used to test the stability, robustness, and stability of the proposed system as well as its capacity to reduce harmonic distortions. It is also compared to other well-known control techniques in order to ensure that the real-time implementation is properly validated.

https://doi.org/10.30501/jree.2022.312874.1274

چکیده

سیستم فتوولتائیک خورشیدی در نرم‌افزار سیمولینک و با استفاده از نرم‌افزار متلب مدل‌سازی شده است. مبدل تقویت کننده، کنترل کننده FOTIDC و اینورتر چند سطحی سوئیچ کاهش یافته، همگی در این سیستم فتوولتائیک (RSMLI) گنجانده شده‌اند. با توجه به سیستم‌های فتوولتائیک خورشیدی، تمرکز این مطالعه بر روی کنترل‌کننده مشتق انتگرال شیب مرتبه کسری (FOTIDC) است. در روش کنترل پیشنهادی، از بهینه‌سازی ترکیبی ذرات ژنتیکی ازدحام Jaya برای بهینه‌سازی پارامترهای کنترل (HGPSJO) استفاده می‌شود. روش بهینه‌سازی Jaya یا (JO) ترکیبی از تکنیک‌های بهینه‌سازی ازدحام ذرات (PSO)، الگوریتم ژنتیک (GA) و بهینه‌سازی الگوریتم GA/PSO است که بهترین‌ها را برای اجرای کنترل‌های بهبود یافته ترکیب می‌کند. عملکرد کنترل با استفاده از یک تکنیک مبتنی بر حساب کسری برای طراحی مجدد کنترل کننده مشتق انتگرال شیب (TIDC) به منظور کاهش نویز و اعوجاج هارمونیک افزایش می‌یابد. اغتشاش هارمونیک و بزرگی ولتاژ با اعمال روش کنترل پیشنهادی برای سیستم PV کاهش می‌یابد. محیط های شبیه‌سازی شده متلب برای آزمایش پایداری، استحکام و پایداری سیستم پیشنهادی و همچنین ظرفیت آن برای کاهش اغتشاش هارمونیک استفاده می‌شود. همچنین با سایر تکنیک‌های کنترل شناخته شده مقایسه شده تا اطمینان حاصل شود که پیاده‌سازی بلادرنگ به درستی اعتبارسنجی شده است.

Bio-Based Lubricant Synthesis by Chemical Modification of Linoleic and Oleic Acid Mixture

Sharareh Esmaeili [a], Kambiz Tahvildari [a*], Barat Ghobadian [b], Masoud Dehghani-Soufi [c*], Sanaz Mohammadzadeh Koumleh [d], Tirth Panchal [e]

[a] *Young Researchers and Elites Club, North Tehran Branch, Islamic Azad University, Tehran, Tehran, Iran.*
[b] *Department of Biosystems Engineering, School of Agriculture, University of Tarbiat Modares, P. O. Box: 14115-111, Tehran, Tehran, Iran.*
[c] *School of Environment, College of Engineering, University of Tehran, P. O. Box: 1417853111, Tehran, Tehran, Iran.*
[d] *Faculty of Chemistry, Shahroud University of Technology, P. O. Box: 3619995161, Shahroud, Semnan, Iran.*
[e] *C1 Water Industries LLC, Dubai Industrial City, Dubai, United Arab Emirates.*

PAPER INFO

Paper history:
Received: 18 January 2022
Revised in revised form: 05 May 2022
Scientific Accepted: 21 May 2022
Published: 11 December 2022

Keywords:
Biolubricant,
Epoxidation,
Esterification,
Linoleic Acid,
Oleic Acid

ABSTRACT

The presence of increasing concerns and enforcement of growing regulations over environmental pollution are nowadays at play. The pollution arising from mineral oils is among the major concerns. With the gradual reducation of the world oil reserves, an increasing pressure comes into play for finding sustainable alternatives. Being appealing alternatives, vegetable oils consist of different fatty acids; however, they cannot be applied directly to internal combustion engines owing to their poor oxidation stability and high pour point value. Biolubricants are considered to be a new generation of lubricants, which are renewable and biodegradable and are produced from the chemical modification of vegetable oils. There are few studies investigating the feasibility of using the mixture of fatty acids as biolubricant feedstock. In this study, epoxidation, oxirane ring opening with palmitic acid and p-Toluenesulfonic acid, esterification reaction with octanol, and reaction of the remaining hydroxyl group with stearic acid were applied to modify the mixture of oleic and linoleic fatty acids and produce biolubricant. For this purpose, the IR spectrums of each epoxide, monoester, diester, and triester products were obtained and analyzed. At the end of the experiments, monoester, diester, and triester were obtained with 94 % yield, with 96 % yield, and with 98 % yield, respectively. Eventually, the final product was found with physicochemical properties comparable with the physicochemical properties of the lubricant standard ISO VG10.

https://doi.org/10.30501/jree.2022.316482.1282

چکیده

امروزه وجود نگرانی‌های در حال رشد و اجرای مقررات فزاینده در مورد آلودگی محیط زیست مطرح است. یکی از نگرانی‌های عمده، آلودگی ناشی از روانکارهای نفتی است. با کاهش ذخایر نفت جهان، فشارها برای یافتن جایگزین‌های پایدار در حال افزایش است. روغن های گیاهی جایگزین‌های جذابی هستند که از اسیدهای چرب مختلف تشکیل شده‌اند. با این حال، آنها را نمی توان به طور مستقیم در موتورهای درون‌سوز به دلیل پایداری اکسیداسیون ضعیف و نقطه ریزش بالا استفاده کرد. روانکارهای زیستی نسل جدیدی از روان کننده‌ها هستند که تجدیدپذیر و زیست‌تخریب‌پذیر بوده و از اصلاح شیمیایی روغن‌های گیاهی تولید می‌شوند. مطالعات کمی وجود دارند که امکان استفاده از مخلوط اسیدهای چرب را به عنوان ماده اولیه روان‌کننده زیستی بررسی می‌کنند. در این مطالعه از اپوکسیداسیون، باز شدن حلقه اکسیران با اسید پالمیتیک و پاراتولوئن سولفونیک اسید، واکنش استریفیکاسیون با اکتانول و واکنش گروه هیدروکسیل باقیمانده با اسید استئاریک برای اصلاح مخلوط اسیدهای چرب اولئیک و لینولئیک و تولید روان‌کننده زیستی استفاده شد. برای این منظور، طیف‌های IR هر یک از محصولات اپوکسید، مونو استر، دی استر و تری استر به دست آمد و مورد تجزیه و تحلیل قرار گرفت. در پایان آزمایشات، مونو استر، دی استر و تری استر به ترتیب با عملکرد ۹۴ درصد، ۹۶ درصد و ۹۸ درصد به دست آمد. در نهایت، خواص فیزیکوشیمیایی محصول نهایی با ویژگی‌های استاندارد روان‌کننده ISO VG10 قابل مقایسه بود.

Multiobjective Design Optimization of a Multi-Phase Outer-Rotor Permanent Magnet Wind Generator

Ali Ebadi *, Ali Akbar Abdoos, Mohammad Ebrahim Moazzen, Sayyed Asghar Gholamian

Department of Electrical and Computer Engineering, Babol Noshiravani University of Technology, P. O. Box: 47148-71167, Babol, Mazandaran, Iran.

PAPER INFO

Paper history:
Received: 28 February 2022
Revised in revised form: 02 June 2022
Scientific Accepted: 20 June 2022
Published: 18 December 2022

Keywords:
Optimization,
Permanent Magnet Generator,
Wind Power,
Genetic Algorithm

ABSTRACT

Nowadays, the Permanent Magnet (PM) generator has become an instrumental tool for wind power generation due to its high performance. In this study, an optimal design is established to provide a cost-effective multiphase outer-rotor PM wind generator (OR-PMWG). The cost of the generation system (generator and power converter) as well as the annual energy output must be optimized to ensure cost-effective PM wind generation. In fact, the main novelty of this paper lies in the presentation of an accurate model of OR-PMWG and the investigation of the design variables affecting annual energy output and the generation system cost (GSC). In this respect, a multi-objective framework is presented to make satisfactory agreement among all objectives. At first, the main optimal design objectives namely generation system cost and annual energy output are optimized separately and then, a multi-objective optimization is established, in which all the objectives are considered simultaneously. In order to tackle these optimization problems, Genetic Algorithm (GA) is adopted herein to determine the design variables. It is also shown that simultaneous optimization with 71.39 (MWh) AEO and 2651.51 (US$) GSC leads to a more optimal design for a PM wind generation system. In addition, the effectiveness of the presented optimal design is demonstrated by making a comparison between a prototype outer-rotor PM wind generator and the theoretical counterpart. Finally, a finite element analysis (FEA) is carried out for the validation of the outcomes obtained from the proposed optimal design.

https://doi.org/10.30501/jree.2022.317176.1287

چکیده

امروزه، ژنراتورهای آهنربای دائم به دلیل کارایی بالایی که دارند به تجهیزی مناسب جهت تولید انرژی الکتریکی از نیروی باد تبدیل شده‌اند. در این پژوهش، طراحی بهینه یک ژنراتور آهنربای دائم رتور خارجی چند فازه مقرون به‌صرفه انجام شده است. به منظور دستیابی به یک ژنراتور بادی مقرون به‌صرفه، هزینه سیستم (ژنراتور و مبدل الکترونیک قدرت) و همچنین انرژی تحویلی سالیانه به شبکه بهینه شده‌اند. درواقع نوآوری این مقاله ارائه یک مدل دقیق از ژنراتور آهنربای دائم رتور خارجی و همچنین بررسی تأثیر متغیرهای طراحی بر انرژی تحویلی سالیانه به شبکه و هزینه سیستم تولید می‌باشد. در همین راستا، یک چارچوب چند هدفه برای ایجاد هماهنگی رضایت‌بخش میان همه اهداف ارائه شده است. ابتدا، اهداف اصلی طراحی بهینه یعنی هزینه سیستم تولید و انرژی تحویلی سالیانه به شبکه به طور جداگانه بهینه شده و سپس بهینه‌سازی چند هدفه به منظور بهینه‌سازی همزمان اهداف مورد نظر انجام شده است. برای انجام بهینه‌سازی از الگوریتم ژنتیک به منظور تعیین متغیرهای طراحی استفاده شده است. نشان داده شده است که بهینه‌سازی همزمان با انرژی تحویلی سالیانه به شبکه ۷۱/۳۹ مگاوات ساعت و هزینه سیستم تولید ۲۶۵۱/۵۱ دلار آمریکا، منجر به بهینه‌سازی بهتر برای ژنراتور آهنربای دائم بادی شده است. علاوه براین، به منظور نشان دادن اثربخشی طراحی بهینه ارائه شده، با یک نمونه ژنراتور آهنربای دائم رتور خارجی بهینه شده واقعی مقایسه شده است. در پایان نیز از تحلیل اجزای محدود به منظور اعتبارسنجی نتایج بدست آمده از طراحی بهینه استفاده شده است.

CONTENTS

Journal Homepage: www.jree.ir